

University of New Hampshire

University of New Hampshire Scholars' Repository

Doctoral Dissertations

Student Scholarship

Spring 2020

Broadband radio mapping and imaging of lightning processes

Julia Napolin Tilles

University of New Hampshire, Durham

Follow this and additional works at: <https://scholars.unh.edu/dissertation>

Recommended Citation

Tilles, Julia Napolin, "Broadband radio mapping and imaging of lightning processes" (2020). *Doctoral Dissertations*. 2519.

<https://scholars.unh.edu/dissertation/2519>

This Dissertation is brought to you for free and open access by the Student Scholarship at University of New Hampshire Scholars' Repository. It has been accepted for inclusion in Doctoral Dissertations by an authorized administrator of University of New Hampshire Scholars' Repository. For more information, please contact nicole.hentz@unh.edu.

BROADBAND RADIO MAPPING AND IMAGING OF LIGHTNING PROCESSES

BY

JULIA NAPOLIN TILLES

BS, Physics, University of Massachusetts Amherst, USA, 2008
MS, Physics, New Mexico Tech, USA, 2015

DISSERTATION

Submitted to the University of New Hampshire
in Partial Fulfillment of
the Requirements for the Degree of

Doctor of Philosophy

in

Physics

May 2020

ALL RIGHTS RESERVED

©2020

Julia Napolin Tilles

This dissertation has been examined and approved in partial fulfillment of the requirements for the degree of Doctor of Philosophy in Physics by:

Advisor, Ningyu Liu,
Professor of Physics
and Space Science Center

Co-advisor, Joseph R. Dwyer,
Professor of Physics
and Space Science Center

Shawna Hollen,
Assistant Professor of Physics

Harlan Spence,
Professor of Physics
and Space Science Center

Paul R. Krehbiel,
Professor of Physics,
New Mexico Tech,
Socorro, NM

on 5/4/2020.

Original approval signatures are on file with the University of New Hampshire Graduate School.

This thesis is dedicated to my mother and father, Elizabeth and Richard Tilles.

ACKNOWLEDGMENTS

The work herein was possible because of the many people who helped me along the way. First and foremost, I would like to thank my advisor, Ningyu Liu, who both encouraged me and challenged me to be a better scientist. I cannot thank him enough for continually focusing my energy in a forward direction – without his patience and support, this dissertation would not have been possible. I would also like to thank my committee member Joe Dwyer, specifically for sharing his invaluable insight into relativistic processes, but in general for being another supportive mentor in New Hampshire. I would also like to thank my committee member Paul Krehbiel at New Mexico Tech, who is a wealth of lightning knowledge and has played an active role in my research throughout my career as a lightning scientist. Without his involvement, and the involvement of New Mexico Tech in general – notably Mark Stanley, Bill Rison, and Dan Rodeheffer – as well as Robert Brown and Jennifer Wilson at Kennedy Space Center, the work presented in this dissertation would not have been possible. Thank you to all my committee members, to include also Shawna Hollen and Harlan Spence, for their guidance in the PhD proposal process, for serving at the PhD defense, and for ultimately helping shape this dissertation. Thank you to my friend and unofficial lightning mentor Michael Stock, who, aside from developing the instrument that is the main crux of my dissertation, took me under his wing when I first started studying lightning in 2013, and has been an immense source of enthusiasm and knowledge on both lightning and interferometry. In addition, I would like to thank Ron Thomas at New Mexico Tech, who also helped shape my early experience as a lightning scientist. There are so many people at the University of New Hampshire that I would like to thank for supporting me during my studies, but in particular I would like to thank my fellow lightning students and office mates, Chris Sterpka and Jacob Koile, for our daily discussions on lightning (and other non-lightning topics) – I never felt like a quitter with them around. Lastly, thank you to Hamid Rassoul for helping me start my PhD research at the Florida Institute of Technology, which ultimately led to this dissertation.

TABLE OF CONTENTS

	Page
ACKNOWLEDGMENTS	v
NOMENCLATURE	ix
LIST OF TABLES	ix
LIST OF FIGURES	xi
ABSTRACT	xxxvi
I Introduction	1
1. OVERVIEW	2
2. PHENOMENOLOGY	6
2.1 Thunderstorms	7
2.2 Lightning leaders	13
2.3 Streamers	21
2.3.1 Streamers in the lab	21
2.3.2 Streamers in thunderstorms	25
2.4 Narrow bipolar events (NBEs)	29
2.5 Initial breakdown pulses (IBPs)	34
2.6 Terrestrial gamma-ray flashes (TGFs)	39
3. LIGHTNING PROBLEMS AND HYPOTHESES	48
4. SCIENTIFIC CONTRIBUTIONS	51
II Instrumentation and methods	53
5. BROADBAND RADIO INTERFEROMETRY	55

5.1	Hardware	55
5.2	Concept	58
5.3	Imaging and mapping algorithm	61
5.4	Image simulations	66
6.	FAST ELECTRIC FIELD ANTENNA	69
6.1	Hardware	69
6.2	Electric field due to vertical radiating antenna	71
7.	LIGHTNING MAPPING ARRAY	73
7.1	Hardware and processing	73
7.2	Data analysis	75
III	Results	81
8.	FAST NEGATIVE BREAKDOWN	82
8.1	Overview	82
8.2	Fast breakdown events in an NBE-prolific thunderstorm	83
8.3	Fast breakdown polarity	88
8.4	NBE source characterization	88
8.5	Fast breakdown simulation	92
8.6	Discussion	94
8.7	Appendix	97
8.7.1	Image morphologies	97
8.7.2	Angular resolution	100
9.	INITIAL BREAKDOWN PULSES	101
9.1	Overview	101
9.2	Example lightning flashes	102
9.3	Classic IBPs	107
9.4	Narrow IBPs	110
9.5	FA-quiet periods	113
9.6	Discussion	115
9.7	Appendix	119
9.7.1	Additional example lightning flashes	119
9.7.2	Events analyzed during the initial stage	123
9.7.3	Lightning mapping array (LMA) data	129

10. ENERGETIC IN-CLOUD PULSE	135
10.1 Overview	135
10.2 EIP detection	136
10.3 EIP-generating flash	139
10.4 Pre-EIP breakdown	142
10.5 EIP detailed observations	144
10.6 Storm Context	148
10.7 Discussion	150
10.8 Appendix	154
11. SUMMARY AND OUTLOOK.....	160
BIBLIOGRAPHY	163

LIST OF TABLES

Table		Page
8.1	Fast breakdown characteristics for NBEs 1, 2, and 9. The polarity is that of the initial fast breakdown of each NBE, and does not correspond to the sferic polarity. v is the INTF-determined speed of the fast breakdown, Δz is the INTF-determined vertical extent of the fast breakdown, and P_{pk} is the LMA-determined peak source power. I_{pk} and Q_m correspond to the peak current and charge-moment change during fast breakdown, as determined from FA sferic simulations similar to those in Rison <i>et al.</i> (2016), and ΔQ is the charge transfer. Two double-exponential current pulses were used to simulate each sferic. The first and second current pulses have rise and fall e -folding times of $\tau_{1,r}$, $\tau_{1,f}$, and $\tau_{2,r}$, $\tau_{2,f}$, respectively.	89
9.1	INTF source altitude change (Δz), 2-D extent (Δd), source duration Δt , 2-D speed (v), and total 2-D extent (ΔD) during the classic IBPs or FA-quiet breakdown in each example flash. A minimum/maximum/average value is given for each entry except ΔD . For Δz , the '+' and '-' symbols indicate the direction of propagation in altitude. The entries correspond to average values obtained during the initial stage of each flash, as indicated in panel c of Figures 9.9-9.12, which are shown in more detail in Section 9.7. In addition, the overall contribution in length (ΔD) to the initial channel development is given for classic IBPs and FA-quiet breakdown.	107
10.1	Summary of the EIP and NBE characteristics, namely the NLDN peak current I_{pk} , peak FA sferic ΔE_{pk} , peak current-moment $M_{I,pk}$, total charge-moment change M_Q , LMA peak power P_{pk} , rise time τ_{rise} of INTF VHF power, and vertical extents Δz of the flash-initiating NBE and the EIP. Note that the peaks in I , ΔE , M_I , and P are not necessarily simultaneous for each event. M_I and M_Q are obtained by once- and twice-integrating the FA signal, respectively. The integration starts at time $t=0$ for the NBE, and at $t=3.2$ ms for the EIP. τ_{rise} is determined by fitting a line to the natural log of the squared INTF VHF signal for each event. The vertical extent of each event is determined from the INTF elevation observations and the plan distance determined by the LMA locations, and depicts the span of INTF sources from the integration start time up to the peak in M_I	139

10.2	LMA and NLDN output corresponding to Figure 10.8. The LMA data includes the source time in microseconds since the flash-initiating NBE LMA source, the LMA-determined peak VHF power, the χ^2_ν goodness-of-fit value, the number of stations participating in a LMA source solution, the LMA source latitude, longitude, and altitude, the time in seconds since midnight, the LMA source plan distance from the INTF/FA, and the LMA source azimuth and elevation with respect to the INTF/FA. Note that the average LMA plan distance before and after the EIP remains around 30.6 km. For comparison, the NLDN data includes the time in microseconds since the flash-initiating NBE LMA source, the pulse peak current and polarity, the determined pulse type (either 'C' for in-cloud or 'G' for cloud-to-ground), the longitude and latitude of the pulse, and the time of the pulse in seconds since midnight.	159
------	--	-----

LIST OF FIGURES

Figure	Page
<p>1.1 Cloud-to-ground lightning leader optical and radio emissions. (a) A $142\ \mu\text{s}$ exposure optical image shows lightning leaders exit the cloud and propagate to ground. (b) A high-speed streak-camera photograph shows a lightning leader propagating 360 m below the cloud base to ground over time (dim features progressing downward, left to right), followed by connection to ground and the return stroke (large surge of luminosity) along the channel. Adapted from Berger & Vogelsanger (1966). (b) A streak photograph of the lowest $\simeq 1\ \text{km}$ of a lightning leader connected to ground, showing variations in luminosity, i.e., current, along the channel over time (left to right). Adapted from Jordan <i>et al.</i> (1995). (c) The currents from large-scale (km-length) leaders produce emissions in very-low and low frequency radio, as illustrated for a lightning return stroke measured by a $\sim 1\ \text{Hz}$-400 kHz passband sensor. Adapted from Bitzer <i>et al.</i> (2013).</p>	2
<p>1.2 Streamers in lightning observation and simulation. (a) A $100\text{-}\mu\text{s}$ optical image of a lightning leader tip propagating to ground. The original image, (1), is inverted in (2), and enhanced in (3). The white features in (1) are due to optical light from a hot lightning leader, whereas the gray filaments indicated by the bracket in (3) are due to streamer-zone streamers. Adapted from Petersen & Beasley (2013). (b) Streamer simulation results show, from top to bottom, a cross-section of streamer electron density, space charge density, electric field, and longitudinal current density, showing a concentration at the streamer head. The growth rate of the current leads to electromagnetic emissions extending to $\sim 100\ \text{MHz}$. Adapted from Shi <i>et al.</i> (2016).</p>	4
<p>1.3 Depiction of terrestrial gamma-ray flash (TGF). High-energy electrons (yellow), positrons (green), and gamma-rays (pink) begin to emanate from a thundercloud top, moving progressively upward into the near-space environment over time (from the left to the right panel). The charged particles (electrons and positrons) travel along magnetic field lines. Credit: NASA/Goddard Space Flight Center/J. Dwyer, Florida Institute of Technology.</p>	5

2.1	Normal-polarity thunderstorms. (a) The deepest convection occurs in tropical regions at sea level, such as in Florida, where the troposphere is deepest. In regions at higher latitude, thunderstorms are less deep, especially in high-elevation regions such as New Mexico. Winter thunderstorms, such as those that occur in Japan, are much less deep due to reduced heating at lower altitudes. Adapted from Krehbiel (1986). (b) Heavy negatively-charged graupel pellets fall to lower storm altitudes than positive-charged ice crystals, forming a dipole charge structure in thunderstorms. Adapted from Williams (2006).	7
2.2	Thundercloud temperature and hydrometeor profile. Strong updrafts (upward-pointing arrows) suspend liquid water and water ice throughout the thundercloud. Below the 0°C level, the water content is all liquid, and above the -40°C level, the water content is all ice. However, between the 0°C and -40°C levels, a mixed region of liquid and ice water exists. Downdrafts outside of the main convective core are shown with the downward-curving arrows. Adapted from Korolev <i>et al.</i> (2017).	9
2.3	Charging to graupel in the mixed phase region of thunderstorms. (a) A graupel particle falls due to gravity, and grows as a result of liquid water freezing on its surface. Charge transfer between graupel and an ice crystal occurs after collision. Adapted from Emersic (2006). (b) The charge imparted to graupel after collision with an ice particle is not of a fixed sign, but is dependent on the temperature and the amount of liquid water present. The temperature axis can be identically interpreted as thunderstorm altitude, with the dotted curves representing possible storm charge configurations. For instance, the storm could be dominated by a deep positive charge layer (top curve), or varying depths of dominant negative charge (bottom three curves). Adapted from Bruning <i>et al.</i> (2014).	10

- 2.4 Lightning activity superimposed on vertical cross-section of thundercloud radar reflectivity. Lightning source locations were determined by a three-dimensional VHF (60-66 MHz) mapping instrument, and show sources associated with the negative leader (magenta '+') propagating through positive cloud charge, and the positive leader (blue '-') propagating through negative cloud charge. The triangle shows the location of the flash initiation point. Radar reflectivity is given in relative units of dB and shows cloud precipitation from the lightest values (cyan) on the cloud edge to the heaviest values (purple) in the cloud core. In (a), the flash initiates at about 9 km altitude between inferred regions of upper positive and mid-level negative charge, above the thundercloud core, and the two leaders propagate bidirectionally away from the initiation point. In (b), a cloud-to-ground flash initiates at about 5 km altitude between inferred regions of mid-level negative charge and weaker lower positive charge, and the two leaders again propagate bidirectionally away from the initiation point. Adapted from Krehbiel *et al.* (2005). 11
- 2.5 Normal polarity charge structure and electrical quantities. (a) The thunderstorm charge structure is reconstructed using VHF lightning data, with orange regions depicting negative leaders propagating through positive charge, and blue regions depicting positive leaders propagating through negative charge. In (b) and (c), model-estimated values of the vertical electric field and electric potential, respectively, are shown at different altitudes along the central axis of the thunderstorm in (a). The values are shown before (solid line) and after (dashed line) a cloud-to-ground lightning flash. Adapted from Krehbiel *et al.* (2008). 12
- 2.6 Balloon-borne thundercloud electric field sounding. Left: vertical cross-section of thundercloud radar reflectivity, superimposed by balloon trajectory (black curve), electric field vector, i.e., directions and strengths (blue line segments) along the flight path, and inferred charge regions (red '+' for positive charge, blue '-' for negative charge). Right: sounding results, including the vertical component of the electric field, E_z , in black, and temperature, T , in dark blue, along the balloon trajectory. Adapted from Lang *et al.* (2004). 13
- 2.7 Schematic of bidirectional leader formation and propagation in thunderstorms. (a) Once formed, the lightning leader is a highly-conductive plasma in the thundercloud electric field, and so acts like a polarized linear conductor. (b) Schematic of streamer/leader initial bidirectional development, showing positive-polarity breakdown initiates first and begins to elongate before the initiation of the negative polarity breakdown. The system starts off streamer-based (a cold discharge), and becomes a leader once the currents become large enough to thermalize the system. Adapted from Williams (2006). 14

- 2.8 X-ray image of lightning leader coming to ground. A high-speed pin-hole X-ray camera produced a $0.5\text{-}\mu\text{s}$ exposure (hexagonal pixels) of a dart leader coming to ground during rocket-triggered lightning. The tip of the dart leader (yellow line) appears to be co-located with 36 MeV X-ray emission. Adapted from Dwyer *et al.* (2011). 15
- 2.9 Rocket-triggered lightning three-dimensional VHF mapping observations. VHF sources from individual lightning activity is color-coded according to leader polarity, with red markers corresponding to negative leaders that propagate through inferred positive charge, and blue markers corresponding to positive leaders that propagate through inferred negative charge. The triggered lightning flash is colored black, and propagates horizontally through negative storm charge. Adapted from Edens *et al.* (2012). 16
- 2.10 Schematic of the negative stepped leader process. The schematic depicts a one-dimensional vertically-oriented leader propagating downward, originating from a negative high-voltage electrode, and continuous “snapshots” of the leader stepping process are shown for a $50\text{ }\mu\text{s}$ time period, progressing in time, left to right. Starting with a negative corona burst from the negative electrode, the main leader channel (1) is formed, and from the negative leader tip (2) a negative streamer zone (3) exists. Both the negative leader and its streamer zone propagate downward smoothly for some time. Meanwhile, the initial negative corona burst had established patches of enhanced ionization, also known as space stems (4), from which positive streamers can be established and propagate upward to meet the downward negative streamers (3) from the main leader channel; also downward-propagating negative streamers (5) emanate from the space stem. At some point, the space stem becomes thermalized, and becomes a space leader (6) that develops bidirectionally. When the main leader channel and space leader electrically connect (7) a new negative corona burst (8) emanates from the newly-established main leader tip, and the step process repeats. A typical time-synchronous electric field measurement is shown at the bottom of the figure, showing the characteristic “step” pulses that give the leader its name. Adapted from Gorin *et al.* (1976); Biagi *et al.* (2010, 2014). 17
- 2.11 Broadband radio frequency emissions (sferics) of a stepped leader and return stroke in cloud-to-ground lightning. The bottom trace shows the electric field change record of a stepped leader coming to ground followed by the return stroke field (‘R’). The bottom timescale shows $40\text{ }\mu\text{s}$ per division. The top trace shows just the first $80\text{ }\mu\text{s}$ of the same record, but with the magnitude multiplied by -2, showing the individual stepped leader pulses (‘L’), which are $\sim 1\text{ }\mu\text{s}$ wide and mostly unipolar. The top timescale shows $8\text{ }\mu\text{s}$ per division. The measurements were made using a high-pass electric field change sensor, having a decay time constant of about 2 ms (i.e., sensing down to 500 Hz). Adapted from Krider *et al.* (1977). 18

- 2.12 High-speed optical observations of leader stepping in lab and thunderstorm leaders. (a) Steak photograph of the propagating space stem in a meter-long gap. The location of the space stem (ionized patch) can be identified as the location from which bidirectional streamer development (upward positive and downward negative streamers) occurs. The downward negative streamers facilitate creation of new space stem locations, which advance downward over time (left to right), and do not thermalize in the roughly $10\ \mu\text{s}$ window. Adapted from Reess *et al.* (1995). (b) High-speed photograph of streamers and space leaders near lightning leader tip. (1) shows a $100\text{-}\mu\text{s}$ exposure image of a lightning leader tip, (2) shows an inverted image of (1), and (3) shows an enhanced image of (2). The black regions in (2) and (3) likely depict leaders, since leaders are compact, highly-conductive and hot, and thus optically bright. The main leader channel extends vertically through almost the entire image, whereas space leaders are formed in the high field region near the main leader but some distance away from the main leader, and are visible as short black segments (e.g., bracket b). Streamers can be seen in (3) as wispy gray filamentary structures emanating from the main leader (e.g., bracket a), bridging the gap between the main and space leaders, and are also visible emanating from the tips of some of the space leaders. Adapted from Petersen & Beasley (2013). 19
- 2.13 Leader branching in tower-triggered upward lightning. (a) Current waveform measured at an instrumented tower as an initial stepped leader propagates upward from the tower. (b) First four frames of high-speed video ($30.29\ \mu\text{s}$ per frame), showing single leader steps during each frame, and corresponding to the single step pulses in (a). (c) Example image of branching during a frame, which corresponds to multi-peaked wider waveforms in (a). Adapted from Pu *et al.* (2017). 20
- 2.14 Intensified charge coupled device (ICCD) photographs of positive streamers at various exposure times. For the shortest exposure time (far right), optical emissions can only be seen emanating from the streamer heads, where ionization actively takes place. For the longest exposure time (far left), the paths traced by the streamer heads become visible, but the channels are not actually radiating. Adapted from Ebert *et al.* (2006). 22

- 2.15 Electron avalanche schematic. (a) In the presence of an electric field, a free electron (-) impacts a neutral atom, ionizing the atom by liberating one electron (-) and leaving the atom with equal magnitude positive charge (+), so that two free electrons and a positive ion result. The two free electrons can then impact two more neutral atoms, liberating two more electrons, and so on, creating an electron avalanche. (b) Illustration of the separation of charges in an electron avalanche over time between parallel plate electrodes, with the electron avalanche progressing toward the positively-charged electrode, leaving positive ions in the wake, which progress more-slowly toward the negatively-charged electrode. Adapted from Beroual & Fofana (2016). 22
- 2.16 Schematic showing development of streamers. Streamers propagate via impact ionization and photoionization (with photons of energy $h\nu$) across a gap, shown for two instances of time (left to right) for (a) a negative streamer, directed toward the positively-charged anode ('A'), and (b) a positive streamer, directed toward the negatively-charged cathode ('C'). In (a) and (b), the right-most figure shows the space charge field near the streamer head, which is higher than the field in the gap, E_0 . Adapted from (Raizer, 1991, pp. 335,338) 24
- 2.17 Streamer to leader transition. Positive streamers (black traces) initiating from a needle electrode (top of each panel) propagate downward through a 1-meter gap in successive images (a)-(o) over the course of 1 μ s. As the positive streamers get closer to the grounded electrode (bottom of each panel) in (d) and (e), the electric field near the grounded electrode becomes enhanced and allows for upward propagation of negative streamers. By panel (j), the air near the positive streamer initiation point becomes substantially thermalized (indicated in orange) by the recurrent streamer activity, forming a propagating hot leader, and by (o) the thermalized channel bridges the gap and short-circuits the gap. Adapted from Kochkin *et al.* (2012a). 27
- 2.18 Illustration of streamers initiating from an ice crystal in a sub-breakdown electric field. Left: the electric field is enhanced locally near an ice crystal, which initiates positive streamers that propagate in the direction of the ambient electric field. Right: after some time, after a substantial negative space charge is deposited back at the positive streamer initiation point, negative streamers can propagate in the opposite direction of the ambient electric field. Adapted from Petersen *et al.* (2008). 28
- 2.19 Narrow bipolar event (NBE) sferics. (a) Simple bipolar NBE sferic. Adapted from Villanueva *et al.* (1994). (b) More complex bipolar sferic with perturbations. Adapted from Willett *et al.* (1989). 30

2.20	Narrow bipolar event (NBE) energy spectral density, compared to that of lightning return strokes. At frequencies above about 1 MHz, NBE emissions surpass that of return strokes. Adapted from Willett <i>et al.</i> (1989).	30
2.21	Simulation of NBE sferic. (a) Assumed NBE channel geometry. (b) Sferic due to a simulated negative (downward-directed) current pulse propagating at 10^8 m/s along the channel. Adapted from Le Vine (1980).	31
2.22	Fast positive breakdown generates narrow bipolar pulse. The positive initial pulse of the NBE sferic (red waveform) indicates a negative current (i.e., positive charge moving downward, or negative charge moving upward). However, given the coincident downward propagation of the detected VHF sources (circular markers), a downward-propagating positive-polarity breakdown appears to generate the sferic, and with a fast $\sim 10^7$ m/s propagation speed. The raw VHF signal (blue waveform) associated with the fast positive breakdown quickly saturates the sensor. Adapted from Rison <i>et al.</i> (2016).	32
2.23	Positive and negative NBE locations with respect to parent flash and storm charge. (a) The red circle indicates the VHF (60-66 MHz) source location of the positive NBE in Figure 2.22, which initiates an intra-cloud lightning flash. The upward-propagating VHF sources of the ensuing flash represent negative leaders propagating upward into positive charge (indicated by red markers), and the downward-propagating VHF sources represent positive leaders propagating downward into negative charge (indicated by blue markers). (b) The NBE location is superimposed on the overall thundercloud charge structure, determined by lightning VHF source activity, showing that the storm is of normal polarity (Krehbiel, 1986) and that the NBE is a positive NBE, i.e., generated by negative current. Adapted from Rison <i>et al.</i> (2016). (c) Schematic of positive and negative NBE locations with respect to storm charge structure. Adapted from Wu <i>et al.</i> (2012).	34
2.24	Classic initial breakdown pulse (IBP) sferics in cloud-to-ground lightning. Top: at $40 \mu\text{s}$ per division (scale at bottom of figure), a single classic IBP sferic (indicated by the arrow) is shown, having a relatively large amplitude and being largely bipolar, with a $\simeq 20 \mu\text{s}$ wide initial pulse that is superimposed by narrow ($\sim 1 \mu\text{s}$) pulses. Middle: at 0.4 ms per division, the IBP “pulse train” is visible, consisting of similarly-spaced classic IBPs. The same event is indicated by the arrow. Bottom: at 2 ms per division, the IBP pulse train is shown with respect to the return stroke, and also shows the same event indicated by the arrow. Adapted from Weidman & Krider (1979).	35

2.25	Initial breakdown pulse (IBP) sferic and luminosity observations in intra-cloud lightning. Top: intra-cloud lightning sferic (blue waveform), showing the IBP pulse train (black box). Bottom: The largest classic IBP coincides with a clear luminosity increase (orange curve). The inset shows an expanded view of the classic IBP sferic. Adapted from Stolzenburg <i>et al.</i> (2016).	36
2.26	Classic initial breakdown pulse (IBP) sferic and luminosity observations in cloud-to-ground lightning. Top: sequential 20 μ s frames from a high-speed optical video of electrical activity below a thundercloud base. Bottom: a single classic IBP sferic (blue waveform) in a cloud-to-ground lightning flash coincides with downward vertical elongation of luminous channel in cloud-to-ground lightning. Adapted from Stolzenburg <i>et al.</i> (2014).	38
2.27	Narrow initial breakdown pulse (IBP) sferics. (a) Bipolar narrow IBP during an intra-cloud lightning flash. (b) Two narrow IBPs of opposite polarities in a cloud-to-ground lightning flash. Adapted from Nag <i>et al.</i> (2009).	39
2.28	Bremsstrahlung schematic. A relativistic electron travels close to charged matter, such as a nucleus, deflecting and emitting a X-ray or gamma-ray to conserve momentum. Credit: NASA/GSFC.	40
2.29	Effective frictional force felt by an electron as a function of kinetic energy. For an electron (or positron) placed in an ambient electric field E (the solid horizontal line depicts the force due to $E=5\times 10^6$ V/m at STP in air), the electron feels a force eE . However, the force is countered by a frictional force due to inelastic scattering with air molecules (solid curve), but if the electron has an initial kinetic energy above ϵ_{th} , then the electron can effectively “run away,” feeling a lesser frictional force as it gains more energy. If the ambient field is instead E_c , then any electron can run away, regardless of its initial kinetic energy. E_b is the break-even field, or minimum field required to produce a runaway electron. The dashed curve includes energy loss due to bremsstrahlung. Adapted from Dwyer (2012); Dwyer <i>et al.</i> (2012).	41
2.30	From left to right: a single runaway electron, relativistic runaway electron avalanche via electron-electron interactions (Møller scattering), relativistic feedback via positron and X-ray interactions. Adapted from Dwyer <i>et al.</i> (2012).	42
2.31	Thundercloud electric field balloon sounding. The dashed green curve shows the break-even field, E_b , as a function of altitude, and the dotted blue curve shows the RREA threshold field, E_{RREA} . Note that the magnitude of the measured electric field can be above E_b , but stays below E_{RREA} , except when lightning occurs (‘L’). Adapted from Stolzenburg <i>et al.</i> (2007).	44

2.32	Ambient electric field as a function of field region length in order to make $\gamma=1$. The relationship is determined from Monte Carlo simulations, and is shown for air (black) and also for a hydrogen-helium atmosphere (red), such as that on any of the gas giants: Jupiter, Saturn, Uranus, and Neptune. The horizontal lines show the RREA threshold, E_{RREA} , and the dotted lines show the conventional breakdown threshold, E_k . Adapted from Dwyer (2007).	45
2.33	Schematic of thermal electrons accelerated to relativistic energies at the tip of a powerful lightning leader. The relativistic runaway electrons produced at the leader tip / streamer zone radiate X-rays and gamma-rays via Bremsstrahlung. Adapted from Celestin <i>et al.</i> (2015).	46
2.34	Energetic in-cloud pulses (EIPs) and terrestrial gamma-ray flashes (TGFs). Ground-based sferic measurements made in Florida (black waveforms) are time-aligned with TGF detections (colored boxes) made by the Fermi spacecraft. The EIP detections (large-amplitude, $\sim 100 \mu s$ wide sferic pulses) overlap in time with the TGF detections. Adapted from Lyu <i>et al.</i> (2016).	47
3.1	Lightning sferics. The broadband ~ 3 kHz-3 MHz electric field changes, i.e., sferics, associated with: (a) a CG flash, with the three return strokes indicated by blue arrows, (b) the initial stage leading up to the first CG return stroke, (c) the CG flash-initiating NBE and IBP train, (d) the CG flash-initiating NBE, (e) an example IBP in the CG flash, and (f) an EIP from a different (intra-cloud) lightning flash.	50
4.1	Instrument locations in 2016 Florida deployment. (a) Plan view of the Florida coastline, showing the eight inner-most stations of a ten-station Lightning Mapping Array (LMA) (green squares) and the location of the broadband interfereomer (INTF) (white dot). (b) Close-in plan view of the INTF, showing the three INTF antennas, A, B, C, arranged in an equilateral triangle configuration with 100-meter baselines. The fast electric field antenna (FA) is located near the center of the array (green balloon).	54
5.1	INTF site panorama at Kennedy Space Center in 2016. Three flat-plate antennas (labeled A, B, C) and fast electric field change antenna (FA) are indicated by arrows, with A and B in the foreground, and C in the background (the photograph was taken from the right side of Figure 4.1b, looking toward the west). The signal from each sensor ran along a dedicated coaxial cable to the data acquisition building (orange-white checkered building) where it was digitized and stored.	55

5.2	INTF antenna at Kennedy Space Center in 2016. The circular flat-plate antenna covers a housing (cake pan) containing signal amplifiers. The amplified signal runs from the housing along a coaxial cable to the data acquisition building (orange-white checkered building in the background), where it is filtered and further amplified before being digitized and stored.	56
5.3	Circuit elements of dE_z/dt sensor. (a) An inverting op-amp circuit. (b) Circuit elements, including the sensing plate and showing the output voltage, used to record dE_z/dt	58
5.4	Interferometry conceptual diagram. (a) Two antennas, A and B , separated by baseline length d_{AB} , receive an electromagnetic plane wave that makes an angle θ_{AB} with the baseline. After reaching B , the signal must travel an additional distance $c\tau_{AB}$ to reach A , where τ_{AB} is the time delay between the signals at A and B . (b) Same as (a) but in three dimensions, showing orientation of AB with respect to cardinal directions.	59
5.5	Transition from 3-D space to 2-D cosine plane projection. (a) A point source (orange line) makes an angle α with respect to the east direction, an angle β with respect to the north direction, and an angle θ_{AB} with respect to the baseline AB (dotted blue line). The source is projected on a unit hemisphere, and then straight down into the instrument plane (cosine plane), which forms a unit disk. (b) The angle θ_{AB} defines a line of constant time delay (orange solid line) in the cosine plane where the source may be.	60
5.6	Cosine plane and source direction determination. (a) Two baselines produce two lines of constant time delay (orange solid lines) in the cosine plane which are perpendicular to their respective baseline orientations (blue dotted lines), and the intersection of which defines the source location in the cosine plane. (b) Sky projection by a fish-eye lens, which similarly represents and distorts the sky as compared to the cosine plane. Photo by (Anastasiia-S, 2018).	61
5.7	Azimuth and elevation angle and relation to cosine plane. (a) The direction to a source (orange line) makes an azimuth angle Az with respect to north, and elevation angle El with respect to ground. The direction to the source in the cosine plane is depicted by the orange dot. (b) Cosine plane, with the source azimuth and elevation angles shown.	61
5.8	INTF waveforms. (a) Time domain VHF signals recorded by antennas A , B , and C during the first $12 \mu s$ of a narrow bipolar event (NBE). (b) Cross correlations of every two signals in (a), showing a peak at the most probable time offset between any two signals.	63

5.9	Cross correlations from each baseline projected into cosine plane. The cross correlations projected into the cosine plane correspond to baseline: (a) AB , (b) AC , and (c) BC	64
5.10	Cross correlations from all three baselines projected into cosine plane and azimuth-elevation projection. (a) The cross correlations (radio image) of the NBE source is projected into the cosine plane. (b) The same image as in (a), but projected into azimuth-elevation.	65
5.11	Interferometer mapping example. Centroids from successive $1.4 \mu s$ -exposure radio images (with a $0.35 \mu s$ shift between images) are colored by received VHF power and are plotted in (a) azimuth and elevation, showing the spatial structure of the flash, and (b) elevation versus time, showing the (roughly) vertical growth of the flash over time. (c) The original received VHF signal is shown in gray, and the signal from a synchronously-digitized fast electric field antenna is shown in black.	65
5.12	INTF point spread function (PSF) and comparison to real lightning source. (a) PSF imaged in the cosine plane. (b) Close-in view of PSF main lobe. (c) Close-in view of real source in a thunderstorm, which is similar to the PSF but shows a slightly different morphology.	66
5.13	INTF point spread function (PSF) frequency domain and time domain signals. (a) Simulated frequency-domain INTF signals contributing to PSF (band-limited to 20-80 MHz). (b) Simulated time-domain INTF signals contributing to PSF.	67
5.14	INTF images of two simulated point sources at various degrees separation in elevation. Two point sources are located near the horizon, and are separated by elevations of (a) 0° , (b) 3° , (c) 6° , and (d) 9°	68
6.1	Electric field change sensor. (a) An integrating op-amp circuit with time constant $R_{out}C$ effectively integrates a time-varying input signal, V_{in} , giving an output signal V_{out} . (b) The fast antenna (FA) used in the Florida studies herein is shown at the INTF site. The sensing plate is exposed to the ground, and shielded from rain by a salad bowl, which also holds electronics to amplify the signal. Coaxial cables run the amplified FA signal out the top of the salad bowl via PVC piping and to the data acquisition building (orange-white checkered building in the background), where the signal is additionally amplified, then digitized and stored.	70

6.2	Vertical radiating antenna geometry used in equation 6.4. A vertical radiating antenna extends from altitude H_B to H_T , a radial distance, r , from an observation point on the ground ($z'=0$) where the vertical electric field, E_z , is sampled. A current waveform, i , travels vertically along the antenna. The current amplitude along the antenna at time t' and height z' (also slant range, R , with respect to the observation point) is given by $i(z', t')$	72
7.1	Lightning mapping array (LMA) station at Kennedy Space Center (KSC). The sensing element is the vertical antenna protruding from the ground plane (three downward-sloping elements). The LMA electronics (e.g., digitizer and hard drive) are located in the tan metal box, and are powered by the solar panel.	74
7.2	Lightning mapping array (LMA) geometry. The schematic depicts the LMA stations (red dots) on the ground with respect to a radio source located at (x, y, z) and emitting at time t . The radio signal is received at the i^{th} station, with fixed location (x_i, y_i, z_i) , at a later time t_i . The slant range from the radio source to the i^{th} station is given by $c^2(t - t_i)^2$. Credit: New Mexico Tech / Langmuir Laboratory for Atmospheric Research.	75
7.3	Ten minutes of LMA data. LMA sources are (a) colored by time (sources with $\chi_\nu^2 < 1$ are plotted), (b) colored and sized by the log of the emitted VHF power (sources with $\chi_\nu^2 < 5$ are plotted, which shows the NBEs – large red diamonds – in the storm), and (d) colored by thundercloud charge, with red for positive charge and blue for negative charge (sources with $\chi_\nu^2 < 1$ are plotted).	77
7.4	LMA data for an intra-cloud lightning flash. LMA sources are (a) colored by time (sources with $\chi_\nu^2 < 1$ are plotted), (b) colored and sized by the log of the emitted VHF power (sources with $\chi_\nu^2 < 5$ are plotted, which shows a NBE – large orange diamond – at the beginning of the flash), and (d) colored by thundercloud charge, with red for positive charge and blue for negative charge (sources with $\chi_\nu^2 < 1$ are plotted).	78
7.5	LMA data for a cloud-to-ground lightning flash. LMA sources are (a) colored by time (sources with $\chi_\nu^2 < 1$ are plotted), (b) colored and sized by the log of the emitted VHF power (sources with $\chi_\nu^2 < 5$ are plotted), and (d) colored by thundercloud charge, with red for positive charge and blue for negative charge (sources with $\chi_\nu^2 < 1$ are plotted).	79

- 7.6 Detailed lightning mapping data for two NBEs (NBEs 1 and 2 in Section 8). (a,d) LMA maps of the complete activity for each NBE, showing how the NBEs are mis-located relative to the subsequent, lower-power activity, and how the subsequent activity more accurately indicates the NBE's actual location. (b,c) Numerical listings of the source times, power (dBW units), goodness-of-fit χ^2_ν (chisq) value, and number of stations (nsta) participating in the solutions. 80
- 8.1 Lightning mapping observations of storm producing narrow bipolar events. VHF Lightning Mapping Array data from the Kennedy Space Center LMA for the 24 August 2016 storm. (a) Overview of the height-time evolution of the three-hour storm, (b) 10 minutes of enhanced activity during the bracketed interval of (a), coloured by the lightning-inferred polarity of the storm charge (red = upper and lower positive charge, blue = mid-level negative charge), showing the NBE events (black), (c) zoomed-in view of 6 seconds of high-rate NBE activity (~ 40 NBEs within one minute), indicated by the bracket in (b), coloured and sized by VHF source power and showing NBEs 1, 2 and 9. Note that the initial high-power sources of the NBEs (large diamond markers) were mis-located in altitude from the subsequent, smaller, and correctly-located lower-power sources (blue markers), with NBE 1 altitude being particularly incorrect (see Section 7.2). The low-power sources indicate that all 10 NBEs occurred at similar altitudes between 13 and 15 km MSL, immediately below or within the inferred upper positive charge region. (d, e, f) Plan and vertical cross-section views of the storm charge structure, coloured by charge as in (b) and showing that the NBEs occurred in close proximity to a positively charged western anvil of the normally-electrified storm. The inset in the east-west cross-section of (d) shows the full-duration INTF centroid observations for each of the three NBEs relative to the storm location, with marker colors corresponding to relative VHF power. The inset shows that each NBE had a vertical extent of $\simeq 1.5$ km on the lower edge of the upper positive charge region. The plan view of (e) shows the NBE locations as white circles. The cyan boxes in (d) and (f) indicate their locations in the vertical cross-sections. The black triangle in (e) indicates the INTF location at KSC. 84

- 8.2 Interferometer data for NBE 1. (a,c) Radiation centroids (circular markers, coloured and sized by VHF power) for NBE 1, plotted in elevation vs. azimuth, showing the breakdown activity was primarily vertical. Each marker denotes the average angular position of the 128 source solutions in each $0.7\text{-}\mu\text{s}$ window, and error bars denote the standard deviations. (b,d) Radiation centroids and fast electric field change (sferic) observations (black waveform) superimposed on the VHF waveform (gray), showing the downward propagation of the VHF source. The positive sferic waveform is indicative of a downward-directed current, consistent with the NBE occurring below the storm's upper positive charge, and indicating the downward development was due to positive-polarity breakdown. The breakdown descended $\simeq 700\text{ m}$ in $14\text{ }\mu\text{s}$, corresponding to a speed of $\simeq 5 \times 10^7\text{ m s}^{-1}$. (e) Semilog plot of the VHF power vs. time, showing the fast exponential rise of the radiation (rise time $\tau = 0.21\text{ }\mu\text{s}$), coincident with the fast rise of the electric field change (panel (d)). The peak current of the breakdown was -75 kA 85
- 8.3 Interferometer data for NBE 2. (a,c) Radiation centroids (circular markers, coloured and sized by VHF power) for NBE 2, plotted in elevation vs. azimuth, showing the breakdown activity was primarily vertical. Each marker denotes the average angular position of the 128 source solutions in each $0.7\text{-}\mu\text{s}$ window, and error bars denote the standard deviations. (b,d) Radiation centroids and fast electric field change (sferic) observations (black waveform) superimposed on the VHF waveform (gray), showing the upward propagation of the VHF source. The positive sferic waveform is indicative of a downward-directed current, consistent with the NBE occurring below the storm's upper positive charge, and indicating the upward development was due to negative-polarity breakdown. The breakdown ascended $\simeq 600\text{ m}$ in $15\text{ }\mu\text{s}$, corresponding to a speed of $\simeq 4 \times 10^7\text{ m s}^{-1}$. (e) Semilog plot of the VHF power vs. time, showing the fast exponential rise of the radiation (rise time $\tau = 0.24\text{ }\mu\text{s}$), coincident with the fast rise of the electric field change (panel (d)). The peak current of the breakdown was -47 kA 86

- 8.4 Interferometer data for NBE 9. (a,c) Radiation centroids (circular markers, coloured and sized by VHF power) for NBE 9, plotted in elevation vs. azimuth, showing the breakdown activity was primarily vertical. Each marker denotes the average angular position of the 128 source solutions in each $0.7\text{-}\mu\text{s}$ window, and error bars denote the standard deviations. (b,d) Radiation centroids and fast electric field change (sferic) observations (black waveform) superimposed on the VHF waveform (gray), showing the upward propagation of the VHF source. The positive sferic waveform is indicative of a downward-directed current, consistent with the NBE occurring below the storm's upper positive charge, and indicating the upward development was due to negative-polarity breakdown. The breakdown ascended $\simeq 400\text{ m}$ in $10\text{ }\mu\text{s}$, corresponding to a speed of $\simeq 4 \times 10^7\text{ m s}^{-1}$. (e) Semilog plot of the VHF power vs. time, showing the fast exponential rise of the radiation (rise time $\tau = 0.23\text{ }\mu\text{s}$), coincident with the fast rise of the electric field change (panel (d)). The peak current of the breakdown was -58 kA 87
- 8.5 Radio images of NBE 2. Elevation vs. azimuth images of (a) an ideal point source at NBE 2's location ($Az, El = 50^\circ, 23^\circ$), called the point spread function (PSF), (b-e) sample images at $\simeq 4\text{ }\mu\text{s}$ intervals during the first $15\text{ }\mu\text{s}$ of NBE 2, corresponding to its upward fast negative breakdown (FNB) phase, and (f-i) sample images during successive $15\text{ }\mu\text{s}$ intervals. In each case the images are $0.7\text{ }\mu\text{s}$ exposures, normalized to the peak amplitude of the centroid. The central lobe of the PSF shows the angular resolution of the three-antenna array and, along with the side lobes, remains essentially unchanged during the FNB, consistent with the VHF radiation being from a localized source. Following the FNB, the central lobe becomes increasingly elongated and the side lobes intensify and become disorganized, indicative of extended and/or multiple radiation sources. (j) Standard deviations (SD) of the central lobe in the $(\cos\alpha, \cos\beta)$ projection plane vs. time (red, blue symbols), compared to the SD of the PSF function (grey line), quantitatively showing the radiation to be localized during the FNB and increasingly non-localized and random subsequent to the FNB. 90
- 8.6 NBE 2 simulation. Simulated radiation centroids (circular markers, coloured and sized by VHF power) of a vertically-propagating point source, having the same VHF amplitudes, altitudes, and speed of NBE 2. Each marker denotes the average angular position of the 128 source solutions in each $0.7\text{-}\mu\text{s}$ window, and error bars denote the standard deviations. (a,b) Centroid locations without added noise, plotted in elevation vs. azimuth and elevation vs. time, respectively, and (c,d) same, but with the pre-flash noise of NBE 2 added, showing that the resulting scatter in elevation and azimuth is partially but not fully accounted for by the pre-flash noise. 93

- 8.7 Radio images of different source types. Simulated images and related information of: (a-e) an ideal point source, corresponding to the point spread function (PSF) of the antenna array, (f-j) the effect of uncorrelated noise on the observations, and the effect of angular separation of two equal-power point sources in azimuth (k-o), and elevation (p-t). Each image shows the normalized intensity (\tilde{I}) of a $0.7 \mu\text{s}$ exposure of sources at the location of NBE 2. Panels (c) and (d) show that the central lobe of the PSF has a standard deviation (SD) of 0.011 in both the $\cos\alpha$ and $\cos\beta$ directions, corresponding to SDs of 1.6° and 3.8° in azimuth and elevation. As seen in panel (j), added noise has little effect on the size of the central lobe, remaining close to the PSF value of 0.011 (horizontal grey line) for signal to noise ratios as large as unity (0 dB). Binary sources have a much stronger effect, with the two sources being readily distinguishable for azimuthal separations of 2° or elevation separations of $5\text{-}6^\circ$. The fixed central lobe becomes noticeably deformed well before that (panels (o) and (t)). 99
- 9.1 2016.08.24 CG2 flash overview. (a) The whole flash, showing the FA and VHF waveforms (black and blue waveforms, respectively), and INTF sources (markers colored by time) are shown in elevation versus azimuth, and elevation versus time. (b) Same as (a), but for the highlighted light-gray region in (a). The panel shows the (downward) negative leader development, followed later by visible positive leader development back near the flash initiation location. The flash initially developed one main vertical breakdown channel, but became increasingly branched and developed more horizontally over time, with the leader reaching ground after $\simeq 30$ ms. (c) Same as (a) and (b), but for the highlighted dark-gray region in (b) and with INTF sources colored by VHF power. The panel shows detail of the initial breakdown stage of the flash, which was initiated without an apparent NBE or fast breakdown event, and instead was initiated by low-power VHF activity / FA-quiet activity. From 0 to 1.5 ms, $\simeq 12$ narrow IBPs and 8 classic IBPs occurred, with FA-quiet periods occurring in-between most pulses. 103

- 9.2 2016.09.14 IC3 flash overview. (a) The whole flash, showing the FA and VHF waveforms (black and blue waveforms, respectively), and INTF sources (markers colored by time) are shown in elevation versus azimuth, and elevation versus time. (b) Same as (a), but for the highlighted light-gray region in (a). The panel shows the (upward) negative leader development, followed later by visible positive leader development back near the flash initiation location. The flash initially developed one main vertical breakdown channel, but became increasingly branched and developed more horizontally over time. (c) Same as (a) and (b), but for the highlighted dark-gray region in (b) and with INTF sources colored by VHF power. The panel shows detail of the initial breakdown stage of the flash, which was initiated without an apparent NBE or fast breakdown event, and instead was initiated by low-power VHF activity / FA-quiet activity. From 0 to 7 ms, $\simeq 23$ narrow IBPs and 2 classic IBPs occurred, with FA-quiet periods occurring in-between most pulses. 105
- 9.3 Classic IBPs in CG flashes. An example classic IBP (CIBP) is shown from each of the three CG flashes: from CG1 on the top, CG2 in the middle, and CG3 on the bottom. INTF sources (circular markers) are shown in elevation versus azimuth (left plots), and elevation versus time (right plots). The FA and VHF signals (black and blue waveforms, respectively) are also shown in the right-most plots. In the elevation versus time plots (right panels), the colored markers indicate sources used for computing extent and speed during each CIBP, the black sources denote activity just before the CIBP, and white sources denote activity just after the CIBP. This same color scheme is used in the elevation versus azimuth plots (left panels), with the entire preceding flash activity colored gray. 108
- 9.4 Classic IBPs in IC flashes. An example classic IBP (CIBP) is shown from each of the three IC flashes: from IC1 on the top, IC2 in the middle, and IC3 on the bottom. INTF sources (circular markers) are shown in elevation versus azimuth (left plots), and elevation versus time (right plots). The FA and VHF signals (black and blue waveforms, respectively) are also shown in the right-most plots. In the elevation versus time plots (right panels), the colored markers indicate sources used for computing extent and speed during each CIBP, the black sources denote activity just before the CIBP, and white sources denote activity just after the CIBP. This same color scheme is used in the elevation versus azimuth plots (left panels), with the entire preceding flash activity colored gray. 109

- 9.5 Narrow IBPs in CG flashes. An example narrow IBP (NIBP) is shown from each of the three CG flashes: from CG1 on the top, CG2 in the middle, and CG3 on the bottom. INTF sources (circular markers) are shown in elevation versus azimuth (left plots), and elevation versus time for two different time ranges (two right plots). The FA and VHF signals (black and blue waveforms, respectively) are also shown in the right-most plots. The colored markers indicate sources during the NIBP, the black markers denote activity just before the NIBP, and white sources denote activity just after the NIBP. In the left panels, the entire preceding flash activity is colored gray. 111
- 9.6 Narrow IBPs in IC flashes. An example narrow IBP (NIBP) is shown from each of the three IC flashes: from IC1 on the top, IC2 in the middle, and IC3 on the bottom. INTF sources (circular markers) are shown in elevation versus azimuth (left plots), and elevation versus time for two different time ranges (two right plots). The FA and VHF signals (black and blue waveforms, respectively) are also shown in the right-most plots. The colored markers indicate sources during the NIBP, the black markers denote activity just before the NIBP, and white sources denote activity just after the NIBP. In the left panels, the entire preceding flash activity is colored gray 112
- 9.7 FA-quiet activity in CG flashes. An example FA-quiet period (FAQ) is shown from each of the three CG flashes: from CG1 on the top, CG2 in the middle, and CG3 on the bottom. INTF sources (circular markers) are shown in elevation versus azimuth (left plots), and elevation versus time (right plots). The FA and VHF signals (black and blue waveforms, respectively) are also shown in the right-most plots. In the elevation versus time plots (right panels), the colored markers indicate sources used for computing extent and speed during each FAQ, the black sources denote activity just before the FAQ, and white sources denote activity just after the FAQ. This same color scheme is used in the elevation versus azimuth plots (left panels), with the entire preceding flash activity colored gray. 113
- 9.8 FA-quiet activity in IC flashes. An example FA-quiet period (FAQ) is shown from each of the three IC flashes: from IC1 on the top, IC2 in the middle, and IC3 on the bottom. INTF sources (circular markers) are shown in elevation versus azimuth (left plots), and elevation versus time (right plots). The FA and VHF signals (black and blue waveforms, respectively) are also shown in the right-most plots. In the elevation versus time plots (right panels), the colored markers indicate sources used for computing extent and speed during each FAQ, the black sources denote activity just before the FAQ, and white sources denote activity just after the FAQ. This same color scheme is used in the elevation versus azimuth plots (left panels), with the entire preceding flash activity colored gray. 114

- 9.9 2016.08.24 CG1 flash overview. (a) The whole flash, showing the FA and VHF waveforms (black and blue waveforms, respectively), and INTF sources (markers colored by time) are shown in elevation versus azimuth, and elevation versus time. (b) Same as (a), but for the highlighted light-gray region in (a). The flash initially developed with few and relatively small branches, but became increasingly branched and developed more horizontally over time, with the leader first reaching ground at $\simeq 12$ ms. (c) Same as (b), but for the highlighted dark-gray region in (b) and with INTF sources colored by VHF power. The flash was initiated by a NBE generated by fast positive breakdown, and was immediately followed by a FA-quiet period lasting $\simeq 200$ μ s. From $\simeq 200$ μ s to $\simeq 2$ ms, $\simeq 19$ narrow IBPs and 5 classic IBPs occurred, with FA-quiet periods occurring in-between most pulses. 119
- 9.10 2016.09.02 CG3 flash overview. (a) The whole flash, showing the FA and VHF waveforms (black and blue waveforms, respectively), and INTF sources (markers colored by time) are shown in elevation versus azimuth, and elevation versus time. (b) Same as (a), but for the highlighted light-gray region in (a). The flash initially developed two main branches, each having relatively small branches for the first 1.5 ms, but becoming increasingly branched and developing more horizontally over time, with the leader reaching ground after $\simeq 130$ ms. (c) Same as (b), but for the highlighted dark-gray region in (b) and with INTF sources colored by VHF power. The flash was initiated without an apparent NBE or fast breakdown, and instead was initiated by low-power VHF activity, similar to the FA-quiet INTF sources immediately following the NBE in Figure 9.9c, and lasting $\simeq 180$ μ s. From $\simeq 180$ μ s to 1.5 ms, $\simeq 19$ narrow IBPs and 6 classic IBPs occurred, with FA-quiet periods occurring in-between most pulses. 120
- 9.11 2016.08.09 IC1 flash overview. (a) The whole flash, showing the FA and VHF waveforms (black and blue waveforms, respectively), and INTF sources (markers colored by time) are shown in elevation versus azimuth, and elevation versus time. (b) Same as (a), but for the highlighted light-gray region in (a). The flash initially developed vertically, but became increasingly branched and developed more horizontally over time. (c) Same as (b), but for the highlighted dark-gray region in (b) and with INTF sources colored by VHF power. The flash was initiated without an apparent NBE or fast breakdown, and instead was initiated by low-power VHF activity, similar to the FA-quiet INTF sources immediately following the NBE in Figure 9.9c and the initiating breakdown in Figure 9.10c, lasting $\simeq 100$ μ s. From $\simeq 100$ μ s to 4.0 ms, $\simeq 18$ narrow IBPs and 6 classic IBPs occurred, with FA-quiet periods occurring in-between most pulses. 121

- 9.12 2016.09.02 IC2 flash overview. (a) The whole flash, showing the FA and VHF waveforms (black and blue waveforms, respectively), and INTF sources (markers colored by time) are shown in elevation versus azimuth, and elevation versus time. (b) Same as (a), but for the highlighted light-gray region in (a). The flash initially developed without visible branching, developing several branches and developing more horizontally over time. (c) Same as (b), but for the highlighted dark-gray region in (b) and with INTF sources colored by VHF power. The flash was initiated without an apparent NBE or fast breakdown, and instead was initiated by low-power VHF activity, similar to the FA-quiet INTF sources immediately following the NBE in Figure 9.9c and the initiating breakdown in Figures 9.10c and 9.11c, lasting $\simeq 550 \mu\text{s}$. From $\simeq 550 \mu\text{s}$ to 4.0 ms, $\simeq 14$ narrow IBPs and 4 classic IBPs occurred, with FA-quiet periods occurring in-between most pulses. 122
- 9.13 20160824 CG1 analysis. The 2-D speeds of classic IBPs (black lines) and FA-quiet periods (white lines) are shown superimposed on activity during the initial flash development shown in Figure 9.9c. The black circles denote the sources corresponding to each narrow IBP. 123
- 9.14 20160824 CG2 analysis. The 2-D speeds of classic IBPs (black lines) and FA-quiet periods (white lines) are shown superimposed on activity during the initial flash development shown in Figure 9.9c. The black circles denote the sources corresponding to each narrow IBP. 124
- 9.15 20160902 CG3 flash analysis. The 2-D speeds of classic IBPs (black lines) and FA-quiet periods (white lines) are shown superimposed on activity during the initial flash development shown in Figure 9.10c. The black circles denote the sources corresponding to each narrow IBP. 125
- 9.16 20160809 IC1 analysis. The 2-D speeds of classic IBPs (black lines) and FA-quiet periods (white lines) are shown superimposed on activity during the initial flash development shown in Figure 9.11c. The black circles denote the sources corresponding to each narrow IBP. 126
- 9.17 20160902 IC2 analysis. The 2-D speeds of classic IBPs (black lines) and FA-quiet periods (white lines) are shown superimposed on activity during the initial flash development shown in Figure 9.12c. The black circles denote the sources corresponding to each narrow IBP. 127
- 9.18 20160914 IC3 analysis. The 2-D speeds of classic IBPs (black lines) and FA-quiet periods (white lines) are shown superimposed on activity during the initial flash development shown in Figure 9.12c. The black circles denote the sources corresponding to each narrow IBP. 128

9.19	20160824 CG1 lightning mapping array (LMA) data. LMA sources are colored by time, with blue sources indicating earlier times, and red sources indicating later times. The negative cloud-to-ground flash initiated about 6 km plan distance southeast of the INTF, at an altitude of about 6 km.	129
9.20	20160824 CG2 lightning mapping array (LMA) data. LMA sources are colored by time, with blue sources indicating earlier times, and red sources indicating later times. The negative cloud-to-ground flash initiated about 9.1 km plan distance southeast of the INTF, at an altitude of about 6.5 km.	130
9.21	20160902 CG3 lightning mapping array (LMA) data. LMA sources are colored by time, with blue sources indicating earlier times, and red sources indicating later times. The negative cloud-to-ground flash initiated about 6.1 km plan distance nearly due south of the INTF, at an altitude of about 6 km.	131
9.22	20160809 IC1 lightning mapping array (LMA) data. LMA sources are colored by time, with blue sources indicating earlier times, and red sources indicating later times. The normal-polarity intracloud flash initiated about 15.5 km plan distance southeast of the INTF, at an altitude of about 6 km.	132
9.23	20160902 IC2 lightning mapping array (LMA) data. LMA sources are colored by time, with blue sources indicating earlier times, and red sources indicating later times. The normal-polarity intra-cloud flash initiated about 7.8 km plan distance nearly due east of the INTF, at an altitude of about 7 km.	133
9.24	20160914 IC3 lightning mapping array (LMA) data. LMA sources are colored by time, with blue sources indicating earlier times, and red sources indicating later times. The normal-polarity intra-cloud flash initiated about 6.8 km plan distance nearly due east of the INTF, at an altitude of about 7.5 km.	134
10.1	Observations of the Florida EIP, showing (a) the fast $E(t)$ and Duke ($\sim dB/dt$) waveforms for the first 4.5 ms of the flash, and (c,d) expanded views of the waveforms for the initiating NBE and EIP event. The panels also show the time-integrated estimate of $B(t)$ (blue waveforms) and their comparison with the directly-measured $E(t)$ waveforms (red). Panels (e) and (f) show the corresponding current- and charge-moment changes, M_I (orange) and M_Q (pink), obtained by integrating the $E(t)$ waveform (black). The changes are superimposed on the VHF waveform from the INTF, along with the times of the LMA and NLDN detections ('o' and 'x' symbols, respectively). The plan view map of panel (b) shows the offshore locations of the NBE and EIP by the LMA and NLDN relative to the INTF at KSC (black triangle), and the Duke sensor at FIT (black '+'), along with the locations of four of the KSC LMA stations (green squares).	137

10.2	Overview of the EIP-generating flash and storm. (a,b) LMA observations of the EIP flash (white dots) overlaid on LMA-determined storm charge structure (red for positive charge, blue for negative charge) in orthogonal East-West and North-South vertical projections. The storm charge corresponds to a $\simeq 5$ -minute period of vertical storm growth that includes the EIP flash. (c,d) INTF observations for the flash, colored and sized by VHF power, and the corresponding LMA observations (white dots), plotted in elevation versus azimuth, and elevation versus time, respectively. The NBE and EIP correspond to the two groupings of high-power INTF sources in the first few milliseconds of the flash, near 14° and 18° elevation, respectively. (e) FA fast electric field change (black) and INTF VHF (gray) waveforms of the EIP flash, corresponding to the same time period as in (c) and (d).....	141
10.3	Early stages of the EIP-generating flash. (a) INTF sources for the first 3.8 ms of the flash plotted in altitude/elevation versus time, colored and sized by detected VHF power, along with the corresponding FA electric field-change (black) and INTF VHF (gray) waveforms. The vertical dashed lines separate different stages of the flash evolution, shown in altitude/elevation vs. azimuth plots in (b)-(h), where the INTF sources in each stage are colored by time and prior sources are colored in black. The stages consist of: (b) the flash-initiating NBE, lasting about $40 \mu\text{s}$, (c) about 1.5 ms of non-propagating, quiescent and scattered activity after the NBE preceding the negative leader development, (d) onset and development of the initially fast ($\simeq 3.2 \times 10^6 \text{ m/s}$) negative leader, (e) a $\simeq 10\text{-}\mu\text{s}$ downward “step” that interrupted the upward development of the negative leader, (f) resumption of the slowed-down ($\simeq 5 \times 10^5 \text{ m/s}$) leader, (g) exceptionally fast ($6 \times 10^6 \text{ m/s}$) upward progression of INTF sources, and (h) the EIP-associated INTF sources, which depict a rapid succession of fast-propagating ($10^7\text{-}10^8 \text{ m/s}$) breakdown events. (i) INTF sources for the full 3.8 ms interval, colored and sized by detected VHF power.	143

- 10.4 EIP detailed evolution. (a) The INTF sources during the EIP (i.e., during the time interval shown in Figure 10.3h) are plotted in altitude/elevation versus time, and are colored and sized by detected VHF power, with sources prior to the EIP colored in black, along with the corresponding FA electric field-change (black) and VHF (gray) waveforms, and the times of the NLDN ('x') and LMA ('o') events. (b) The natural log of the VHF power shows the onset of an exponential rise in VHF power (thick dashed line at 3.284 ms) up to the moment the signal saturated. The thin vertical dashed lines in (a) and (b) identify 4 successive intervals that are examined in altitude/elevation vs. azimuth plots in (c)-(f), where the sources in each interval are colored by time and prior sources are colored in black. A 12- μ s offset is visible between the onset of main EIP pulse (thin dashed line at 3.272 ms) and the onset of the large VHF burst (thick dashed line at 3.824 ms). (c) Apparent downward source motion with speed 2.6×10^8 m/s, (d) apparent upward source motion with speed 1.2×10^8 m/s, (e) apparent downward source motion with an initial speed of 5.7×10^7 m/s, then a faster speed of 1.0×10^8 m/s, and (f) upward fast negative breakdown with an initial speed of 4.2×10^7 m/s, then a slower speed of 1.3×10^7 m/s. (g) The INTF sources during the entire EIP, colored and sized by detected VHF power. 145
- 10.5 Comparisons of the flash-initiating NBE and the EIP. The INTF sources, FA (black) and VHF (light blue) waveforms, and times of the NLDN ('x') and LMA ('o') events for the NBE (a,c) and the EIP (b,d). Displayed on similar vertical scales, (a) and (b) compare the NBE and EIP for a 140 μ s interval, and (c) and (d) compare the NBE and EIP in a zoomed-in view for a 40 μ s interval. Both the NBE and EIP have a VHF burst associated with fast positive breakdown (FPB) of similar duration, extent, and speed. The FPB is associated with spikey perturbations on the FA waveform in (c), and in (d) similar perturbations are superimposed on the much larger, more smoothly-developing EIP sferic between 3287 and 3297 μ s. The perturbation on the smooth EIP pulse near 3282 μ s is apparently due to radio frequency interference (RFI) of unknown origin, because similar RFI occurs on only one of the three INTF VHF waveforms. 147
- 10.6 EIP storm activity. (a) Flash activity around the EIP flash. Two intracloud flashes (blue and green) preceded the EIP flash (red), and a cloud-to-ground (brown) occurred subsequently. Flashes "IC2" and "CG5" occurred in the same newly-developing eastern cell where the EIP flash occurred, whereas the green flash occurred in the older part of the storm to the west. (b) The LMA-determined flash density. The black arrows point to the approximate location of the EIP. 149

10.7	LMA and NLDN observations for the EIP flash, showing its bilevel nature between negative charge at 6–8 km altitude MSL and upper positive charge between 10–12 km. The flash began with an upward negative leader into a compact region of positive charge, and produced the EIP as soon as it entered the positive region. Instead of turning horizontal and propagating through horizontally-distributed positive charge, as occurred during other IC flashes in the storm, for about 200 ms the flash continued to discharge relatively localized positive and negative charge regions before shutting off in the upper positive charge and developing horizontally within the negative charge region. positive positive charge region (black ‘*’).	154
10.8	LMA and NLDN data for the NBE and EIP. NBE and EIP NLDN sources are indicated by a black ‘*’ and ‘x’, respectively, and LMA sources are (a) colored and sized by VHF power, and (b) colored by time. Lower-power LMA sources following the NBE can be seen clustered near the NBE NLDN location.	155
10.9	Detailed radio observations of flash-initiating NBE. (a), (c) INTF sources (circular markers, colored and sized by VHF power), plotted in elevation vs. azimuth, showing the primarily vertical breakdown activity of the NBE. (b), (d) INTF sources and FA (black) and VHF (light blue) waveforms, showing the downward propagation of the INTF sources. The fast positive breakdown descended about 400 meters in 5 μ s, corresponding to a speed of about 10^8 m/s. (e) Semilog plot of the VHF power vs. time, showing the fast exponential rise of the radiation (rise time $\tau = 0.24 \mu$ s), coincident with the fast rise of the electric field change in (d).	156
10.10	Detailed radio observations of step. (a) 350 μ s showing the multi-pulsed FA waveform (black) and VHF waveform (light blue) around the step, along with the downward then upward motion of associated INTF sources. (b) Zoomed-in 30 μ s around the step, showing the $\sim 10^8$ m/s apparent downward then upward INTF source propagation.	157

10.11 Results of a simplified technique for identifying perturbations in the EIP sferic waveform. The blue waveform is the original sferic, which is separated into two components utilizing envelope analysis. The red curve is the lower envelope of the peak sferic values obtained from the Matlab ‘envelope’ function. The black waveform is the difference between original sferic and the lower envelope. Three distinct perturbations are seen, first on the leading edge of the initial sferic peak, which is correlated with fast upward negative and downward positive VHF sources between 3.255 and 3.262 ms in panels (a) and (c) of Figure 4. The second, more impulsive perturbation is produced by a combination of weak positive events associated with downward fast positive breakdown prior to the main sferic peak at 3.284 ms in Figure 4a, and coincidental, brief radio frequency interference (RFI) of unknown origin during the first half of the perturbation. The final, large perturbation is caused by the high power NBE-like fast positive downward and negative upward sequence and strong VHF radiation that was triggered by the main relativistic avalanche. The amplitude of the initial part of the NBE-like perturbation is under-estimated, owing to larger, unknown d.c. offsets (i.e., larger undershoot in the red curve) not being detected by the envelope technique. Still, the technique provides a valuable method for analyzing EIP waveforms. 158

ABSTRACT

Broadband Radio Mapping and Imaging of Lightning Processes

by

Julia Napolin Tilles

University of New Hampshire, May, 2020

Though thunderstorms and lightning are commonplace on Earth, it is still unclear how lightning initiates, propagates, and how it is involved in generating intense bursts of gamma-rays that can be detected by spacecraft. Lightning is a hot, highly-ionized plasma channel, capable of carrying up to hundreds of kiloamperes electric current, and extending many kilometers in length for hundreds of milliseconds at a time. Despite its immensity, lightning can be difficult to observe, as it primarily initiates and propagates deep within thunderclouds, optically obscured by thousands of cubic kilometers of cloud water and ice. Broadband radio interferometry has been developed to study lightning at radio frequencies, offering us a way to “see” inside the clouds. The technique, which is still in its infancy for lightning research, allows for lightning radio emissions to be mapped and/or imaged with extremely fine time resolution. In this dissertation, a newly-developed three-element, broadband VHF ($\simeq 14\text{--}88$ MHz), 16-bit radio interferometer (INTF) is used to investigate extremely transient thunderstorm electrical phenomena involved in lightning initiation, propagation, and high-energy photon production. The investigations demonstrate the novel science that can be done with the INTF system, and reveal previously unforeseen dynamics of lightning formation.

Specifically, we image and map the VHF emissions of narrow bipolar events (NBEs), initial breakdown pulses (IBPs), and an energetic in-cloud pulse (EIP) with sub-microsecond resolution. NBEs have long been of interest to the lightning community because they are the most powerful natural emitters of high-frequency and very-high-frequency radio waves on Earth. Moreover, NBEs are readily identifiable by their narrow (~ 10 μs wide), bipolar sferics (~ 3 kHz–3 MHz radio emissions). NBEs are not lightning, but appear to be a precursor to lightning, occurring either in complete isolation, or at the beginning of a lightning flash. IBPs, in contrast, never occur in isolation, but rather are the hallmark of lightning channel formation. IBPs typically occur in long trains of sferic pulses, and indicate the imminence of lightning during the first milliseconds after lightning initiation. An IBP is also identified by its sferic, having a bipolar waveform some tens of microseconds wide, the initial pulse of which is superimposed by ~ 1 μs -wide subpulses. Lastly, EIPs are high-peak-current (> 200 kA) events that are involved in the generation of terrestrial gamma-ray flashes (TGFs), which are intense bursts of gamma-rays that radiate out the tops of thunderclouds and are detected in space. EIPs have a signature high-amplitude, ~ 50 μs -wide sferic, which is time-aligned with satellite-borne gamma-ray detections. EIPs can thus serve as

a proxy for TGFs, offering a way to investigate TGFs using ground-based radio sensors, without necessarily needing satellite data.

The physical natures of NBEs, IBPs, and EIPs have been active areas of research over the last decade. For over half a century, the role that IBPs play in initial hot channel formation has been under debate. More recently, intense investigation has been focused on exactly how NBEs are involved in lightning initiation. Just in the last few years, EIPs were discovered, offering a new way to investigate the role that lightning plays in TGF generation.

By investigating NBEs with the INTF, we discovered a newly-identified form of streamer-based breakdown, termed fast negative breakdown, that does not fit with our current understanding of lightning initiation. Streamers are cold filamentary plasma channels, and based on conventional dielectric theory, it was hypothesized that lightning should be initiated by positive streamers, which carry electric current in their propagation direction. However, fast negative breakdown carries electric current opposite its propagation direction, propagating ~ 500 m through virgin air with an unusually fast speed of $\sim 10^7$ m/s. Aside from breakdown polarity, fast negative breakdown is in many ways similar to recently reported fast positive breakdown that generates the majority of NBEs, and that is expected from conventional dielectric theory.

We additionally show that similarly fast breakdown is involved in the production of both IBPs and EIPs. Using the INTF, we show that the IBP process is dominated by a fast-propagating $\sim 10^7$ m/s streamer-based negative breakdown that propagates the channel about ~ 100 m into virgin air, similar to the fast negative breakdown associated with NBEs. We show that the streamer-based channel extension leads to a sustained electric current, indicating the existence of a hot conductive lightning channel. Fast-propagating $\sim 10^7$ - 10^8 m/s breakdown of both polarities is also a prominent feature during the EIP, but occurs over a larger (>1 -km altitude) volume than during NBEs or IBPs. We show that repeated downward- and upward-propagating fast positive and negative breakdown are somehow coupled to the generation of relativistic electrons and associated ionization. We conclude that the electric current that produces the EIP sferic is generated by a newly discovered type of self-sustaining discharge termed a relativistic feedback discharge (RFD), which involves multiple generations of relativistic electron avalanches and back-scattered positrons and X-rays. Our study further demonstrates that TGFs can be produced by RFDs.

The INTF was developed by New Mexico Tech, and deployed and operated at Kennedy Space Center (KSC) in Florida during summer 2016 to obtain the data used herein.

Part I

Introduction

CHAPTER 1

OVERVIEW

Some of the most basic questions about lightning, e.g., how lightning initiates and how it propagates, are still not fully understood (Petersen *et al.*, 2008). The problem is due partly to the stochastic nature of lightning, so that direct measurements such as channel current, temperature, nearby electric and magnetic fields, and high-energy photon emissions are incredibly difficult, if

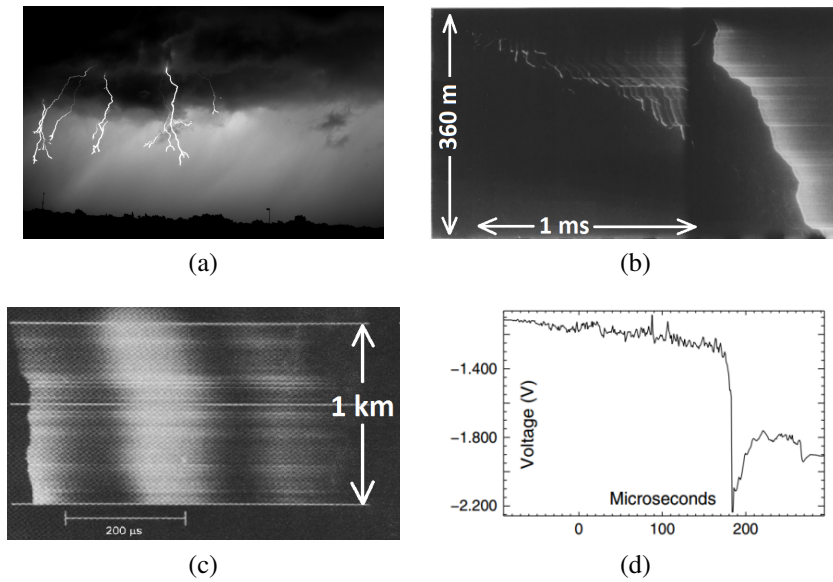


Figure 1.1: Cloud-to-ground lightning leader optical and radio emissions. (a) A $142 \mu\text{s}$ exposure optical image shows lightning leaders exit the cloud and propagate to ground. (b) A high-speed streak-camera photograph shows a lightning leader propagating 360 m below the cloud base to ground over time (dim features progressing downward, left to right), followed by connection to ground and the return stroke (large surge of luminosity) along the channel. Adapted from Berger & Vogelsanger (1966). (b) A streak photograph of the lowest $\simeq 1$ km of a lightning leader connected to ground, showing variations in luminosity, i.e., current, along the channel over time (left to right). Adapted from Jordan *et al.* (1995). (c) The currents from large-scale (km-length) leaders produce emissions in very-low and low frequency radio, as illustrated for a lightning return stroke measured by a ~ 1 Hz-400 kHz passband sensor. Adapted from Bitzer *et al.* (2013).

not impossible, to obtain. The problem is also partly due to the vast spatial (meters to kilometers) and temporal (sub-microsecond to milliseconds) scales involved in lightning, which ultimately requires high data throughput and storage. The problem is further exacerbated by lightning’s locale – the exceptionally turbulent, wet, and icy interiors of thunderclouds, which are also optically opaque. Some direct measurements of electric current can be obtained by triggering lightning to ground-based sensors using rockets (Dwyer *et al.*, 2003; Biagi *et al.*, 2010; Dwyer *et al.*, 2011), while high-speed optical sensors have been used extensively to investigate the morphology and dynamics of lightning below the cloud base (Saba *et al.*, 2008; Biagi *et al.*, 2010; Hill *et al.*, 2011; Petersen & Beasley, 2013), as well as channel temperature (Orville, 1968; Chang *et al.*, 2017). For example, the high-speed optical images in Figures 1.1 and 1.2 demonstrate the morphology and dynamics of lightning below the cloud base, which involves a branched lightning channel that “steps” to ground, followed by the connection to ground and a large surge in current along the channel. However, lightning that comes to ground makes up only a small portion of all lightning activity (Boccippio *et al.*, 2000). Moreover, channels exiting the cloud base, like those seen in Figures 1.1a, constitute a very small portion of the overall lightning channel. Optical measurements cannot reveal how lightning initiates deep inside thunderclouds, nor how lightning is involved in generating intense bursts of gamma radiation that can be detected in space (Figure 1.3).

Though it is unclear exactly how lightning initiates and propagates, much of what is known about lightning comes from remote electromagnetic radio measurements. Thunderclouds are largely transparent to radio frequencies, and fortunately lightning is a strong radio emitter in a broad range of frequencies. Lightning leaders are hot, highly-ionized channels that can maintain large currents along channels many kilometers long for many milliseconds (Bruning & MacGorman, 2013). Lightning leaders thus emit strongly at low radio frequencies ($\sim 1\text{-}100$ kHz) (Bitzer *et al.*, 2013). For example, the streak photograph in Figure 1.1b shows lightning leaders coming to ground (dim features progressing downward, left to right). When the leader connects to ground, a huge surge in current and luminosity propagates upward along the channel, termed the “return stroke”, which is typically what people identify as lightning by eye. Variations in current (and hence luminosity)

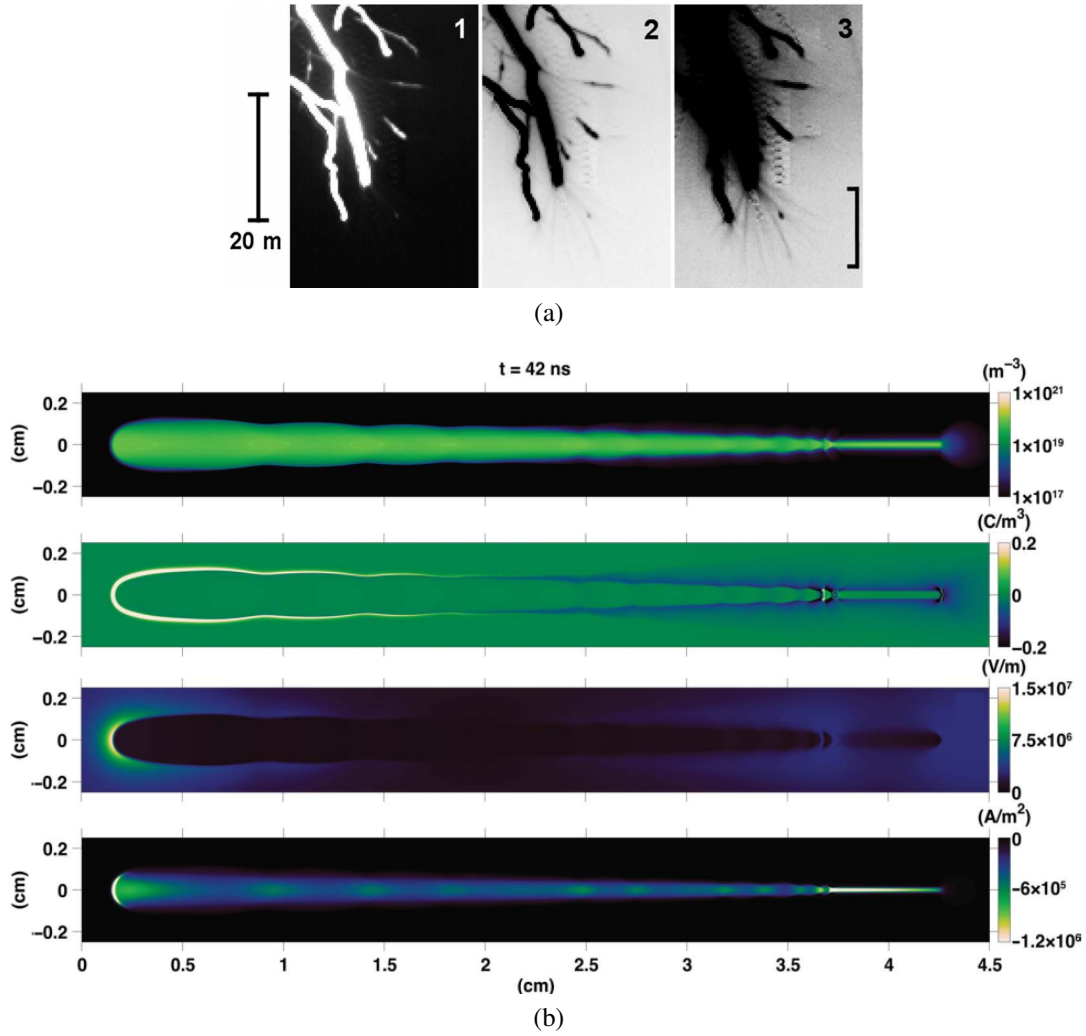


Figure 1.2: Streamers in lightning observation and simulation. (a) A $100\text{-}\mu\text{s}$ optical image of a lightning leader tip propagating to ground. The original image, (1), is inverted in (2), and enhanced in (3). The white features in (1) are due to optical light from a hot lightning leader, whereas the gray filaments indicated by the bracket in (3) are due to streamer-zone streamers. Adapted from Petersen & Beasley (2013). (b) Streamer simulation results show, from top to bottom, a cross-section of streamer electron density, space charge density, electric field, and longitudinal current density, showing a concentration at the streamer head. The growth rate of the current leads to electromagnetic emissions extending to ~ 100 MHz. Adapted from Shi *et al.* (2016).

along the channel (Figure 1.1c) create strong emissions at low radio frequencies. Such sferics, or broadband radio frequency emissions, are shown for a return stroke in Figure 1.1d.

Lightning is also composed of a lesser-known type of discharge called a streamer. Streamers are cold filamentary plasma channels, forming in the high electric fields at the tips of lightning

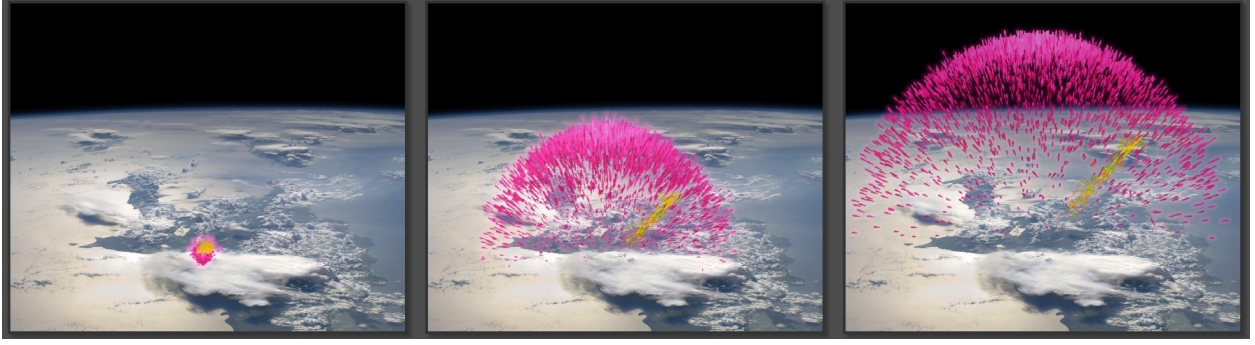


Figure 1.3: Depiction of terrestrial gamma-ray flash (TGF). High-energy electrons (yellow), positrons (green), and gamma-rays (pink) begin to emanate from a thundercloud top, moving progressively upward into the near-space environment over time (from the left to the right panel). The charged particles (electrons and positrons) travel along magnetic field lines. Credit: NASA/Goddard Space Flight Center/J. Dwyer, Florida Institute of Technology.

leaders. For instance, Figure 1.2a shows a $100\text{-}\mu\text{s}$ optical image of a leader tip, which can be seen as bright (i.e., white) features in panel 1. In the inverted and enhanced image in panel 3, the streamers can be seen as wispy gray features emanating from the leader tip. Streamers at thunderstorm altitudes emit up to high and very high frequency ($\sim 1\text{-}100$ MHz) radio (Shi *et al.*, 2016; Liu *et al.*, 2019). For instance, Figure 1.2b shows that the longitudinal current density of a simulated streamer is concentrated at the streamer head. The growth rate of the current leads to electromagnetic emissions extending to at least tens of MHz.

By making measurements of lightning at various radio frequencies simultaneously, it is possible to probe different properties of the emitters, such as electric current on large (\sim kilometer) and small (\sim meter) spatial scales. In addition, by using a network of radio sensors, it is possible to image and/or map the motion of lightning in radio, providing the extents, speeds, and general morphology and dynamics of the emitting processes.

Mapping and imaging lightning processes in broadband (i.e., high-speed) radio is the crux of this dissertation. The remainder of Part I introduces the lightning processes studied herein, and lists the main scientific contributions of this dissertation. Part II describes the broadband radio interferometer used for mapping and imaging lightning, and also describes complementary measurement systems. In Part III, the detailed results are given.

CHAPTER 2

PHENOMENOLOGY

2.1 Thunderstorms

Thunderstorms take place in the troposphere, which is the lowest region of Earth's atmosphere, where temperature decreases with height. Thundercloud development is driven by heating at lower altitudes, which causes moist air to rise, and as the air rises and cools, it condenses to form cloud, which releases latent heat and creates further lift. Given enough heating and moisture at lower altitudes, thunderclouds can develop, with fierce updrafts ranging from $\simeq 1$ m/s up to more than 40 m/s (i.e., 90 mph) (Marshall *et al.*, 1995a). Thundercloud tops can reach up to ~ 20 km altitude near the equator (Ushio *et al.*, 2001) where the tropopause is highest (Hoinka, 1999). The bottom-most portion of a thundercloud is warm, consisting entirely of liquid water, and takes place below $\simeq 5$ km altitude in a typical Florida thunderstorm, as depicted in Figure 2.1. However, at about -40°C ($\simeq 10$ km altitude in a typical Florida thunderstorm), all water becomes solid ice, either in the form of small ice crystals, or in larger pellets known as graupel. In between the 0°C and -40°C

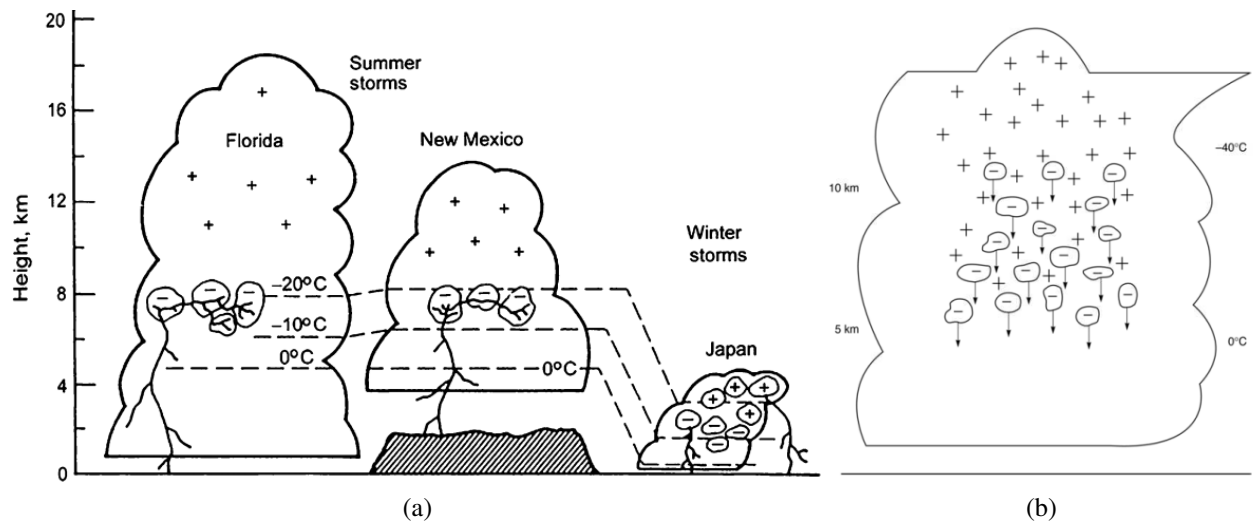


Figure 2.1: Normal-polarity thunderstorms. (a) The deepest convection occurs in tropical regions at sea level, such as in Florida, where the troposphere is deepest. In regions at higher latitude, thunderstorms are less deep, especially in high-elevation regions such as New Mexico. Winter thunderstorms, such as those that occur in Japan, are much less deep due to reduced heating at lower altitudes. Adapted from Krehbiel (1986). (b) Heavy negatively-charged graupel pellets fall to lower storm altitudes than positive-charged ice crystals, forming a dipole charge structure in thunderstorms. Adapted from Williams (2006).

levels, a “mixed phase” exists, which consists of ice and super-cooled water still in its liquid phase. Figure 2.2 shows a conceptual drawing of a thundercloud vertical cross section, showing a strong central updraft that suspends water and ice inside the cloud, with downdrafts existing outside of the main convective core. Because temperature decreases with altitude in the troposphere, stratified regions of different hydrometeors are established in the cloud. Liquid water content in the mixed phase region largely controls what sign of charge is attributed to graupel, and so it is primarily responsible for the different charge configurations that can be found in thunderclouds (Takahashi, 1978; Bruning *et al.*, 2014). For example, Figure 2.3a shows a diagram of graupel becoming charged after a collision with an ice crystal in the mixed-phase region. The ice crystal then takes the opposite charge as the graupel. Figure 2.3b demonstrates how the sign of the charge to graupel depends on the liquid water content and temperature. Since temperature is another way to indicate thundercloud altitude, the dotted curves represent possible charge configurations as a function of thunderstorm altitude, with the top curve representing a storm dominated by a deep positive charge region, and the bottom three curves representing storms with varying depths of dominant negative charge.

For instance, a “normal-polarity” storm consists of a dipole or tripole storm charge structure that has a main negative storm charge at mid-altitudes, with a region of lesser positive charge on top (Figure 2.1), and sometimes an even lesser positive region at the base of the cloud. Normal-polarity charge structures are prominent in “air mass” storms in New Mexico, Florida, and Japan where many of the earliest studies on storm charge structure took place (Krehbiel, 1986). In addition, more recent “anomalous” charge structures have been identified, particularly in the Great Plains area of the United States (Fuchs *et al.*, 2015). Anomalous storms generally feature a main positive charge region at mid-altitudes, and are associated much more with severe weather and tornadic storms (MacGorman & Burgess, 1994; Smith *et al.*, 2000).

Due to the influence of gravity, the formation of stratified regions of different cloud water particles, or hydrometeors, naturally occurs, as illustrated in Figure 2.1b. Heavier graupel falls to lower altitudes but remains suspended by strong updrafts in the cloud, while lighter ice crystals can

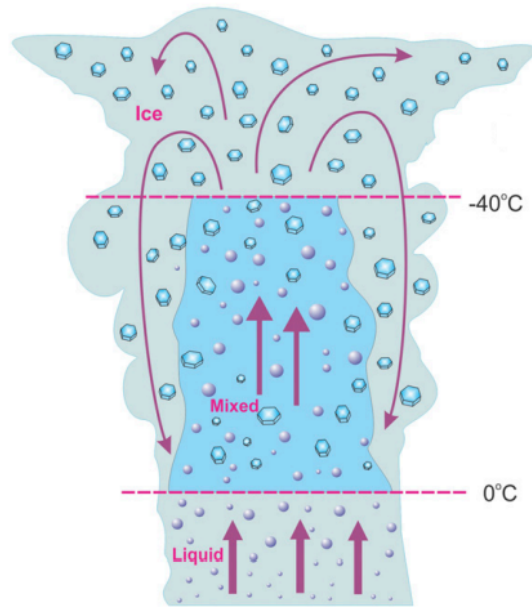


Figure 2.2: Thundercloud temperature and hydrometeor profile. Strong updrafts (upward-pointing arrows) suspend liquid water and water ice throughout the thundercloud. Below the 0°C level, the water content is all liquid, and above the -40°C level, the water content is all ice. However, between the 0°C and -40°C levels, a mixed region of liquid and ice water exists. Downdrafts outside of the main convective core are shown with the downward-curving arrows. Adapted from Korolev *et al.* (2017).

float higher aloft. It is hypothesized that a normal-polarity storm forms when graupel pellets carry negative charge to mid-altitudes, and ice crystals carry positive charge to higher altitudes, forming the storm charge dipole. In addition, a lower positive charge region sometimes forms, creating a storm charge tripole, but it is not entirely clear how this region forms (Williams, 1989, 2006). The altitudes of the different thundercloud regions depend largely on the latitude and season where a thunderstorm occurs. Figure 2.1a shows that the temperature profiles of summer-time Florida and New Mexico thunderstorms tend to be similar, whereas for winter-time thunderstorms, such as those that take place in Japan, the entire thundercloud is at a drastically lower altitude. Moreover, because of the higher elevations and higher latitudes in New Mexico than Florida, New Mexico thunderstorms will generally not be as deep as Florida thunderstorms, having higher cloud bases

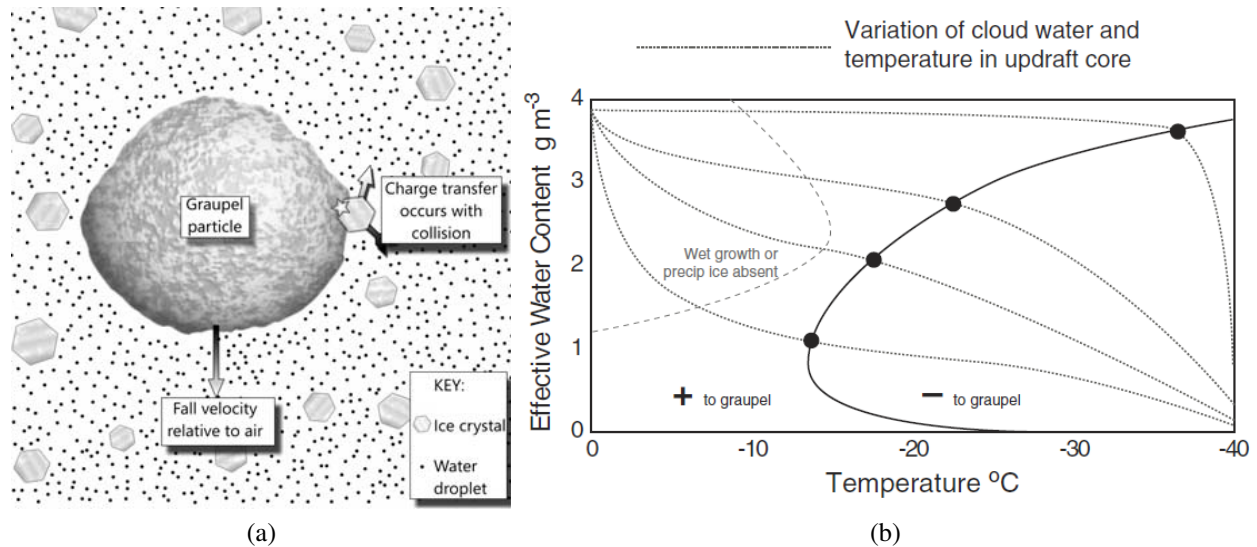


Figure 2.3: Charging to graupel in the mixed phase region of thunderstorms. (a) A graupel particle falls due to gravity, and grows as a result of liquid water freezing on its surface. Charge transfer between graupel and an ice crystal occurs after collision. Adapted from Emersic (2006). (b) The charge imparted to graupel after collision with an ice particle is not of a fixed sign, but is dependent on the temperature and the amount of liquid water present. The temperature axis can be identically interpreted as thunderstorm altitude, with the dotted curves representing possible storm charge configurations. For instance, the storm could be dominated by a deep positive charge layer (top curve), or varying depths of dominant negative charge (bottom three curves). Adapted from Bruning *et al.* (2014).

(due in part to terrain) and lower cloud tops (due in part to a lower tropopause at higher latitudes) than in Florida.

Lightning is thought to initiate in between stratified regions of storm charge, where the electric fields would be highest. For example, Figure 2.4 shows the VHF radio sources associated with lightning developing bidirectionally away from an initiation point in a thunderstorm, superimposed on the vertical cross-section of thundercloud radar reflectivity. Presumably, the initiation point occurred between stratified regions of charge. Lightning, once formed, is a highly-ionized conductor that becomes polarized in the thundercloud electric field. One end of the lightning channel will have a net negative charge – this is termed the negative leader – and the other end of the lightning channel will have a net positive charge – this is termed the positive leader. Negative and positive leaders behave differently (Section 2.2), which allows them to be distinguished in VHF mapping

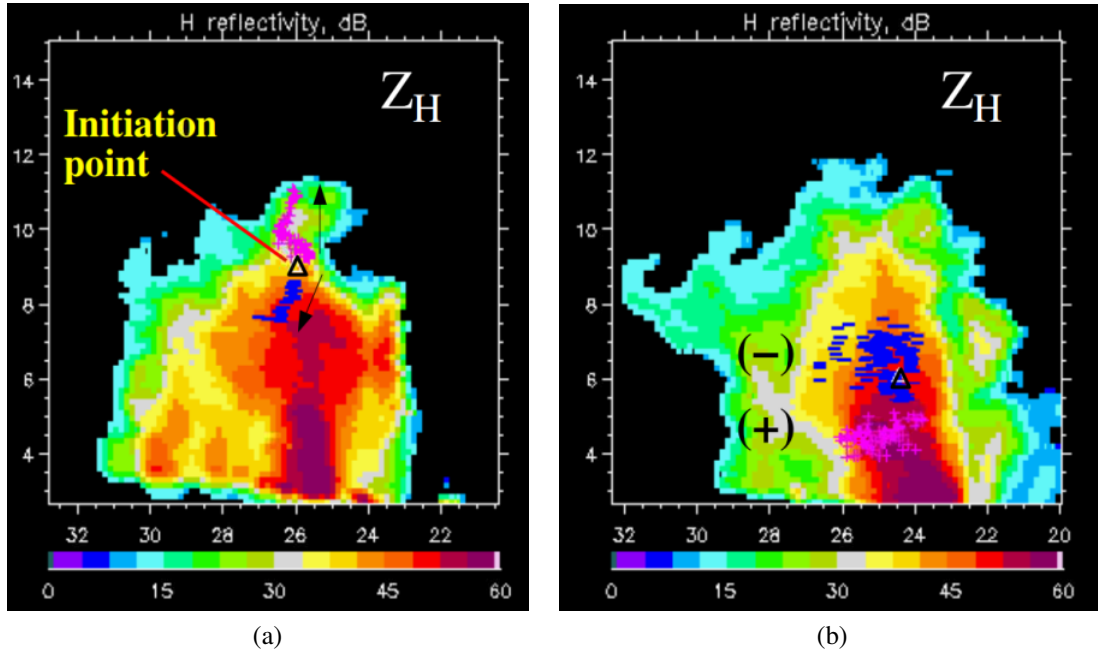


Figure 2.4: Lightning activity superimposed on vertical cross-section of thundercloud radar reflectivity. Lightning source locations were determined by a three-dimensional VHF (60-66 MHz) mapping instrument, and show sources associated with the negative leader (magenta '+') propagating through positive cloud charge, and the positive leader (blue '-') propagating through negative cloud charge. The triangle shows the location of the flash initiation point. Radar reflectivity is given in relative units of dB and shows cloud precipitation from the lightest values (cyan) on the cloud edge to the heaviest values (purple) in the cloud core. In (a), the flash initiates at about 9 km altitude between inferred regions of upper positive and mid-level negative charge, above the thundercloud core, and the two leaders propagate bidirectionally away from the initiation point. In (b), a cloud-to-ground flash initiates at about 5 km altitude between inferred regions of mid-level negative charge and weaker lower positive charge, and the two leaders again propagate bidirectionally away from the initiation point. Adapted from Krehbiel *et al.* (2005).

data (Section 7.2). For instance, Figure 2.5a shows the charge structure of a thundercloud that is reconstructed by observing the negative and positive leaders of lightning during a ten-minute period, while panels b and c show model-estimated values of the vertical electric field and electric potential in the cloud before and after a lightning flash to ground.

In general, there are two regions in a normal-polarity storm where lightning initiates: either above or below the main negative charge region. Figure 2.4a shows lightning initiating in the upper levels of the storm, forming what is termed intra-cloud (IC) lightning. IC lightning forms

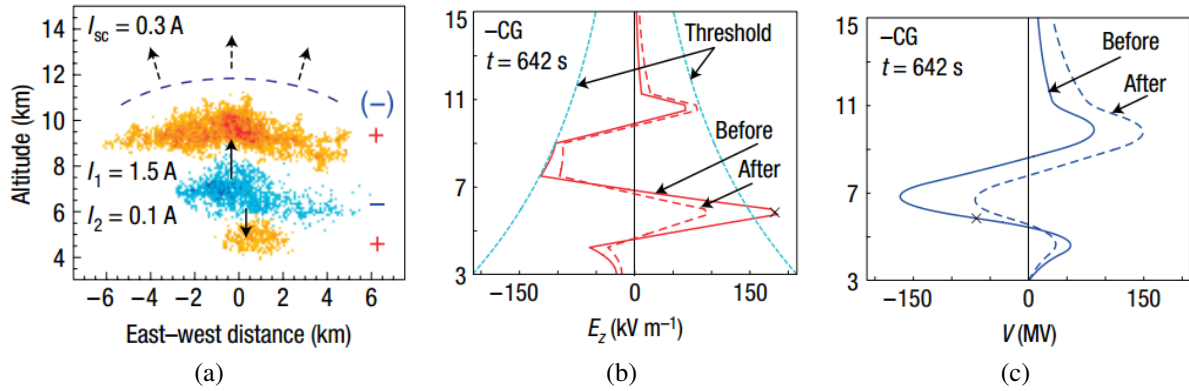


Figure 2.5: Normal polarity charge structure and electrical quantities. (a) The thunderstorm charge structure is reconstructed using VHF lightning data, with orange regions depicting negative leaders propagating through positive charge, and blue regions depicting positive leaders propagating through negative charge. In (b) and (c), model-estimated values of the vertical electric field and electric potential, respectively, are shown at different altitudes along the central axis of the thunderstorm in (a). The values are shown before (solid line) and after (dashed line) a cloud-to-ground lightning flash. Adapted from Krehbiel *et al.* (2008).

between the mid-level negative and upper-positive storm charge in a normal-polarity storm. In fact, most lightning ($>70\%$) remains entirely in the cloud (Boccippio *et al.*, 2000). Figure 2.4b, on the other hand, shows lightning initiating in the lower reaches of the storm, forming what is termed cloud-to-ground (CG) lightning. CG lightning forms between the mid-level negative and lower-positive storm charge in a normal-polarity storm. The lower positive charge is generally quite weak, so lightning will propagate through it all the way to ground, eventually electrically shorting the thundercloud potential ($\sim 100 \text{ MV}$) to ground potential (0 V) (Krehbiel *et al.*, 2008). The short causes a huge surge of current to propagate up the lightning channel, which manifests as a luminosity wave that travels at $\sim 10^8 \text{ m/s}$ up the channel, and is termed a return stroke (Orville, 1968).

Despite the relatively simple picture painted above, one of the biggest problems in the field of atmospheric electricity is how lightning is initiated in a thundercloud. Dielectric breakdown can initiate when the ambient electric field is more than the threshold field, which is $\simeq 3 \times 10^6 \text{ V/m}$ at sea level (Section 2.3.1). The threshold field scales with pressure (Section 2.3.2), so can be determined for lightning initiation at the higher altitudes, i.e., lower pressures, inside thunderstorms.

However, the problem is that in-situ measurements of the thundercloud electric field are consistently an order of magnitude too low to initiate lightning (Winn *et al.*, 1974; Marshall & Rust, 1991; Marshall *et al.*, 1995b; Stolzenburg *et al.*, 2007). Figure 2.6 demonstrates how in-situ thundercloud electric field and temperature, among other parameters, can be measured using a balloon payload, which also serves to determine cloud charge structure.

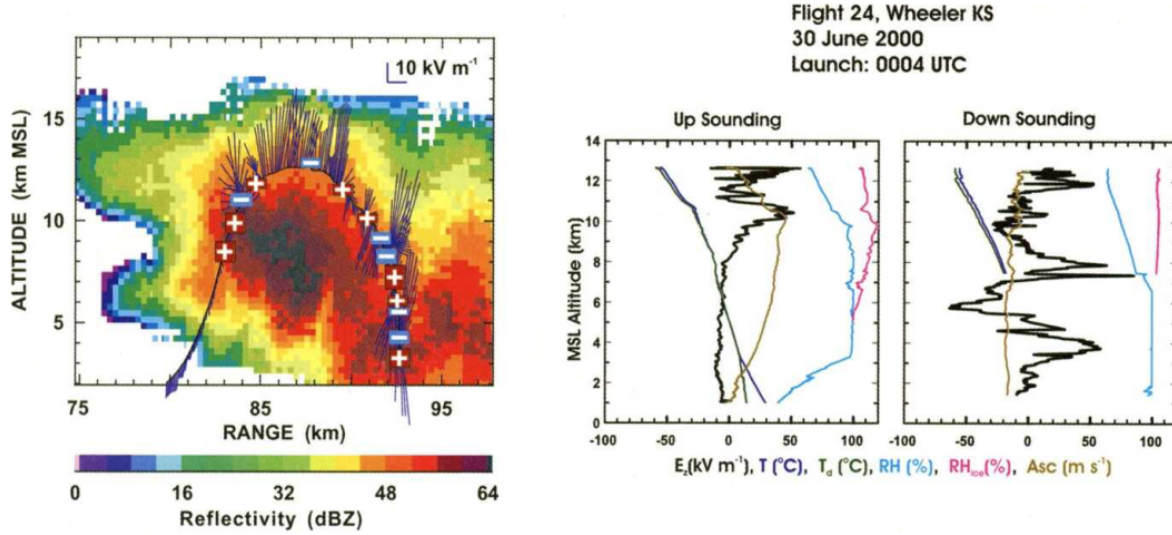


Figure 2.6: Balloon-borne thundercloud electric field sounding. Left: vertical cross-section of thundercloud radar reflectivity, superimposed by balloon trajectory (black curve), electric field vector, i.e., directions and strengths (blue line segments) along the flight path, and inferred charge regions (red '+' for positive charge, blue '-' for negative charge). Right: sounding results, including the vertical component of the electric field, E_z , in black, and temperature, T , in dark blue, along the balloon trajectory. Adapted from Lang *et al.* (2004).

2.2 Lightning leaders

Leaders are hot, highly-ionized, highly-conductive lightning plasma channels (Petersen *et al.*, 2008; da Silva & Pasko, 2013) that can travel and carry electric currents for tens to hundreds of kilometers in a thunderstorm. The physical properties of lightning leaders, for instance channel temperature, can be inferred from high speed optical video. Return strokes (the luminosity/current waves that propagate up a lightning channel after it electrically connects to ground) were shown

to be at least 36,000 K in temperature (Orville, 1968). However, the temperature of propagating stepped leaders is somewhat lower, $\simeq 14,000$ K in the overall channel, and $\simeq 15,000$ K in the leading tip (Chang *et al.*, 2017).

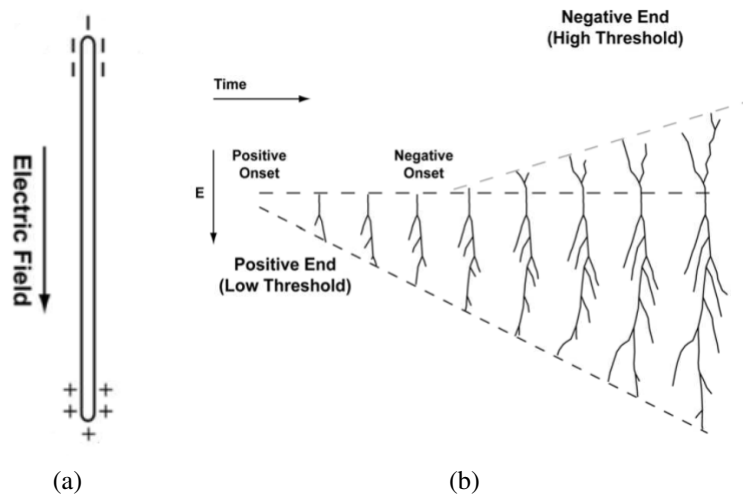


Figure 2.7: Schematic of bidirectional leader formation and propagation in thunderstorms. (a) Once formed, the lightning leader is a highly-conductive plasma in the thundercloud electric field, and so acts like a polarized linear conductor. (b) Schematic of streamer/leader initial bidirectional development, showing positive-polarity breakdown initiates first and begins to elongate before the initiation of the negative polarity breakdown. The system starts off streamer-based (a cold discharge), and becomes a leader once the currents become large enough to thermalize the system. Adapted from Williams (2006).

Once formed, the lightning leader is bidirectional, having both a positive and a negative end as demonstrated in Figure 2.4, and the two leader polarities behave very differently (Williams, 2006). A lightning leader is a highly-ionized and therefore highly-conductive plasma, and because it is placed in an electric field, i.e., the thundercloud electric field, it acts like a polarized conductor, as illustrated in Figure 2.7 for a vertically-oriented lightning leader in a vertical thundercloud field. The large amount of negative (positive) charge at the tip of a negative (positive) leader creates high electric fields near the tips, which can ionize the air around them, resulting in negative (positive) streamer development (Section 2.3), or the development of a “streamer zone” at the tips (see Figure 1.2a). Streamers are cold, filamentary plasma channels, and negative and positive streamers form at different critical fields, with the critical field for positive streamers being about half the

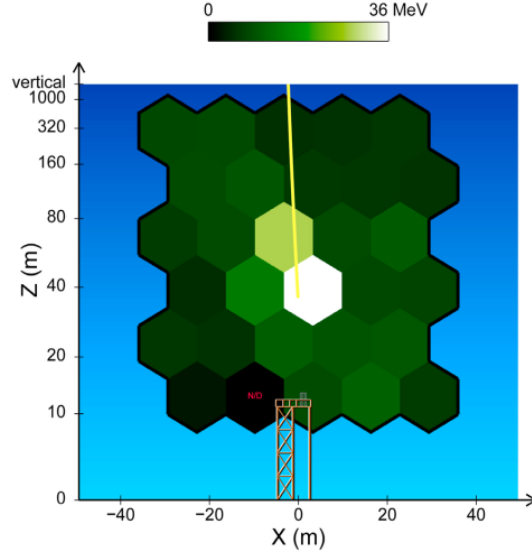


Figure 2.8: X-ray image of lightning leader coming to ground. A high-speed pin-hole X-ray camera produced a $0.5\text{-}\mu\text{s}$ exposure (hexagonal pixels) of a dart leader coming to ground during rocket-triggered lightning. The tip of the dart leader (yellow line) appears to be co-located with 36 MeV X-ray emission. Adapted from Dwyer *et al.* (2011).

critical field for negative streamers (Qin & Pasko, 2014). Due in part to the asymmetry of how negative and positive streamers form, and hence the asymmetry of how negative and positive leaders form, we see asymmetries in their propagation characteristics. For instance, negative leaders clearly propagate in a “stepped” manner (Reess *et al.*, 1995; Petersen & Beasley, 2013; Hill *et al.*, 2011) (more on this below), while positive leaders propagate apparently without a stepping process (Saba *et al.*, 2008), in-cloud negative leaders propagate at higher speeds ($1\text{--}3 \times 10^5$ m/s (Shao *et al.*, 1995; Shao & Krehbiel, 1996; van der Velde & Montanya, 2013)) than positive leaders ($1\text{--}2 \times 10^4$ m/s (Ogawa & Brook, 1964; Shao & Krehbiel, 1996; van der Velde & Montanya, 2013)), negative leaders emit more copious amounts of VHF radiation than positive leaders (Edens *et al.*, 2012), and negative leaders are involved in both X-ray and gamma-ray generation (Dwyer *et al.*, 2005a; Lu *et al.*, 2010; Lu *et al.*, 2011; Cummer *et al.*, 2015; Lyu *et al.*, 2018) (e.g., see Figure 1.3), whereas it is unclear if the same goes for positive leaders. In fact, negative leaders can be “photographed” in X-ray – Figure 2.8 shows a $0.5\text{-}\mu\text{s}$ X-ray image of a negative leader coming to ground, showing that the negative leader tip is co-located with 36 MeV X-rays.

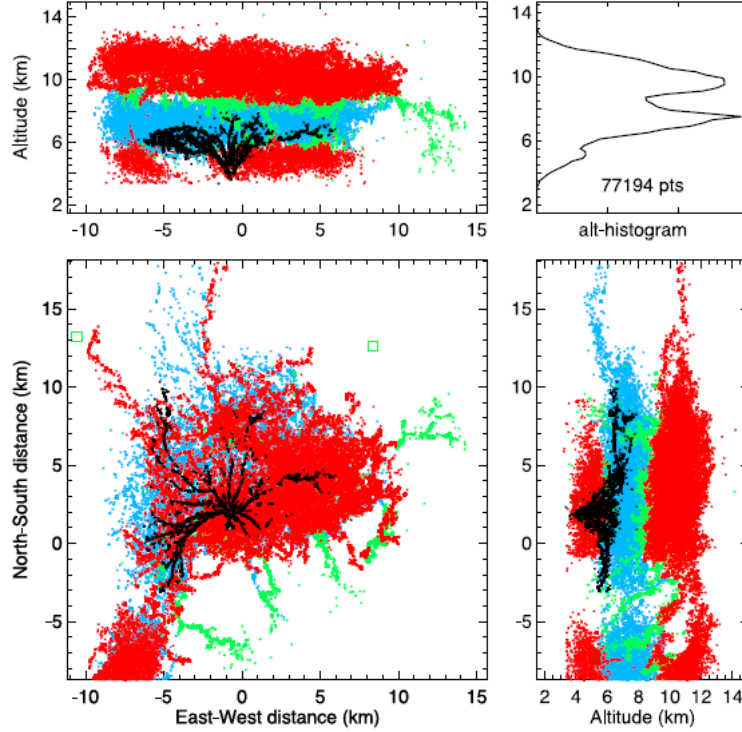


Figure 2.9: Rocket-triggered lightning three-dimensional VHF mapping observations. VHF sources from individual lightning activity is color-coded according to leader polarity, with red markers corresponding to negative leaders that propagate through inferred positive charge, and blue markers corresponding to positive leaders that propagate through inferred negative charge. The triggered lightning flash is colored black, and propagates horizontally through negative storm charge. Adapted from Edens *et al.* (2012).

Lightning tends to initiate in between thundercloud charge layers in regions of strongest electric field (Section 2.1). Therefore, the initial lightning leader tends to be largely vertically oriented, as in Figure 2.7. However, a charge region is typically more extensive in the horizontal than the vertical direction, so that eventually the leaders tend to branch and turn in the horizontal direction to travel through the more extensive charge (Shao & Krehbiel, 1996; Rison *et al.*, 1999; Rioussset *et al.*, 2007). This is illustrated in Figure 2.9, which shows the three-dimensional VHF sources of a rocket-triggered lightning flash in black, with leader development becoming increasingly horizontal to propagate through the mid-level negative storm charge. Charge regions are determined based on the leader development over a 15-minute period, where red markers indicate VHF sources

of negative leaders propagating through positive storm charge, and blue markers indicate VHF sources of positive leaders propagating through negative storm charge.

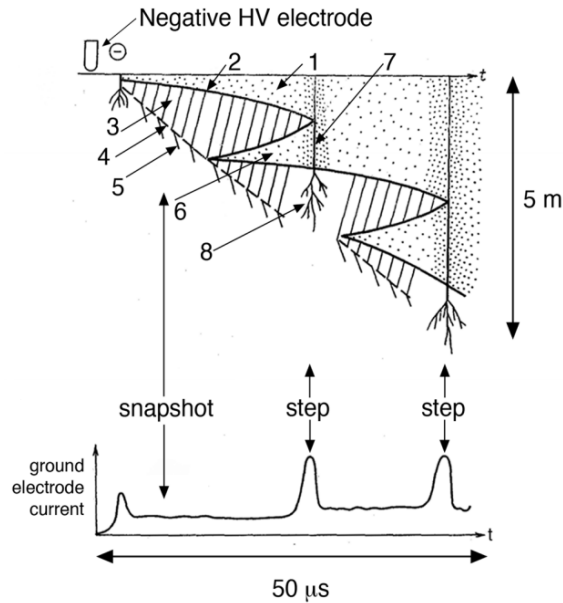


Figure 2.10: Schematic of the negative stepped leader process. The schematic depicts a one-dimensional vertically-oriented leader propagating downward, originating from a negative high-voltage electrode, and continuous “snapshots” of the leader stepping process are shown for a $50\ \mu\text{s}$ time period, progressing in time, left to right. Starting with a negative corona burst from the negative electrode, the main leader channel (1) is formed, and from the negative leader tip (2) a negative streamer zone (3) exists. Both the negative leader and its streamer zone propagate downward smoothly for some time. Meanwhile, the initial negative corona burst had established patches of enhanced ionization, also known as space stems (4), from which positive streamers can be established and propagate upward to meet the downward negative streamers (3) from the main leader channel; also downward-propagating negative streamers (5) emanate from the space stem. At some point, the space stem becomes thermalized, and becomes a space leader (6) that develops bidirectionally. When the main leader channel and space leader electrically connect (7) a new negative corona burst (8) emanates from the newly-established main leader tip, and the step process repeats. A typical time-synchronous electric field measurement is shown at the bottom of the figure, showing the characteristic “step” pulses that give the leader its name. Adapted from Gorin *et al.* (1976); Biagi *et al.* (2010, 2014).

Leaders can also be studied in the lab to better understand many of the same processes that take place in thunderstorms. For instance, negative leaders in the lab propagate forward in a step-wise manner, as depicted in Figure 2.10. The basic idea is that negative streamers require a higher field to propagate than do positive streamers, so that the high field ahead of the negative leader not

only facilitates negative streamers (in the streamer zone), but also positive streamers that propagate backward toward the main negative leader channel. The positive streamers initiate on “privileged” patches of air (the space stem) that are more highly ionized than their surroundings, and eventually the patches can become thermalized via Joule heating due to streamer activity. Once thermalized, these small patches are termed space leaders, and they can propagate bidirectionally, eventually electrically connecting with the main leader channel. When the connection occurs, the main negative leader channel is suddenly elongated, with its tip potential transferred to the newly-established tip via a surge of current. This surge of current generates step-like pulses in the electromagnetic field waveform that can be measured remotely, as shown in Figure 2.11.

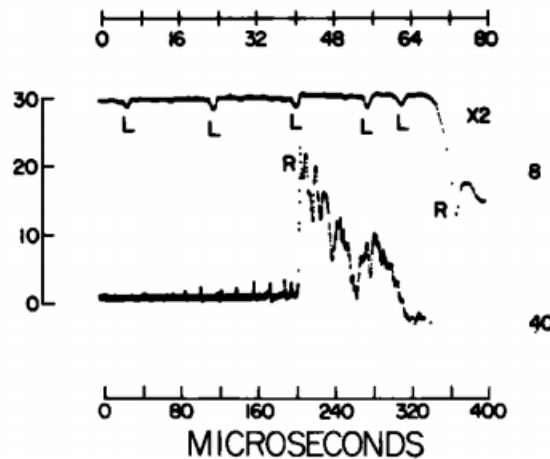


Figure 2.11: Broadband radio frequency emissions (sferics) of a stepped leader and return stroke in cloud-to-ground lightning. The bottom trace shows the electric field change record of a stepped leader coming to ground followed by the return stroke field (‘R’). The bottom timescale shows $40 \mu\text{s}$ per division. The top trace shows just the first $80 \mu\text{s}$ of the same record, but with the magnitude multiplied by -2, showing the individual stepped leader pulses (‘L’), which are $\sim 1 \mu\text{s}$ wide and mostly unipolar. The top timescale shows $8 \mu\text{s}$ per division. The measurements were made using a high-pass electric field change sensor, having a decay time constant of about 2 ms (i.e., sensing down to 500 Hz). Adapted from Krider *et al.* (1977).

Figure 2.12 shows photographs of the evident stepping process in negative lab leaders and in natural lightning. In the lab case, bidirectional streamer activity can be seen emanating away from the space stem location, which proceeds downward over the course of $\simeq 10 \mu\text{s}$, facilitated by downward-propagating negative streamers (Reess *et al.*, 1995). In the lightning leader case, space

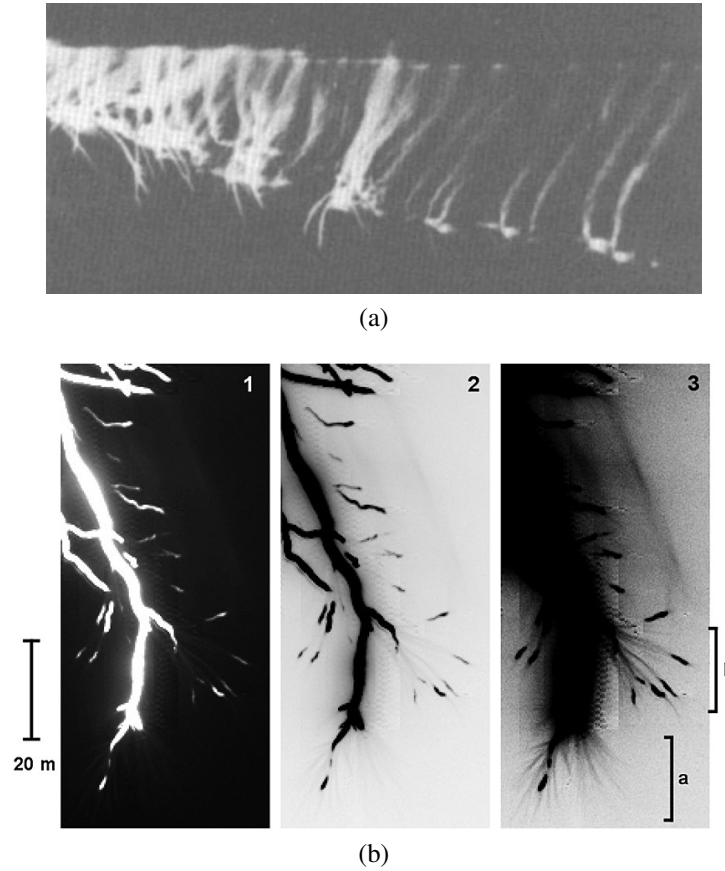


Figure 2.12: High-speed optical observations of leader stepping in lab and thunderstorm leaders. (a) Steak photograph of the propagating space stem in a meter-long gap. The location of the space stem (ionized patch) can be identified as the location from which bidirectional streamer development (upward positive and downward negative streamers) occurs. The downward negative streamers facilitate creation of new space stem locations, which advance downward over time (left to right), and do not thermalize in the roughly $10 \mu\text{s}$ window. Adapted from Reess *et al.* (1995). (b) High-speed photograph of streamers and space leaders near lightning leader tip. (1) shows a $100\text{-}\mu\text{s}$ exposure image of a lightning leader tip, (2) shows an inverted image of (1), and (3) shows an enhanced image of (2). The black regions in (2) and (3) likely depict leaders, since leaders are compact, highly-conductive and hot, and thus optically bright. The main leader channel extends vertically through almost the entire image, whereas space leaders are formed in the high field region near the main leader but some distance away from the main leader, and are visible as short black segments (e.g., bracket b). Streamers can be seen in (3) as wispy gray filamentary structures emanating from the main leader (e.g., bracket a), bridging the gap between the main and space leaders, and are also visible emanating from the tips of some of the space leaders. Adapted from Petersen & Beasley (2013).

leaders (i.e., thermalized space stems) can be seen as patches that are of comparable luminosity to the main leader channel, from which wispy bidirectional streamer features emerge. Note that

if more than one space leader is present, the main leader has more than one way to step forward, and so a branch point can occur (Pu *et al.*, 2017). Branching during a leader step may increase the associated sferic pulse width and/or create a multi-peaked sferic, as demonstrated in Figure 2.13.

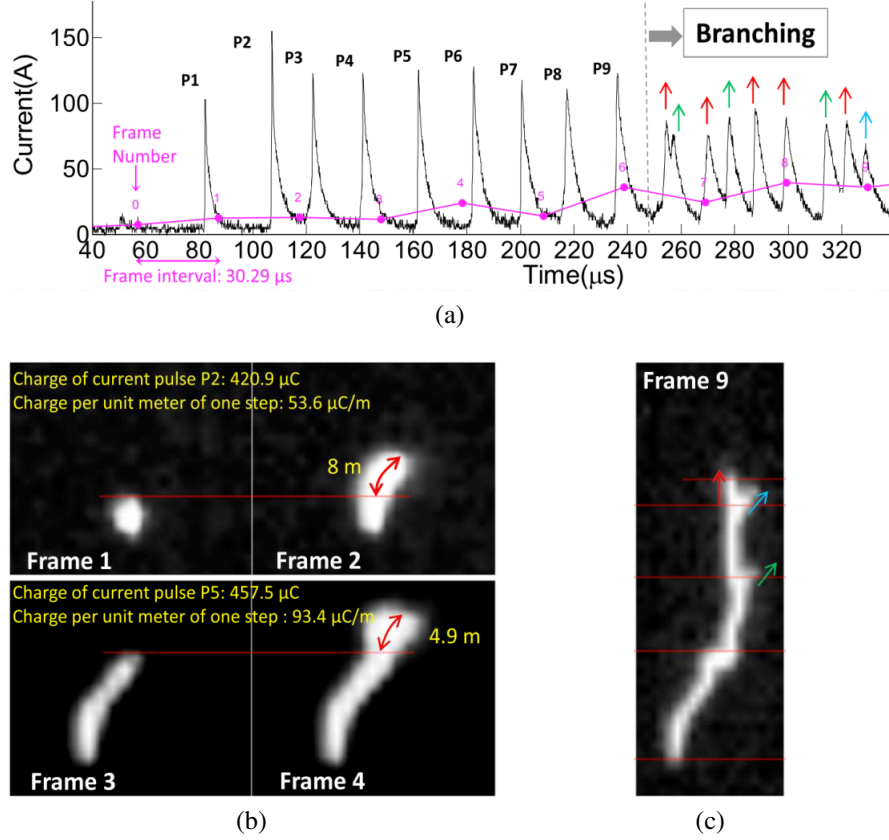


Figure 2.13: Leader branching in tower-triggered upward lightning. (a) Current waveform measured at an instrumented tower as an initial stepped leader propagates upward from the tower. (b) First four frames of high-speed video (30.29 μs per frame), showing single leader steps during each frame, and corresponding to the single step pulses in (a). (c) Example image of branching during a frame, which corresponds to multi-peaked wider waveforms in (a). Adapted from Pu *et al.* (2017).

In addition, stepping in negative lab leaders (Dwyer *et al.*, 2005b) and in natural lightning (Dwyer *et al.*, 2005a) is associated with X-ray emissions (Figure 2.8), which are due to electrons accelerated to relativistic speeds in the high leader and streamer fields (see Section 2.6).

2.3 Streamers

2.3.1 Streamers in the lab

Streamers (Bazelyan & Raizer, 1998; Liu & Pasko, 2004) are cold, filamentary plasma discharge waves that form and propagate in a sufficiently high electric field in air and other gasses, forming a partially conductive path. Photographs of streamers at various exposure times are shown in Figure 2.14, demonstrating the filamentary conducting paths in the longer 300-ns exposure image (far left panel), while the shorter 1-ns exposure image (far right panel) shows that the optical emissions coincide just with the ionization taking place at the streamer front, or streamer head. Though plasma consists of roughly equal parts free electrons and ions (Piel, 2010, p.38), the streamer process is largely facilitated by the motions of electrons, which are much less massive than ions (each proton in an ion is $\simeq 1836$ times as massive as a single free electron). Streamers have accumulations of like-charges at their extremities, with charge densities that can become very large (e.g., see Figure 1.2b). However, a streamer is conductive, as indicated by the high electron density inside a streamer, so the net charge on an isolated individual streamer would be zero.

Even before the notion of an electron was established, the electrical discharge was a known and documented phenomenon as early as 1676 (Picard, 1676), and was related to lightning in Benjamin Franklin's famed kite experiment in 1751 (Franklin, 1751). Not surprisingly, the study of electrical discharges is what led to the discovery of the electron by J. J. Thomson over a hundred years later in 1897 (Falconer, 1997). Shortly thereafter in 1900, J. S Townsend proposed his theory of what is now termed the Townsend discharge (Townsend, 1900), which describes how rarefied gas in a sufficiently high electric field becomes electrically conductive over short distances. The basic mechanism of Townsend's theory is the electron avalanche, whereby electrons, freed from atoms and molecules via impact ionization by free electrons, go on to free more electrons via impact ionization, and so on. The result is an exponential increase of free electrons in the direction of the electric field and over time, as illustrated in Figure 2.15 for a gas between two parallel plate electrodes.

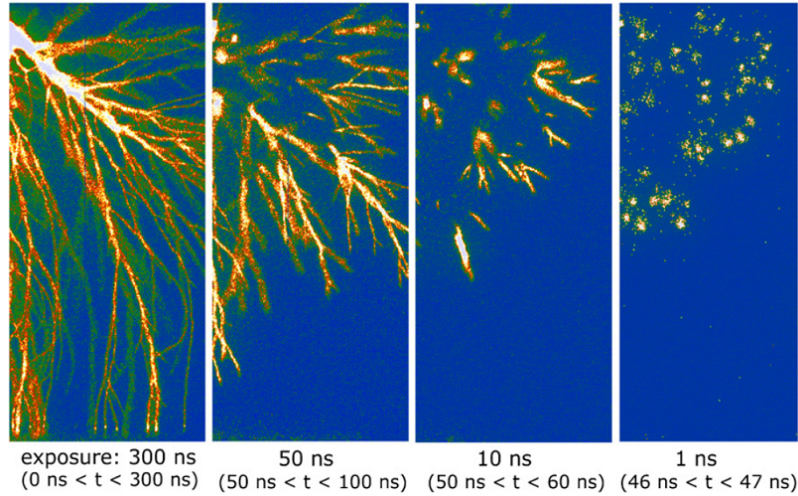


Figure 2.14: Intensified charge coupled device (ICCD) photographs of positive streamers at various exposure times. For the shortest exposure time (far right), optical emissions can only be seen emanating from the streamer heads, where ionization actively takes place. For the longest exposure time (far left), the paths traced by the streamer heads become visible, but the channels are not actually radiating. Adapted from Ebert *et al.* (2006).

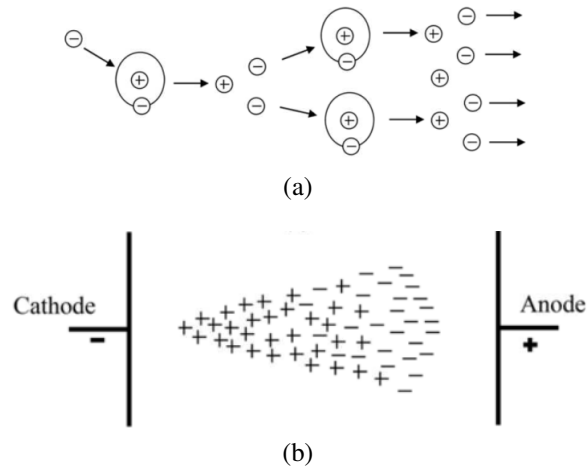


Figure 2.15: Electron avalanche schematic. (a) In the presence of an electric field, a free electron (-) impacts a neutral atom, ionizing the atom by liberating one electron (-) and leaving the atom with equal magnitude positive charge (+), so that two free electrons and a positive ion result. The two free electrons can then impact two more neutral atoms, liberating two more electrons, and so on, creating an electron avalanche. (b) Illustration of the separation of charges in an electron avalanche over time between parallel plate electrodes, with the electron avalanche progressing toward the positively-charged electrode, leaving positive ions in the wake, which progress more slowly toward the negatively-charged electrode. Adapted from Beroual & Fofana (2016).

In Townsend’s theory, “secondary” ionization occurs when positive ions, traveling more slowly and in the opposite direction of free electrons in the electric field, impact the negative electrode, releasing free electrons that can then avalanche toward the positive electrode. This secondary ionization mechanism can lead to a self-sustaining Townsend discharge (Raizer, 1991, pp. 72-73), or electrical breakdown. Based on Townsend’s second ionization mechanism, the theory predicted that conditions for spark generation should be strongly dependent upon the electrode properties. However, by 1940 (Loeb & and, 1940), experiment clearly showed that the voltage required for spark generation wasn’t always dependent on electrode material.

Townsend’s theory only accurately describes discharges in short (\sim cm-wide) gaps and in relatively low gas pressures (i.e., in partially evacuated air), or for $Pd < 200$ Torr·cm (Raizer, 1991, p. 325), where d is the gap length and P is the gas pressure. Thus, Townsend’s theory does not apply to streamers (Loeb & and, 1940; Beroual & Fofana, 2016), and cannot describe kilometer-length lightning discharges. Photoionization and space charge accumulation become increasingly important in air at STP, and in thunderstorms. For instance, space charge accounts for the filamentary structure of streamers (Figures 1.2, 2.14), and photoionization accounts for the swift development of the breakdown, which cannot be accounted for by the slow speeds of ion drift (Loeb & and, 1940).

Looking back at Figure 2.15b, an electron avalanche creates regions of space charge in the gap, with avalanching electrons progressing toward a positively-charged electrode, leaving positive ions in their wake. If the electric field produced by the space charge remains small compared to the applied field in the gap, then the discharge proceeds just as an electron avalanche. However, if the space charge field becomes comparable to the applied field, then the discharge becomes very different from a single electron avalanche (Raizer, 1991, p. 334). Figure 2.16a shows a schematic of a negative streamer propagating in a gap. Electrons avalanche in the gap, and if space charge accumulates such that the resulting field is of the same order as the background field, E_0 , then electrons collectively avalanche away from the high field region, facilitated also by photoionization ($h\nu$). This forms an ionization wave, in front of which electrons avalanche in

the strong space charge field, forming the negative streamer head, and behind the field is weaker, and ions and electrons form a quasi-neutral plasma (the streamer tail). The negative streamer head propagates in the opposite direction of the ambient field, effectively moving negative charge in the direction of propagation.

Besides propagating the ionized path forward faster than what particle drift and electron impact ionization allow, photoionization allows for streamers of both polarities to occur. Figure 2.16b shows a schematic of a positive streamer initiating at a positively-charged planar electrode (anode). Electrons avalanche in the gap, and if space charge accumulates such that the space charge field is of the same order as the background field, E_0 , then electrons collectively avalanche into the positive-charge region. Photoionization facilitates the production of free electrons out in front of the space charge region so that avalanches can occur. Again, this forms an ionization wave, in front of which the field is strong and avalanching electrons leave behind a strong positive charge in their wake, forming the positive streamer head, and behind the field is weaker, and again ions and electrons form a quasineutral plasma (the streamer tail) there. The positive streamer head

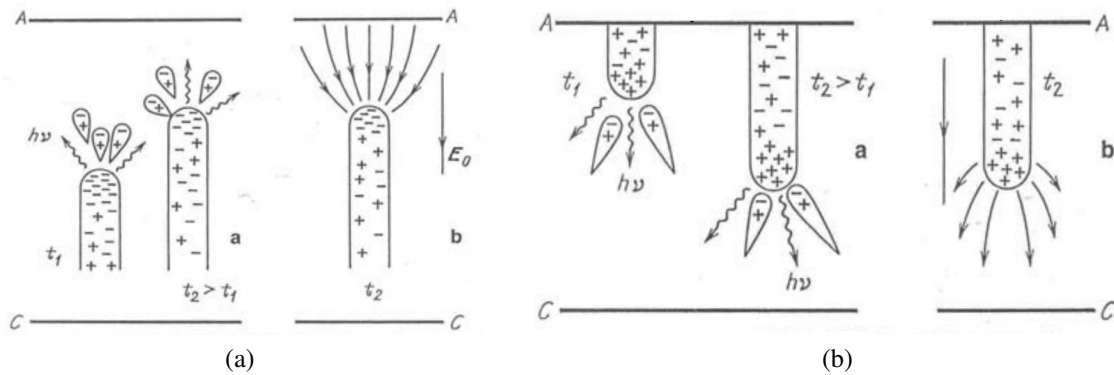


Figure 2.16: Schematic showing development of streamers. Streamers propagate via impact ionization and photoionization (with photons of energy $h\nu$) across a gap, shown for two instances of time (left to right) for (a) a negative streamer, directed toward the positively-charged anode ('A'), and (b) a positive streamer, directed toward the negatively-charged cathode ('C'). In (a) and (b), the right-most figure shows the space charge field near the streamer head, which is higher than the field in the gap, E_0 . Adapted from (Raizer, 1991, pp. 335,338)

propagates in the same direction as the ambient field, effectively moving positive charge in the direction of propagation.

The strong streamer head fields are also capable of accelerating electrons to relativistic speeds, which can emit X-rays via bremsstrahlung (see Section 2.6). Interestingly, lab studies (Kochkin *et al.*, 2012a,b) show that the existence of negative streamers are a necessary condition for X-ray generation, whereas positive streamers alone do not appear to emit X-rays. Rather, it appears that interactions between negative and positive streamers facilitate X-ray generation, though it is not well understood at present.

Streamers can initiate when the ambient field is over the breakdown threshold field, often denoted E_k , which is defined by equating the ionization and dissociative attachment frequencies (Raizer, 1991, pp. 135-136), and is approximately $E_k=3\times 10^6$ V/m in air at STP (standard temperature and pressure, or at 0°C and 100 kPa). Above E_k , electron avalanches can occur, which can lead to streamer development. However, differences in negative and positive streamer head formation creates an asymmetry between the two polarities (Williams, 2006) that is quantitatively manifest by the so-called critical field, which is the electric field required to sustain streamer propagation. The critical field is about half the magnitude for positive streamers (4.4×10^5 V/m at sea level) as it is for negative streamers ($10\text{-}15\times 10^5$ V/m at sea level) (Qin & Pasko, 2014), and both are lower in magnitude than the threshold field, E_k .

2.3.2 Streamers in thunderstorms

Streamers are an integral part of lightning, heating the air in the initial formation of a hot, highly-conductive lightning leader, and streamers are also involved in the subsequent propagation of a leader once formed. Streamers can initiate in thunderclouds so long as the electric field exceeds the breakdown threshold, so that streamers can occur in isolation without necessarily heating the air sufficiently to initiate lightning. At thunderstorm altitudes, the air pressure, P , is substantially lower than at sea level (as is the temperature, T ; see, e.g., the balloon-borne temperature sounding in Figure 2.6), but we have defined E_k at sea level. Fortunately, many streamer parameters scale

in some manner with the neutral gas density, N (where $N = \frac{P}{k_B T}$ from the ideal gas law, where $k_B \approx 1.38 \times 10^{-23} \text{ m}^2 \cdot \text{kg} \cdot \text{s}^{-2} \cdot \text{K}^{-1}$ is the Boltzmann constant). This makes streamer lab experiments at sea level (with neutral gas density, N_0) directly translatable to thunderstorm conditions. This scaling is collectively referred to as the similarity laws (Pasko *et al.*, 1998), and some important relations used later in this dissertation are as follows:

$$L = L_0 \frac{N_0}{N} \quad (2.1)$$

$$\tau = \tau_0 \frac{N_0}{N} \quad (2.2)$$

$$E = E_0 \frac{N}{N_0} \quad (2.3)$$

where L is any length scale (e.g., streamer radius or length) at the the desired pressure (e.g., at thunderstorm altitudes), L_0 is the reference length scale (e.g., as measured at sea level), τ is any time scale at the desired pressure (e.g., the ionization timescale), τ_0 is the reference time scale, E is the electric field at the desired pressure (e.g., the electric field required for streamer initiation), and E_0 is the reference electric field (e.g., E_k as measured at sea level). As can be seen from equations 2.1 and 2.2, length and time scale in the same way, so that streamer speeds are not affected by altitude. From equation 2.3, we can see that the equivalent breakdown threshold at thunderstorm altitudes will be lower than at ground pressure.

Given the similarity laws, the critical field for positive streamers is still about half that for negative streamers at thunderstorm altitudes, and so it has long been proposed that positive streamers initiate lightning (Loeb, 1966; Dawson & Winn, 1965; Griffiths & Phelps, 1976), conditioning (i.e., heating) the air to eventually form a lightning leader (Petersen *et al.*, 2008; da Silva & Pasko, 2013). That is, recurrent (originally cold) streamer activity through a common region will eventually heat the air sufficiently through Joule heating to create the hot, thermally-ionized arc, or leader, generally associated with lightning. This process is illustrated in Figure 2.17, whereby

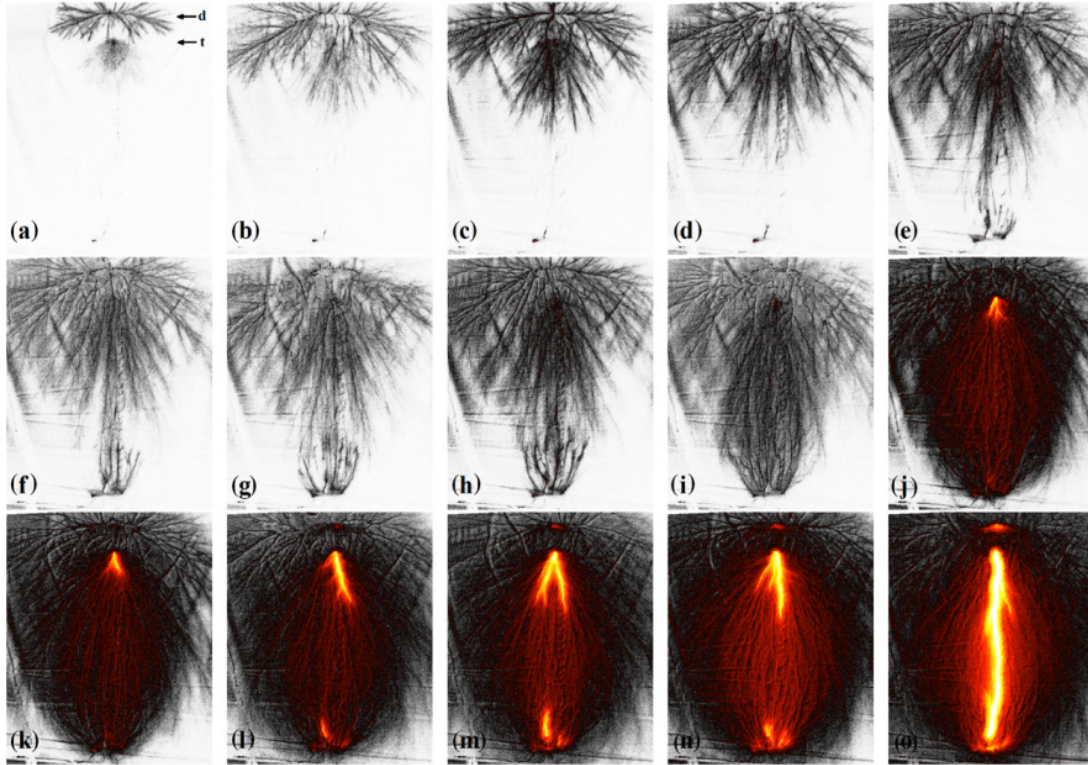


Figure 2.17: Streamer to leader transition. Positive streamers (black traces) initiating from a needle electrode (top of each panel) propagate downward through a 1-meter gap in successive images (a)-(o) over the course of $1 \mu s$. As the positive streamers get closer to the grounded electrode (bottom of each panel) in (d) and (e), the electric field near the grounded electrode becomes enhanced and allows for upward propagation of negative streamers. By panel (j), the air near the positive streamer initiation point becomes substantially thermalized (indicated in orange) by the recurrent streamer activity, forming a propagating hot leader, and by (o) the thermalized channel bridges the gap and short-circuits the gap. Adapted from Kochkin *et al.* (2012a).

positive streamers initiating from an electrode bridge a spark gap and eventually heat the air sufficiently, leading to thermal ionization (Raizer, 1991, p. 276).

However, in contrast to the lab case, the electrodes from which streamers initiate in a thundercloud are not obvious. Moreover, in-situ thundercloud measurements (e.g., the balloon sounding in Figure 2.6) suggest that thunderstorm electric fields are generally an order of magnitude below the conventional breakdown threshold field, E_k (Winn *et al.*, 1974; Marshall & Rust, 1991; Marshall *et al.*, 1995b; Stolzenburg *et al.*, 2007). Since lightning does indeed occur, streamers must originate in localized regions of relatively strong electric field (Winn *et al.*, 1974), which largely

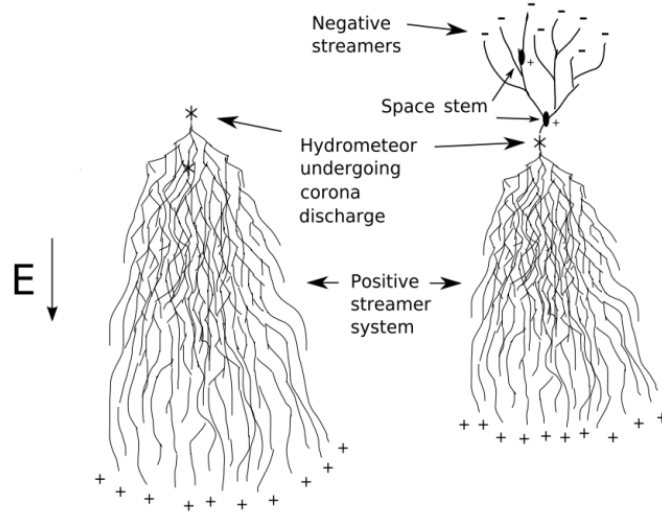


Figure 2.18: Illustration of streamers initiating from an ice crystal in a sub-breakdown electric field. Left: the electric field is enhanced locally near an ice crystal, which initiates positive streamers that propagate in the direction of the ambient electric field. Right: after some time, after a substantial negative space charge is deposited back at the positive streamer initiation point, negative streamers can propagate in the opposite direction of the ambient electric field. Adapted from Petersen *et al.* (2008).

go undetected by instrumented balloons, with the positive streamers initiated by ice hydrometeors (e.g., at the pointy extremities of ice crystals) at ambient field strengths well below E_k . Figure 2.18 depicts a system of positive streamers initiating from an ice crystal placed in a sub-breakdown ambient electric field. After some time, after substantial negative space charge is deposited back at the positive streamer initiating point, negative streamers can propagate in the opposite direction of the ambient electric field, so that streamer development becomes bi-directional.

Laboratory (Petersen *et al.*, 2006, 2015) and modeling (Liu *et al.*, 2012; Sadighi *et al.*, 2015; Shi *et al.*, 2016) work have indeed found that positive streamers, which propagate in the direction of the electric field and carry electric currents in the propagation direction, can be initiated from isolated ice hydrometeors placed in an electric field well below the threshold for air electrical breakdown. Moreover, it was found that negative streamers, which propagate in the opposite direction, are absent during streamer initiation from the hydrometeors, and likely initiate some time later, as illustrated in Figure 2.18.

Once a lightning leader is formed, the strong electric fields at the leader tip continue to facilitate streamer production. This “streamer zone” (see Figure 1.2) heats the air ahead of the leader and helps maintain leader propagation (Petersen *et al.*, 2008). Therefore, streamers are an integral part of both lightning initiation and propagation.

2.4 Narrow bipolar events (NBEs)

Compact intra-cloud discharges called narrow bipolar events (NBEs) (Le Vine, 1980; Willett *et al.*, 1989; Smith *et al.*, 1999) almost always occur either in isolation or at the beginning of a lightning flash (Willett *et al.*, 1989; Smith *et al.*, 1999; Rison *et al.*, 1999; Nag *et al.*, 2010; Karunarathne *et al.*, 2015; Rison *et al.*, 2016), strongly suggesting that they are the initiating breakdown events of thunderstorm electrical discharges. This makes NBEs of particular interest in studying lightning initiation. NBEs are so-named due to their “narrow” ($\sim 10 \mu\text{s}$) bipolar spheric, examples of which are shown in Figure 2.19, and are also characterized by their extremely bright VHF emissions, as illustrated in Figure 2.20 by comparing the VHF emissions of NBEs with lightning return strokes. In fact, NBEs are the most powerful natural emitter of very high frequency (VHF) radio waves on Earth (Willett *et al.*, 1989), rivaling the emissions of lightning return strokes. This allows high-power NBEs to be easily detected by space-borne detectors, where they were originally identified as transionospheric pulse pairs or TIPP events (Holden *et al.*, 1995) because the satellites received the first spheric pulse by line-of-sight, and a second pulse later due to ground-ionosphere reflection delays (Smith *et al.*, 2004). Moreover, NBEs are associated with strong convection (Wu *et al.*, 2011, 2012; Karunarathna *et al.*, 2015), and could potentially serve as a proxy for storm convective strength that would be useful for space-borne global monitoring and climatology (Suszcynsky & Heavner, 2003; Jacobson & Heavner, 2005; Wiens *et al.*, 2008).

Despite their strong VHF emissions, NBEs are not well mapped by time-of-arrival VHF sensors (Chapter 7) due to NBEs emitting continuously throughout a processing window, as opposed to impulsively (Rison *et al.*, 2016). Still, as early as the first mention of NBEs in the literature in

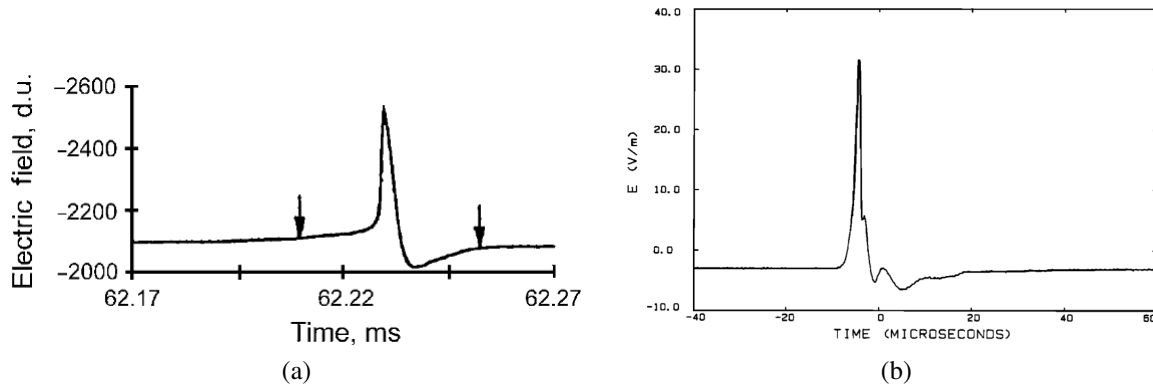


Figure 2.19: Narrow bipolar event (NBE) sferics. (a) Simple bipolar NBE sferic. Adapted from Villanueva *et al.* (1994). (b) More complex bipolar sferic with perturbations. Adapted from Willett *et al.* (1989).

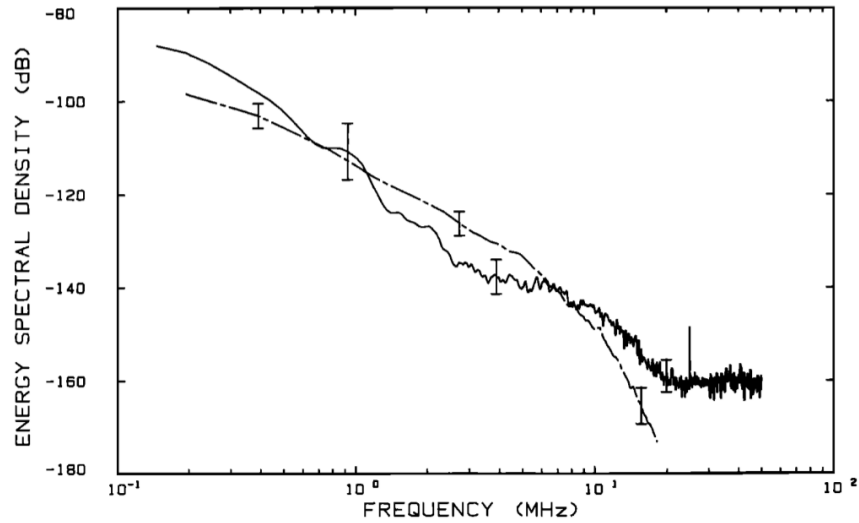


Figure 2.20: Narrow bipolar event (NBE) energy spectral density, compared to that of lightning return strokes. At frequencies above about 1 MHz, NBE emissions surpass that of return strokes. Adapted from Willett *et al.* (1989).

1980 (Le Vine, 1980), it was conceived that the bipolar NBE sferic could be reasonably reproduced by simulating a current pulse traveling vertically (at $\sim 10^8$ m/s) along a linear vertically-oriented conductor in the cloud, as illustrated in Figure 2.21 for a negative (downward-directed) current pulse. The vertical orientation of NBE discharges continues to be validated by different studies (da Silva & Pasko, 2015; Karunarathne *et al.*, 2016; Rison *et al.*, 2016).

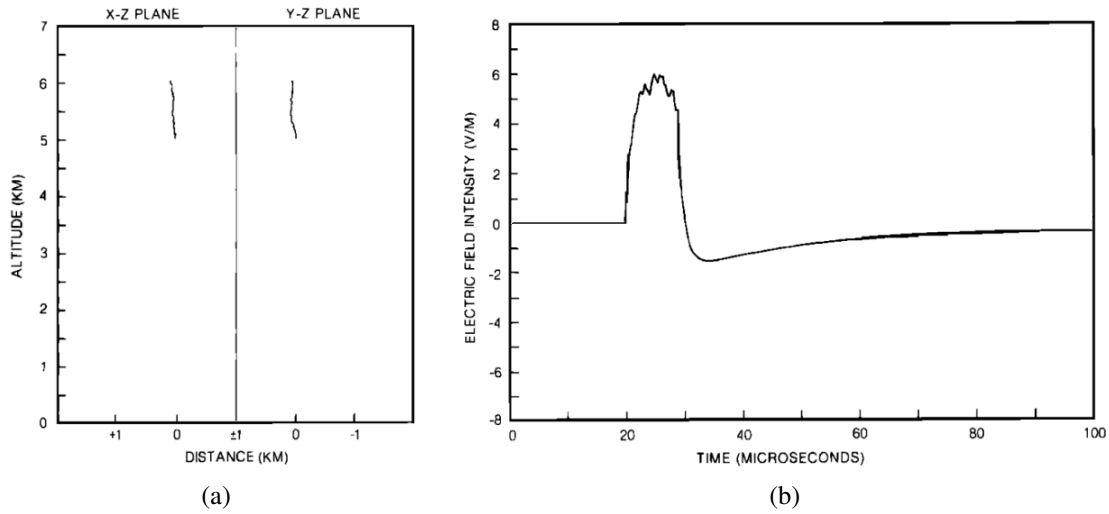


Figure 2.21: Simulation of NBE sferic. (a) Assumed NBE channel geometry. (b) Sferic due to a simulated negative (downward-directed) current pulse propagating at 10^8 m/s along the channel. Adapted from Le Vine (1980).

NBEs are typically about 0.5-1 km in vertical extent, have charge moment changes of about 0.1-1 C-km (Smith *et al.*, 1999; Karunarathne *et al.*, 2016; Rison *et al.*, 2016), and peak currents of 10-100 kA (Eack, 2004; Nag & Rakov, 2010; Karunarathne *et al.*, 2015, 2016; Rison *et al.*, 2016). Moreover, Rison *et al.* (2016) discovered that NBEs are generated by a newly-recognized process, termed fast positive breakdown, which carries electric current in its propagation direction, propagating downward in the same direction as the (mostly vertical) thundercloud electric field at an unusually fast speed of $\sim 10^7$ m/s. Figure 2.22 demonstrates the breakdown activity during a NBE. The NBE bipolar sferic is shown in red, with the positive initial pulse indicative of a negative current, i.e., positive charge moving downward, or negative charge moving upward (see Section 6.2). The VHF source locations, determined by using a broadband radio interferometer, propagate downward with a speed of 3.5×10^7 m/s during the positive sferic pulse, indicating a positive breakdown polarity. The strong VHF emissions (blue) can be seen to quickly saturate the VHF sensor. Rison *et al.* (2016) concluded that many or possibly all lightning flashes are initiated by fast positive breakdown, given the relationship between NBEs and lightning initiation. Moreover, the observation agrees with the notion that lightning is initiated by positive streamers

(Section 2.3.2). However, fast positive breakdown has a much larger current magnitude (~ 50 kA), spatial extent (~ 500 m) and temporal scale (~ 10 μ s) than for a single streamer (~ 1 A, ~ 1 m, and ~ 0.1 μ s, respectively, assuming an altitude of 9 km, or pressure of about 30 kPa (Liu & Pasko, 2004; Liu *et al.*, 2012; Sadighi *et al.*, 2015; Shi *et al.*, 2016), and using the similarity laws presented in Section 2.3.1). Therefore, a natural explanation for fast positive breakdown is that it is composed of a system of positive streamers or a discharge wave driven by positive streamers (Rison *et al.*, 2016).

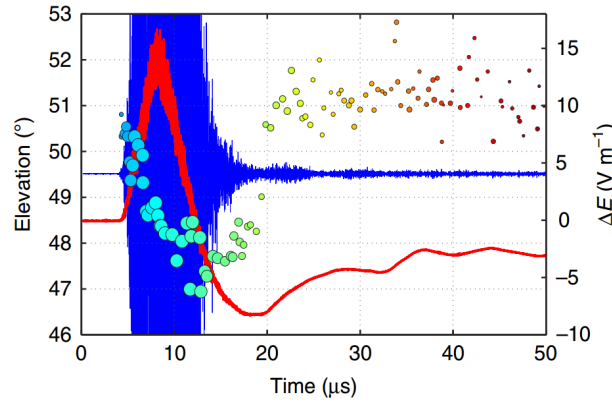


Figure 2.22: Fast positive breakdown generates narrow bipolar pulse. The positive initial pulse of the NBE sferic (red waveform) indicates a negative current (i.e., positive charge moving downward, or negative charge moving upward). However, given the coincident downward propagation of the detected VHF sources (circular markers), a downward-propagating positive-polarity breakdown appears to generate the sferic, and with a fast $\sim 10^7$ m/s propagation speed. The raw VHF signal (blue waveform) associated with the fast positive breakdown quickly saturates the sensor. Adapted from Rison *et al.* (2016).

The NBEs studied by Rison *et al.* (2016) are termed positive NBEs due to the initial positive peak of the bipolar sferic, indicating a negative current (physics sign convention is used, i.e., an upward current is positive while a downward current is negative). The term positive NBE does not indicate the breakdown polarity of the NBE, but rather indicates the location of the NBE within a thundercloud charge structure. That is, in order for a positive NBE to occur, it must initiate in between lower-altitude negative charge and higher-altitude positive charge (breakdown between these two regions should always give a negative-going current, i.e., positive charge moving downward or negative charge moving upward). In a normal-polarity storm (Krehbiel, 1986) (Section 2.1), which

has a strong mid-level negative charge region sandwiched between two weaker positive charge regions, positive NBEs occur in between the mid-level negative charge and the upper-positive charge (Wu *et al.*, 2012). Figure 2.23a shows a NBE location (red circle) with respect to the ensuing bi-directional leader development of an intra-cloud (IC) lightning flash. The NBE initiates the flash, and Figure 2.23b shows the parent storm charge structure, as determined by lightning VHF source activity during a ten-minute period (blue sources indicate positive leaders propagating through negative storm charge, and red sources indicate negative leaders propagating through positive charge). Positive NBEs that initiate lightning in normal-polarity storms initiate “normal-polarity” IC lightning (Williams, 1989), with negative leaders propagating upward into positive charge, and positive leaders propagating downward into negative charge. Not coincidentally, because intra-cloud lightning is more than twice as common as cloud-to-ground lightning (Boccippio *et al.*, 2000), most NBEs are of the positive type (Wu *et al.*, 2012).

However, negative NBEs can occur as well (Willett *et al.*, 1989; Smith *et al.*, 2004; Wu *et al.*, 2011, 2012), and are characterized by an initial negative peak in the bipolar sferic, indicating a positive current. A negative NBE must initiate in between lower-altitude positive charge and higher-altitude negative charge (breakdown between these two regions should always give a positive-going current, i.e., positive charge moving upward or negative charge moving downward). In a normal-polarity storm, negative NBEs typically occur in between the upper-positive charge and an upper-negative screening charge layer (Smith *et al.*, 2004; Wu *et al.*, 2011, 2012), as depicted in the diagram in Figure 2.23c, and so are thought to be indicative of particularly intense convection that produces particularly tall thunderstorms. However, negative NBEs can also occur between the lower positive and mid-level negative charge regions in a normal polarity storm, and can initiate cloud-to-ground lightning.

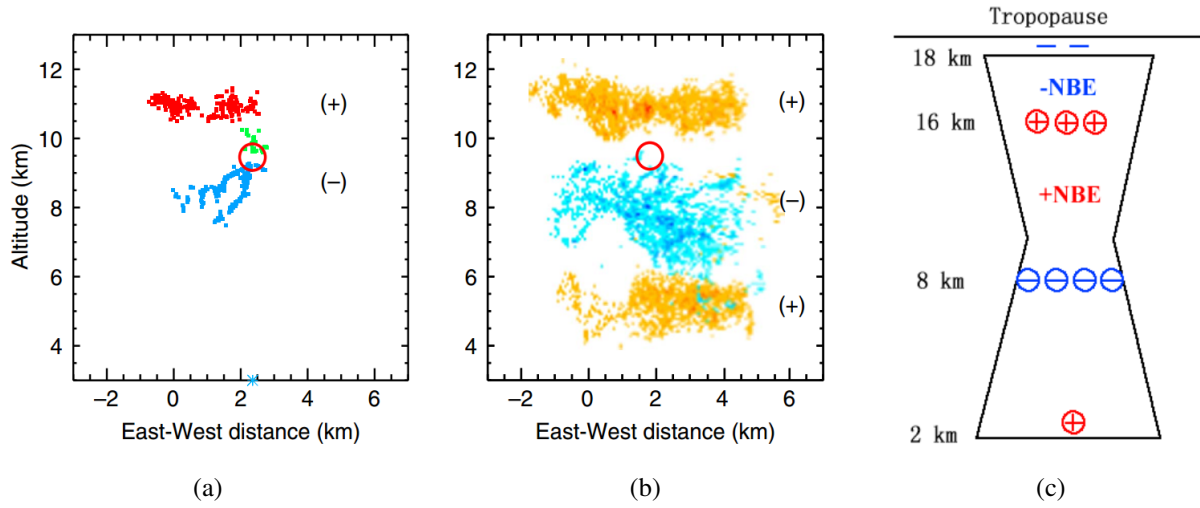


Figure 2.23: Positive and negative NBE locations with respect to parent flash and storm charge. (a) The red circle indicates the VHF (60-66 MHz) source location of the positive NBE in Figure 2.22, which initiates an intra-cloud lightning flash. The upward-propagating VHF sources of the ensuing flash represent negative leaders propagating upward into positive charge (indicated by red markers), and the downward-propagating VHF sources represent positive leaders propagating downward into negative charge (indicated by blue markers). (b) The NBE location is superimposed on the overall thundercloud charge structure, determined by lightning VHF source activity, showing that the storm is of normal polarity (Krehbiel, 1986) and that the NBE is a positive NBE, i.e., generated by negative current. Adapted from Rison *et al.* (2016). (c) Schematic of positive and negative NBE locations with respect to storm charge structure. Adapted from Wu *et al.* (2012).

2.5 Initial breakdown pulses (IBPs)

The first few milliseconds of a lightning flash typically coincide with a “pulse train” consisting of large-amplitude, bipolar $\sim 10 \mu\text{s}$ wide sferics, often superimposed by narrower $\sim 1\text{-}\mu\text{s}$ “subpulses” on the leading edge of the initial pulse (Weidman & Krider, 1979; Krider *et al.*, 1979; Beasley *et al.*, 1982; Nag *et al.*, 2009; Karunarathne *et al.*, 2013; Wu *et al.*, 2013; Stolzenburg *et al.*, 2013). These characteristic pulses will be referred to herein as classic initial breakdown pulses, or classic IBPs, and a typical classic IBP sferic is shown in Figure 2.24 (top trace). Figure 2.24 also demonstrates that classic IBPs occur in pulse trains lasting on the order of a millisecond (middle trace), and, for cloud-to-ground lightning, classic IBPs precede the return stroke (bottom trace), as well as formation of the stepped leader to ground. Unlike NBEs (Section 2.4), which can occur

in total isolation without initiating a lightning flash, classic IBPs seem to signal that a lightning flash (i.e., a bidirectional leader) will ensue. That is, classic IBPs occur after a flash initiates (i.e., after a NBE or other indicator (Marshall *et al.*, 2014; Lyu *et al.*, 2019; Marshall *et al.*, 2019)), but before the signature stepped leader sferics (Section 2.2). There is some consensus that classic IBPs are associated with the initial stepped leader formation (Beasley *et al.*, 1982; Rhodes & Krehbiel, 1989; Villanueva *et al.*, 1994; Marshall *et al.*, 2013; Stolzenburg *et al.*, 2013; Karunarathne *et al.*, 2013; Stolzenburg *et al.*, 2014; Karunarathne *et al.*, 2014; Kolmasova *et al.*, 2018), and that they are distinct from leader stepping, given the different pulse widths ($\sim 10 \mu\text{s}$ for classic IBPs, $\sim 1 \mu\text{s}$ for leader steps), inter-pulse time intervals (0.5-7 ms for classic IBPs, 15-50 μs for leader steps (Marshall *et al.*, 2013)), pulse shapes (bipolar for classic IBPs, unipolar for leader steps), and the different step distances (50-600 m for classic IBPs, 5-50 m for leader steps (Marshall *et al.*, 2013)) determined from optical data. Classic IBPs in cloud-to-ground lightning have typical charge moment changes of about 0.015-0.3 C-km (Karunarathne *et al.*, 2014; da Silva & Pasko, 2015; Karunarathne *et al.*, 2020), and current moments of $\sim 10 \text{ kA-km}$ (da Silva & Pasko, 2015).

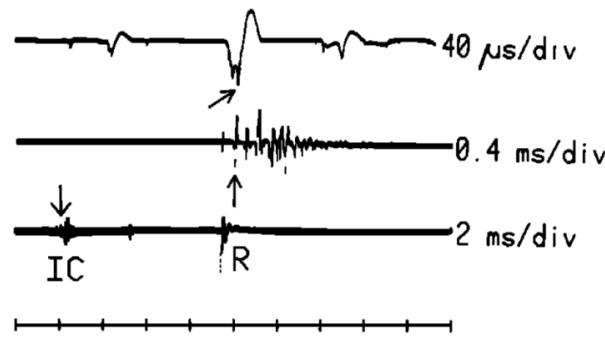


Figure 2.24: Classic initial breakdown pulse (IBP) sferics in cloud-to-ground lightning. Top: at 40 μs per division (scale at bottom of figure), a single classic IBP sferic (indicated by the arrow) is shown, having a relatively large amplitude and being largely bipolar, with a $\simeq 20 \mu\text{s}$ wide initial pulse that is superimposed by narrow ($\sim 1 \mu\text{s}$) pulses. Middle: at 0.4 ms per division, the IBP “pulse train” is visible, consisting of similarly-spaced classic IBPs. The same event is indicated by the arrow. Bottom: at 2 ms per division, the IBP pulse train is shown with respect to the return stroke, and also shows the same event indicated by the arrow. Adapted from Weidman & Krider (1979).

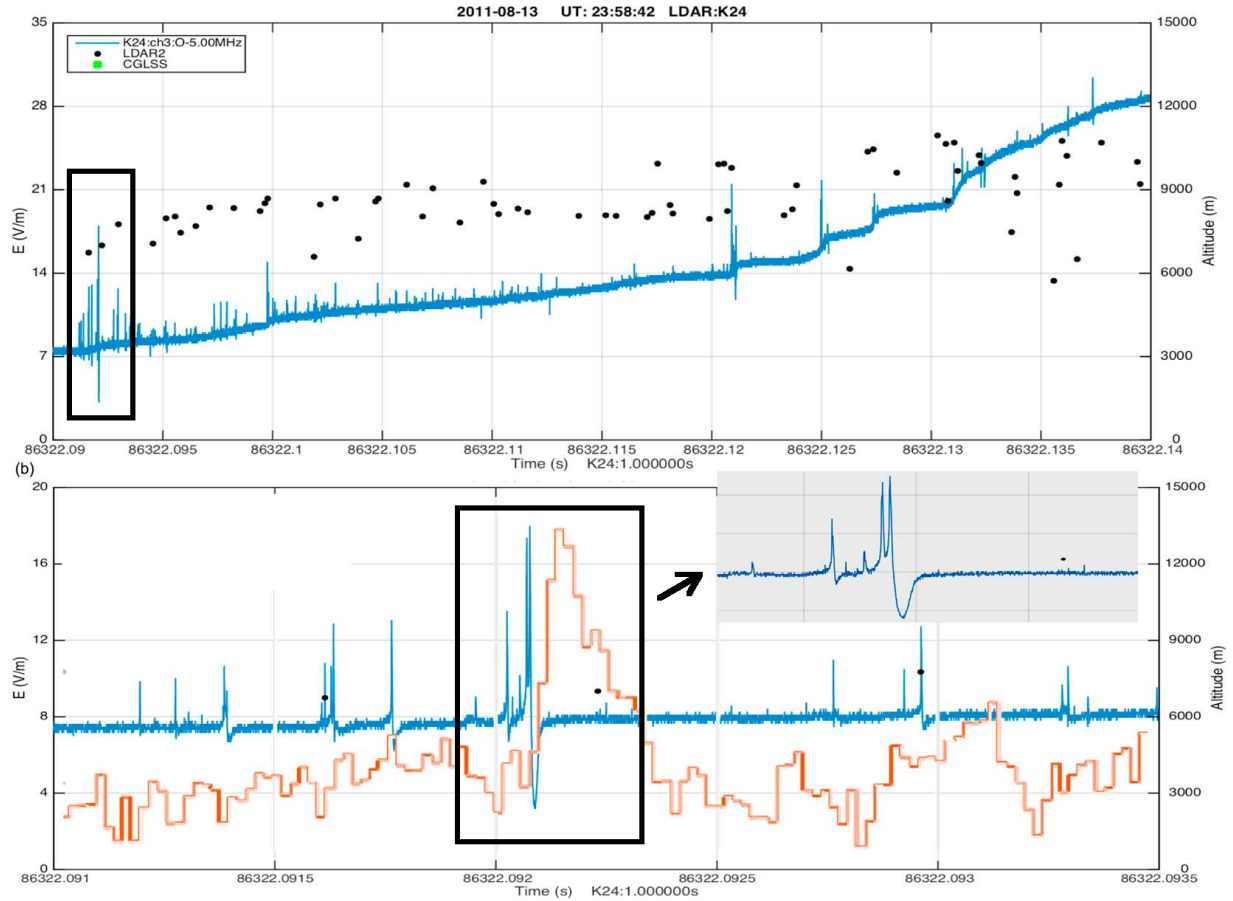


Figure 2.25: Initial breakdown pulse (IBP) sferic and luminosity observations in intra-cloud lightning. Top: intra-cloud lightning sferic (blue waveform), showing the IBP pulse train (black box). Bottom: The largest classic IBP coincides with a clear luminosity increase (orange curve). The inset shows an expanded view of the classic IBP sferic. Adapted from Stolzenburg *et al.* (2016).

As with NBEs, the processes generating classic IBPs generally occur deep within thunderclouds, even in cloud-to-ground lightning, since IBPs occur near the beginning of flashes, and flashes tend to initiate between cloud charge regions (Section 2.2). Classic IBP sferics are closely correlated in amplitude and time with VHF emissions (Krider *et al.*, 1979; Stock, 2014; Wu *et al.*, 2016; Kolmasova *et al.*, 2018; Stanley *et al.*, 2018b), but are not well mapped by time-of-arrival VHF sensors (Section 7) due to IBPs emitting continuously throughout a processing window, as opposed to impulsively (Kolmasova *et al.*, 2018), similar to NBEs. However, classic IBPs are associated with bright optical emissions (Stolzenburg *et al.*, 2013, 2014, 2016) that can be detected

through the cloud during the beginning of the initial breakdown stage when classic IBPs occur. The optical emission of IBPs is demonstrated in Figure 2.25, which shows a large luminosity increase (orange curve) coincident with the largest IBP in the pulse train (blue curve) . Moreover, later in the initial breakdown stage, luminous channel can sometimes be observed propagating downward out of the cloud base for a cloud-to-ground flash (Campos & Saba, 2013; Stolzenburg *et al.*, 2013, 2014). In fact, it was shown that classic IBPs, like leader steps, were associated with sudden lightning channel elongation of $\sim 10\text{-}100$ m. For example, Figure 2.26 shows several $20\text{-}\mu\text{s}$ frames of a high speed video during an IBP – the downward-propagating channel brightens and elongates at the channel tip during the initial IBP sferic pulse. Notably, during the initial breakdown stage in cloud-to-ground lightning, there was never a luminous channel propagating upward, i.e., the positive leader had not yet formed or else did not emit strongly enough in optical to be detected. In fact, positive leader activity often went undetected up until the time of the first return stroke, so that the visible top of the return stroke channel coincided with the first IBP locations.

Narrower $\sim 1\text{ }\mu\text{s}$ wide sferic pulses also occur during the initial breakdown stage (Nag *et al.*, 2009; Karunarathne *et al.*, 2013; Stolzenburg *et al.*, 2014), and are mostly bipolar, but can also be unipolar or have more complex waveforms. These pulses will be referred to as narrow IBPs herein, and typical narrow IBP sferics are shown in Figure 2.27. Like classic IBPs, narrow IBPs are also associated with increased luminosity and channel extension (Stolzenburg *et al.*, 2014), but are much dimmer than classic IBPs.

Because classic IBPs take place near the flash origin, i.e., in the vicinity of a strong, largely vertical electric field, there is speculation that IBPs may just be especially large, energetic, vertical leader steps, and that this is the reason for the large amplitude and wide pulse of classic IBPs (Wu *et al.*, 2013; Petersen & Beasley, 2014; da Silva & Pasko, 2015). However, the subpulses of classic IBPs have more in common with stepped leader pulses, having similar widths and rise times, and so there is also speculation that subpulses are instead an indication of leader stepping (Weidman & Krider, 1979; Marshall *et al.*, 2013). In addition, it is speculated that the large bipolar sferics of classic IBPs are generated by relativistic electrons (Marshall *et al.*, 2013; Stolzenburg *et al.*,

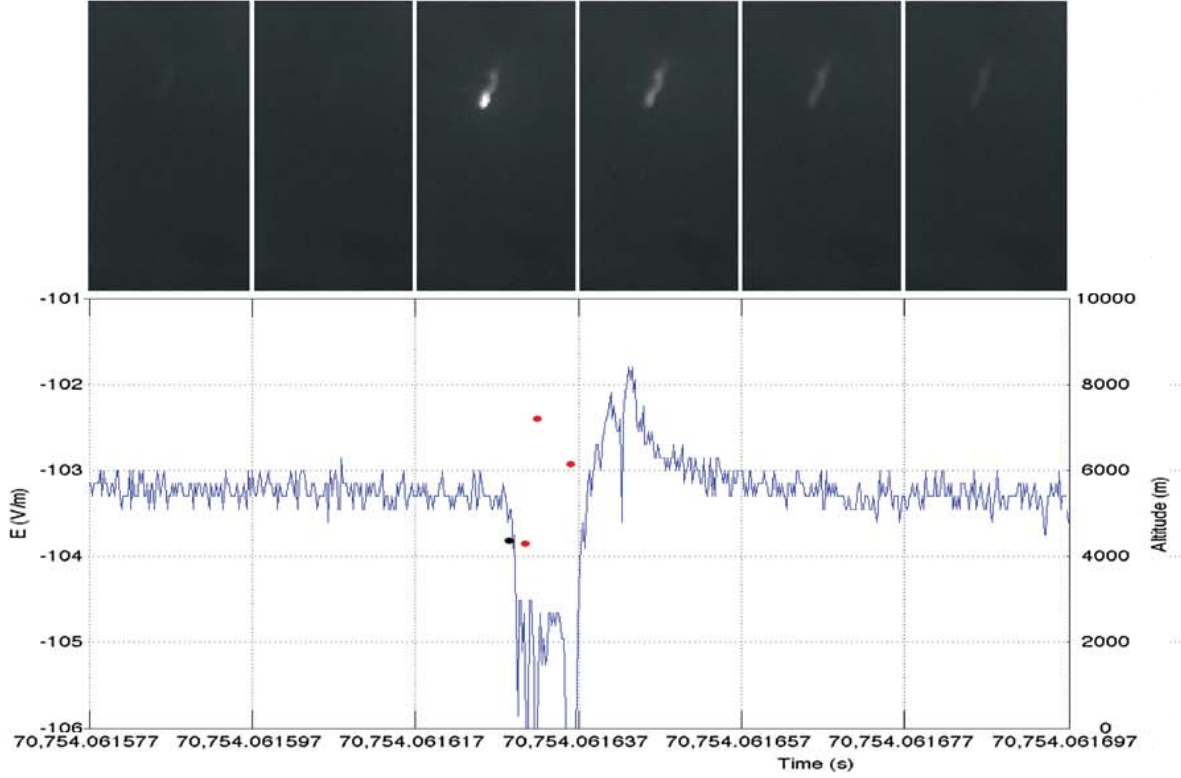


Figure 2.26: Classic initial breakdown pulse (IBP) sferic and luminosity observations in cloud-to-ground lightning. Top: sequential $20 \mu\text{s}$ frames from a high-speed optical video of electrical activity below a thundercloud base. Bottom: a single classic IBP sferic (blue waveform) in a cloud-to-ground lightning flash coincides with downward vertical elongation of luminous channel in cloud-to-ground lightning. Adapted from Stolzenburg *et al.* (2014).

2016). In such a scenario, the subpulses might indicate leader stepping, and the ensuing bipolar sferic would be largely due to relativistic electrons avalanching in the strong leader/streamer fields during the step(s). Relativistic electrons emit X-rays and gamma-rays via bremsstrahlung (braking radiation), and it is suggested that especially large or energetic classic IBPs may be a manifestation of the relativistic electrons and associated ionization producing terrestrial gamma-ray flashes (Section 2.6).

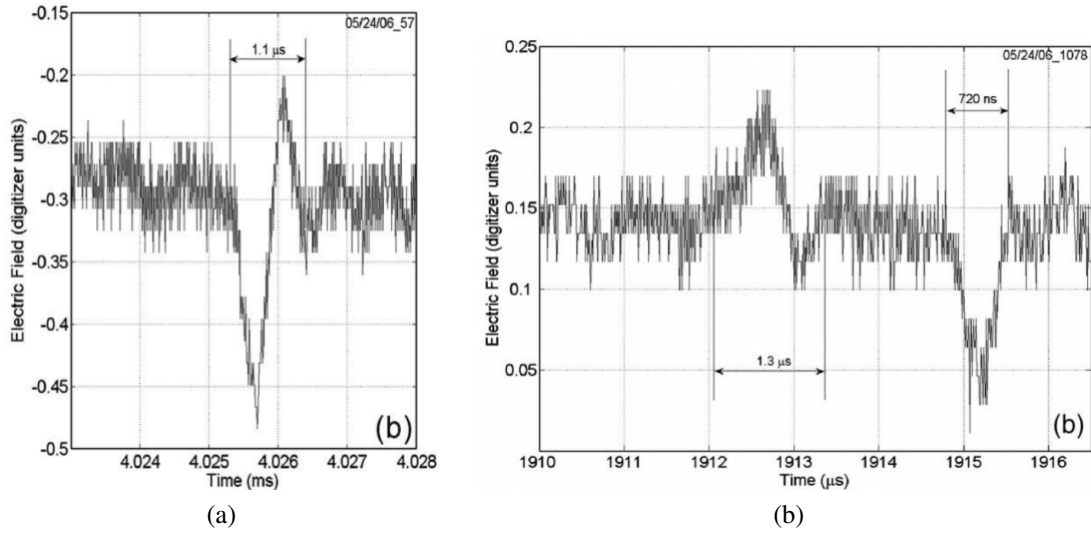


Figure 2.27: Narrow initial breakdown pulse (IBP) sferics. (a) Bipolar narrow IBP during an intra-cloud lightning flash. (b) Two narrow IBPs of opposite polarities in a cloud-to-ground lightning flash. Adapted from Nag *et al.* (2009).

2.6 Terrestrial gamma-ray flashes (TGFs)

In 1994, terrestrial gamma-ray flashes (TGFs) were discovered by the Burst and Transient Source Experiment aboard the Compton Gamma Ray Observatory (Fishman *et al.*, 1994), and have since been observed by numerous space-borne instruments, including the Reuven Ramaty High Energy Solar Spectroscopic Imager (Smith *et al.*, 2005), Astro-rivelatore Gamma a Immagini Leggero (AGILE) (Marisaldi *et al.*, 2010), Fermi (Briggs *et al.*, 2010) and, most recently, the Atmosphere-Space Interactions Monitor (ASIM) (Neubert *et al.*, 2020). TGFs are brief bursts of energetic (up to tens of MeV) photons originating inside thunderstorms, lasting tens to hundreds of microseconds, and are generated as the result of bremsstrahlung (braking radiation) by relativistic runaway electrons (Lehtinen *et al.*, 1996). Figure 2.28 demonstrates the concept of bremsstrahlung, depicting a relativistic electron that gets deflected by a (positively charged) nucleus, thus emitting a X-ray or gamma-ray photon in order to conserve momentum. Initial low-frequency electric field change measurements (160 Hz–500 kHz) showed that TGFs are generated during intra-cloud (IC) lightning (Stanley *et al.*, 2006). In particular, analysis of low-frequency electric (Shao *et al.*, 2010)

and magnetic (Lu *et al.*, 2011; Cummer *et al.*, 2015) field waveforms, as well as very high frequency (60–66 MHz) lightning mapping observations (Lu *et al.*, 2010; Lyu *et al.*, 2018), showed that TGFs occur during the upward development of normal-polarity (Williams, 1989) IC lightning, i.e., associated with the upward propagation of a negative leader.

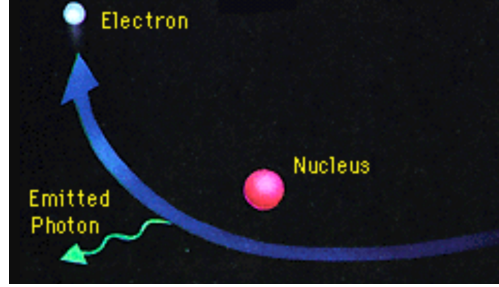


Figure 2.28: Bremsstrahlung schematic. A relativistic electron travels close to charged matter, such as a nucleus, deflecting and emitting a X-ray or gamma-ray to conserve momentum. Credit: NASA/GSFC.

Thunderstorm electric fields and strong fields at the tips of streamers and leaders have the potential to accelerate electrons to relativistic speeds, producing so-called runaway electrons (Wilson, 1925). Figure 2.29 shows the effective frictional force, F , felt by an electron as a function of its kinetic energy. If the initial kinetic energy of an electron is larger than ϵ_{th} , then the electric force (eE) is larger than the frictional force, and the electron can gain more energy from the field than it loses due to the frictional force. If the initial kinetic energy is less than ϵ_{th} , then the electron feels an effective frictional force greater than the force it feels from the field, and so it will lose energy and not run away. At very low kinetic energies, the effective frictional force will increase as the kinetic energy of the electron increases in the field. Note that if the ambient electric field reaches some critical value, E_c , then the electric force is greater than F , regardless of the initial kinetic energy of an electron, and the electron will run away. E_c is quite large – about ten times the conventional breakdown field, E_k (Dwyer, 2004, 2008).

The minimum field required to produce runaway electrons in air at STP is called the break-even field, $E_b = 2.18 \times 10^5$ V/m (Dwyer, 2003; Dwyer *et al.*, 2012) (dotted horizontal line in Figure 2.29). Relativistic runaway electron avalanches (RREAs) (Gurevich *et al.*, 1992) can occur, much in the

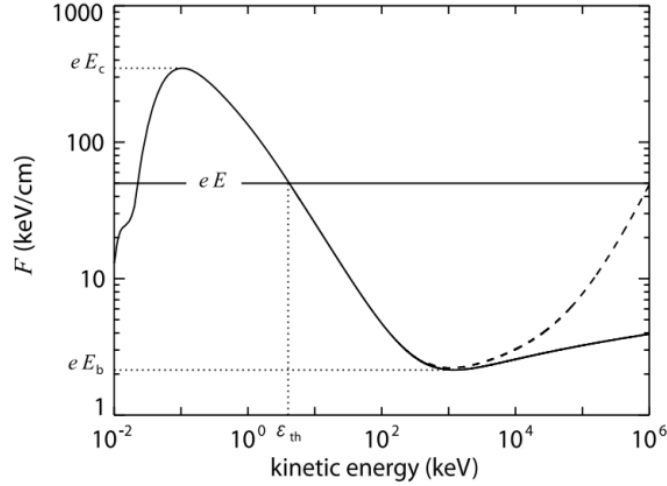


Figure 2.29: Effective frictional force felt by an electron as a function of kinetic energy. For an electron (or positron) placed in an ambient electric field E (the solid horizontal line depicts the force due to $E=5 \times 10^6$ V/m at STP in air), the electron feels a force eE . However, the force is countered by a frictional force due to inelastic scattering with air molecules (solid curve), but if the electron has an initial kinetic energy above ϵ_{th} , then the electron can effectively “run away,” feeling a lesser frictional force as it gains more energy. If the ambient field is instead E_c , then any electron can run away, regardless of its initial kinetic energy. E_b is the break-even field, or minimum field required to produce a runaway electron. The dashed curve includes energy loss due to bremsstrahlung. Adapted from Dwyer (2012); Dwyer *et al.* (2012).

same way that a non-relativistic electron avalanche occurs, with the number of runaway electrons increasing in the opposite direction of the ambient electric field and over the distance the avalanche has traveled (Dwyer, 2003):

$$N_{RE} = N_0 \cdot e^{L/\lambda} \quad (2.4)$$

where λ is the RREA e -folding length, which is inversely proportional to the ambient electric field (i.e., $\sim 1/E$), N_0 is the number of initial runaway electrons entering the avalanche region, and N_{RE} is the number of runaway electrons at the end of the avalanche region of length L . However, RREAs take place at a slightly higher threshold field than E_b , at what is called the RREA threshold field, $E_{RREA}=2.8 \times 10^5$ V/m (Dwyer, 2012). The higher RREA threshold field is required due to Coulomb scattering (electron scattering off of atomic nuclei) and Møller scattering (electron scattering of atomic electrons), which causes the scattering electrons to deviate from the

field direction (Dwyer *et al.*, 2012). The magnitude of E_{RREA} can be determined from Monte Carlo simulations that take into account all relevant processes.

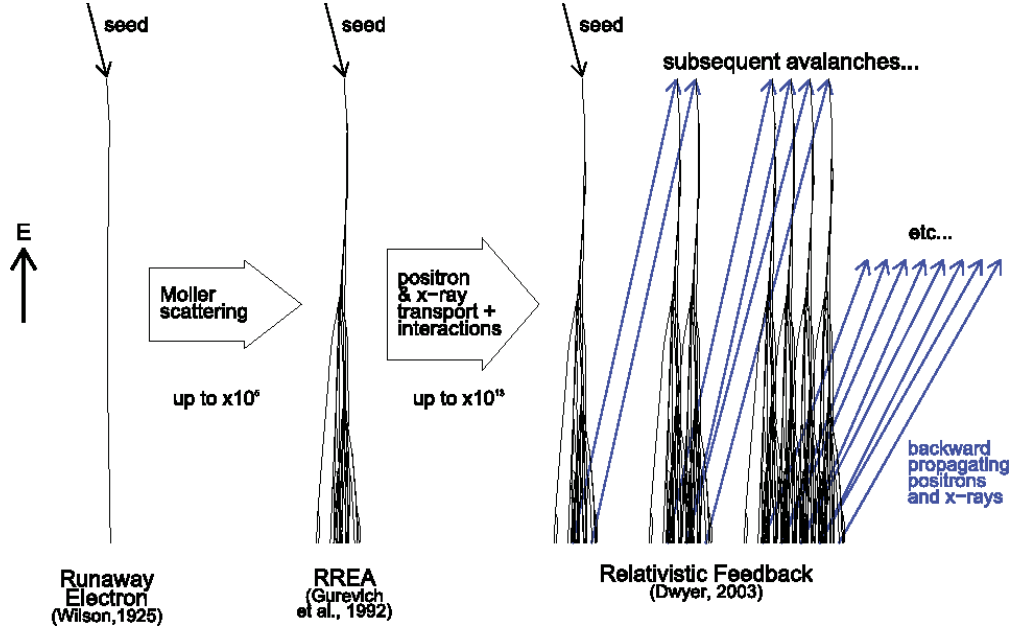


Figure 2.30: From left to right: a single runaway electron, relativistic runaway electron avalanche via electron-electron interactions (Møller scattering), relativistic feedback via positron and X-ray interactions. Adapted from Dwyer *et al.* (2012).

At relativistic energies, there are other processes that can contribute to ionization, and hence runaway electron production. Gamma-rays produced by bremsstrahlung can pair-produce, decaying into electron-positron pairs, and positively-charged positrons can run away in the opposite direction of their negatively-charged electron counterparts, liberating high-energy electrons that can also runaway and cause RREAs. Moreover, back-scattered X-rays produced by bremsstrahlung can liberate more electrons back along the avalanche region too. The X-ray and positron feedback process is collectively termed the relativistic feedback mechanism (Dwyer, 2003), where generations of relativistic runaway electron avalanches repeatedly go through the same electric field region, driven by positron and energetic photon feedback. The feedback mechanism is illustrated in Figure 2.30. One “feedback cycle” considers the average time, τ_{fb} , that it takes for runaway electrons and backward-propagating X-rays/positrons to complete one round trip in the avalanche region. That is, given one initial “seed” electron with kinetic energy at least as large as ϵ_{th} (see

Figure 2.29) and starting location x_0 , τ_{fb} is the time it takes for an ensuing RREA to reach the end of the avalanche region and for feedback to generate the next batch of seed electrons at the starting point x_0 . The “amount” of feedback can then be quantified by the feedback factor, γ , which is defined as the fractional increase in the number of runaway electrons over the time τ_{fb} (from Monte Carlo simulations, $\gamma \propto L/\lambda$, and so is proportional to both L and E (Dwyer, 2003)). The number of runaway electrons at the end of an avalanche region is then increased from the values obtained in equation 2.4 (Dwyer, 2003, 2012):

$$N_{RE} = \frac{N_0 \cdot e^{L/\lambda}}{1 - \gamma}, \quad \gamma < 1 \quad (2.5)$$

$$N_{RE} = N_0 \cdot \gamma^{t/\tau_{fb}} \cdot e^{L/\lambda}, \quad \gamma > 1 \quad (2.6)$$

where t is time from the initial electron entering the avalanche region. For $\gamma=0$, no feedback occurs, and we get back equation 2.4. For $0 < \gamma < 1$ (equation 2.5), feedback occurs and enhances the number of runaway electrons in the avalanche region, and as γ approaches 1, the flux of seed runaway electrons becomes very large, with the ensuing RREAs quickly discharging the ambient field (Dwyer, 2012). Thus, the RREA threshold field, E_{RREA} , serves as a sort of upper limit over large spatial scales in thunderstorms (Dwyer, 2003). This fundamental limit on the electric field is supported by in-situ thundercloud measurements (Stolzenburg *et al.*, 2007), which show that E_{RREA} is generally the maximum observed field, aside from fields produced by lightning discharges. For example, Figure 2.31 shows the electric fields measured in a thundercloud by a balloon-borne sensor as it rises through the cloud. In the figure, the green dashed curve shows the break-even field, E_b , above which runaway electrons can be generated, and the RREA threshold field, E_{RREA} , is indicated by the blue dotted line. Note that the measured thundercloud field can be above E_b , but stays below E_{RREA} , except when lightning occurs; then the electric field can be much higher. Figure 2.31 also demonstrates how the electric field magnitudes scale, i.e., decrease, with altitude.

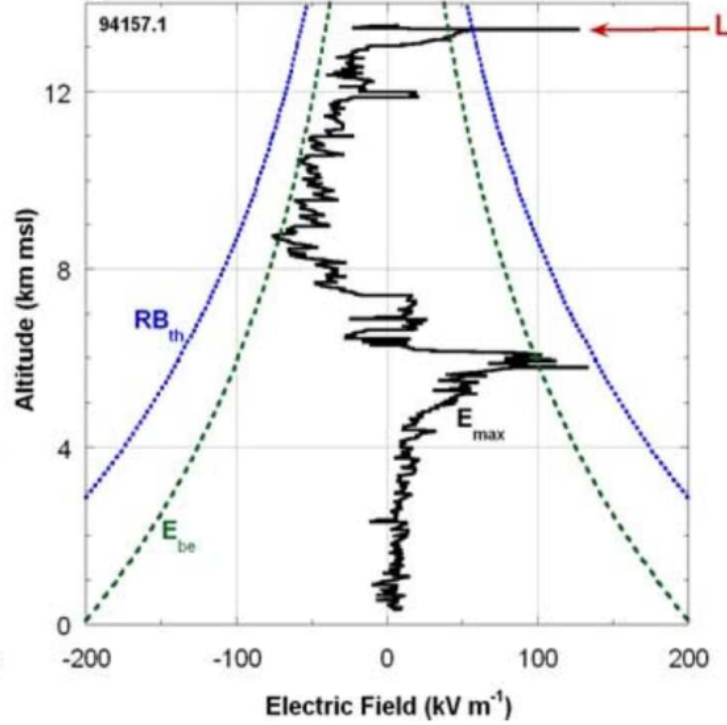


Figure 2.31: Thundercloud electric field balloon sounding. The dashed green curve shows the break-even field, E_b , as a function of altitude, and the dotted blue curve shows the RREA threshold field, E_{RREA} . Note that the magnitude of the measured electric field can be above E_b , but stays below E_{RREA} , except when lightning occurs ('L'). Adapted from Stolzenburg *et al.* (2007).

However, if the thunderstorm conditions push the feedback factor up to $\gamma > 1$ (equation 2.6), e.g., after a sufficiently rapid increase of the thunderstorm electric field, then the number of runaway electrons increases exponentially with time, with seed electrons produced almost entirely from the feedback process (Dwyer, 2012). For $\gamma > 1$, a so-called relativistic feedback discharge (RFD) (Dwyer, 2012; Liu & Dwyer, 2013) develops, and is a self-sustained breakdown much in the same way as a streamer (Section 2.3). In order for a RFD to take place, the ambient electric field must be large enough (i.e., at least above E_{RREA}) over a “large enough” region. The relationship between E and L in order to make $\gamma = 1$ is demonstrated in Figure 2.32, and can be obtained from Monte Carlo simulations (Dwyer, 2003, 2007). The figure shows that for lower values of ambient electric field, the field region must extend over larger spatial scales in order for a RFD to form. At thunderstorm altitudes, if a sudden high-field region about ~ 1 km deep in the vertical

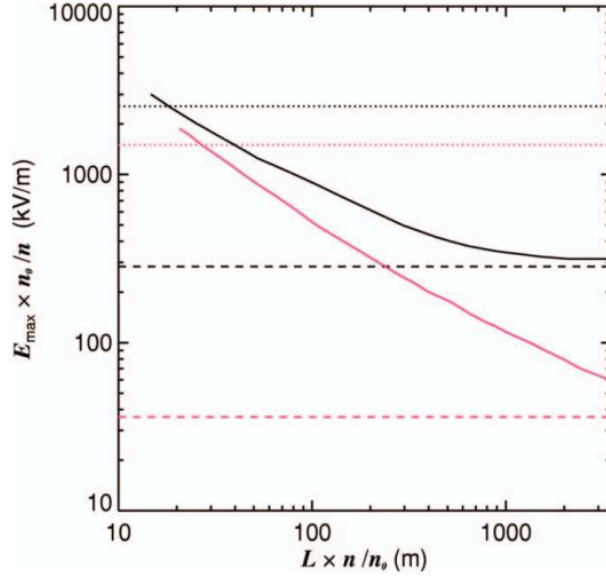


Figure 2.32: Ambient electric field as a function of field region length in order to make $\gamma=1$. The relationship is determined from Monte Carlo simulations, and is shown for air (black) and also for a hydrogen-helium atmosphere (red), such as that on any of the gas giants: Jupiter, Saturn, Uranus, and Neptune. The horizontal lines show the RREA threshold, E_{RREA} , and the dotted lines show the conventional breakdown threshold, E_k . Adapted from Dwyer (2007).

and horizontal directions is created, e.g., by a lightning event, then a RFD can be created in the high-field region (Dwyer, 2012).

Based on the descriptions above, there are currently two main theories for the physical mechanism of TGFs (Dwyer, 2008; Dwyer *et al.*, 2012), and intense investigations are being carried out to determine how each theory might be involved in the production of the large number of energetic (MeV) runaway electrons produced inside thunderstorms. The first theory is known as the cold runaway mechanism and is based on conventional electrical discharge processes – leaders and streamers – that are constituents of lightning. It suggests that the free electrons produced by leaders and streamers are accelerated to the required energies in a compact region of extremely strong electric field immediately ahead of an advancing powerful lightning leader (Moss *et al.*, 2006; Celestin *et al.*, 2012), as illustrated in Figure 2.33. The strong field must be at least as large as the critical field, E_c , shown in Figure 2.29, that allows all electrons to run away, regardless of

their initial kinetic energy. The other theory involves the self-sustained relativistic discharge – a RFD (Figure 2.30) – as a physical mechanism for TGF generation.

Electromagnetic measurements indicate that TGFs are at least sometimes time aligned (within $\simeq 10 \mu\text{s}$) with sferics tens to hundreds of microseconds long. The pulse amplitudes of the sferics have been found to match the temporal variations of the TGF photon intensity (Lu *et al.*, 2011; Cummer *et al.*, 2011; Pu *et al.*, 2019), indicating that the sferic is produced by the TGF-generating discharge process (Cummer *et al.*, 2011; Pu *et al.*, 2019). There has been speculation (Marshall *et al.*, 2013; Stolzenburg *et al.*, 2016) that the sferics of TGFs are energetic versions of the initial breakdown pulses (Section 2.5) associated with the initial stepped leader formation (Beasley *et al.*, 1982; Rhodes & Krehbiel, 1989; Villanueva *et al.*, 1994; Marshall *et al.*, 2013; Stolzenburg *et al.*, 2013; Karunarathne *et al.*, 2013, 2014; Kolmasova *et al.*, 2018). More recently, a special class of high peak-current IC radio pulses, termed energetic in-cloud pulses (EIPs), was discovered to coincide with TGFs (Cummer *et al.*, 2014; Lyu *et al.*, 2015). Figure 2.34 shows three example EIPs, i.e., the $\sim 50 \mu\text{s}$ wide sferics shown in black, which were recorded at the ground. The EIPs

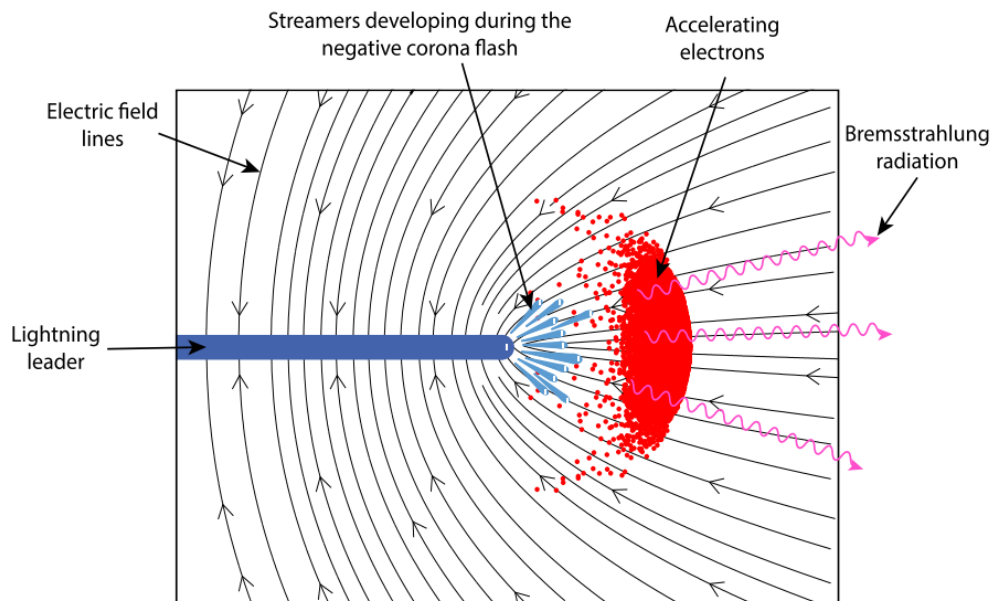


Figure 2.33: Schematic of thermal electrons accelerated to relativistic energies at the tip of a powerful lightning leader. The relativistic runaway electrons produced at the leader tip / streamer zone radiate X-rays and gamma-rays via Bremsstrahlung. Adapted from Celestin *et al.* (2015).

were coincident with gamma-ray detections made by the Fermi spacecraft (colored boxes), after taking into account travel time between the source and sensor locations. In fact, a one-to-one correspondence has been found between EIPs and TGFs that occur within range of a spacecraft detector (Lyu *et al.*, 2016; Cummer *et al.*, 2017). It has been shown that RFDs can create large peak currents (~ 10 kA), peak current moments (~ 10 kA-km), and charge-moment changes (~ 1 C-km) (Dwyer, 2012; Liu & Dwyer, 2013), similar to those produced by EIPs. In addition to the associated sferics, EIPs likely produce detectable optical emissions in the lower ionosphere (Liu *et al.*, 2017) due to their large current moments. In fact, Neubert *et al.* (2020) recently confirmed that lower ionospheric optical emissions can accompany TGFs.

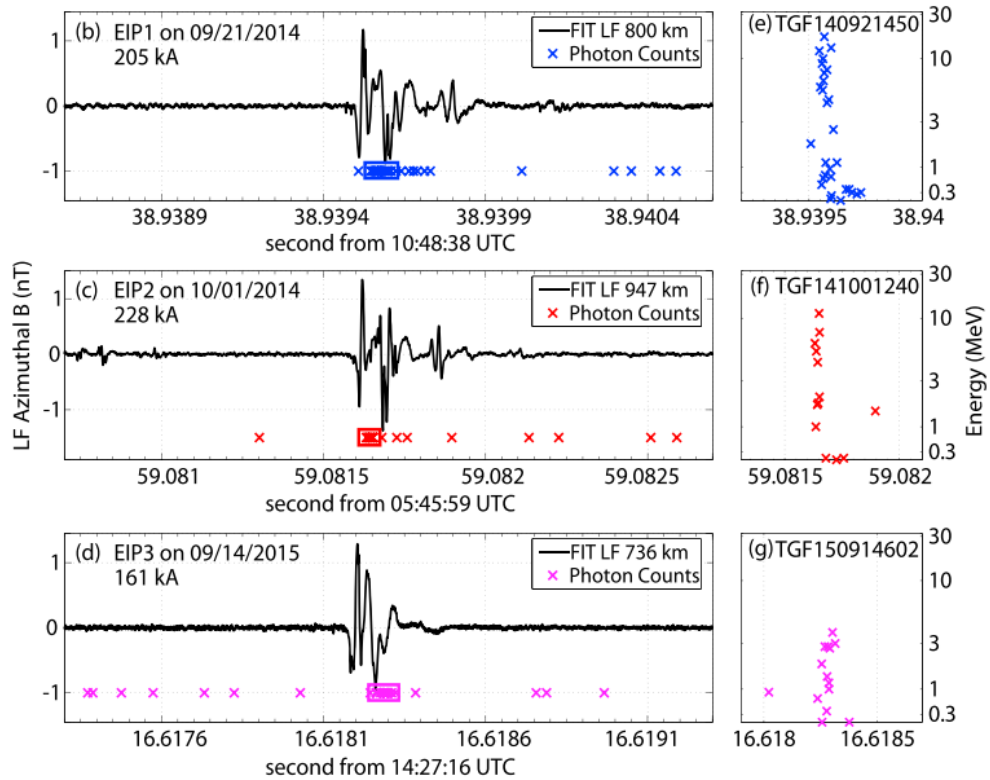


Figure 2.34: Energetic in-cloud pulses (EIPs) and terrestrial gamma-ray flashes (TGFs). Ground-based sferic measurements made in Florida (black waveforms) are time-aligned with TGF detections (colored boxes) made by the Fermi spacecraft. The EIP detections (large-amplitude, ~ 100 μ s wide sferic pulses) overlap in time with the TGF detections. Adapted from Lyu *et al.* (2016).

CHAPTER 3

LIGHTNING PROBLEMS AND HYPOTHESES

In this dissertation, there are three main problems in atmospheric electricity that we address, and they come with three hypotheses, respectively. Namely:

Lightning problems and hypotheses	
Problem 1:	Ambient thunderstorm electric fields are ten times lower than the electrical breakdown threshold field of air, so how is lightning initiated?
Hypothesis:	Positive streamers initiate lightning.
Problem 2:	Lightning begins with streamers, but when/how is the leader or the first hot channel formed?
Hypothesis:	Initial breakdown pulses (IBPs) are involved in initial leader formation.
Problem 3:	Only a small fraction of lightning events result in terrestrial gamma-ray flashes (TGFs), so how is lightning involved in TGF generation?
Hypothesis:	Enhanced cold runaway and/or relativistic feedback by lightning generates TGFs.

In order to address these three problems, we investigate narrow bipolar events (NBEs), initial breakdown pulses (IBPs), and an energetic in-cloud pulse (EIP) by using a broadband radio interferometer. To recap, NBEs were found to be generated by fast positive breakdown, a finding which is consistent with the idea that positive streamers initiate lightning. Hence, we can study NBEs to either further validate or otherwise call into question the hypothesis that positive streamers initiate

all lightning. However, streamers are a necessary but not sufficient condition for lightning formation, and incidentally, NBEs can occur in complete isolation without generating lightning. IBPs are believed to be the first indication that leaders form and that lightning will ensue. Hence, we can study IBPs to better determine when and how lightning leaders form. Lastly, EIPs are radio signatures associated with the generation of a subset of TGFs. Hence, we can study EIPs to learn how lightning is involved in TGF generation.

Figure 3.1 summarizes the sferics (i.e., broadband ~ 3 kHz-3 MHz electric field change measurements) that are used to identify NBEs, IBPs, and EIPs. For instance, Figure 3.1a shows the entire sferic of a ~ 100 ms long cloud-to-ground flash, with the three blue arrows indicating large (~ 100 V/m) electric field changes that coincide with a leader touching ground at three different times, each producing a large current surge and luminosity wave (i.e., return stroke) that travels from the ground upward along the channel. The huge current surges occur as a result of the leaders shorting ~ 100 million volts of cloud potential to ground. Figure 3.1b shows an expanded view of the same flash from initiation up until the first return stroke, showing a train of relatively high-amplitude sferic pulses that occur during the first several milliseconds of the flash. The pulse train is shown expanded in Figure 3.1c, with the flash-initiating NBE and a single IBP indicated with the single and double red boxes, respectively. As can be seen from Figure 3.1c, NBEs, if they occur, will be the very first pulse in a lightning flash, and from the expanded view in Figure 3.1d, we can see that the NBE sferic is relatively narrow (~ 10 μ s wide) and roughly bipolar in shape. IBPs, in contrast, are embedded in later activity of the flash, but usually occur within the first few milliseconds of a flash – in a cloud-to-ground flash, IBPs occur before the leader first touches ground. IBPs typically occur in trains, as shown here, that last for several milliseconds. From the expanded view in Figure 3.1e, we see that IBPs are similarly bipolar compared with NBEs, but can be somewhat wider (~ 10 -100 μ s wide), and are typically superimposed by spikey subpulses on the leading pulse of the sferic. In addition, though not produced in the cloud-to-ground flash of Figure 3.1a-e, an EIP sferic is shown in Figure 3.1f for comparison. EIPs, like IBPs, tend to occur within the first few milliseconds of a lightning flash, are typically as wide as the widest IBPs (~ 50 -100 μ s), but do

not occur in trains and are relatively rare. EIPs are defined by the high amplitude of their sferics, which can be seen here to rival the electric field change of the return strokes shown in Figure 3.1a (~ 100 V/m), despite taking place entirely in the cloud. EIPs are associated with high peak currents in excess of 100 kA, similar to some of the highest peak currents associated with return strokes.

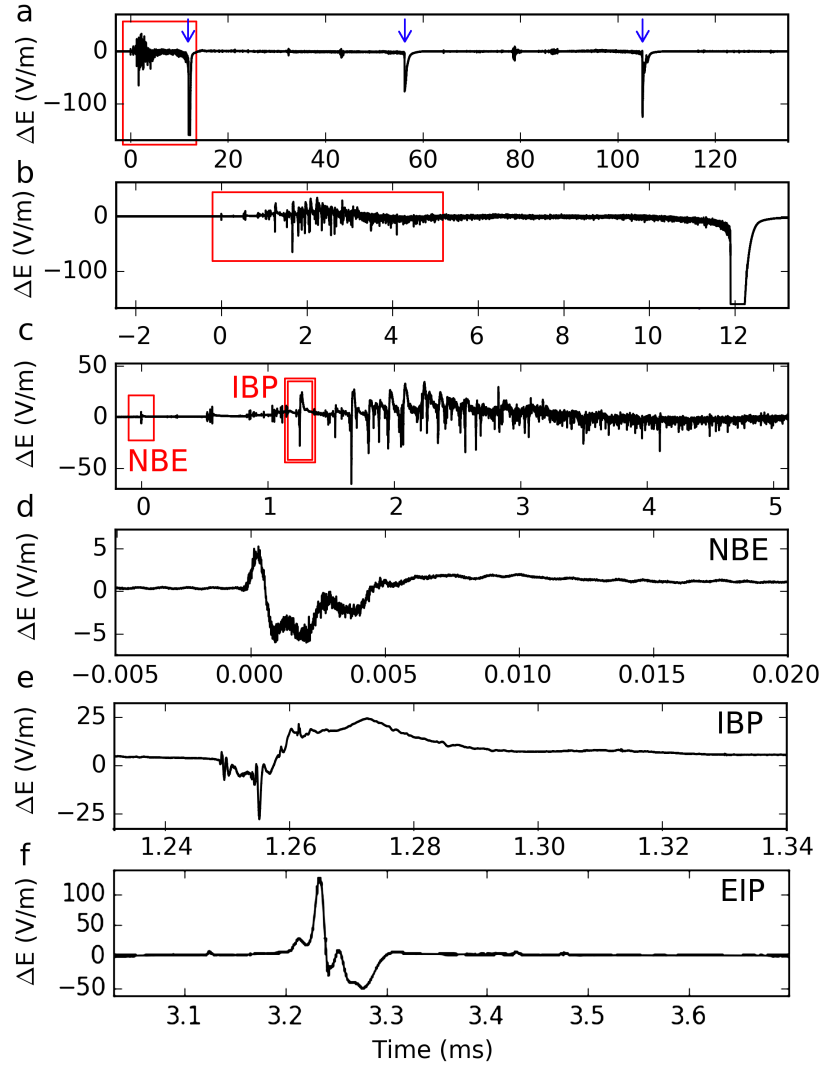


Figure 3.1: Lightning sferics. The broadband ~ 3 kHz-3 MHz electric field changes, i.e., sferics, associated with: (a) a CG flash, with the three return strokes indicated by blue arrows, (b) the initial stage leading up to the first CG return stroke, (c) the CG flash-initiating NBE and IBP train, (d) the CG flash-initiating NBE, (e) an example IBP in the CG flash, and (f) an EIP from a different (intra-cloud) lightning flash.

CHAPTER 4

SCIENTIFIC CONTRIBUTIONS

In this dissertation, broadband radio interferometry (Stock, 2014) is used to map and image VHF radio sources associated with fast thunderstorm electrical processes, with the purpose of investigating the fast dynamics with sub-microsecond resolution. Specifically, major scientific contributions include:

1. Discovery and characterization of fast negative breakdown in thunderstorms. Fast negative breakdown is a newly-identified fast-propagating $\sim 10^7$ m/s streamer process, which plays important roles in lightning initiation and propagation, and generates various types of sferics.
2. Adaptation of radio astronomy techniques to simulate and characterize radio images due to single-source and multi-source thunderstorm emissions.
3. New physical description of classic IBPs. The initial pulse of a classic IBP sferic is produced by fast negative breakdown, which extends the channel ~ 100 m into virgin air, whereas the long tail of the sferic is generated by sustained currents through a leader.
4. Identification of a new process in lightning initial stage. IBPs are preceded by slower-propagating ($\sim 10^6$ m/s) negative breakdown that emits no detectable fast sferics, with both IBPs and the slower process contributing equally in length to initial lightning channel development.
5. Development of a novel radio-based method for distinguishing relativistic from conventional thunderstorm discharges. By comparing EIP sferics and VHF emissions, we determine that EIPs are generated by relativistic electrons and associated ionization.

6. Identification of a new causal relationship between conventional and relativistic thunderstorm processes. Relativistic avalanching develops during the occurrence of downward-then-upward fast positive-then-negative breakdown that repeatedly discharges a large volume.
7. Observational verification that EIPs, and hence TGFs, can be produced by relativistic feedback discharges (RFDs), which involve multiple generations of relativistic electron avalanches and back-scattered positrons and X-rays.

The results herein have been published (Tilles *et al.*, 2019), submitted for publication (Tilles *et al.*, 2020b), or are under preparation for journal submission (Tilles *et al.*, 2020a).

Part II

Instrumentation and methods

In summer 2016, the New Mexico Tech broadband VHF interferometer (INTF) and fast electric field change antenna (FA) (Stock, 2014; Stock *et al.*, 2014; Rison *et al.*, 2016) were deployed to Kennedy Space Center (KSC), FL, as a follow-up study to Rison *et al.* (2016). The INTF site location is shown in Figure 4.1. The INTF observations were complemented by three-dimensional lightning VHF source locations from the KSC Lightning Mapping Array (LMA) (Rison *et al.*, 1999; Thomas *et al.*, 2004).

The combination of INTF, FA, and LMA observations provides a detailed picture of the altitude, physical extent, propagation speed, polarity, and other electrical characteristics of the observed breakdown events, as well as information about the storm context in which they occur. Each instrument is described in more detail in the following sections.



Figure 4.1: Instrument locations in 2016 Florida deployment. (a) Plan view of the Florida coastline, showing the eight inner-most stations of a ten-station Lightning Mapping Array (LMA) (green squares) and the location of the broadband interfereometer (INTF) (white dot). (b) Close-in plan view of the INTF, showing the three INTF antennas, A, B, C, arranged in an equilateral triangle configuration with 100-meter baselines. The fast electric field antenna (FA) is located near the center of the array (green balloon).

CHAPTER 5

BROADBAND RADIO INTERFEROMETRY

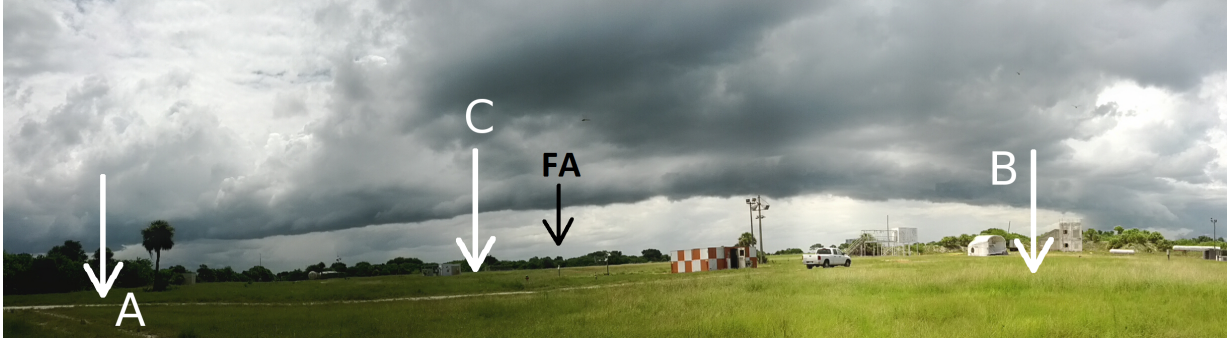


Figure 5.1: INTF site panorama at Kennedy Space Center in 2016. Three flat-plate antennas (labeled A, B, C) and fast electric field change antenna (FA) are indicated by arrows, with A and B in the foreground, and C in the background (the photograph was taken from the right side of Figure 4.1b, looking toward the west). The signal from each sensor ran along a dedicated coaxial cable to the data acquisition building (orange-white checkered building) where it was digitized and stored.

5.1 Hardware

The New Mexico Tech broadband VHF radio interferometer (INTF) was operated at KSC in 2016–17 (Stock *et al.*, 2014; Rison *et al.*, 2016), and utilized three broadband VHF ($\simeq 14\text{--}88$ MHz) flat-plate receiving antennas, “A”, “B”, and “C”, arranged in a 100-meter equilateral triangle baseline configuration, as shown in Figure 4.1b from a bird’s eye view, and in Figure 5.1, looking west across the array. The time series waveforms from each receiver and from a fast electric field change antenna co-located with the INTF (see Section 6) were amplified and sent along coaxial cables to a central data-acquisition building, where the signals were filtered and further amplified before being synchronously digitized at 180 MSps with 16-bit resolution. Recording of the INTF (and FA) signals was triggered either by strong VHF emissions from antenna C (the most quiet

of the three VHF sensors during non-thunderstorm activity), typically with a 50 ms pre- and post-trigger, or by a strong signal from a co-located slow antenna (see Section 6.1) with a time constant of 10 s, and a much longer typical pre- and post-trigger of 1.5 s.



Figure 5.2: INTF antenna at Kennedy Space Center in 2016. The circular flat-plate antenna covers a housing (cake pan) containing signal amplifiers. The amplified signal runs from the housing along a coaxial cable to the data acquisition building (orange-white checkered building in the background), where it is filtered and further amplified before being digitized and stored.

The INTF utilizes circular flat metal plates as the sensing elements, as shown in Figure 5.2, and when placed in an ambient electric field (\vec{E}), a charge density (ρ) is induced on the exposed surface area (A) of the sensor. The quantities are related by Gauss' law, $\nabla \cdot \vec{E} = \rho / \epsilon_0$, which can be rewritten:

$$\rightarrow \int \left(\nabla \cdot \vec{E} = \frac{\rho}{\epsilon_0} \right) dV \rightarrow \oint \vec{E} \cdot d\vec{A} = \int \frac{\rho}{\epsilon_0} dV \rightarrow E_z A = \frac{Q}{\epsilon_0} \quad (5.1)$$

where Q is the total charge induced on the exposed surface of the sensor, and the divergence theorem was used to convert the integral over the volume surrounding the sensor, V , into an closed integral over the exposed surface area of the sensor, A .

For \vec{E} changing with time (as it naturally does due to charge movement in a thunderstorm), it induces a current I_{in} on the plate, which can flow into a circuit connected to the plate:

$$\frac{dE_z}{dt} = \frac{d}{dt} \left(\frac{Q}{A\epsilon_0} \right) = \frac{I_{in}}{A\epsilon_0} \quad (5.2)$$

If this circuit is an inverting op-amp circuit, which is depicted in Figure 5.3a, then $I_{in}=I_{out}$, or rather $V_{out}=-I_{in}R_{out}$, and the measured output voltage, V_{out} , is:

$$V_{out} = -I_{in}R_{out} = -A\epsilon_0 \frac{dE_z}{dt} R_{out} \quad (5.3)$$

The instrument sketched in Figure 5.3b depicts the flat metal plate as the sensing element of a time-varying vertical electric field, which can be encompassed by its time derivative, dE_z/dt . The current induced on the plate serves as the input into an inverting op-amp circuit, and thus, by rearranging the terms in equation 5.3, we see that the instrument provides a measurement of dE_z/dt :

$$\frac{dE_z}{dt} = -\frac{V_{out}}{R_{out}A\epsilon_0}. \quad (5.4)$$

By using the instantaneous dE_z/dt signal for determining VHF source locations (Section 5.3), we take advantage of the full bandwidth provided by the digitizer ($\simeq 14$ -88 MHz, and $\simeq 5.5$ -ns temporal resolution).

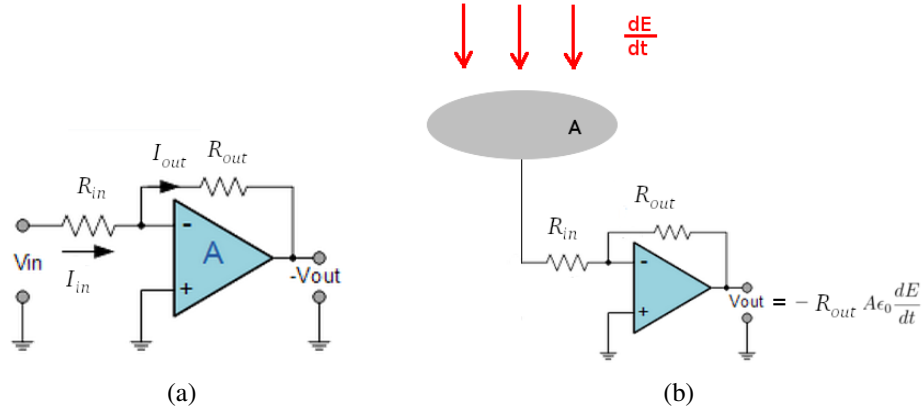


Figure 5.3: Circuit elements of dE_z/dt sensor. (a) An inverting op-amp circuit. (b) Circuit elements, including the sensing plate and showing the output voltage, used to record dE_z/dt .

5.2 Concept

The basic concept of interferometry can be explained using two antennas as an illustration. Figure 5.4a shows a two-dimensional diagram of two antennas, A and B , separated a distance d_{AB} , which denotes the length of the baseline AB . We assume that a source is radiating a distance much farther away than the distance d_{AB} , so that the incoming electromagnetic signal can be approximated as a plane wave. Then, the signals received by A and B are assumed to be identical, but one must travel an additional distance $c\tau_{AB}$ to reach A after reaching B , where τ_{AB} is the time delay between the signals received at A and B , and c is the speed of light. The angle θ_{AB} that the source makes with respect to AB is related to $c\tau_{AB}$ and d_{AB} by simple trigonometry:

$$d_{AB} = c\tau_{AB} \cos(\theta_{AB}) \quad (5.5)$$

and we are ultimately interested in finding the angle θ_{AB} in the direction of the emitting source. Since d_{AB} and c are knowns, we need only find the time delay τ_{AB} between the two incoming signals in order to solve for θ_{AB} .

In reality the problem exists in three-dimensional (3-D) space. The baseline AB is shown to have some orientation with respect to the cardinal directions (north-south and east-west) in

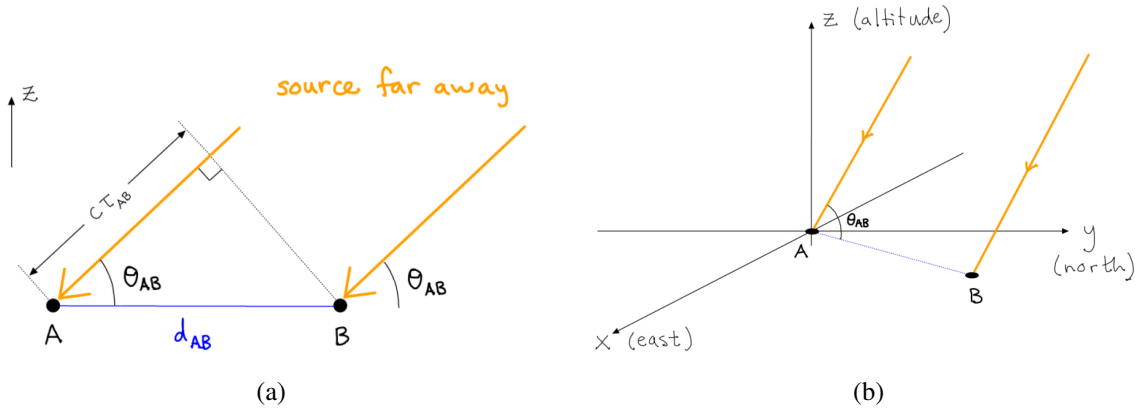


Figure 5.4: Interferometry conceptual diagram. (a) Two antennas, A and B , separated by baseline length d_{AB} , receive an electromagnetic plane wave that makes an angle θ_{AB} with the baseline. After reaching B , the signal must travel an additional distance $c\tau_{AB}$ to reach A , where τ_{AB} is the time delay between the signals at A and B . (b) Same as (a) but in three dimensions, showing orientation of AB with respect to cardinal directions.

Figure 5.4b. With just one baseline, we can obtain one angle θ_{AB} to the source, which alone cannot give a direction to the source. Adding a third antenna, C , brings the total number of baselines from one to three, and each baseline is oriented differently with respect to the cardinal directions, providing three angles to the source (θ_{AB} , θ_{AC} , and θ_{BC}). With just two angles, the direction (2-D location) to the source can be determined.

Note that solving for a third angle does not make the system three-dimensional, but acts as a redundant measurement. Recall that this problem has been set up by assuming that the source is infinitely far away (with the incoming radiation a plane wave), so it does not make sense to talk about triangulating to the source as if it has a finite distance from the antennas. Rather, the interferometer output is the angular direction to a source (as in an ordinary 2-D photograph). Thus, a cartesian coordinate system is not an ideal choice for representing source locations herein. We instead utilize a coordinate system called the “cosine plane” (Stock, 2014) that has as its axes the cosines of the angles, α and β , that a source makes with respect to the east and north directions, respectively, as depicted in Figure 5.5a. A source is projected first onto a unit hemisphere, and then straight down onto the instrument plane. The resulting unit disk is called the cosine plane,

as shown in Figure 5.6a. Note that sources projected near the horizon (near a radius of 1) will be more compressed on the cosine plane than sources directly overhead, near the disk center. This is similar to the projection of the sky by a fish-eye lens, an example of which is shown in Figure 5.6b.

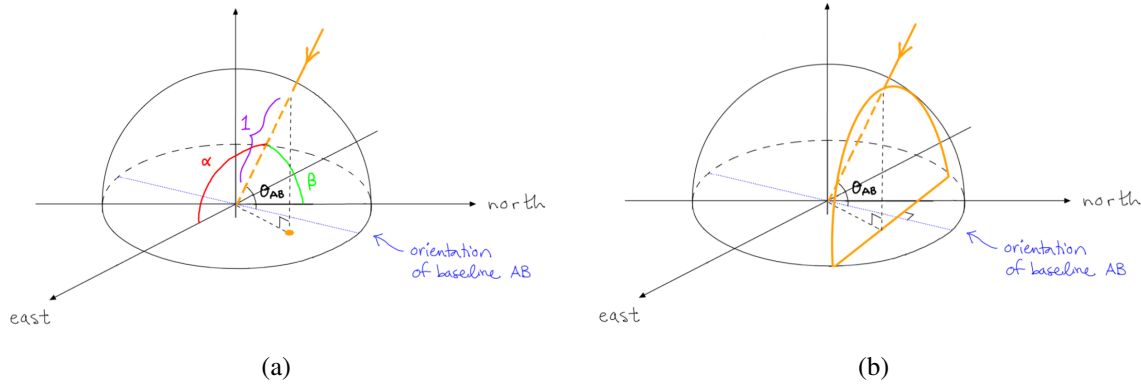


Figure 5.5: Transition from 3-D space to 2-D cosine plane projection. (a) A point source (orange line) makes an angle α with respect to the east direction, an angle β with respect to the north direction, and an angle θ_{AB} with respect to the baseline AB (dotted blue line). The source is projected on a unit hemisphere, and then straight down into the instrument plane (cosine plane), which forms a unit disk. (b) The angle θ_{AB} defines a line of constant time delay (orange solid line) in the cosine plane where the source may be.

Figures 5.5b and 5.6a demonstrate that for a given baseline orientation in the cosine plane (blue dashed lines in the figures), a line perpendicular to the baseline orientation represents a line of constant time delay (orange solid lines). With a second baseline, we find a second line in the cosine plane where the source may exist. The intersection of the two lines defines the location of the source in the cosine plane. Note that a third baseline will produce yet another line of constant time delay, and this line would perfectly intersect the other two lines at a point given the ideal scenario that the emitter is a point source and that there is no noise in the measurement.

The sky can equivalently be viewed in an azimuth-elevation projection (as in a 2-D photograph), where azimuth (Az) is the angle made clockwise with respect to north, ranging from 0° to 360° , and elevation ($E\ell$) ranges from 0° (the horizon) to 90° (directly overhead). Figure 5.7 shows how coordinates in the cosine plane are related to azimuth and elevation.

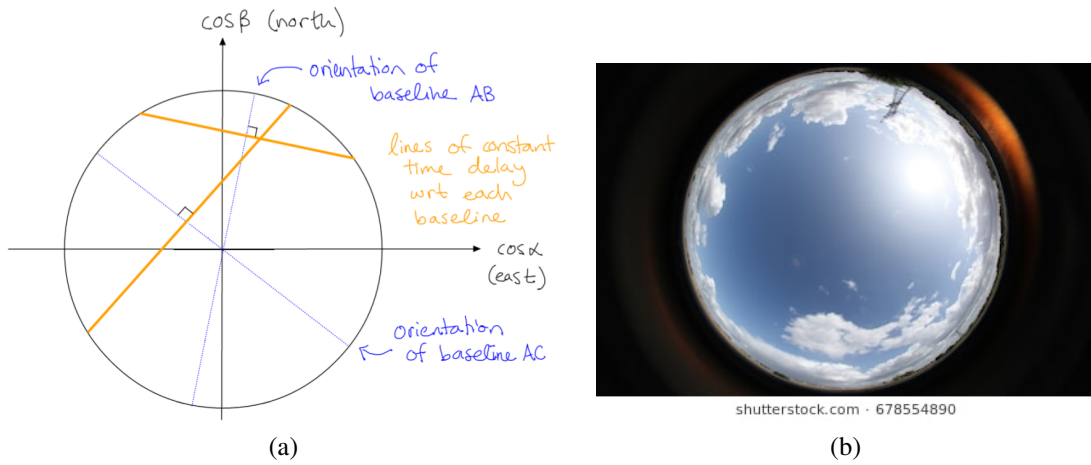


Figure 5.6: Cosine plane and source direction determination. (a) Two baselines produce two lines of constant time delay (orange solid lines) in the cosine plane which are perpendicular to their respective baseline orientations (blue dotted lines), and the intersection of which defines the source location in the cosine plane. (b) Sky projection by a fish-eye lens, which similarly represents and distorts the sky as compared to the cosine plane. Photo by (Anastasiia-S, 2018).

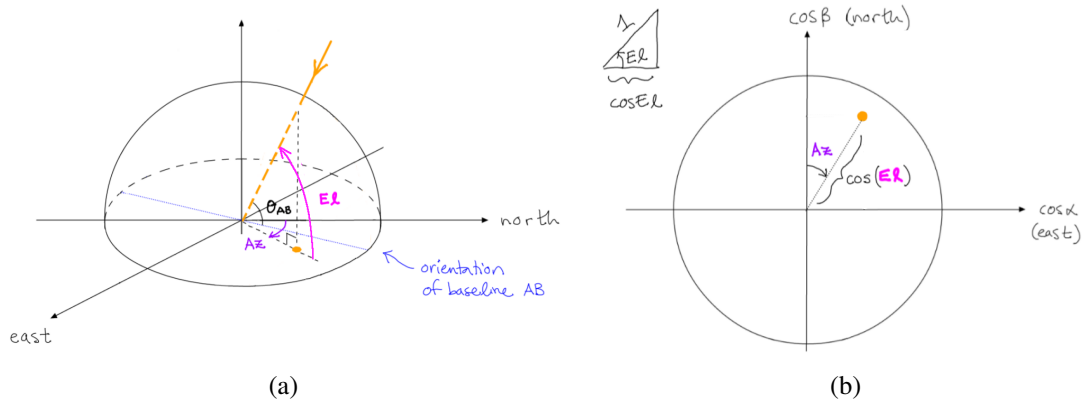


Figure 5.7: Azimuth and elevation angle and relation to cosine plane. (a) The direction to a source (orange line) makes an azimuth angle Az with respect to north, and elevation angle El with respect to ground. The direction to the source in the cosine plane is depicted by the orange dot. (b) Cosine plane, with the source azimuth and elevation angles shown.

5.3 Imaging and mapping algorithm

The time-differences-of-arrival (TDOAs) for the three antenna pairs constrain the source to lie along three straight lines in the cosine plane, where each line is oriented perpendicular to its re-

spective baseline, and the source location corresponds to the intersection of the lines. The problem boils down to determining time delays τ_{AB} , τ_{AC} , and τ_{BC} that an emitting source makes with respect to baselines AB , AC , and BC , respectively. While determining the time delays for a stationary impulsive event might be trivial, a lightning signal may be produced continuously by many sources that are in motion with respect to the baselines. The time delay τ_{XY} can be obtained by cross correlating two signals f_X and f_Y arriving at antennas X and Y , respectively:

$$(f_X \star f_Y)(\tau) = \int f_X^*(t) f_Y(t + \tau) dt \quad (5.6)$$

where $*$ denotes the complex conjugate, and t denotes time. Note that $(f_X \star f_Y)$ is a function of τ , and for each τ the integral is taken over all possible values t . The cross correlation will be a maximum when f_Y and f_X are aligned in time after shifting f_Y by a time delay $\tau = \tau_{XY}$. When the two signals are not aligned in time, the cross correlation will be less than the maximum value. Thus, τ_{XY} is determined by finding the τ at which $(f_X \star f_Y)$ is maximum.

For a baseline XY , with length d_{XY} and azimuthal orientation Az_{XY} , the time delay can be related to the cosine plane coordinates, $(\cos\alpha, \cos\beta) = (\ell, m)$, using the relation (Stock, 2014)

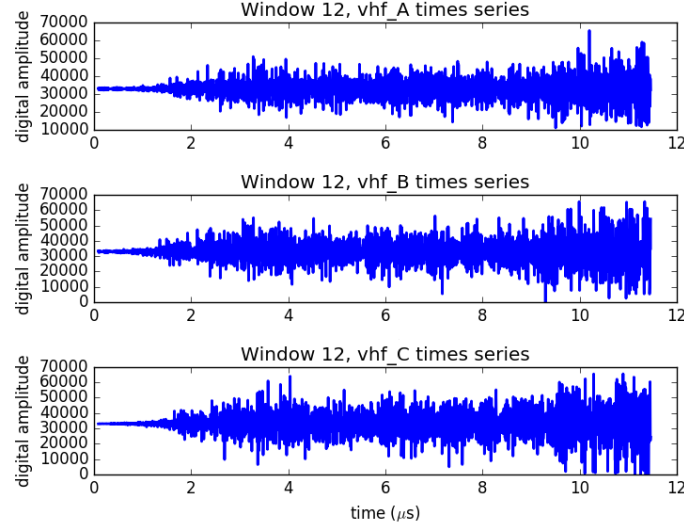
$$\tau_{XY,\ell m} = \frac{d_{XY}}{c} (\ell \sin Az_{XY} + m \cos Az_{XY}) \quad (5.7)$$

which is simply a consequence of the geometry. Put into words, equation (5.7) says that each location (ℓ, m) in the cosine plane represents a time delay $\tau_{XY,\ell m}$ with respect to baseline XY .

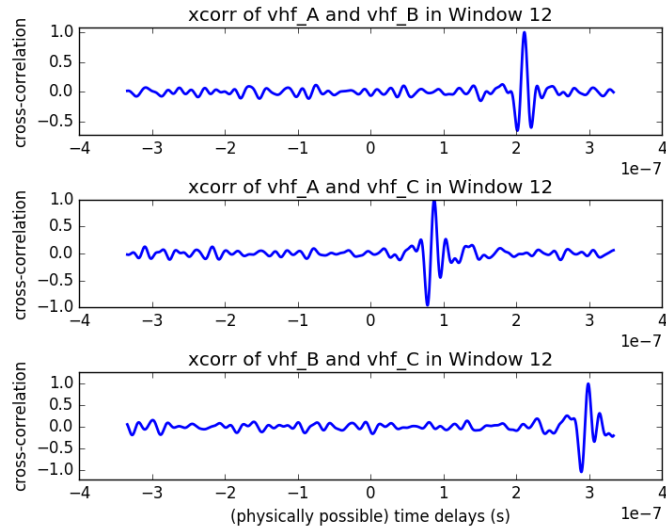
Figure 5.8a illustrates three time-domain VHF signals arriving at antennas A , B , and C from the onset of a NBE. By eye, a slight temporal offset can be seen between the three similar (but not completely identical) signals. Figure 5.8b shows the cross correlations of every two signals in Figure 5.8a. The peak in each cross correlation occurs at the most probable time delay between each of the two corresponding signals in Figure 5.8a.

TDOA mapping uses the time delay at the peak of each cross correlation to map a source into the cosine plane using equation (5.7), similar to what is shown in Figure 5.6a. Alternatively, we

can make images based on the innovative algorithm of Stock 2014 (Stock & Krehbiel, 2014; Stock, 2014), which uses the full cross-correlation functions to produce the images directly in the cosine plane (Stock & Krehbiel, 2014; Stock, 2014). That is, we use equation (5.7) to map each cross



(a)



(b)

Figure 5.8: INTF waveforms. (a) Time domain VHF signals recorded by antennas A, B, and C during the first $12 \mu\text{s}$ of a narrow bipolar event (NBE). (b) Cross correlations of every two signals in (a), showing a peak at the most probable time offset between any two signals.

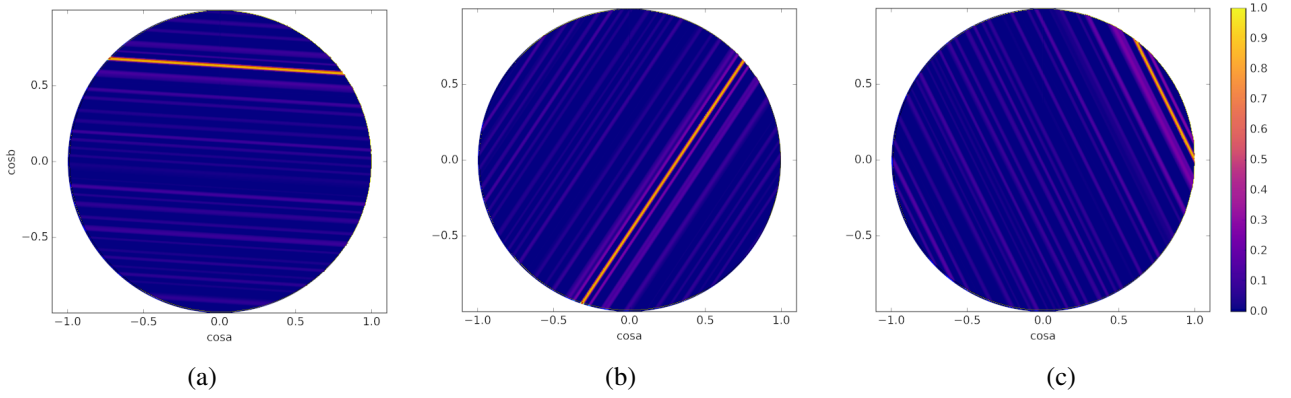


Figure 5.9: Cross correlations from each baseline projected into cosine plane. The cross correlations projected into the cosine plane correspond to baseline: (a) AB , (b) AC , and (c) BC .

correlation “waveform” into the cosine plane, so that each pixel (ℓ, m) in the plane has associated with it an amplitude $(f_A \star f_B)(\tau_{AB,\ell m}) + (f_A \star f_C)(\tau_{AC,\ell m}) + (f_B \star f_C)(\tau_{BC,\ell m})$. As an illustration, the cross correlation from each baseline is mapped into the cosine plane in Figure 5.9. To construct a radio image of the sky, the three cross-correlations are added together in the cosine plane, as shown in Figure 5.10a. Alternatively, the sky can be mapped in azimuth (Az) and elevation ($E\ell$) via a transformation from the cosine plane:

$$Az = \tan^{-1}(\cos \beta / \cos \alpha) \quad (5.8)$$

$$E\ell = \cos^{-1}(\cos \beta^2 + \cos \alpha^2) \quad (5.9)$$

as shown in Figure 5.10b.

We use the “centroid” or weighted center of the image to represent the source location, and map the centroids from successive (but slightly overlapping) processing windows to show the development of a breakdown event in time. An example of mapping a full-fledged intra-cloud lightning flash that lasts for $\simeq 400$ ms is shown in Figure 5.11, where each marker represents the centroid from one $1.4\text{-}\mu\text{s}$ exposure image. If the sources being imaged are localized, then the centroid will represent the source’s location reasonably well (see Section 5.4 and 8.7). However, for multiple sources occurring in the same processing window, or for extended sources, the centroid

becomes the average location of the sources. The advantage of imaging in addition to mapping is that we obtain additional information about the emitting source (e.g., Section 8.4).

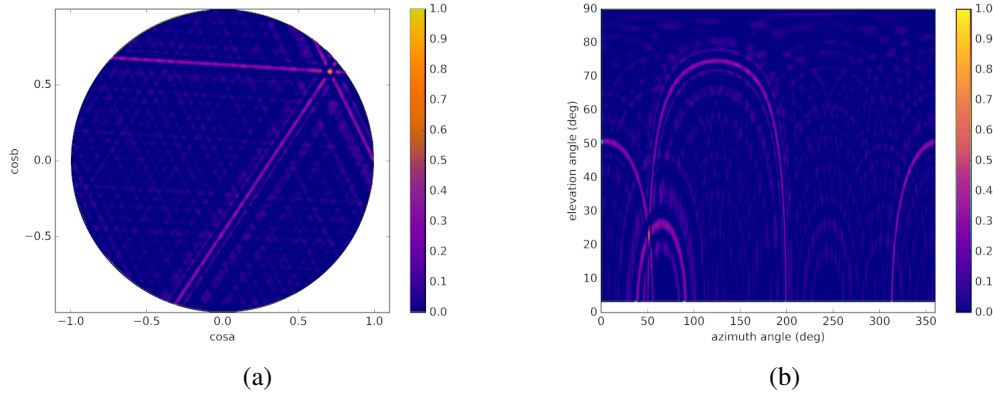


Figure 5.10: Cross correlations from all three baselines projected into cosine plane and azimuth-elevation projection. (a) The cross correlations (radio image) of the NBE source is projected into the cosine plane. (b) The same image as in (a), but projected into azimuth-elevation.

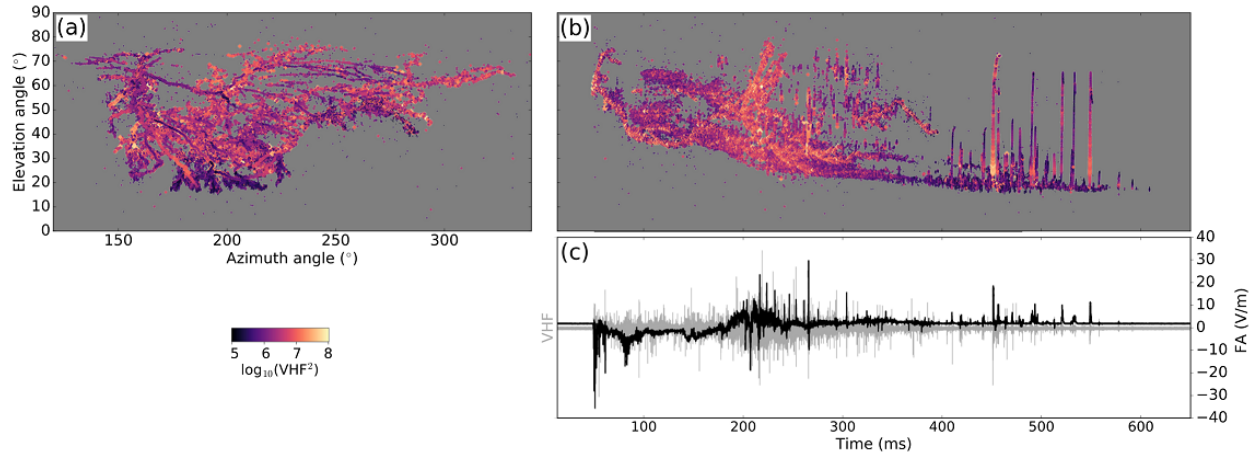


Figure 5.11: Interferometer mapping example. Centroids from successive $1.4 \mu\text{s}$ -exposure radio images (with a $0.35 \mu\text{s}$ shift between images) are colored by received VHF power and are plotted in (a) azimuth and elevation, showing the spatial structure of the flash, and (b) elevation versus time, showing the (roughly) vertical growth of the flash over time. (c) The original received VHF signal is shown in gray, and the signal from a synchronously-digitized fast electric field antenna is shown in black.

5.4 Image simulations

The intensity pattern of an ideal point source is called the point spread function (PSF) (Taylor *et al.*, 1999; Stock, 2014) of the INTF, and depends on INTF specifications such as bandwidth, and baseline lengths and orientations. The PSF is characterized by a bright main lobe, with an angular size that indicates the resolution of the INTF, and lower-intensity side lobes, as shown in Figure 5.12a,b. Note that the $1.4\text{-}\mu\text{s}$ exposure image taken near the beginning of a NBE (Figure 5.10) closely resembles the image of a point source (albeit in a different location in the sky), indicating that the emitting NBE source is fairly localized within the resolution of the INTF.

The PSF is the instrument response to an ideal point source. In an ideal case, a delta-function-like point source in time would have a flat (constant) Fourier transform in the frequency domain. Therefore, in order to generate the INTF PSF, we can start in the frequency domain by setting the amplitude to a constant (say, 1) for all frequencies in the INTF bandwidth. Figure 5.13a shows a 20-80 MHz band-limited PSF signal for all three INTF antennas in the frequency domain. Transforming these signals into the time domain produces a sharply-peaked simulated signal in all three antennas with zero time delay (Figure 5.13b). By performing the cross correlations of all three

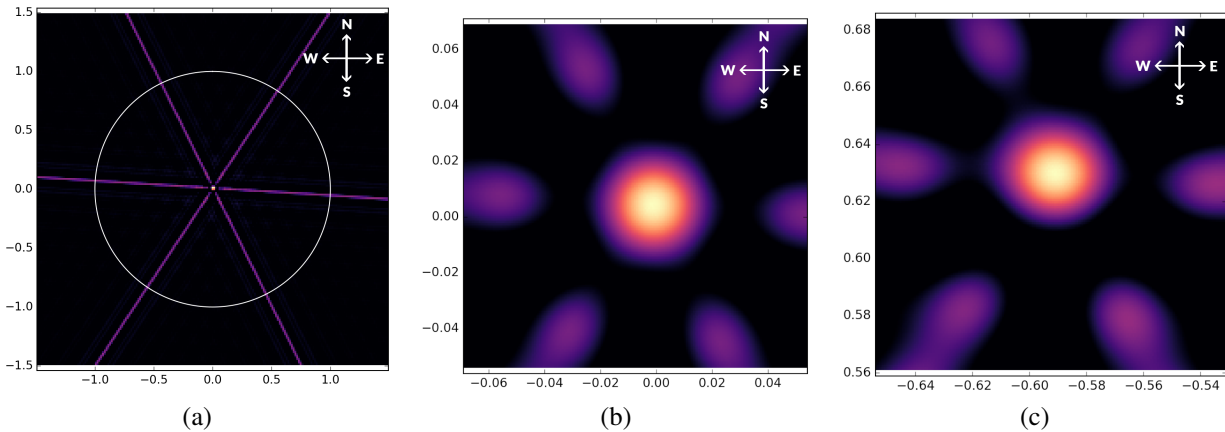


Figure 5.12: INTF point spread function (PSF) and comparison to real lightning source. (a) PSF imaged in the cosine plane. (b) Close-in view of PSF main lobe. (c) Close-in view of real source in a thunderstorm, which is similar to the PSF but shows a slightly different morphology.

signals and projecting them into the cosine plane (Section 5.3), we get the PSF, which is the ideal image of a point source, located at the zenith, or phase center, of the image (Figure 5.12a). The central bright node where the peak in the three cross correlations intersect in the cosine plane is called the main lobe. The size of the main lobe reflects the width of the main cross-correlation peak, with the side lobes corresponding to subsidiary, periodic peaks, oriented according to the baseline directions. A close-in view in Figure 5.12b shows that the main lobe intensity is roughly a two-dimensional Gaussian distribution. Comparing to the main lobe of a real lightning source (Figure 5.12c), there are slight differences in the main lobe morphology that we can exploit for better understanding the source geometry (e.g., Section 8.7).

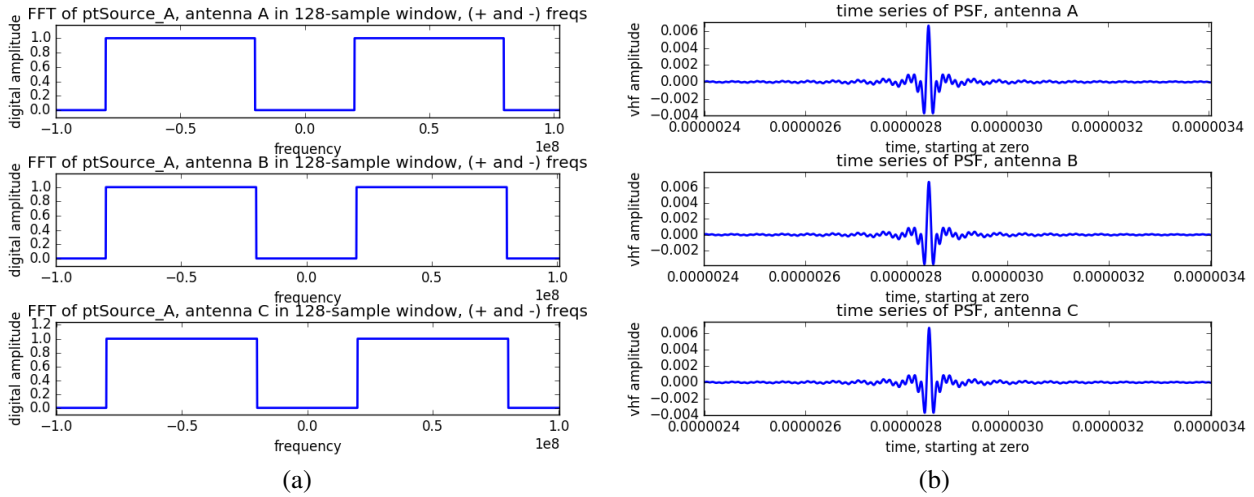


Figure 5.13: INTF point spread function (PSF) frequency domain and time domain signals. (a) Simulated frequency-domain INTF signals contributing to PSF (band-limited to 20-80 MHz). (b) Simulated time-domain INTF signals contributing to PSF.

A point source can be simulated anywhere in the sky by time shifting the time-domain PSF signals (e.g., the waveforms in Figure 5.12b) by the correct amounts (i.e., according to equation 5.7). Moreover, two (or more) point sources at different locations in the sky can be simulated within the same image by creating the two (or more) time-domain signals, and simply adding them together (electric fields obey superposition) before cross-correlating. An example is shown in Figure 5.14, for two point sources separated by various degrees in elevation.

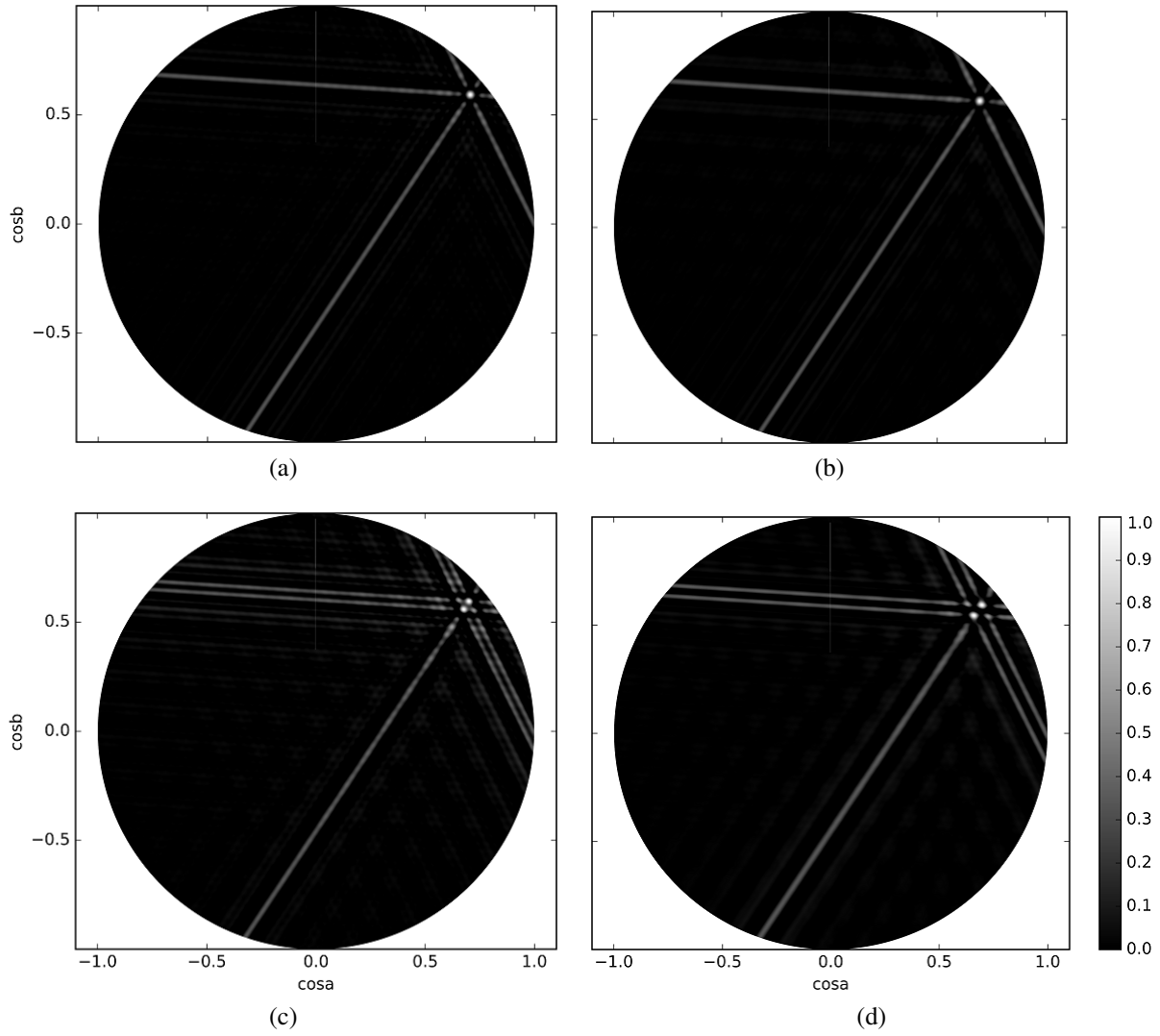


Figure 5.14: INTF images of two simulated point sources at various degrees separation in elevation. Two point sources are located near the horizon, and are separated by elevations of (a) 0° , (b) 3° , (c) 6° , and (d) 9° .

CHAPTER 6

FAST ELECTRIC FIELD ANTENNA

6.1 Hardware

As described in Section 5.1, a flat metal plate can be used as the sensing element in an electric field sensor. Moreover, a flat plate provides a geometry for readily determining quantitatively the ambient vertical electric field, E_z , above and normal to the plate. An instrument for detecting dE_z/dt was presented in Figure 5.3. However, for fitting parameters in physical models (e.g., see Section 6.2), often we are not after the instantaneous dE_z/dt , but instead want to measure the change ΔE_z over some time. The starting point for the ΔE_z sensor is the dE_z/dt sensor, but with a capacitor C connected across the op-amp in an inverting op-amp circuit as shown in Figure 6.1a. With a time-varying input signal V_{in} , a voltage V_{out} is induced “across” C . That is:

$$C \frac{dV_{out}}{dt} = \frac{dQ}{dt} = I_C \quad (6.1)$$

For a large R_{out} , the circuit in Figure 6.1a becomes an integrating circuit with $I_{out} = -I_C$. Equating I_{out} in equation (5.2) with $-I_C$ in equation (6.1) gives:

$$A\epsilon_0 \frac{dE_z}{dt} = -C \frac{dV_{out}}{dt} \rightarrow \int_{E_z(t_1)}^{E(t_2)} dE_z(t) = -\frac{C}{A\epsilon_0} \int_{V_{out}(t_1)}^{V_{out}(t_2)} dV_{out}(t) \quad (6.2)$$

The right-hand side of equation (6.2) gives the desired change in electric field over some time interval, $\Delta t = t_2 - t_1$. Note that Figure 6.1a is an RC circuit, so that V_{out} decays by a factor of e after a decay time $\tau_{decay} = R_{out}C$. The signal of interest must be short enough in duration so

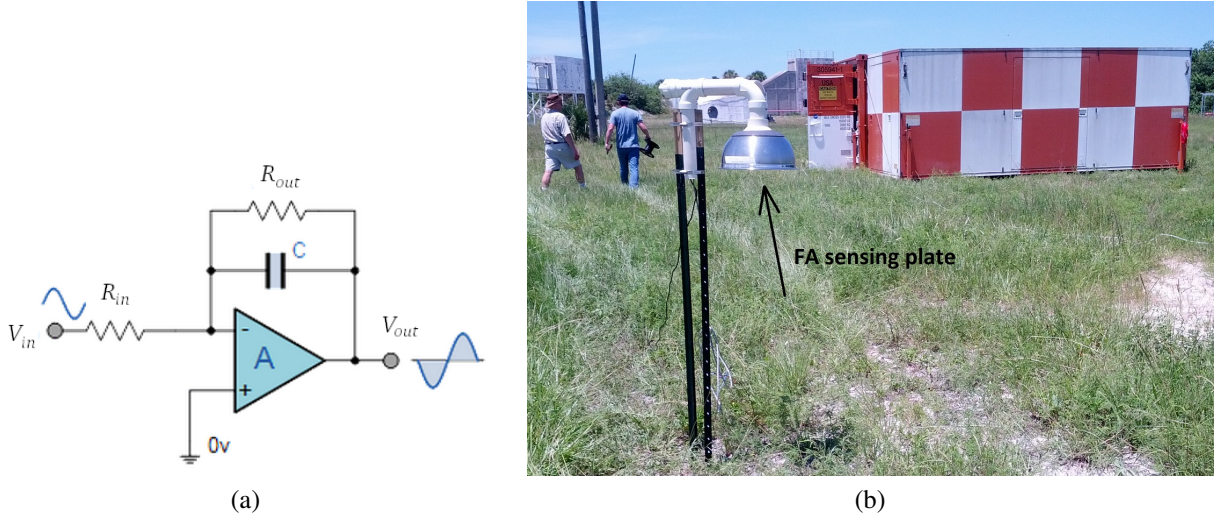


Figure 6.1: Electric field change sensor. (a) An integrating op-amp circuit with time constant $R_{out}C$ effectively integrates a time-varying input signal, V_{in} , giving an output signal V_{out} . (b) The fast antenna (FA) used in the Florida studies herein is shown at the INTF site. The sensing plate is exposed to the ground, and shielded from rain by a salad bowl, which also holds electronics to amplify the signal. Coaxial cables run the amplified FA signal out the top of the salad bowl via PVC piping and to the data acquisition building (orange-white checkered building in the background), where the signal is additionally amplified, then digitized and stored.

that the decay of the output voltage is negligible, i.e., we want $\Delta t \ll \tau_{decay}$. In addition, we want that τ_{decay} is not too long, or else the desired signal might saturate. We must choose R_{out} and C so that ΔE is measured on timescales of interest. For “faster” processes, such as NBEs, we want that $\tau_{decay} \approx$ milliseconds, and this type of sensor is colloquially called a “fast antenna” (FA). To record “slower” processes, such as a leader coming to ground, we make $\tau_{decay} \approx$ seconds. This type of sensor is colloquially called a “slow antenna,” and doesn’t require as fast a digitizer.

The resulting output of a fast or slow antenna is

$$\Delta V_{out} = \frac{A\epsilon_0}{C} \Delta E_z \quad (6.3)$$

so that the change in vertical electric field is proportional to the change in output voltage.

The FA used in the Florida studies herein had a decay time constant of $100 \mu s$. The FA is shown in Figure 6.1b. The exposed plate area is actually facing downward, and is shielded from

falling rain by a “salad bowl,” which also houses signal amplifiers. The shielding is necessary so that rain doesn’t add additional unwanted signal to the electric field contribution. In contrast, a rain signal doesn’t greatly effect the output from the dE_z/dt (i.e., VHF) INTF sensors, because the rain signal varies on too slow a timescale. Thus, the VHF sensor can be exposed to the sky. In order to adequately sample the change in vertical electric field, however, the FA sensing plate must be raised high enough above the ground so that the electric field lines can bend around the instrument without being too perturbed by objects near the ground.

6.2 Electric field due to vertical radiating antenna

Many lightning processes, such as NBEs (Section 2.4), can be approximated as a vertical radiating antenna positioned above a grounded conducting plane, i.e., the Earth, as described in (Uman, 2001), pp. 134-137. The general expression for the vertical electric field as measured on the ground ($z = 0$) a radial distance r from the antenna, at time t , can be written (Uman, 2001):

$$E_z(r, \phi, z = 0, t) = \frac{1}{2\pi\epsilon_0} \left[\int_{H_B}^{H_T} \frac{2z' - r^2}{R^5} \int_0^t i\left(z', t' - \frac{R}{c}\right) dt' dz' \right. \\ \left. + \int_{H_B}^{H_T} \frac{2z'^2 - r^2}{cR^4} i\left(z', t - \frac{R}{c}\right) dz' \right. \\ \left. - \int_{H_B}^{H_T} \frac{r^2}{c^2 R^3} \frac{\partial}{\partial t} i\left(z', t - \frac{R}{c}\right) dz' \right] \quad (6.4)$$

where $R = \sqrt{z'^2 + r^2}$ is the distance to the observer from the infinitesimal current segment $i(z', t)$ at height $z' = z'(t)$ along the channel at time t . The situation is shown schematically in Figure 6.2. Three field terms contribute to E_z , with one term shown per line in equation 6.4. The top term is called the electrostatic field (integrating i over time and space gives the total charge involved) and is proportional to $1/R^5$, the middle term is the induction field and is proportional to $1/R^4$, and the bottom term is the radiation field and is proportional to $1/R^3$. Note that the radiation field is aptly named – if the measurement is made far from the radiating source (i.e., $r \gg 1$, so that $R \approx r$), then the

electrostatic and induction terms fall away faster than the radiation term, which is approximately proportional to $1/R$. At large radial distances the radiation term dominates the measured signal.

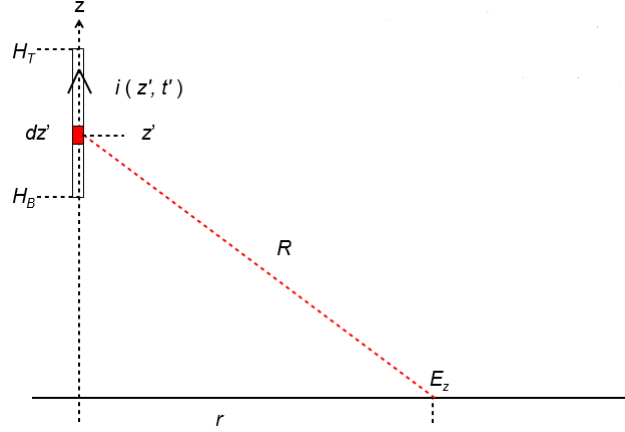


Figure 6.2: Vertical radiating antenna geometry used in equation 6.4. A vertical radiating antenna extends from altitude H_B to H_T , a radial distance, r , from an observation point on the ground ($z'=0$) where the vertical electric field, E_z , is sampled. A current waveform, i , travels vertically along the antenna. The current amplitude along the antenna at time t' and height z' (also slant range, R , with respect to the observation point) is given by $i(z', t')$.

If we also know the plan distance (r) and extent (z) of a vertically-oriented discharge (e.g., a NBE), then we can model the sferic by trying different values of $i(z', t - \frac{R}{c})$ in equation (6.4) until the simulated waveform matches the observed one. From this exercise we can obtain an estimate of peak current, total charge involved in the discharge, and current-rise e -folding time (Rison *et al.*, 2016). Plan distance to an event is readily obtained from three-dimensional VHF mapping using a lightning mapping array (LMA) (see Section 7), while vertical extent can be determined by combining LMA plan distance with the source elevation obtained using the INTF (Section 5).

Alternatively, if a discharge is far away ($r \gg 1$), then the measured FA signal is dominated by the radiation term, which is proportional to the time derivative of the current moment: dM_i/dt . Thus, if we know the radial distance, r , and height, $z'(t)$, of the discharge, then we can simply integrate the measured FA signal in time (and multiply by some factors out front) to obtain the current-moment, $M_i = \int i(z') dz'$ (da Silva & Pasko, 2015). In addition, we can integrate the FA signal a second time (and multiply by some factors out front) to obtain the charge-moment change, $M_Q = \int q(z') dz'$, where q is the charge involved in the field generation.

CHAPTER 7

LIGHTNING MAPPING ARRAY

7.1 Hardware and processing

The Lightning Mapping Array (LMA) (Rison *et al.*, 1999; Thomas *et al.*, 2004) is a time-of-arrival (TOA) system that determines the three-dimensional location and time of impulsive lightning events every $80\text{-}\mu\text{s}$. The array is composed of ≥ 6 “stations,” and each station has a narrow-band VHF antenna (60-66 MHz) as the sensing dE_z/dt element, a 25 MHz digitizer, a hard drive, and a GPS antenna for station location and clock synchronization. Figure 7.1 shows a LMA station at Kennedy Space Center (KSC). In 2016 and 2017, during the INTF deployment at KSC, seven LMA stations were situated within the confines of KSC and Cape Canaveral Air Force Station (Figure 4.1a), and three outlying stations were located 60–100 km inland and southward along the Florida coast to provide a wide coverage area.

At each LMA station, if the signal goes above a threshold value, then the peak signal in a $80\text{ }\mu\text{s}$ window is recorded. The threshold value is set at each station so that in the absence of lightning, only about 100-1000 values are recorded per second, which generally throws out signals due to background noise (i.e., due to power lines, radios, etc.), and also nearby but small discharges from objects on the ground when a thunderstorm is overhead (Thomas *et al.*, 2004). This allows for up to 12,500 events to be detected per second for a $80\text{ }\mu\text{s}$ system.

The LMA data is then post-processed once collected from all of the (GPS time-synchronized) LMA stations in the array, solving for the latitude, longitude, altitude, and time (i.e., x, y, z, t) of a radiating source with 40-ns temporal resolution (the time resolution of the digitizer) in each $80\text{ }\mu\text{s}$ window. It is assumed that the VHF-emitting events are impulsive and can be treated as



Figure 7.1: Lightning mapping array (LMA) station at Kennedy Space Center (KSC). The sensing element is the vertical antenna protruding from the ground plane (three downward-sloping elements). The LMA electronics (e.g., digitizer and hard drive) are located in the tan metal box, and are powered by the solar panel.

isotropically emitting point sources. The three spatial coordinates and time of the emitting source are then related by:

$$c(t_i - t) = \sqrt{(x_i - x)^2 + (y_i - y)^2 + (z_i - z)^2} \quad (7.1)$$

where c is the speed of light, (x_i, y_i, z_i) denotes the latitude, longitude, and altitude of the i^{th} station, respectively, and t_i is the time when the signal reaches the i^{th} station. The quantities in equation 7.1 are depicted schematically in Figure 7.2.

In practice, lightning radiates many VHF pulses closely-spaced in time, and so the solutions (x, y, z, t) will not be unique. Thus, the method for determining the location and timing of VHF sources is non-deterministic, and instead employs the (nonlinear inverse) Levenberg-Marquardt method (Thomas *et al.*, 2004; Aster *et al.*, 2013; Tilles, 2015) to obtain a best-fit solution of

the timing, t , between the LMA stations in each $80 \mu s$ window. With each solution comes a goodness-of-fit value, or reduced chi-square value, χ_ν^2 – the lower the value of χ_ν^2 , the better the timing agreement between the involved LMA stations, and the more reliable the solution (i.e., VHF source) timing and location.

Moreover, once a source location is determined in post-processing, the received power at an individual LMA station (i.e, the peak voltage value recorded in the $80 \mu s$ window) can be used to estimate the peak power radiated by the source in the 60-66 MHz passband (Thomas *et al.*, 2001, 2004).

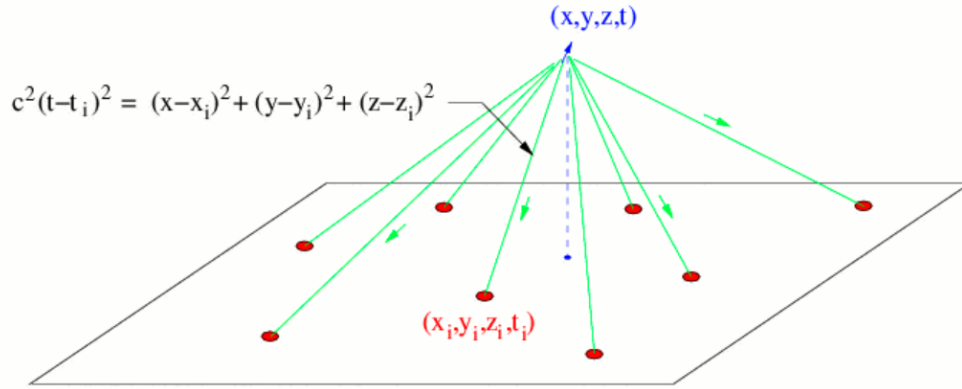


Figure 7.2: Lightning mapping array (LMA) geometry. The schematic depicts the LMA stations (red dots) on the ground with respect to a radio source located at (x, y, z) and emitting at time t . The radio signal is received at the i^{th} station, with fixed location (x_i, y_i, z_i) , at a later time t_i . The slant range from the radio source to the i^{th} station is given by $c^2(t - t_i)^2$. Credit: New Mexico Tech / Langmuir Laboratory for Atmospheric Research.

7.2 Data analysis

LMA data provides information about the overall structure and development of lightning storms and individual flashes, but also provides good estimates of the 3-D locations and VHF source powers of specific fast events (e.g., NBEs, EIPs, IBPs). Examples of the mapped LMA data are shown in Figures 7.3-7.6, displaying the lightning activity for a ten-minute interval, a single intra-cloud lightning flash, a cloud-to-ground flash in Florida, respectively. In each figure, the data is plotted in three different ways, colored first as a function of time, second as a function of radiated power,

and third as a function of thundercloud charge. Determining the thundercloud charge sign must be done manually (Hamlin, 2004; Marshall *et al.*, 2005; Krehbiel *et al.*, 2008; Tilles, 2015), and takes into account the morphology of each lightning flash in a storm. For instance, negative leaders are generally composed of more sources and have brighter VHF emissions compared to positive leaders, which tend to have fewer sources and lower powers, but are also more filamentary (e.g., see the plan displays in Figures 7.4c and 7.5c). By assuming that negative leaders (red) propagate through positive storm charge, and assuming that positive leaders (blue) propagate through negative storm charge, we can obtain an idea of a thundercloud’s charge structure (e.g., Figure 7.3c). Note that not all regions of the flash are assumed to propagate through charge. For instance, near the flash origin or close to the ground, the thundercloud charge is “undetermined,” either because the region is assumed largely neutral or because there is no thundercloud there!

In addition, the LMA is particularly useful for identifying NBEs (Section 2.4), which can then be more finely-resolved with the INTF. Figure 7.6 shows the detailed LMA observations for two NBEs (NBEs “1” and “2”, given in more detail in Section 8). The sources are sized and colored by the logarithmic source power, with the large yellow/orange sources corresponding to the two NBEs. Despite the relatively high peak power of the NBEs (50.2 and 40.6 dBW, or 105 and 12 kW, respectively), their ensuing breakdown lasted only $\simeq 2\text{--}3$ ms, and did not initiate full flashes. Note that both NBEs were substantially mis-located in altitude and/or plan location compared with the subsequent lower power activity, which were presumably in close proximity. Mis-location is a typical feature of high-power NBEs, and is due to the VHF radiation caused by fast breakdown being continually noisy around the time of the peak, with different mapping stations detecting slightly different peaks (Rison *et al.*, 2016). The mis-locations are consistent with the χ^2_ν goodness-of-fit values being relatively large ($\chi^2_\nu=4.67$ and $=2.13$, respectively) compared to the subsequent sources ($\chi^2_\nu\sim 0.1$), as seen in the numerical listings of Figure 7.6. Mis-locations and high χ^2_ν values, coupled with relatively high source powers, turn out to be useful features for identifying fast breakdown in LMA data.

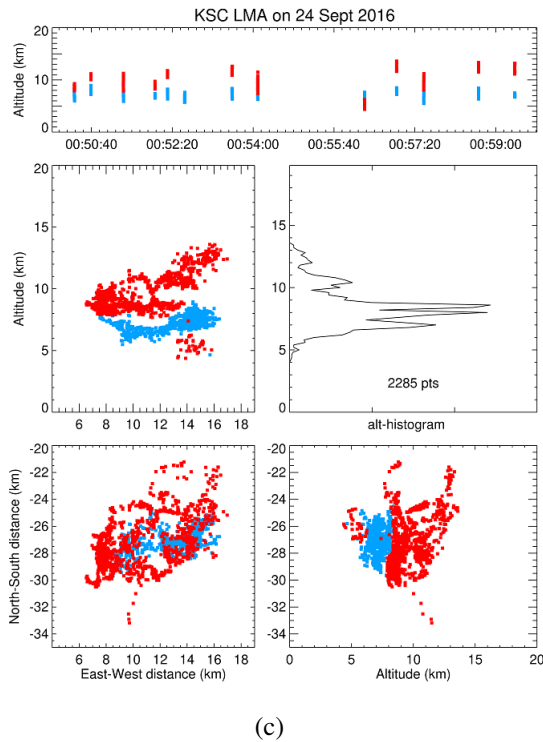
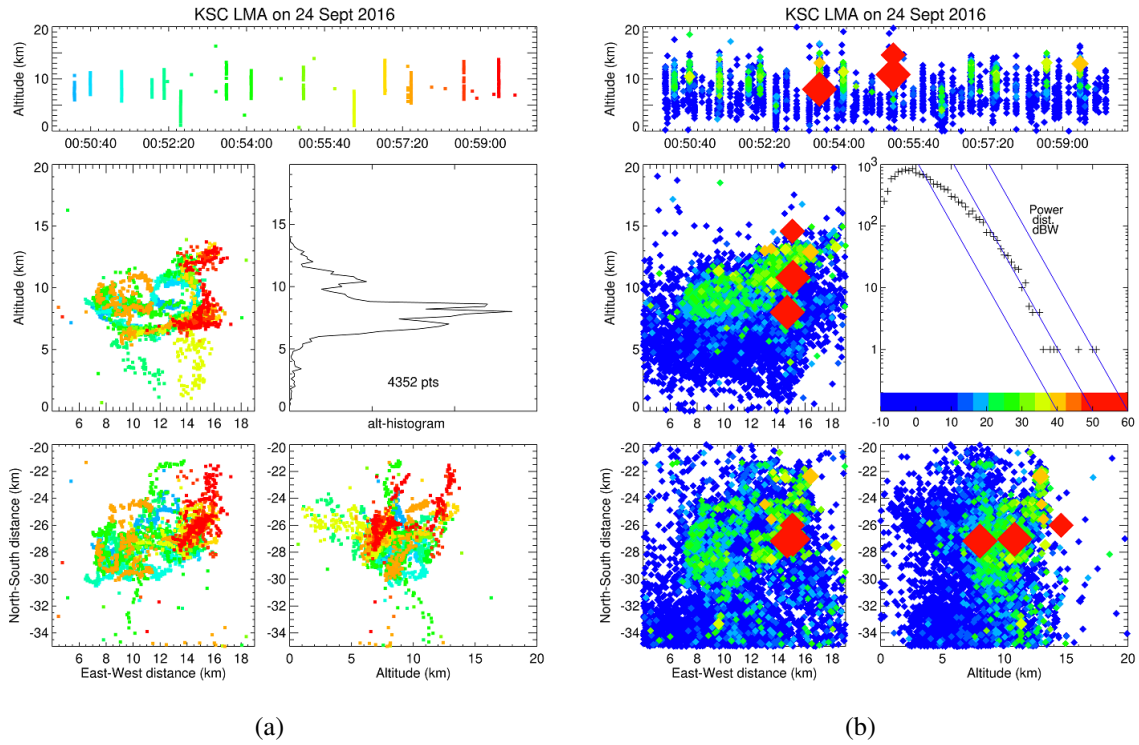


Figure 7.3: Ten minutes of LMA data. LMA sources are (a) colored by time (sources with $\chi^2_\nu < 1$ are plotted), (b) colored and sized by the log of the emitted VHF power (sources with $\chi^2_\nu < 5$ are plotted, which shows the NBEs – large red diamonds – in the storm), and (d) colored by thundercloud charge, with red for positive charge and blue for negative charge (sources with $\chi^2_\nu < 1$ are plotted).

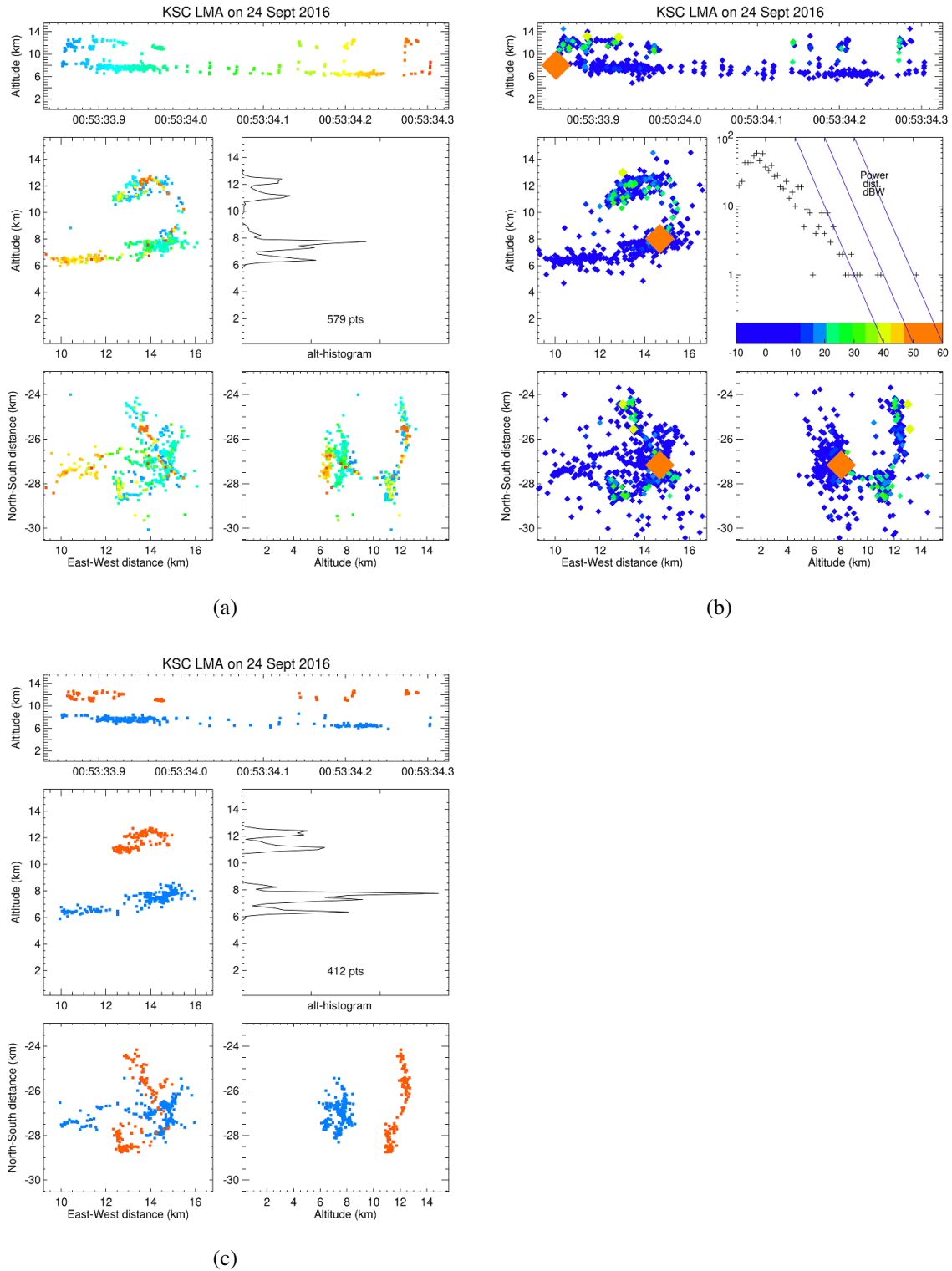


Figure 7.4: LMA data for an intra-cloud lightning flash. LMA sources are (a) colored by time (sources with $\chi^2_\nu < 1$ are plotted), (b) colored and sized by the log of the emitted VHF power (sources with $\chi^2_\nu < 5$ are plotted, which shows a NBE – large orange diamond – at the beginning of the flash), and (d) colored by thundercloud charge, with red for positive charge and blue for negative charge (sources with $\chi^2_\nu < 1$ are plotted).

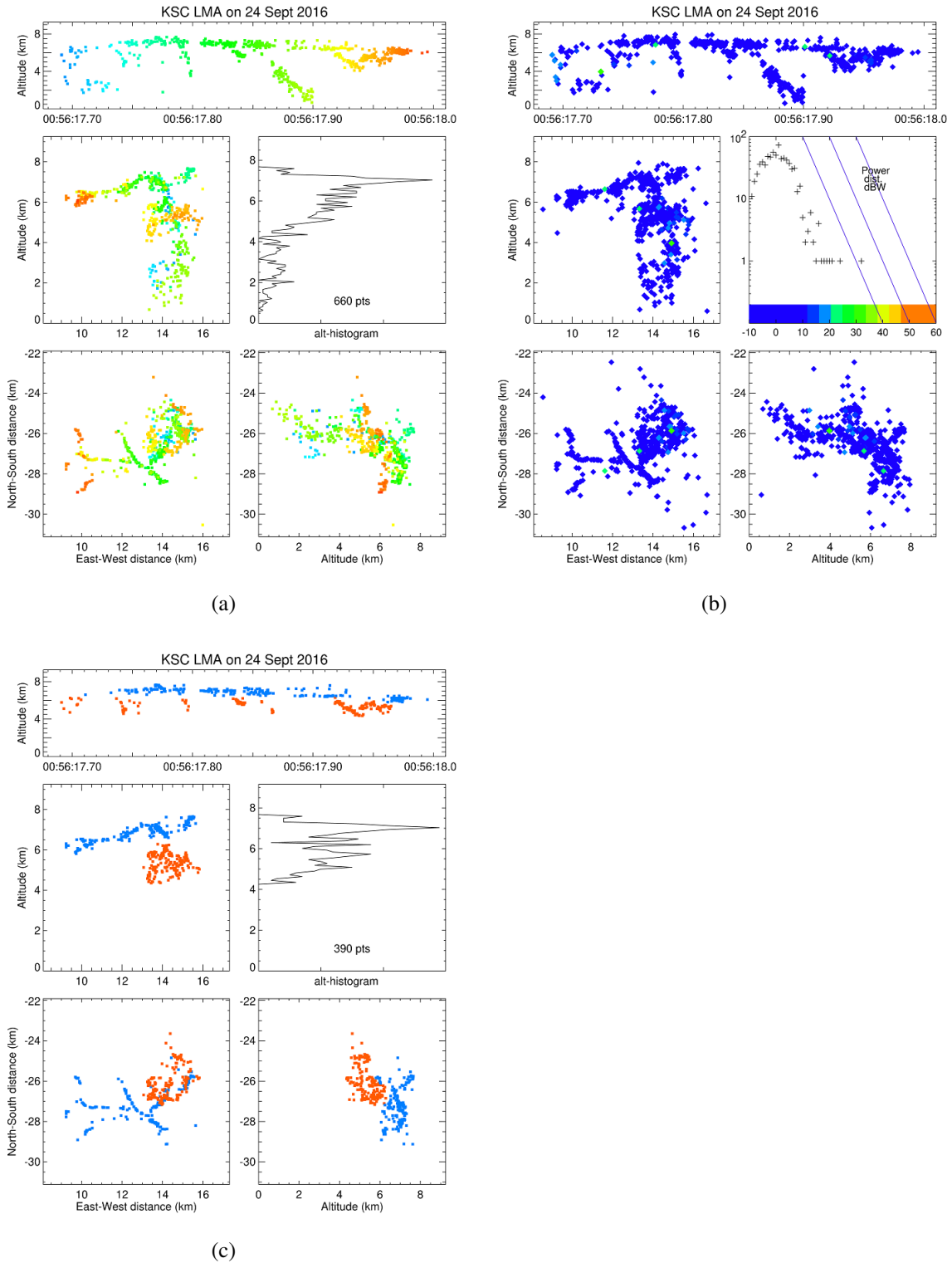


Figure 7.5: LMA data for a cloud-to-ground lightning flash. LMA sources are (a) colored by time (sources with $\chi^2_\nu < 1$ are plotted), (b) colored and sized by the log of the emitted VHF power (sources with $\chi^2_\nu < 5$ are plotted), and (d) colored by thundercloud charge, with red for positive charge and blue for negative charge (sources with $\chi^2_\nu < 1$ are plotted).

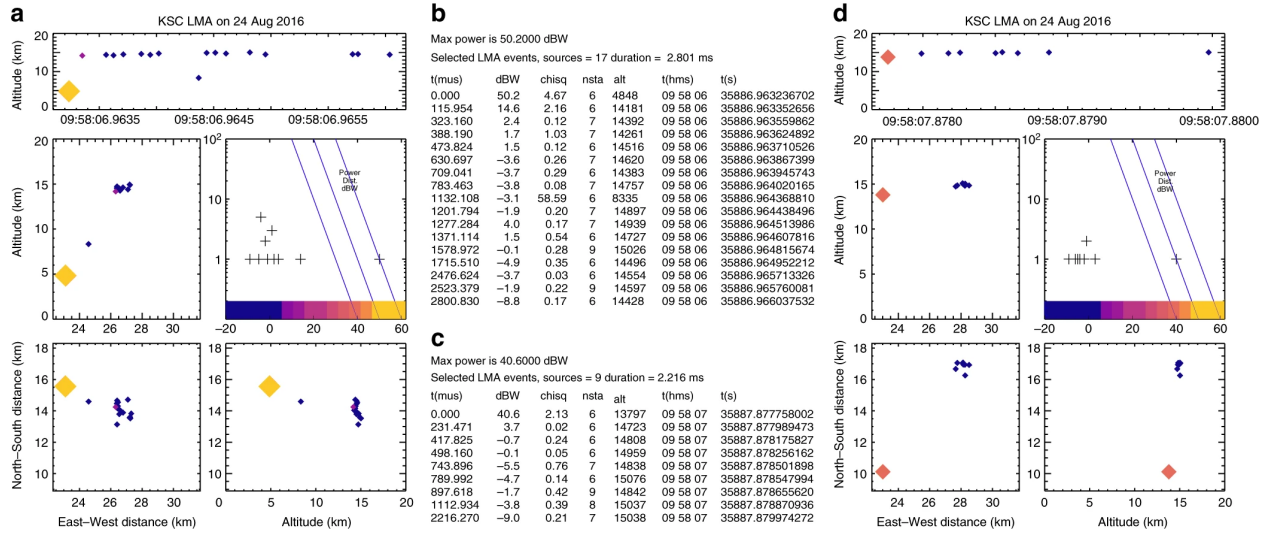


Figure 7.6: Detailed lightning mapping data for two NBEs (NBEs 1 and 2 in Section 8). (a,d) LMA maps of the complete activity for each NBE, showing how the NBEs are mis-located relative to the subsequent, lower-power activity, and how the subsequent activity more accurately indicates the NBE's actual location. (b,c) Numerical listings of the source times, power (dBW units), goodness-of-fit χ^2_ν (chisq) value, and number of stations (nsta) participating in the solutions.

Part III

Results

CHAPTER 8

FAST NEGATIVE BREAKDOWN

8.1 Overview

Here we report observations of electrical breakdown in thunderstorms that starts with negative polarity discharges, in contrast to the fast positive breakdown observed by Rison *et al.* (2016) in association with narrow bipolar events (NBEs). In 2016 and 2017, as a follow-up study, we deployed an improved version of the broadband VHF radio interferometer used by Rison *et al.* (2016) to Kennedy Space Center in Florida. The Florida storms were found to be prolific generators (Tilles *et al.*, 2016) of high-power 30-50 dBW (1-100 kW) narrow bipolar events (NBEs), some of which were caused by fast breakdown that propagated in the opposite direction of similarly-located fast positive events, which were downward-directed. In both cases, and in a number of different storms, the discharges in question occurred between the mid-level negative and upper positive charge regions of the storms (e.g., Figure 8.1), typical of intra-cloud lightning. Thus, upward development would be indicative of negative-polarity breakdown. Because this conflicts with the prevailing view that lightning starts with positive breakdown, and because the non-imaging centroid technique used in previous studies (Rison *et al.*, 2016) cannot rule out the possibility that the propagation is an apparent effect due to a succession of downward positive events starting retrogressively at higher altitudes, we present a combination of radio imaging and centroid analyses to confirm that fast negative breakdown is dominated by a propagating localized source, thereby showing that breakdown can begin with negative as well as positive polarity. This finding challenges the current understanding of dielectric breakdown of air.

8.2 Fast breakdown events in an NBE-prolific thunderstorm

The observations were obtained at Kennedy Space Center, Florida from a 2016 August 24 thunderstorm located offshore. The observations include three-dimensional lightning mapping array (LMA) data (Rison *et al.*, 1999; Thomas *et al.*, 2004) from the 10-station Kennedy Space Center Lightning Mapping Array (KSCLMA), VHF waveforms recorded by the New Mexico Tech Broadband Interferometer (Stock *et al.*, 2014) (INTF), and waveforms recorded by a flat-plate Fast Antenna (FA) that measured the change in vertical electric field at the ground with a $100\ \mu\text{s}$ decay constant.

Figure 8.1 shows an overview of the LMA observations for the 24 August storm and the events of interest. Figure 8.1a shows the full duration of the source altitudes versus UT time, with LMA sources coloured according to time. A ten-minute period of the storm (black bracket in Figure 8.1a) is expanded in Figure 8.1b,d-f, where the LMA sources are coloured according to the polarity of the lightning discharge events, with red sources indicating positive storm charge, and blue sources indicating negative storm charge (Hamlin, 2004; Marshall *et al.*, 2005; Krehbiel *et al.*, 2008). High-power NBEs are colored in black, and typically occurred below the upper positive charge region on the upwind side of the storm. This ten-minute period is marked by an increase in flash rate (from about 1 to 5 fully-developed flashes min^{-1}) and flash initiation altitude (from about 8-10 to 10-15 km above mean sea level (MSL)), as well as an increase in isolated NBE occurrence (from about 1 to 15 min^{-1}) at the flash initiation altitudes. Such high NBE initiating altitudes are not unusual for Florida storms (Nag *et al.*, 2010; Jacobson & Heavner, 2005), but the NBE occurrence rate is exceptional and is in stark contrast to previous studies (Suszcynsky & Heavner, 2003).

One especially high-rate NBE period (~ 40 NBEs within one minute) lasted from 09:58 to 09:59 UT, during which NBEs tended to cluster in space and time (e.g., Stanley 2018 (Stanley *et al.*, 2018a)). A cluster of ten isolated NBEs that took place between the main negative and upper positive charge regions in the normal-polarity storm (Krehbiel, 1986) is indicated by a black bracket in Figure 8.1b, and is shown expanded in Figure 8.1c, where the LMA sources are sized

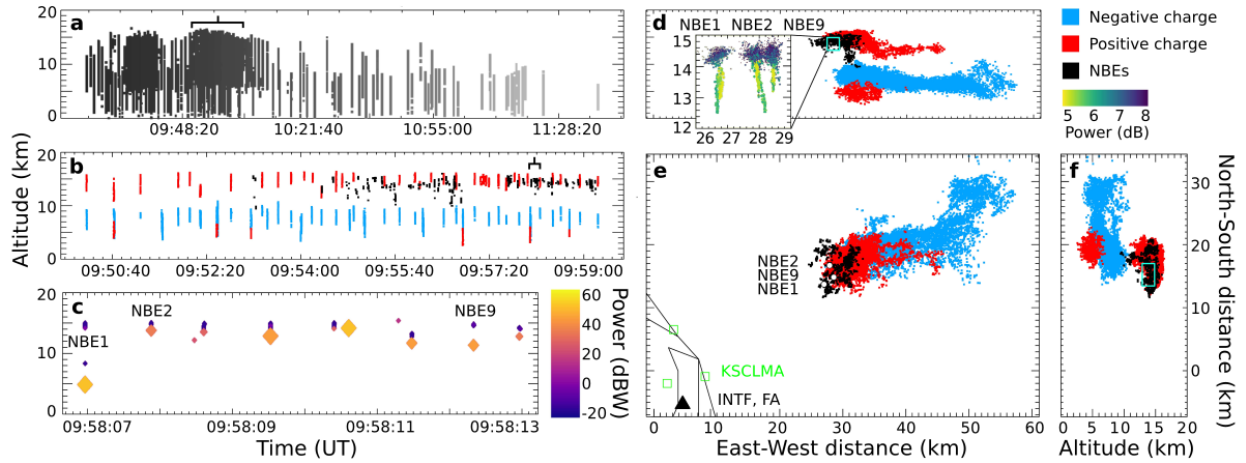


Figure 8.1: Lightning mapping observations of storm producing narrow bipolar events. VHF Lightning Mapping Array data from the Kennedy Space Center LMA for the 24 August 2016 storm. (a) Overview of the height-time evolution of the three-hour storm, (b) 10 minutes of enhanced activity during the bracketed interval of (a), coloured by the lightning-inferred polarity of the storm charge (red = upper and lower positive charge, blue = mid-level negative charge), showing the NBE events (black), (c) zoomed-in view of 6 seconds of high-rate NBE activity (~ 40 NBEs within one minute), indicated by the bracket in (b), coloured and sized by VHF source power and showing NBEs 1, 2 and 9. Note that the initial high-power sources of the NBEs (large diamond markers) were mis-located in altitude from the subsequent, smaller, and correctly-located lower-power sources (blue markers), with NBE 1 altitude being particularly incorrect (see Section 7.2). The low-power sources indicate that all 10 NBEs occurred at similar altitudes between 13 and 15 km MSL, immediately below or within the inferred upper positive charge region. (d, e, f) Plan and vertical cross-section views of the storm charge structure, coloured by charge as in (b) and showing that the NBEs occurred in close proximity to a positively charged western anvil of the normally-electrified storm. The inset in the east-west cross-section of (d) shows the full-duration INTF centroid observations for each of the three NBEs relative to the storm location, with marker colors corresponding to relative VHF power. The inset shows that each NBE had a vertical extent of $\simeq 1.5$ km on the lower edge of the upper positive charge region. The plan view of (e) shows the NBE locations as white circles. The cyan boxes in (d) and (f) indicate their locations in the vertical cross-sections. The black triangle in (e) indicates the INTF location at KSC.

and coloured according to source power in dBW. The ten NBEs were preceded and followed by fully-developed flashes (not shown), i.e., a negative cloud-to-ground flash ended three seconds before the start of the first NBE in the cluster, and a normal-polarity intra-cloud flash began 0.1 seconds after the tenth (final) NBE in the cluster. The INTF triggered on the strong VHF radiation from each of the ten NBEs. As discussed in the next section, the INTF and FA data indicate that NBE 1 (Figure 8.2) was produced by downward-propagating fast positive breakdown similar to

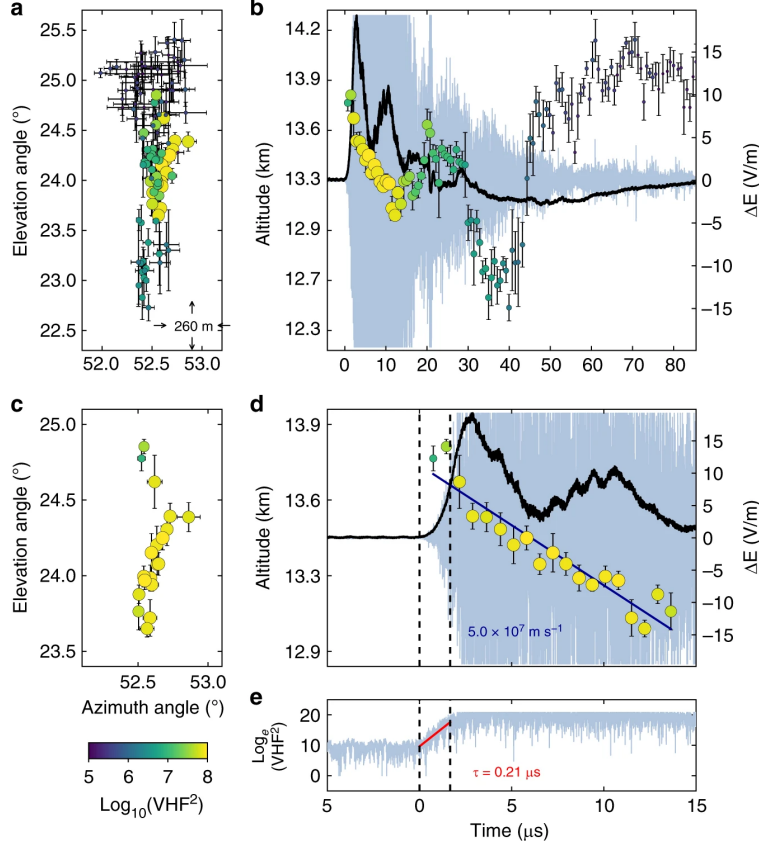


Figure 8.2: Interferometer data for NBE 1. (a,c) Radiation centroids (circular markers, coloured and sized by VHF power) for NBE 1, plotted in elevation vs. azimuth, showing the breakdown activity was primarily vertical. Each marker denotes the average angular position of the 128 source solutions in each $0.7\text{-}\mu\text{s}$ window, and error bars denote the standard deviations. (b,d) Radiation centroids and fast electric field change (sferic) observations (black waveform) superimposed on the VHF waveform (gray), showing the downward propagation of the VHF source. The positive sferic waveform is indicative of a downward-directed current, consistent with the NBE occurring below the storm's upper positive charge, and indicating the downward development was due to positive-polarity breakdown. The breakdown descended $\simeq 700\text{ m}$ in $14\text{ }\mu\text{s}$, corresponding to a speed of $\simeq 5 \times 10^7\text{ m s}^{-1}$. (e) Semilog plot of the VHF power vs. time, showing the fast exponential rise of the radiation (rise time $\tau = 0.21\text{ }\mu\text{s}$), coincident with the fast rise of the electric field change (panel (d)). The peak current of the breakdown was -75 kA .

that reported by Rison *et al.* (2016). In contrast, similarly fast breakdown but upward-directed and of negative polarity produced NBE 2 and NBE 9 (Figures 8.3 and 8.4, respectively). The polarity of the remaining seven NBEs could not be determined because the vertical extent of each event was too small to determine an unambiguous propagation direction.

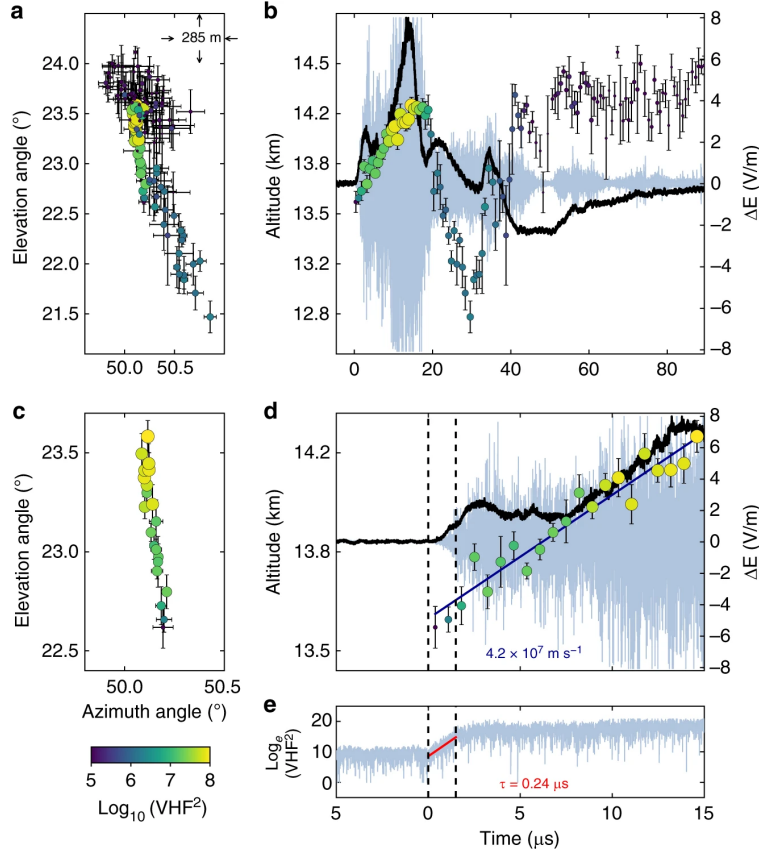


Figure 8.3: Interferometer data for NBE 2. (a,c) Radiation centroids (circular markers, coloured and sized by VHF power) for NBE 2, plotted in elevation vs. azimuth, showing the breakdown activity was primarily vertical. Each marker denotes the average angular position of the 128 source solutions in each $0.7\text{-}\mu\text{s}$ window, and error bars denote the standard deviations. (b,d) Radiation centroids and fast electric field change (sferic) observations (black waveform) superimposed on the VHF waveform (gray), showing the upward propagation of the VHF source. The positive sferic waveform is indicative of a downward-directed current, consistent with the NBE occurring below the storm's upper positive charge, and indicating the upward development was due to negative-polarity breakdown. The breakdown ascended $\simeq 600 \text{ m}$ in $15 \mu\text{s}$, corresponding to a speed of $\simeq 4 \times 10^7 \text{ m s}^{-1}$. (e) Semilog plot of the VHF power vs. time, showing the fast exponential rise of the radiation (rise time $\tau = 0.24 \mu\text{s}$), coincident with the fast rise of the electric field change (panel (d)). The peak current of the breakdown was -47 kA .

Despite differences in breakdown polarity and propagation direction, NBEs 1, 2, and 9 are consistent with the high-power NBEs discussed in Rison *et al.* (2016), having LMA-estimated peak VHF powers of 105 kW, 12 kW, and 43 kW, respectively. Also, the charge-moment changes (-320 C-m , -190 C-m , and -120 C-m), charge transfers (-0.5 , -0.3 , and -0.3 C), peak currents (-75 kA , -47 kA , and -58 kA), and current rise e -folding times ($0.5 \mu\text{s}$, $0.4 \mu\text{s}$, and $0.4 \mu\text{s}$) obtained from

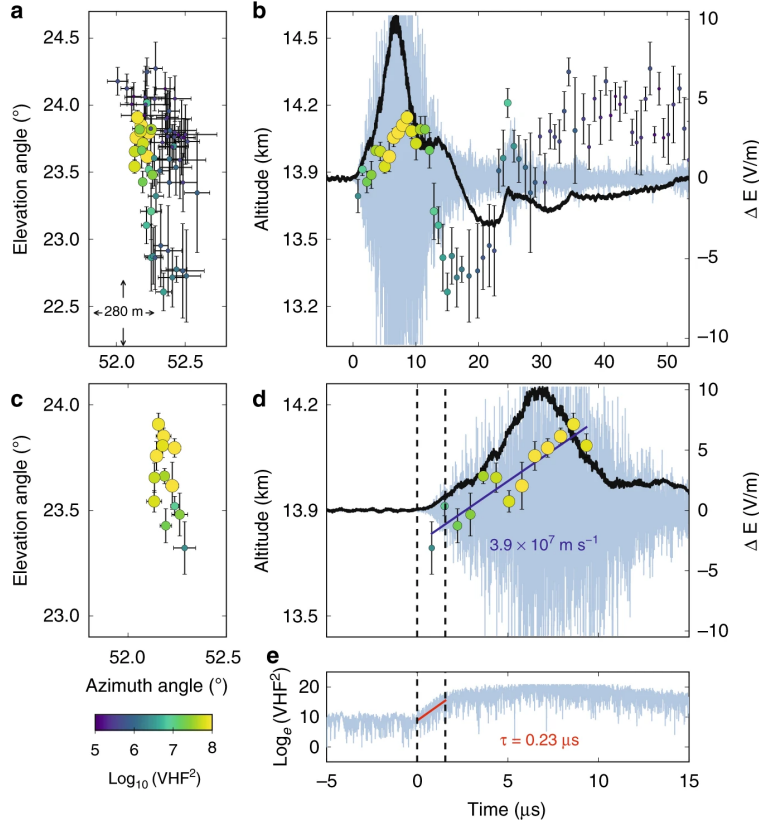


Figure 8.4: Interferometer data for NBE 9. (a,c) Radiation centroids (circular markers, coloured and sized by VHF power) for NBE 9, plotted in elevation vs. azimuth, showing the breakdown activity was primarily vertical. Each marker denotes the average angular position of the 128 source solutions in each $0.7\text{-}\mu\text{s}$ window, and error bars denote the standard deviations. (b,d) Radiation centroids and fast electric field change (sferic) observations (black waveform) superimposed on the VHF waveform (gray), showing the upward propagation of the VHF source. The positive sferic waveform is indicative of a downward-directed current, consistent with the NBE occurring below the storm's upper positive charge, and indicating the upward development was due to negative-polarity breakdown. The breakdown ascended $\simeq 400 \text{ m}$ in 10 μs , corresponding to a speed of $\simeq 4 \times 10^7 \text{ m s}^{-1}$. (e) Semilog plot of the VHF power vs. time, showing the fast exponential rise of the radiation (rise time $\tau = 0.23 \text{ μs}$), coincident with the fast rise of the electric field change (panel (d)). The peak current of the breakdown was -58 kA .

simulations of the fast breakdown sferics for NBEs 1, 2, and 9, are similar to the Rison *et al.* (2016) results. These results are summarized in Table 8.1.

8.3 Fast breakdown polarity

The fast electric field change measured by the fast antenna was positive for all three NBEs, indicative of the current being downward directed (Uman, 2001). The polarity of the events is then determined from INTF observations of the breakdown propagation direction. For each NBE, we construct a series of $0.7 \mu\text{s}$ -exposure VHF images (Stock & Krehbiel, 2014; Stock, 2014) (see Section 5.3), and then locate the centroid, or brightest pixel, in each image, to determine the location of the VHF-emitting source over time. To minimize the effects of noise in each $0.7 \mu\text{s}$ image, which corresponds to 128 VHF samples, we find 128 centroid locations by shifting each imaging window by one sample (5.6 ns) and calculate the average of those 128 locations. The resulting centroid maps for NBEs 1, 2, and 9 are shown in Figures 8.2, 8.3, and 8.4, respectively, where the circular markers correspond to the average centroid location in a $0.7 \mu\text{s}$ time period, and the error bars denote the standard deviation. In particular, for the upward negative-breakdown NBEs, Figures 8.3a,c and 8.4a,c show the centroids of NBE 2 and NBE 9, respectively, in elevation vs. azimuth angle, indicating their development was predominantly vertical, similar to the downward positive-breakdown of NBE 1 in Figure 8.2, and in other observations of NBEs (Rison *et al.*, 2016; Karunarathne *et al.*, 2016). Panels b,d of each of the figures show the NBEs' temporal development, co-plotted with coincident VHF (light blue) and FA (black) waveforms. The altitude vs. time development of the upward negative-breakdown NBEs is similar to that of the downward positive-breakdown example, with both being indicative of a localized source, or single breakdown front (albeit with noticeable scatter in the emitter locations). The measured VHF speeds and rise times are also similar for the three NBEs, ranging from $4\text{-}5 \times 10^7 \text{ m s}^{-1}$ and $0.21\text{-}0.24 \mu\text{s}$, respectively.

8.4 NBE source characterization

Figure 8.5 shows example $0.7 \mu\text{s}$ images used in determining the centroid results of the preceding section. The imaging centroid technique differs from that of Rison *et al.* (2016) in that it makes

NBE	Breakdown polarity	v (m s ⁻¹)	Δz (m)	P_{pk} (kW)	I_{pk} (kA)	Q_m (C·m)	ΔQ (C)	$\tau_{1,r}$ (μ s)	$\tau_{1,f}$ (μ s)	$\tau_{2,r}$ (μ s)	$\tau_{2,f}$ (μ s)
NBE 1	positive	5.0×10^7	600	105	-75	-320	-0.5	0.5	2.6	1.2	3.7
NBE 2	negative	4.2×10^7	600	12	-47	-190	-0.3	0.4	3.6	3.9	1.9
NBE 9	negative	3.9×10^7	400	43	-58	-120	-0.3	0.4	0.4	1.6	2.5

Table 8.1: Fast breakdown characteristics for NBEs 1, 2, and 9. The polarity is that of the initial fast breakdown of each NBE, and does not correspond to the sferic polarity. v is the INTF-determined speed of the fast breakdown, Δz is the INTF-determined vertical extent of the fast breakdown, and P_{pk} is the LMA-determined peak source power. I_{pk} and Q_m correspond to the peak current and charge-moment change during fast breakdown, as determined from FA sferic simulations similar to those in Rison *et al.* (2016), and ΔQ is the charge transfer. Two double-exponential current pulses were used to simulate each sferic. The first and second current pulses have rise and fall e -folding times of $\tau_{1,r}$, $\tau_{1,f}$, and $\tau_{2,r}$, $\tau_{2,f}$, respectively.

use of the full cross-correlation functions of antenna pairs, rather than just their peaks (Stock & Krehbiel, 2014). The centroid locations are similar for the two approaches, but the imaging provides additional information about the spatial distribution of the source (see Section 8.7). If the source is localized, i.e., is contained within the angular resolution of the INTF, then its location is well determined by the centroid location. For extended sources, the centroid does not necessarily represent the source location.

As an example, Figure 8.5 shows sequential images taken from NBE 2. The intensity distribution in each image is normalized, ranging from 0 (dark blue) to 1 (yellow). For comparison, Figure 8.5a shows the simulated image of an ideal noiseless point source positioned at azimuth angle (Az) and elevation angle (El) of 50° and 23° , respectively, similar to the NBE 2 source locations. The intensity pattern of an ideal point source is called the point spread function (PSF) (Taylor *et al.*, 1999; Stock, 2014) of the INTF (Section 5.4), and depends on INTF specifications such as bandwidth, and baseline lengths and orientations. The PSF is characterized by a bright main lobe, with an angular size that indicates the resolution of the INTF, and lower-intensity side lobes. Note that the top row of images (Figure 8.5b-e) corresponds to the first 15 μ s of NBE 2, and the images are qualitatively similar to the PSF, having a single bright main lobe of comparable size and similarly bright and morphologically similar side lobes. This indicates that the first 15 μ s of NBE 2 is consistent with a localized source, and that the sources are well-located by the centroid locations. In contrast, the second row (Figure 8.5f-i) corresponds to the latter (≥ 15 μ s)

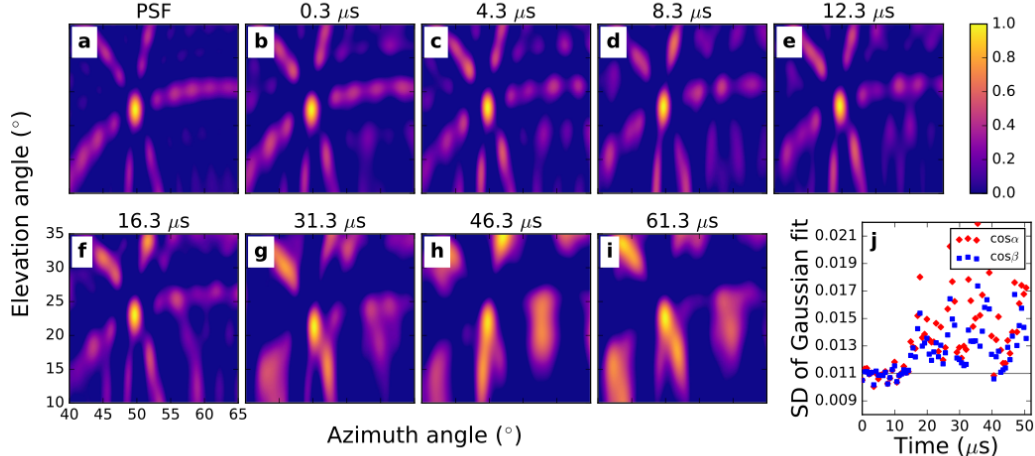


Figure 8.5: Radio images of NBE 2. Elevation vs. azimuth images of (a) an ideal point source at NBE 2's location ($Az, El = 50^\circ, 23^\circ$), called the point spread function (PSF), (b-e) sample images at $\simeq 4 \mu s$ intervals during the first $15 \mu s$ of NBE 2, corresponding to its upward fast negative breakdown (FNB) phase, and (f-i) sample images during successive $15 \mu s$ intervals. In each case the images are $0.7 \mu s$ exposures, normalized to the peak amplitude of the centroid. The central lobe of the PSF shows the angular resolution of the three-antenna array and, along with the side lobes, remains essentially unchanged during the FNB, consistent with the VHF radiation being from a localized source. Following the FNB, the central lobe becomes increasingly elongated and the side lobes intensify and become disorganized, indicative of extended and/or multiple radiation sources. (j) Standard deviations (SD) of the central lobe in the $(\cos\alpha, \cos\beta)$ projection plane vs. time (red, blue symbols), compared to the SD of the PSF function (grey line), quantitatively showing the radiation to be localized during the FNB and increasingly non-localized and random subsequent to the FNB.

portion of NBE 2, and the images look substantially different from the PSF, having both a broader main lobe and morphologically-dissimilar side lobes, as well as higher-intensity content in the side lobes. Such images are inconsistent with a localized source, and the centroid locations may not accurately depict the emitter locations. This is reflected in the increased uncertainty of the altitude values after $\sim 15 \mu s$ in Figures 8.2-8.4, and in the increased standard deviations shown in Figure 8.5j.

The VHF images for NBE 2 (Figures 8.5b-i) were each fitted with a two-dimensional Gaussian to determine their standard deviations (see Section 8.7). The resulting values are shown in Figure 8.5j, which clearly demonstrates two distinct regimes of activity. During the first $15 \mu s$

of NBE 2, i.e., the fast breakdown stage, the standard deviations in both the $\cos\alpha$ and $\cos\beta$ directions (see Section 5.2 for cosine plane projection) are confined to values between 0.010 and 0.012, making the sources consistent with a localized source radiating within the angular resolution of about 1.0° azimuth and 3.5° elevation. Often, the source is indistinguishable from a point source (with both standard deviations ≈ 0.011). In this case, the source locations and progression are well-represented by the centroid values, which show reduced scatter in the propagation (see Figures 8.2a,b, 8.3a,b, and 8.4a,b). After about $15\mu\text{s}$ (Figure 8.5f-i), the standard deviations are noticeably greater and show substantially more scatter in values, ranging between 0.012 and 0.022, indicating the angular source extents are greater than those of the PSF (0.011, corresponding to 1.6° and 3.8° in azimuth and elevation angle, respectively), extending instead up to $>1.6^\circ$ and $>5^\circ$ in azimuth and elevation angle, respectively. In addition, the side lobes are substantially altered. Thus, the latter stage appears to be a mix of localized and extended sources with the centroids not being consistent with a localized source.

Because the first $15\mu\text{s}$ of NBE 2 was consistent with a localized source, four possible models exist to explain the upward-propagating NBE 2 centroid movement depicted in Figure 8.3d. The first and simplest model is a point source, or negative breakdown front, moving upward in altitude, which is the model used to obtain Figure 8.6 (discussed below). A second plausible model is that of an extended source that grows upward in altitude. In this case, upward negative-polarity breakdown is still required to explain the centroid movement. A third model is that of two point sources, one that moves upward in altitude with greater source power, the other moving downward in altitude with lesser source power, so that the overall altitude change of the centroid is positive. Again, this would require an upward negative-polarity breakdown in order to explain the centroid movement, but would also indicate that a positive breakdown occurs concurrently with fast negative breakdown. Also, the fast negative breakdown speed determined in Figure 8.3d would be a lower limit. The fourth model is of two stationary point sources separated by at least 600 m in altitude. If the higher source radiates more strongly over time compared with the lower source, then the centroid movement is an apparent effect. This scenario is not physically plausible. The exponential

increase ($0.24 \mu\text{s}$ rise time) of the measured VHF power requires that the VHF power of the higher (more strongly radiating) source should increase on the same timescale. If the lower source does not also increase on the same timescale, then the centroid location is soon determined by the higher source alone (after $1.5 \mu\text{s}$, the source power increased by a factor of 500). The upward centroid movement must then be due to upward source propagation, not two stationary sources. Alternatively, if both the higher and lower source powers increase on the same timescale, then it is highly likely that an electrical connection exists between the two sources. This would suggest that an extended emitter ($>600 \text{ m}$) already exists at the onset of the exponential rise in VHF power, which is inconsistent with the INTF observations that show that there is no pre-event discharge activity.

Given the above discussion, fast moving, upward breakdown is required to explain the centroid movement of a localized source as depicted in Figures 8.3 and 8.4. Like NBE 2, NBE 9 was also produced by upward fast breakdown of negative polarity, in this case at a speed of $3.9 \times 10^7 \text{ m s}^{-1}$ (Figure 8.4d). In contrast, the fast breakdown of NBE 1 developed downward, in the same direction as the current, and therefore was of positive polarity (Figure 8.2d). In each case, the breakdown was initiated near 13.6 km altitude and had similar vertical extents (400-600 m) and propagation speeds (several times 10^7 m s^{-1}). The features of the initial fast breakdown during NBEs 1, 2, and 9 are summarized in Table 8.1.

8.5 Fast breakdown simulation

To further validate the breakdown developing as a fast propagating event, we simulate the INTF images of a propagating ideal point source, while taking into account the (pre-flash) noise in the INTF measurement (see Section 8.7). In particular, the initial $15 \mu\text{s}$ of NBE 2 is modeled as a fast ($4.2 \times 10^7 \text{ m s}^{-1}$) monotonically ascending point source that begins at 13.6 km altitude and a distance 32.6 km from the INTF, which has the same VHF power per image as for the actual

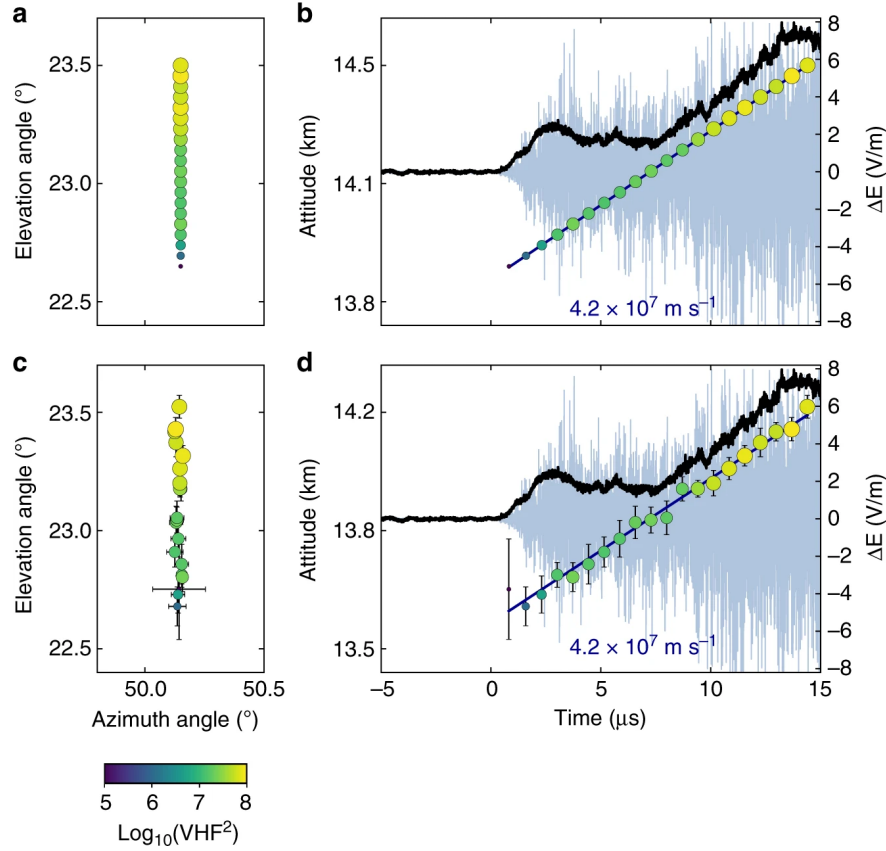


Figure 8.6: NBE 2 simulation. Simulated radiation centroids (circular markers, coloured and sized by VHF power) of a vertically-propagating point source, having the same VHF amplitudes, altitudes, and speed of NBE 2. Each marker denotes the average angular position of the 128 source solutions in each $0.7\text{-}\mu\text{s}$ window, and error bars denote the standard deviations. (a,b) Centroid locations without added noise, plotted in elevation vs. azimuth and elevation vs. time, respectively, and (c,d) same, but with the pre-flash noise of NBE 2 added, showing that the resulting scatter in elevation and azimuth is partially but not fully accounted for by the pre-flash noise.

NBE 2 record. Figure 8.6a,b shows the noise-free model for the fast breakdown of NBE 2, while Figure 8.6c,d shows the model with added noise.

Comparison of Figure 8.3c,d and Figure 8.6c,d shows that the scatter in the source locations of the actual measurements is only partially accounted for by the pre-flash noise. Since our simulation of a monotonically-ascending point source (Figure 8.6c,d) does not fully explain the scatter in centroids that is depicted in the observations (Figure 8.3c,d), it is possible that we have either underestimated the noise, that the source speed fluctuates, or that a spatially-distributed cascading sequence of activity is responsible for the fast negative breakdown observed for NBE 2 (and

NBE 9), and perhaps is also responsible for the fast positive breakdown of NBE 1 and other fast positive breakdown events, given the similarities between fast negative and fast positive breakdown. Regardless, the centroid locations during the initial breakdown of NBE 2 (Figure 8.3c,d) are consistent with fast, upward-propagating breakdown that carries a current opposite to its propagation direction, transporting negative charge upward into the upper positive charge region (inset in Figure 8.1d), and therefore being of negative polarity.

8.6 Discussion

Though dart leaders (Jordan *et al.*, 1992; Shao *et al.*, 1995; Rakov, 1998) and K-processes (Shao & Krehbiel, 1996; Akita *et al.*, 2010) both constitute negative-polarity breakdown events that can reach speeds in excess of 10^7 m s^{-1} , they occur along a path preconditioned by preceding discharges, whereas fast negative breakdown appears to occur in virgin air. Streamers are the only known form of electrical breakdown in virgin air that can reach speeds on the order of 10^7 m s^{-1} (Stanley *et al.*, 1999; McHarg *et al.*, 2002; Liu *et al.*, 2015, 2016), so the high speeds of fast breakdown can be explained by propagating streamers. Although relativistic runaway electron avalanches (RREAs) (Gurevich *et al.*, 1992) also constitute a negative-polarity discharge in virgin air, the propagation speed of the RREAs is $0.89c$ (Coleman & Dwyer, 2006), which is much faster than the observed propagation speed of the fast negative breakdown. Because the runaway electron avalanche length at thunderstorm altitudes is approximately a few hundred meters long (Dwyer, 2003), the characteristic time scale of an individual RREA is about $1 \mu\text{s}$, much shorter than the 10-30 microsecond duration of the fast negative breakdown. As a result, to create such a long timescale, multiple RREAs would be necessary, but then it is not obvious why these multiple RREAs would cause a discharge to propagate in the direction opposite the electric field direction. Finally, it is not clear how RREAs could produce the large VHF power emitted during the fast negative breakdown, nor do they represent a viable mechanism for producing the observed sferics (Arabshahi *et al.*, 2014), given the length scale ($<1 \text{ km}$) of fast negative breakdown.

The current magnitude (Briels *et al.*, 2008; Liu, 2010; Shi *et al.*, 2016) and spatial and temporal scales of a single streamer are much smaller than the scales observed during fast breakdown, so a reasonable interpretation of the fast breakdown in NBEs 2 and 9 is that it consists of a system of many negative streamers. The fact that the VHF signal turns on coincidentally with the FA signal and both develop exponentially agrees with the findings of Rison *et al.* (2016), and is also consistent with modeling of streamer development which shows similar exponential growth (Griffiths & Phelps, 1976; Shi *et al.*, 2016), regardless of polarity.

Negative streamer development alone in virgin air is not immediately consistent with our understanding of dielectric breakdown in virgin air (Williams, 2006; Petersen *et al.*, 2006; Liu *et al.*, 2012; Sadighi *et al.*, 2015; Petersen *et al.*, 2015; Shi *et al.*, 2016). In particular, in investigating the polarity asymmetry in lightning initiation and propagation, it has been suggested that positive streamers originate first at some initiation point and negative streamers are initiated from the point later when the field is sufficiently large (Williams, 2006). However, negative streamers alone can occur in earth's atmosphere if positive streamer development is suppressed, for example, at the edge of the ionosphere for negative sprites (Liu *et al.*, 2016). In this case, both the nonuniformity of the electric field and the location of the initiating breakdown is critical to the breakdown's polarity. During the August 24 storm, a similar nonuniformity of the thundercloud electric field is suggested by the high isolated NBE rate, which indicates localized regions of intense electric field (Rison *et al.*, 2016). Depending on the location of initiating breakdown relative to the nonuniformity, it is possible that negative streamers could propagate in virgin air for some time without a positive-streamer counterpart.

Fast negative breakdown seems to share many similar characteristics with fast positive breakdown, as is evident from the entries in Table 8.1. It is interesting to note that the differences between positive and negative streamers cause no significant difference in the characteristics of the two types of fast breakdown. It has been suggested that electron drift motion being convergent for positive breakdown while divergent for negative breakdown leads to more favorable condition for the positive breakdown to start and propagate (Williams, 2006). The highest electron drift speed

in streamers is on the order of 10^5 m s^{-1} , which is two orders of magnitude slower than the fast breakdown propagation speed. With streamer speeds much larger than electron drift speeds, the properties of streamers are dominated by their ionization wave nature. Whether electron drift is in the same direction or opposite direction of the wave then becomes less important, which results in negligible difference between positive and negative streamers (Babaeva & Naidis, 1997; Shi *et al.*, 2016).

It is interesting to note not only the similarities between the fast negative breakdown events (NBEs 2 and 9) and the fast positive breakdown event (NBE 1) herein, but also the similarities with the three NBE-producing fast positive breakdown events in Rison *et al.* (2016) (NBEs 1, 2, and 3). The similarities exist despite inherent differences between Florida thunderstorms and New Mexico thunderstorms (Krehbiel, 1986; Stolzenburg *et al.*, 1998; Stolzenburg & Marshall, 2008; Caicedo *et al.*, 2018), the Florida storms having higher associated MSL heights, higher negative charge centers, and spanning a greater range of temperatures than New Mexico storms, as is also supported by this study. The Rison *et al.* (2016) NBEs have significantly lower initiation altitudes (9-10 km MSL) compared to those of the NBEs herein (13-14 km MSL). Given that NBE parameters can vary widely, these similarities are surprising, albeit inconclusive, given the small sample of NBEs compared.

Another possibility to consider is that fast negative breakdown is not due to negative streamer development, but is due to positive streamers moving in retrograde motion that gives an apparent upward propagation direction. That is, negative charge deposited at each streamer initiation point (Griffiths & Phelps, 1976; Liu, 2010) could create a sufficiently large electric field to launch positive streamers upwind of the preceding streamers, and so on. Rison *et al.* (2016) used this idea to explain retrograde development at the beginning of one of their positive-polarity NBEs (NBE 2), which was confirmed by the time-resolved retrograde development of a high-altitude screening discharge. Moreover, such a cascading sequence of activity could explain the scatter discrepancy between the INTF observations and the simulations. However, this still requires a highly localized electric field to limit the overall spatial extent of the fast breakdown in the direction of the thunder-

storm field. Furthermore, it is not obvious how a retrograde-motion system of positive streamers can reach $3\text{--}5 \times 10^7 \text{ m s}^{-1}$ in propagation speed, and so retrograde positive breakdown development appears to be an implausible mechanism for explaining fast negative breakdown.

In summary, high-speed radio interferometric observations show that dielectric breakdown can begin with negative polarity in thunderstorms, which propagates at a speed as high as $4 \times 10^7 \text{ m s}^{-1}$, extends over a distance of 500 m, and like other high-power NBEs is a source of the strongest natural VHF emission on Earth. It is unclear what physical mechanism is behind the fast negative breakdown, and a better understanding of the NBE mechanism will have important implications for storm convective strength monitoring (Suszcynsky & Heavner, 2003; Jacobson & Heavner, 2005; Wiens *et al.*, 2008; Wu *et al.*, 2011) that would be particularly useful for space-borne global monitoring and climatology. The observations thus far show that most NBEs are produced by fast positive breakdown, while those produced by fast negative breakdown are less common but constitute a noticeable portion of events. The properties of the fast negative breakdown suggest it consists of a large number of streamers, whether they are negative streamers propagating opposite the direction of the thunderstorm electric field, positive streamers developing in retrograde motion, or another unforeseen mechanism involving many streamers. It appears, regardless, that a suppression of the normal breakdown development in the thunderstorm electric field direction is required in order for fast negative breakdown to take place without readily discernible processes in the opposite direction.

8.7 Appendix

8.7.1 Image morphologies

The image morphologies are investigated by comparing the observed images to simulated images of known source types. The size of the main lobe is used to quantify the spatial extent of the source. Figure 8.7 shows simulated images of several source types. The top row of panels corresponds to an ideal, noiseless point source, the central lobe of which defines the spatial resolution

of the array. In this case, the source was positioned at $(Az, E\ell) = (50^\circ, 23^\circ)$, corresponding to the location of NBE 2. Figure 8.7a shows the source in the cosine projection plane, and illustrates how the source location is determined, namely from the intersection of lines of constant time difference of arrival at the three pairs of antennas. For the point source, the three peaks in the amplitude versus time delay of the corresponding cross-correlation functions intersect (Stock & Krehbiel, 2014; Stock, 2014) to create a Gaussian-distributed strong central lobe that is nearly circularly symmetric (Figure 8.7b). The standard deviation (SD) of the lobe is 0.011 in both directions (Figure 8.7c,d), namely 1.1% of the overall extent of the cosine projection plane. When projected upward onto the celestial hemisphere to determine the Az and $E\ell$ angles, the lobe becomes elongated in elevation, corresponding to standard deviations of 1.6° in azimuth and 3.8° in elevation (Figure 8.7e). The centroid location (white dot) and corresponding azimuth-elevation values (white text) demonstrate that the location of an ideal point source is well determined by the centroid location. The larger scale of the azimuth-elevation plot also shows the characteristic side lobes, which are caused by subsidiary, periodic peaks in the cross-correlation functions. The full image is called the point spread function (PSF) of the array and is a unique function of the antenna geometry (Taylor *et al.*, 1999), fundamental to interpreting observational data.

Figure 8.7f-i shows images of the same point source, but with increasing noise (decreasing signal-to-noise ratio, or SNR) in the VHF signal. By simulating a point source at $(Az, E\ell) = (50^\circ, 23^\circ)$ 100 times with each of the SNR values, we determined that for SNRs greater than 6, on average the centroid is correctly located to within 0.01° in azimuth and elevation angles. Comparing with NBEs 1, 2, and 9, which had SNR values ranging between 10 and 100 and extended about 1° in elevation angle, added noise should have minimal impact on the centroid determinations. An estimate of the INTF noise was obtained from the pre-flash noise levels of the INTF VHF waveforms, determined from the relatively quiet period prior to the NBE in question (for example, the VHF signal (blue waveform) in Figure 8.2, prior to time 0 and about 1 ms in duration). The pre-flash noise content was roughly Gaussian, with a standard deviation about 1% of the INTF dynamic range. Added noise minimally affects the image morphology, which is illustrated by comparing

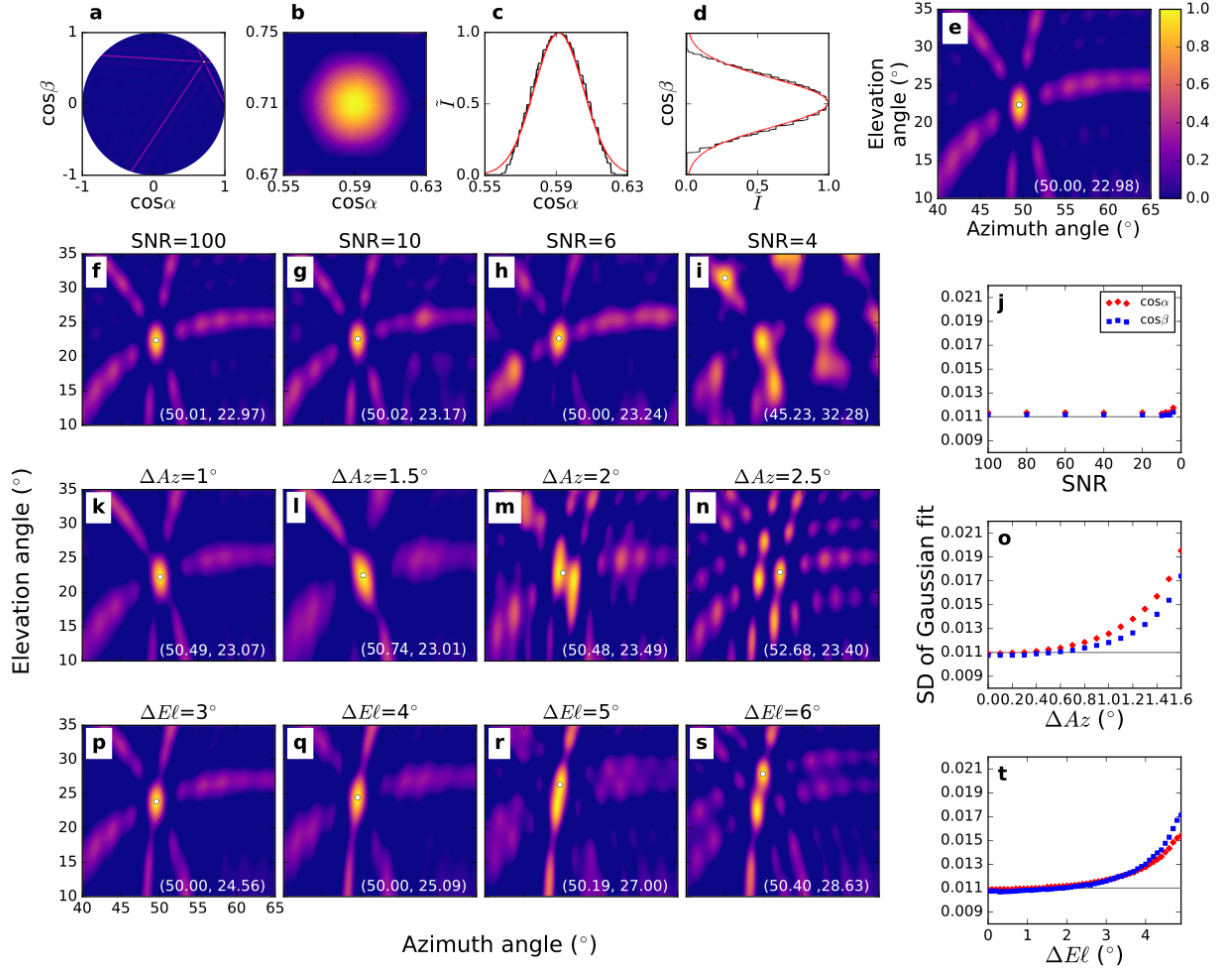


Figure 8.7: Radio images of different source types. Simulated images and related information of: (a-e) an ideal point source, corresponding to the point spread function (PSF) of the antenna array, (f-j) the effect of uncorrelated noise on the observations, and the effect of angular separation of two equal-power point sources in azimuth (k-o), and elevation (p-t). Each image shows the normalized intensity (\tilde{I}) of a $0.7 \mu\text{s}$ exposure of sources at the location of NBE 2. Panels (c) and (d) show that the central lobe of the PSF has a standard deviation (SD) of 0.011 in both the $\cos\alpha$ and $\cos\beta$ directions, corresponding to SDs of 1.6° and 3.8° in azimuth and elevation. As seen in panel (j), added noise has little effect on the size of the central lobe, remaining close to the PSF value of 0.011 (horizontal grey line) for signal to noise ratios as large as unity (0 dB). Binary sources have a much stronger effect, with the two sources being readily distinguishable for azimuthal separations of 2° or elevation separations of 5° - 6° . The fixed central lobe becomes noticeably deformed well before that (panels (o) and (t)).

the standard deviation (SD) of the central lobe with that of the PSF (Figure 8.7j), which shows negligible effect up to 0 dB (unity) SNR.

On the other hand, multiple sources significantly affect the morphology, as illustrated by images of two point sources with increasing angular separation. This is shown in the third and fourth rows of Figure 8.7. A single main lobe exists for angular separations less than the angular resolution (1.6° in azimuth and 3.8° in elevation). The main lobe becomes increasingly elongated as the angular separation grows, with the centroid location becoming the average location of the two individual point sources (Stock, 2014). The two sources become readily distinguishable for an azimuthal separation of 2° or an elevation separation of $5\text{--}6^\circ$, but elongation of the main lobe becomes noticeable well before that, as seen in the SD comparisons of Figure 8.7o,t.

8.7.2 Angular resolution

As mentioned previously, the INTF PSF in the cosine projection plane (Figure 8.7a) has an approximately two-dimensional Gaussian intensity distribution in the main lobe. The resolution in the cosine plane can be approximated from the full-width-half-maximum (FWHM) of the Gaussian fits to the main lobe (Stock, 2014). The angular resolutions in azimuth and elevation angle as a function of elevation angle ($E\ell$) is given by $\Delta Az = \text{FWHM} / \cos(E\ell)$ and $\Delta El = \text{FWHM} / \sin(E\ell)$, respectively, similar to equations (4.4) and (4.5) in Stock 2014 (Stock, 2014). For a source positioned near elevation angle 23° , similar to the NBE sources herein, the angular resolution becomes 1.6° in azimuth angle and 3.8° in elevation angle.

CHAPTER 9

INITIAL BREAKDOWN PULSES

9.1 Overview

Lightning is thought to be initiated by streamers (Griffiths & Phelps, 1976; Petersen *et al.*, 2008; Liu *et al.*, 2012; Rison *et al.*, 2016), but streamers can be generated in thunderstorms without necessarily forming lightning, as in the case of NBEs (Rison *et al.*, 2016; Tilles *et al.*, 2019; Liu *et al.*, 2019). The question then is how and when does a lightning channel form? Classic initial breakdown pulses (IBPs) (Section 2.5) are an indicator of initial channel formation (Beasley *et al.*, 1982; Rhodes & Krehbiel, 1989; Villanueva *et al.*, 1994; Marshall *et al.*, 2013; Stolzenburg *et al.*, 2013; Karunarathne *et al.*, 2013, 2014; Kolmasova *et al.*, 2018), but it is unclear what physical processes generate the complex IBP sferic, which consists of a $\sim 10 \mu\text{s}$ -wide pulse superimposed by $\sim 1 \mu\text{s}$ wide subpulses. Here, we present sub-microsecond radio interferometer (INTF) and fast-antenna (FA) observations of the initial breakdown stage of three cloud-to-ground (CG) and three intra-cloud (IC) lightning flashes in Florida. With the INTF we are able to determine the typical extent, duration, and two-dimensional speed of breakdown associated with 29 classic IBPs, as well as for 33 periods of “FA-quiet” breakdown activity that occurred in between sferic pulses. We show that the initial sferic pulses of both classic IBPs and narrow ($\sim 1 \mu\text{s}$ wide) IBPs (Nag *et al.*, 2009; Karunarathne *et al.*, 2013; Stolzenburg *et al.*, 2014) coincide with enhanced VHF emissions that indicate they are largely generated by streamer activity. Classic IBPs propagated negative charge ~ 100 m into virgin air at a typical speed of $\sim 10^7$ m/s, whereas the breakdown associated with narrow IBPs was too short in duration and extent to determine propagation direction or speed, though the associated breakdown occurred near the tips of the existing breakdown volume. Classic IBPs initiated along paths of previous breakdown activity before they propagated the breakdown

volume forward into virgin air. We show that the initial breakdown volume was developed roughly equally in terms of length by both $\sim 10^6$ m/s breakdown that occurred without detectable sferics, i.e., by FA-quiet activity, and by classic IBPs, which propagated an order of magnitude faster. Finally, the later under-/over-shoot of classic IBP sferics indicates that a sustained current flows following the fast streamer activity; however, we show that the current is maintained without new apparent streamer activity, suggesting the existence of current through a hot conductive channel. These results suggest that the fast streamer processes not only generate the initial IBP pulse, but feed current into an established hot channel that may form prior to the first classic IBP in a flash.

9.2 Example lightning flashes

We investigated the initial stage of six flashes – three negative cloud-to-ground (CG) and three normal-polarity intra-cloud (IC) flashes – that occurred in Florida in 2016 within 16 km of the INTF. The flashes were close enough to the INTF so that the vertical extent of a classic IBP subtended an elevation angle change ($\simeq 1^\circ$) that was on the same order as the resolution of the INTF (this can be approximated as $\lambda/D \approx 2^\circ$, where λ is the shortest wavelength the INTF can measure, and D is the longest INTF baseline (Stock, 2014)). However, the flashes were far enough from the INTF so that vertical propagation could be resolved (for instance, a vertically-propagating event directly overhead of the INTF would appear to be stationary).

The CG and IC flashes (“CG2” and “IC3”) with the most vertical initial development of the six flashes are shown in Figures 9.1 and 9.2, respectively, and the remaining four flashes are shown in Figures 9.9-9.12 of the Appendix (Section 9.7). CG2 and IC3 occurred on August 24 and September 19, 2016, at plan distances of 9.1 km and 6.8 km from the INTF, and initiated at altitudes of about 6.5 and 7.5 km above mean sea level (MSL), respectively. The additional CG flashes (“CG1” and “CG3”) in Figures 9.9 and 9.10 occurred on August 24 and September 2, 2016, at plan distances of 6.0 km and 6.1 km from the INTF, and initiated at altitudes of about 6.0 and 6.5 km MSL, respectively, and the additional IC flashes (“IC1” and “IC2”) in Figures 9.11 and

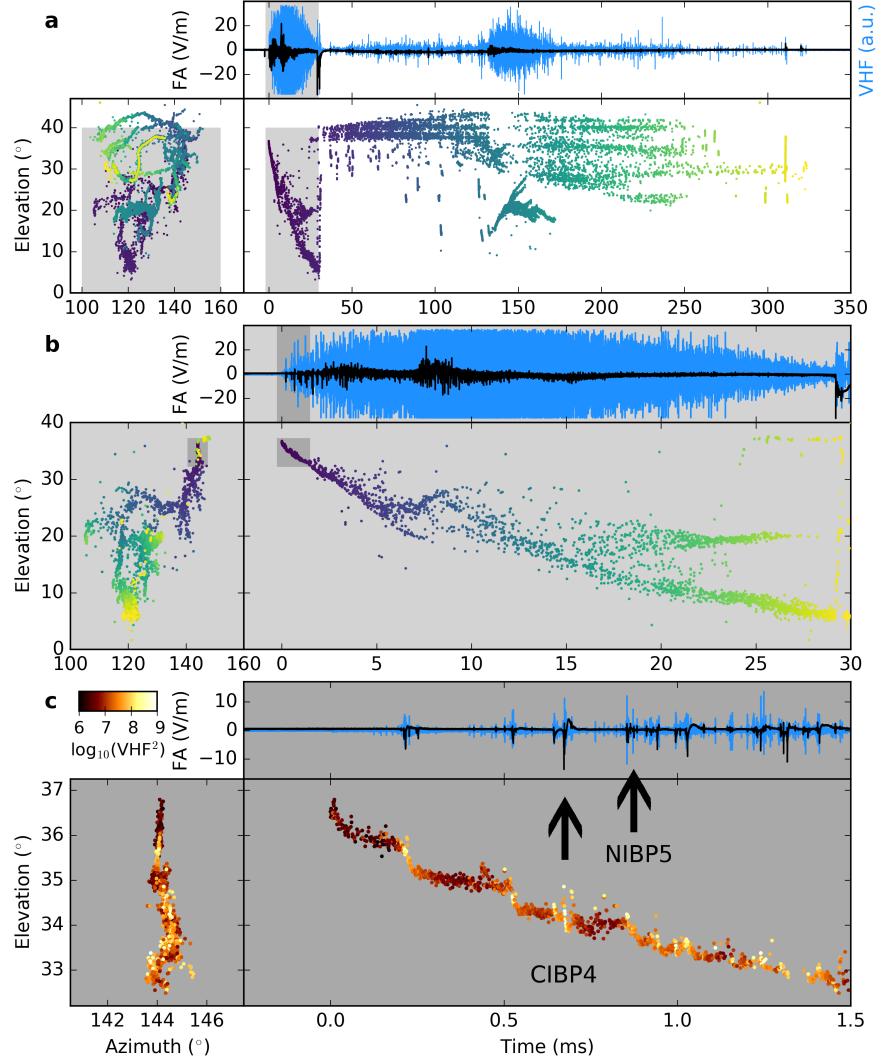


Figure 9.1: 2016.08.24 CG2 flash overview. (a) The whole flash, showing the FA and VHF waveforms (black and blue waveforms, respectively), and INTF sources (markers colored by time) are shown in elevation versus azimuth, and elevation versus time. (b) Same as (a), but for the highlighted light-gray region in (a). The panel shows the (downward) negative leader development, followed later by visible positive leader development back near the flash initiation location. The flash initially developed one main vertical breakdown channel, but became increasingly branched and developed more horizontally over time, with the leader reaching ground after ≈ 30 ms. (c) Same as (a) and (b), but for the highlighted dark-gray region in (b) and with INTF sources colored by VHF power. The panel shows detail of the initial breakdown stage of the flash, which was initiated without an apparent NBE or fast breakdown event, and instead was initiated by low-power VHF activity / FA-quiet activity. From 0 to 1.5 ms, ≈ 12 narrow IBPs and 8 classic IBPs occurred, with FA-quiet periods occurring in-between most pulses.

9.12 occurred on August 9 and September 2, 2016, at plan distances of 15.5 km and 7.8 km from the INTF, and initiated at altitudes of about 5.0 and 7.0 km MSL, respectively. The plan distance for each flash was obtained from three-dimensional Lightning Mapping Array (LMA) data, which is shown for each flash in Figures 9.19-9.24 in the Appendix (Section 9.7). The altitudes were then obtained by combining the LMA-determined plan distances with the INTF source elevation angles.

Figures 9.1, 9.2, and 9.9-9.12 show the general structure of each entire flash over the course of ~ 100 ms, and also demonstrate how the initial stage of each flash was selected for further investigation. During the initial ~ 1 ms of each flash, the breakdown was more vertically-oriented and less complex compared with more extensive branching later in each flash. As the flashes became more branched, individual breakdown channels became less defined, and it became less apparent how the INTF sources contributed to individual channel development and generation of the FA pulse. For instance, panel b of each Figure 9.1, 9.2, and 9.9-9.12 shows that in elevation versus time, at least two “layers” of activity emerged several milliseconds after flash initiation. The layers indicate that at least two persistent breakdown channels developed within the same time frame, with the INTF sources switching back and forth between the two (or more) channels. For example, the development of two or more such channels first occurred at $\simeq 5$ ms in Figure 9.1b and at $\simeq 10$ ms in Figure 9.2b for CG2 and IC3, respectively. Note that this occurred earlier in the other four flashes ($\simeq 2$ ms for CG1, $\simeq 1$ ms for CG3, $\simeq 2$ ms for IC1, and $\simeq 3$ ms for IC2), which did not develop as vertically in the initial stage. In addition, panel b of each Figure 9.1, 9.2, and 9.9-9.12 shows that initially only the development of the negative leader was visible in the INTF data, but later positive leader development became visible back near the flash initiation location. The later development demonstrates that an electrical connection had been maintained in between the initiation location and the subsequent negative leader activity, which was particularly apparent after the return stroke in the CG flashes.

The first or largest classic IBP (CIBP) in each flash is indicated in panel c of Figures 9.1, 9.2, and 9.9-9.12, and these are expanded and investigated in more detail in the next section. The first

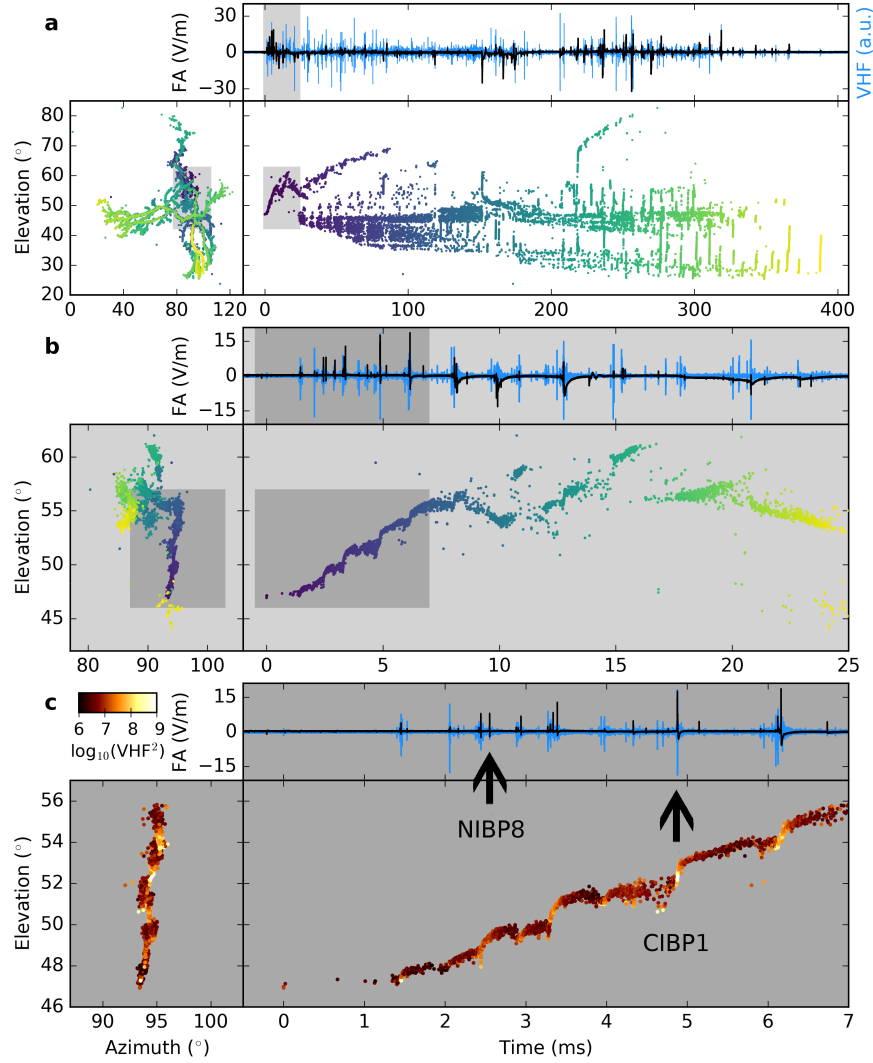


Figure 9.2: 2016.09.14 IC3 flash overview. (a) The whole flash, showing the FA and VHF waveforms (black and blue waveforms, respectively), and INTF sources (markers colored by time) are shown in elevation versus azimuth, and elevation versus time. (b) Same as (a), but for the highlighted light-gray region in (a). The panel shows the (upward) negative leader development, followed later by visible positive leader development back near the flash initiation location. The flash initially developed one main vertical breakdown channel, but became increasingly branched and developed more horizontally over time. (c) Same as (a) and (b), but for the highlighted dark-gray region in (b) and with INTF sources colored by VHF power. The panel shows detail of the initial breakdown stage of the flash, which was initiated without an apparent NBE or fast breakdown event, and instead was initiated by low-power VHF activity / FA-quiet activity. From 0 to 7 ms, ≈ 23 narrow IBPs and 2 classic IBPs occurred, with FA-quiet periods occurring in-between most pulses.

CIBP occurred at different times after flash initiation in each case, occurring at $\simeq 1.3$ ms for CG1, $\simeq 0.2$ ms for CG2, $\simeq 0.3$ ms for CG3, $\simeq 0.2$ ms for IC1, $\simeq 0.6$ ms for IC2, and $\simeq 5$ ms for IC3. However, in each case, FA-quiet breakdown activity extended the breakdown region by $\simeq 100$ -300 meters before the first classic (or narrow) IBP occurred. Also in panel c of Figures 9.1, 9.2, and 9.9-9.12, the location of a narrow IBP (NIBP) is indicated, which is expanded and investigated in more detail later in this chapter.

The minimum, maximum, and average breakdown (i.e., INTF source) extent, duration, and 2-D speed are computed for each CIBP and FA-quiet (FAQ) period in panel c of Figures 9.1, 9.2, and 9.9-9.12. The NIBP duration was too short to determine extent and propagation direction. All the analyzed events (CIBPs, NIBPs, and FAQs) are indicated in Figures 9.13-9.18 in the Appendix (Section 9.7). The results for each flash are shown in Table 9.1, which shows that the breakdown associated with CIBPs had extents between 37 and 224 m, durations between 4 and 22 μ s, and propagation speeds between 0.8 and 7.5×10^7 m/s. The breakdown associated with FA-quiet activity had speeds between 0.2 and 3.4×10^6 m/s, at least an order of magnitude slower than for CIBPs, but had similar extents between 20 and 305 m compared to CIBPs. However, FA-quiet activity had a much larger spread in durations, which could range between 25 and 510 μ s.

In addition, we determined the total length that CIBP and FA-quiet breakdown contributed to the initial development (i.e., panel c in Figures 9.1, 9.2, and 9.9-9.12) of each flash. In CG1, CG2, and CG3, the initial breakdown channel developed 0.7, 0.5, and 0.8 km in extent during CIBPs, whereas the initial channel only developed 0.2, 0.1, and 0.3 km in extent during FA-quiet periods, respectively. In IC1, IC2, and IC3, the initial breakdown channel developed 0.5, 0.3, and 0.3 km in extent during CIBPs, whereas the initial channel developed 0.5, 0.8, and 0.8 km in extent during FA-quiet periods, respectively. A tentative trend can be seen here to distinguish between the initial development in CG and IC flashes. For instance, in CG flashes, CIBPs contribute at least two times as much in length to initial breakdown development as FA-quiet breakdown. In contrast, FA-quiet breakdown in IC flashes makes a larger contribution in length to the initial breakdown development, and can contribute over twice as much in extent compared to CIBPs. However, given the

flash	Classic IBP (CIBP)					FA-quiet period (FAQ)				
	Δz (m)	Δd (m)	Δt (μs)	v ($\times 10^7$ m/s)	ΔD (km)	Δz (m)	Δd (m)	Δt (μs)	v ($\times 10^6$ m/s)	ΔD (km)
08.24 CG1	-97/146/130	114/152/137	8/20/14	1.3/2.4/1.7	0.7	-12/25/16	31/83/50	130/160/144	0.2/0.5/0.3	0.2
08.24 CG2	-37/126/59	37/128/59	4/9/6	1.1/7.5/2.7	0.5	-5/44/26	20/44/32	63/120/90	0.3/0.4/0.4	0.1
09.02 CG3	-62/154/106	75/157/110	6/18/11	0.8/2.4/1.5	0.8	-26/154/62	28/155/63	25/178/58	0.9/1.9/1.5	0.3
08.09 IC1	+75/126/96	80/126/99	6/15/11	1.1/2.5/1.4	0.5	+43/304/100	44/305/102	31/60/47	1.0/3.4/1.7	0.5
09.02 IC2	+73/214/143	85/224/155	10/22/16	1.1/1.2/1.1	0.3	+37/184/76	37/195/87	65/490/229	0.3/0.6/0.4	0.8
09.14 IC3	+142/192/167	142/195/168	10/15/12	1.2/3.1/2.2	0.3	+37/201/89	44/205/94	156/510/262	0.3/0.5/0.4	0.8

Table 9.1: INTF source altitude change (Δz), 2-D extent (Δd), source duration Δt , 2-D speed (v), and total 2-D extent (ΔD) during the classic IBPs or FA-quiet breakdown in each example flash. A minimum/maximum/average value is given for each entry except ΔD . For Δz , the ‘+’ and ‘-’ symbols indicate the direction of propagation in altitude. The entries correspond to average values obtained during the initial stage of each flash, as indicated in panel c of Figures 9.9-9.12, which are shown in more detail in Section 9.7. In addition, the overall contribution in length (ΔD) to the initial channel development is given for classic IBPs and FA-quiet breakdown.

limited number of example flashes herein, this trend requires further validation with more events.

9.3 Classic IBPs

Figure 9.3 and 9.4 show an example classic IBP (CIBP) from each of the three CG and IC flashes, respectively. The temporal and spatial location of each CIBP in its parent flash is indicated in figures 9.1, 9.2, and 9.9-9.12, whereas all the analyzed CIBPs in each of the six flashes are indicated in Figures 9.13-9.18 in the Appendix (Section 9.7). In each case, a bipolar sferic, superimposed by narrow subpulses, was accompanied by elongation of the breakdown region. At the beginning of each CIBP, the sources first propagated backwards with an apparent 2-D speed of $\sim 10^7$ m/s along paths of previous activity before the breakdown extended forward at $\sim 10^7$ m/s into virgin air. The forward propagation lasted on the order of $10 \mu s$ and had a ~ 100 -200 m extent, as indicated by the values of Δd in Table 9.1.

The onset of the backward-propagating sources occurred with the onset of the CIBP sferic and a similar onset in VHF emissions, with INTF sources forward-propagating at $\sim 10^7$ m/s over the course of the initial sferic pulse and a VHF burst. The similar onset and duration of the initial sferic pulse and VHF burst indicates that the sferic pulse was largely produced by streamers, which emit strongly in VHF (Shi *et al.*, 2016, 2019). Moreover, the 10^7 m/s source propagation would

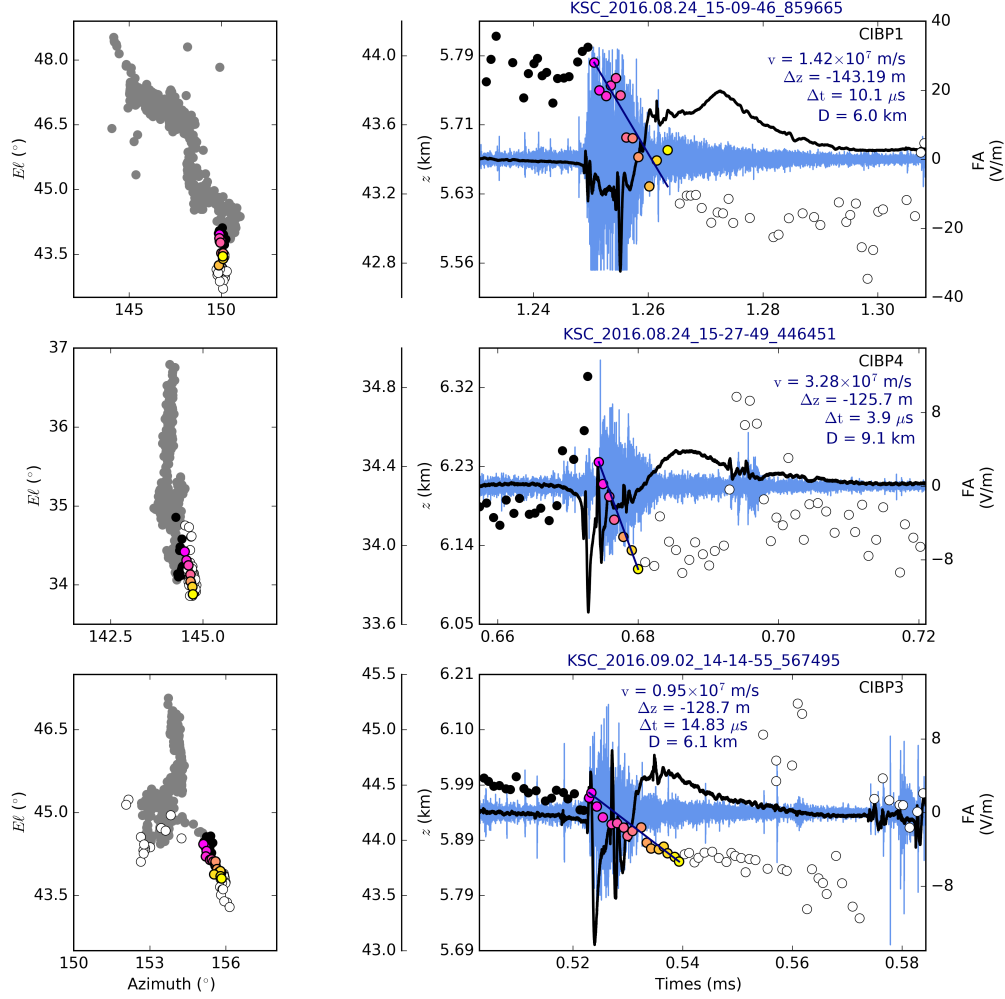


Figure 9.3: Classic IBPs in CG flashes. An example classic IBP (CIBP) is shown from each of the three CG flashes: from CG1 on the top, CG2 in the middle, and CG3 on the bottom. INTF sources (circular markers) are shown in elevation versus azimuth (left plots), and elevation versus time (right plots). The FA and VHF signals (black and blue waveforms, respectively) are also shown in the right-most plots. In the elevation versus time plots (right panels), the colored markers indicate sources used for computing extent and speed during each CIBP, the black sources denote activity just before the CIBP, and white sources denote activity just after the CIBP. This same color scheme is used in the elevation versus azimuth plots (left panels), with the entire preceding flash activity colored gray.

then be a manifestation of fast negative breakdown (Tilles *et al.*, 2019; Liu *et al.*, 2019), a fast-propagating, streamer-based discharge that also produces some narrow bipolar events (NBEs). However, the long-lived ($>10 \mu\text{s}$) over-/under-shoot at the end of the CG/IC CIBP sferics was not

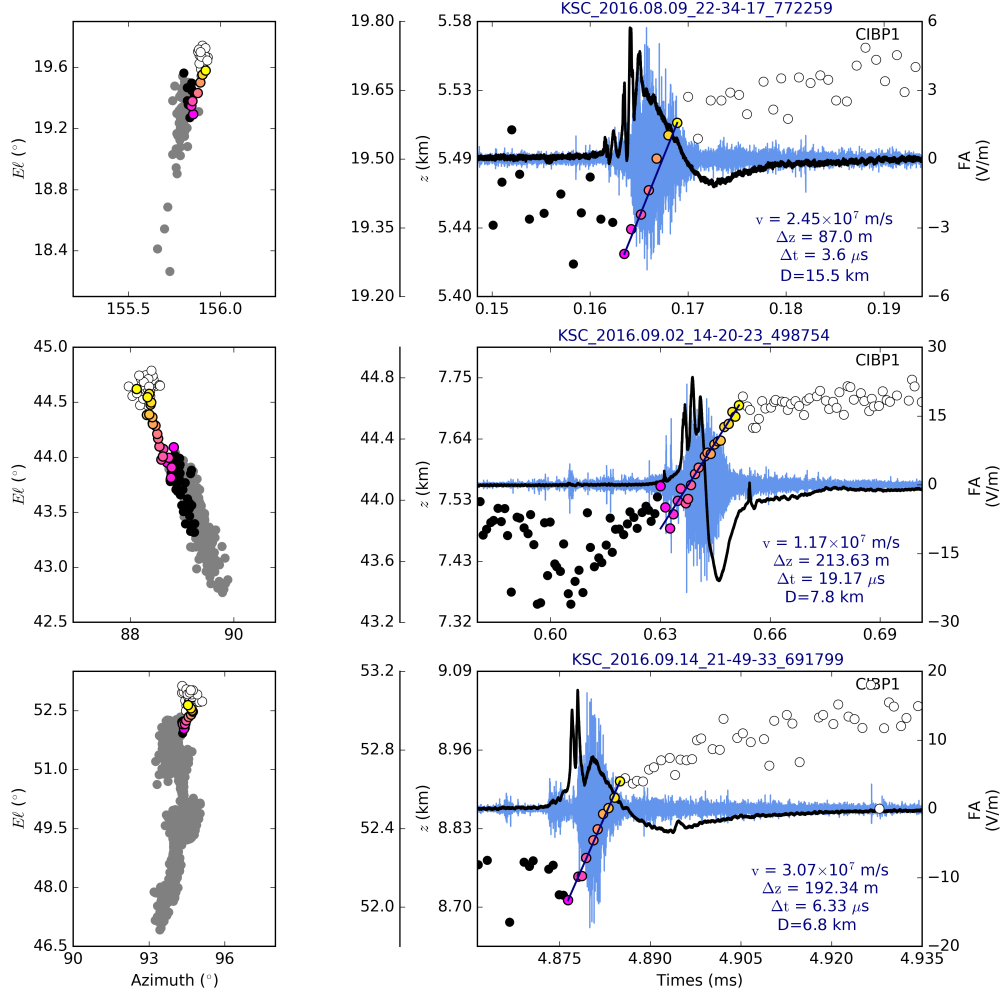


Figure 9.4: Classic IBPs in IC flashes. An example classic IBP (CIBP) is shown from each of the three IC flashes: from IC1 on the top, IC2 in the middle, and IC3 on the bottom. INTF sources (circular markers) are shown in elevation versus azimuth (left plots), and elevation versus time (right plots). The FA and VHF signals (black and blue waveforms, respectively) are also shown in the right-most plots. In the elevation versus time plots (right panels), the colored markers indicate sources used for computing extent and speed during each CIBP, the black sources denote activity just before the CIBP, and white sources denote activity just after the CIBP. This same color scheme is used in the elevation versus azimuth plots (left panels), with the entire preceding flash activity colored gray.

necessarily accompanied by strong VHF emissions (at least, not stronger than before each CIBP onset), suggesting that a long-lived current was generated by activity other than streamers.

In addition, because the backward-propagating sources retraced a region of previous activity, the retraced region must not have established a thermalized channel by the start of the CIBP, or

else such repeated activity would not have occurred, given that leaders can maintain their conductivity for tens of microseconds up to milliseconds (Bazelyan & Raizer, 1998, p. 226). However, it is worth noting that the backward-propagating sources, which depict a positive-polarity breakdown, did not propagate nearly as far in extent as the forward-propagating negative breakdown. It would appear that the backward-developing positive breakdown was somehow suppressed or quickly quenched during each CIBP compared with the forward-developing negative breakdown. A possible explanation is that positive streamer development ceased once it encountered a thermalized channel, which may have formed prior to and “behind” the CIBP.

9.4 Narrow IBPs

Figures 9.5 and 9.6 show an example narrow IBP (NIBP) from each of the three CG and IC flashes, respectively. The figures show that NIBP sferics, like classic IBPs (CIBPs), can be roughly bipolar, but can also be more complicated in shape, and are significantly more narrow ($\sim 1 \mu\text{s}$) compared with CIBPs ($\sim 10 \mu\text{s}$). Like the CIBPs shown in Section 9.3, the NIBPs here have VHF emissions associated with a sferic pulse. Specifically, the onset of a VHF burst coincides with the peak of a preceding sferic pulse, which for these narrow ($\sim 1 \mu\text{s}$ wide) sferics is dominated by the radiation field, which is proportional to the time derivative of the current moment (da Silva & Pasko, 2015). Hence, the peak rate of growth of the current moment coincides with vigorous streamer activity, consistent with streamers producing the NIBP sferic. Note that the NIBP in the middle right-most panel of Figure 9.5 (i.e., NIBP5 in CG2) had fewer INTF sources associated with it than the other NIBPs in Figures 9.5 and 9.6. Moreover, the VHF burst was associated with the peak of the second – not the first – sferic pulse. Possibly, breakdown activity in two or more regions of the flash occurred near-simultaneously, producing overlapping sferics, as well as resulting in poor cross-correlations in the INTF processing algorithm, which would have resulted in the fewer source solutions.

It is worth noting that similar VHF bursts can occur without detectable sferics, as can be seen in the middle panel of Figure 9.6, a little after 4.168 ms. That is, seemingly similar streamer (i.e., VHF) activity may produce drastically different sferics, and it is unclear at this point why some VHF bursts are associated with IBPs, and others are not.

All the analyzed NIBPs in each of the six flashes are indicated in Figures 9.13-9.18 in the Appendix (Section 9.7), showing that NIBPs occurred throughout the initial stage, with similar numbers of occurrence in CG and IC flashes. There is some indication that NIBPs occurred in trains of more than one pulse at a time, similar to CIBPs, but over a shorter timescale (sub-millisecond, com-

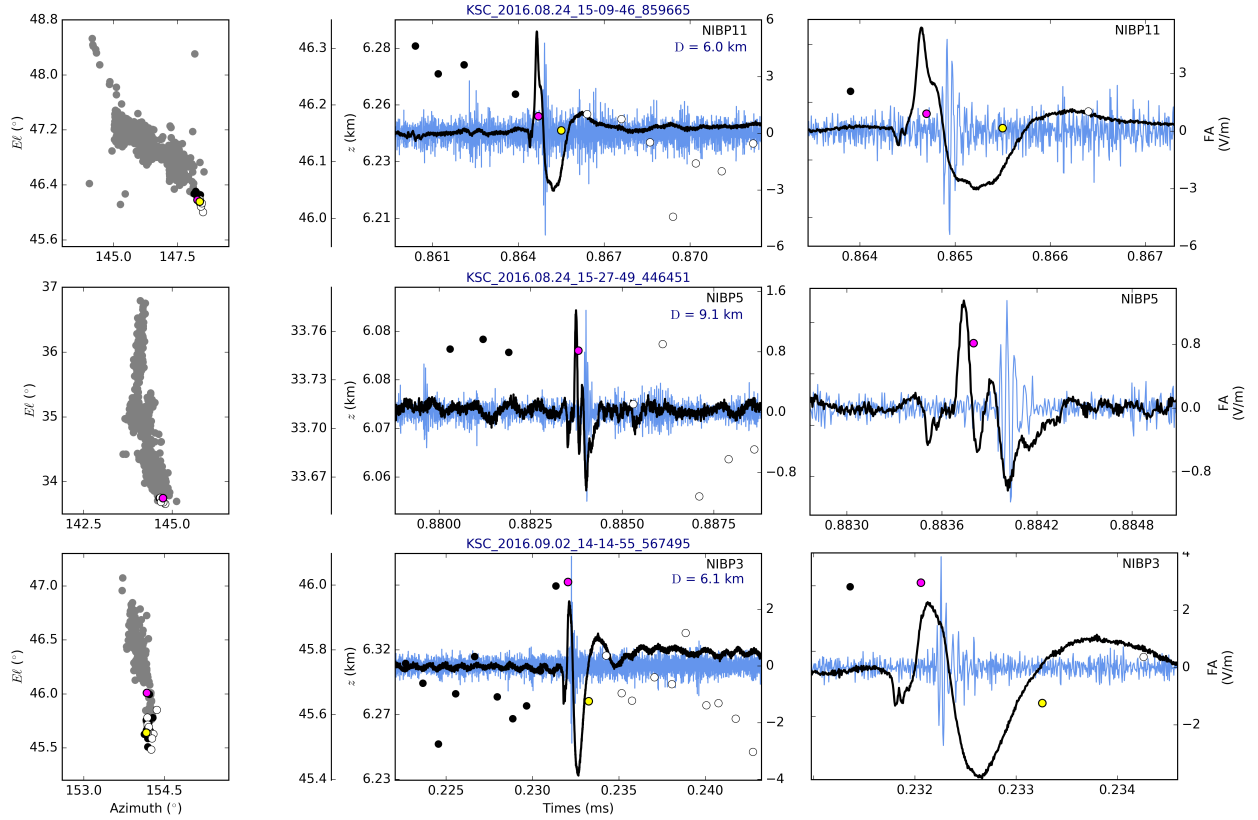


Figure 9.5: Narrow IBPs in CG flashes. An example narrow IBP (NIBP) is shown from each of the three CG flashes: from CG1 on the top, CG2 in the middle, and CG3 on the bottom. INTF sources (circular markers) are shown in elevation versus azimuth (left plots), and elevation versus time for two different time ranges (two right plots). The FA and VHF signals (black and blue waveforms, respectively) are also shown in the right-most plots. The colored markers indicate sources during the NIBP, the black markers denote activity just before the NIBP, and white sources denote activity just after the NIBP. In the left panels, the entire preceding flash activity is colored gray.

pared with the \sim millisecond-long trains of CIBPs). The NIBP sources occurred near the leading edge of breakdown activity, and so were seemingly involved in extending the breakdown volume into virgin air. However, due to the short duration of the NIBPs, we could not determine the source extent or propagation direction or speed.

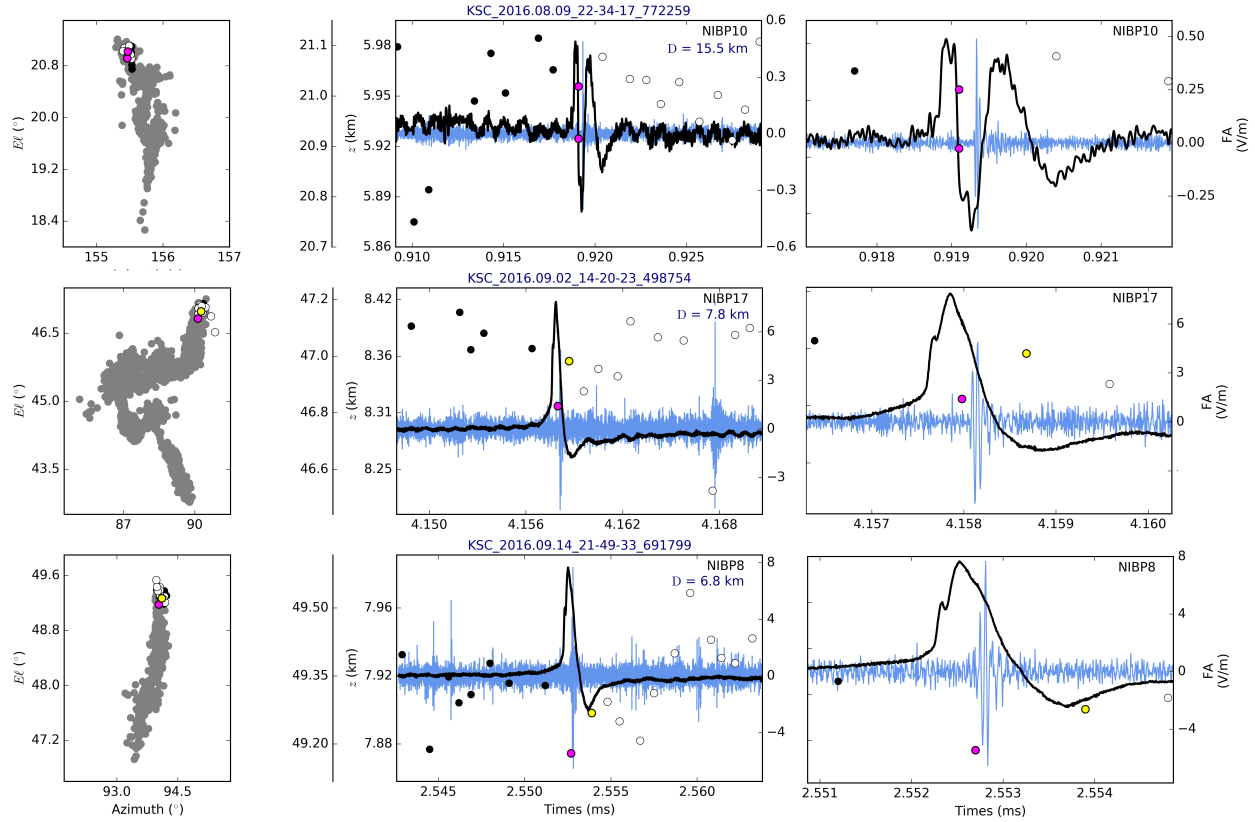


Figure 9.6: Narrow IBPs in IC flashes. An example narrow IBP (NIBP) is shown from each of the three IC flashes: from IC1 on the top, IC2 in the middle, and IC3 on the bottom. INTF sources (circular markers) are shown in elevation versus azimuth (left plots), and elevation versus time for two different time ranges (two right plots). The FA and VHF signals (black and blue waveforms, respectively) are also shown in the right-most plots. The colored markers indicate sources during the NIBP, the black markers denote activity just before the NIBP, and white sources denote activity just after the NIBP. In the left panels, the entire preceding flash activity is colored gray

9.5 FA-quiet periods

Figure 9.7 and 9.8 show an example FA-quiet period (FAQ) from each of the three CG and IC flashes, respectively. FA-quiet activity is marked by $\sim 10^5$ - 10^6 m/s source propagation, at least

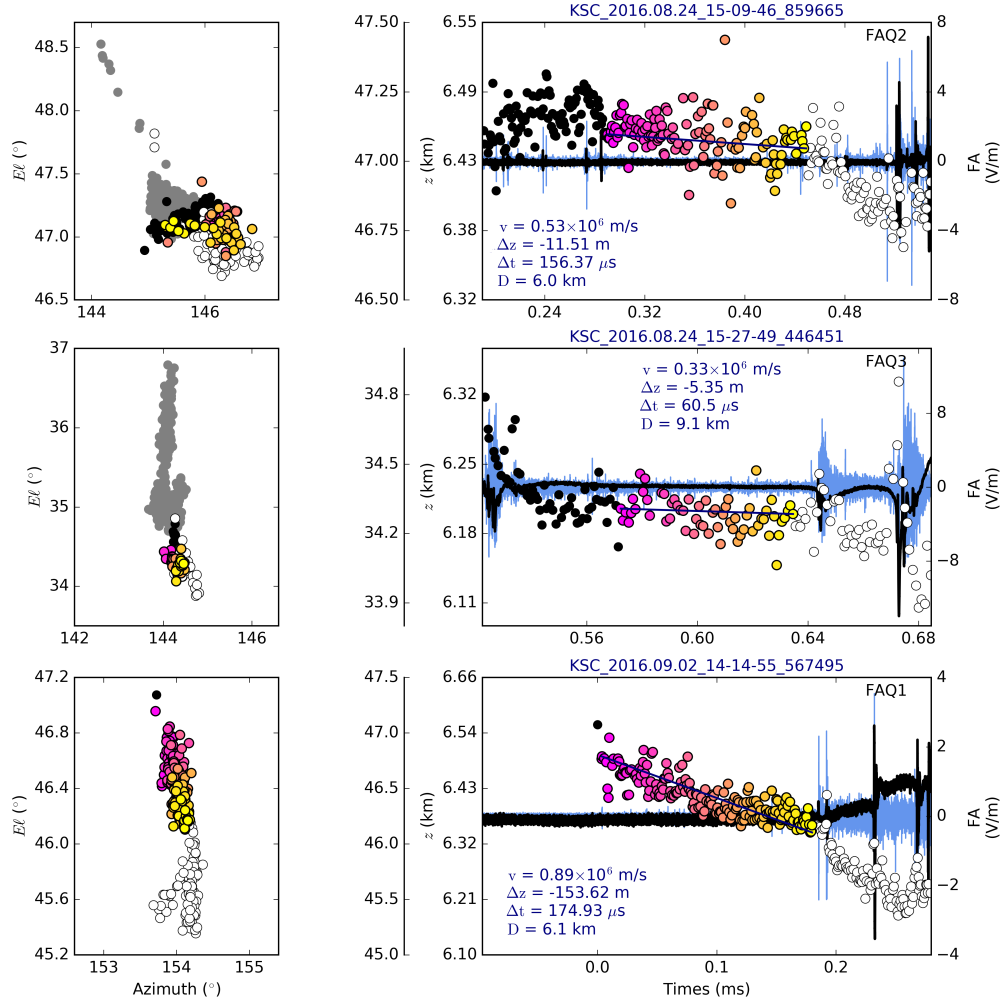


Figure 9.7: FA-quiet activity in CG flashes. An example FA-quiet period (FAQ) is shown from each of the three CG flashes: from CG1 on the top, CG2 in the middle, and CG3 on the bottom. INTF sources (circular markers) are shown in elevation versus azimuth (left plots), and elevation versus time (right plots). The FA and VHF signals (black and blue waveforms, respectively) are also shown in the right-most plots. In the elevation versus time plots (right panels), the colored markers indicate sources used for computing extent and speed during each FAQ, the black sources denote activity just before the FAQ, and white sources denote activity just after the FAQ. This same color scheme is used in the elevation versus azimuth plots (left panels), with the entire preceding flash activity colored gray.

an order of magnitude slower than IBP-associated source propagation. The examples demonstrate that FA-quiet activity can contribute substantially in length to the initial channel development. The values of ΔD in Table 9.1 show that FA-quiet activity contributes to at least half of the initial channel extent compared to IBPs. Figures 9.13-9.18 in the Appendix (Section 9.7) show all the

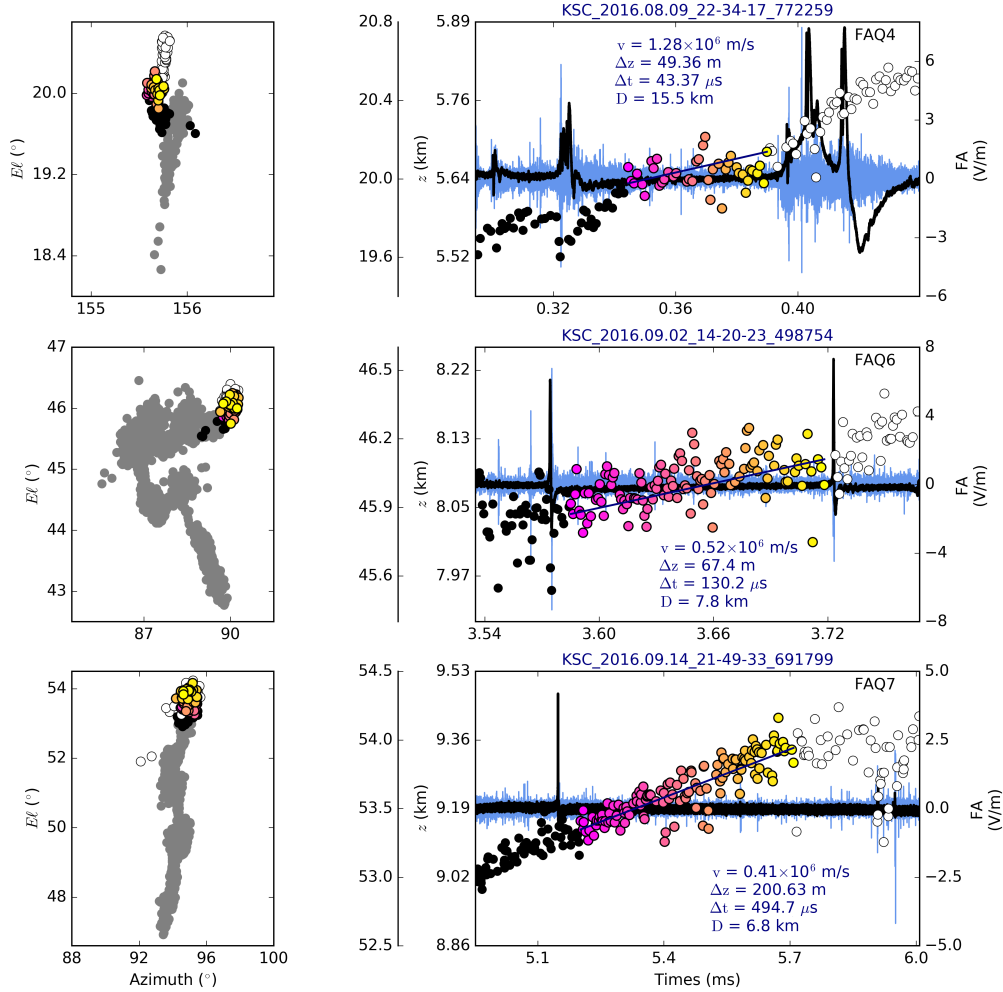


Figure 9.8: FA-quiet activity in IC flashes. An example FA-quiet period (FAQ) is shown from each of the three IC flashes: from IC1 on the top, IC2 in the middle, and IC3 on the bottom. INTF sources (circular markers) are shown in elevation versus azimuth (left plots), and elevation versus time (right plots). The FA and VHF signals (black and blue waveforms, respectively) are also shown in the right-most plots. In the elevation versus time plots (right panels), the colored markers indicate sources used for computing extent and speed during each FAQ, the black sources denote activity just before the FAQ, and white sources denote activity just after the FAQ. This same color scheme is used in the elevation versus azimuth plots (left panels), with the entire preceding flash activity colored gray.

analyzed FA-quiet events in each of the six flashes, which show that FA-quiet activity in CG flashes contributes less to the breakdown channel extent over time. In contrast, there seems to be a less drastic dependence on time in the IC flashes, with FA-quiet activity appearing at more or less regular intervals during the initial stage. It may be that the FA-quiet activity continued for a longer time in the CG flashes, like that of the IC flashes, but radiated much weaker than other activity and so was not detected.

Aside from the absence of detectable sferics and the more slowly-propagating breakdown activity, FA-quiet activity further differs from CIBPs by how the sources are distributed in space. FA-quiet source locations are scattered throughout a larger volume than during the fast IBP source propagation – the leading “tip” of FA-quiet breakdown encompasses a region that can be ~ 100 m deep, as shown in the vertical distribution of sources in the elevation versus time plots of Figures 9.7 and 9.8. The scatter may in part be due to the lower VHF signal-to-noise ratio (SNR) during FA-quiet activity compared with CIBPs.

9.6 Discussion

Using a broadband radio interferometer (INTF) and coincident fast-antenna and LMA observations, we demonstrate the two-dimensional development of VHF sources during the initial breakdown stage in three cloud-to-ground (CG) and three intra-cloud (IC) lightning flashes. In summary, the results show that classic initial breakdown pulses (CIBPs) are produced by fast negative breakdown, similar to that associated with NBEs (Tilles *et al.*, 2019), with INTF sources propagating $\sim 10^7$ m/s and accompanied by a burst in VHF during the initial CIBP sferic pulse. However, the narrow (~ 1 μ s) subpulses superimposed on the initial pulse are due to very fast current transients, and it is unclear what produces them, with one hypothesis being that subpulses are produced by transient hot channels (Abbasi *et al.*, 2019). The resulting long sferic over-/under-shoot may be due to activity other than streamers, and may be the result of prolonged current through a hot channel, which would produce the light observed, for instance, in Stolzenburg *et al.* (2014) during CIBPs.

We also show that narrow IBP (NIBP) sferics are associated with VHF emissions, indicative of streamer activity, comparable to CIBPs but of much shorter duration ($\sim 1 \mu\text{s}$). Also similar to CIBPs, NIBP sources seem to be associated with elongating the breakdown region into virgin air, since NIBPs occur near the leading edge of breakdown activity. Although we show that NIBPs are accompanied by VHF emissions, we also show that the opposite is not necessarily true, with similar VHF emissions occurring without a NIBP. It is not entirely clear what produces the NIBP sferic, but luminosity increases have been observed during cloud-obscured NIBPs in CG lightning (Stolzenburg *et al.*, 2014), indicating the existence of a hot channel at the time of the NIBP. Moreover, very fast current transients must produce the $\sim 1 \mu\text{s}$ -wide NIBP sferics, making them similar to the subpulses in CIBPs. Given the hypothesis by Abbasi *et al.* (2019), NIBPs might also be produced by transient hot channels.

Lastly, we show that during FA-quiet (FAQ) periods, breakdown still propagates substantially into virgin air, contributing roughly equally to the initial channel development compared to CIBPs. This FA-quiet breakdown propagated at a slower speed of $\sim 10^5$ - 10^6 m/s, at least an order of magnitude slower than CIBP sources. Moreover, an initial period of FA-quiet activity always preceded the first IBPs herein, and was likely involved in generating an initial electric field change (IEC) as observed in other studies (Marshall *et al.*, 2014, 2019), which begins some hundreds of microseconds up to a few milliseconds before the first CIBP in a flash. In contrast to CIBPs, the INTF sources associated with FA-quiet periods were scattered throughout a ~ 100 -m deep volume. Though the increased source scatter may have been partly due to the lower signal-to-noise ratio (SNR) during FA-quiet periods, the ~ 100 -m deep volume may depict a breakdown “front” where multiple sources emitted within the volume during the FA-quiet period, and suggesting that the volume did not immediately thermalize during the period, but was discharged by repeated streamer activity. Four lines of evidence suggest that this FA-quiet streamer activity propagated in the presence of a hot conductive channel. These four lines of evidence are as follows: 1) In each flash, a negative breakdown front propagated for the first ~ 10 ms without recurrent breakdown back along the path of previous activity. This shows that the path of previous activity maintained

sub-breakdown electric fields for the first ~ 10 ms of each flash. In particular, this was true for activity leading up to the first CIBP in each flash. 2) After the first ~ 10 ms of each flash, new breakdown activity occurred back near the flash initiation location (associated with the positive leader), which in the CG flashes coincided with the return stroke. This shows that an electrical connection had been maintained in between the initiation location and the subsequent negative leader activity up until that point in time (~ 10 ms after flash initiation). Moreover, it showed that an electrical connection had been maintained between the initiation location and the first CIBP. 3) The FA-quiet periods prior to the first CIBP likely coincided with an IEC. This shows that a current lasted hundreds of microseconds up to several milliseconds along the electrical connection between the initiation location and the first CIBP. Lastly, 4) from modeling studies (da Silva & Pasko, 2013), below $\simeq 10$ km altitude, the streamer-to-leader transition timescale is on the order of a tens of microseconds or less, depending on current through the system. This timescale is substantially lower than the total duration of FA-quiet periods leading up to the first CIBP in each of our observed flashes, and suggests that the streamer-to-leader transition occurred substantially before the first CIBP. If, in contrast, FA-quiet activity depicts streamer activity without the presence of a hot conductive channel, then the hot conductive channel would not have been established until the end of FA-quiet activity. However, FA-quiet activity persisted for over for $\sim 500 \mu\text{s}$ in two of the CG flashes, and over 5 ms in two of the IC flashes (see Figures 9.13-9.18 in the Appendix (Section 9.7)). It is not clear how streamers alone could maintain an electrical connection along the path of previous activity for several milliseconds in duration without recurrent breakdown along that path. Rather, taking 1), 2), 3), and 4) together provides strong evidence that a leader was formed prior to the first CIBP in each flash, with FA-quiet activity being a manifestation of that leader's formation. The FA-quiet activity may denote the streamer zone of a nascent leader, with the 10^5 - 10^6 m/s speeds dependent on the speeds of both the leader and the system of streamers at its tip.

In conclusion, we have demonstrated two distinct breakdown processes that take place during lightning's initial development, namely classic IBPs and FA-quiet activity, with classic IBPs caused

by fast negative breakdown, and FA-quiet activity indicative of hot channel formation. Together, IBPs and FA-quiet activity somehow cooperate/compete to develop the eventual stepped leader that can be observed below cloud base.

9.7 Appendix

9.7.1 Additional example lightning flashes

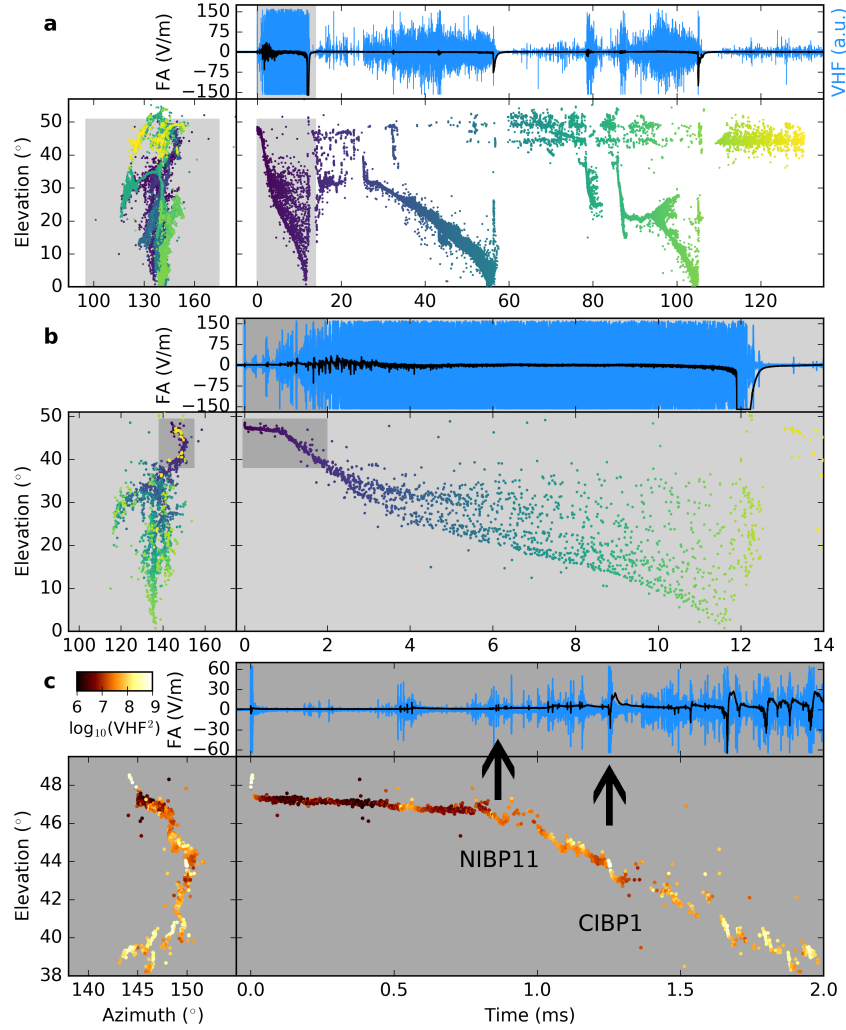


Figure 9.9: 2016.08.24 CG1 flash overview. (a) The whole flash, showing the FA and VHF waveforms (black and blue waveforms, respectively), and INTF sources (markers colored by time) are shown in elevation versus azimuth, and elevation versus time. (b) Same as (a), but for the highlighted light-gray region in (a). The flash initially developed with few and relatively small branches, but became increasingly branched and developed more horizontally over time, with the leader first reaching ground at $\simeq 12$ ms. (c) Same as (b), but for the highlighted dark-gray region in (b) and with INTF sources colored by VHF power. The flash was initiated by a NBE generated by fast positive breakdown, and was immediately followed by a FA-quiet period lasting $\simeq 200 \mu\text{s}$. From $\simeq 200 \mu\text{s}$ to $\simeq 2$ ms, $\simeq 19$ narrow IBPs and 5 classic IBPs occurred, with FA-quiet periods occurring in-between most pulses.

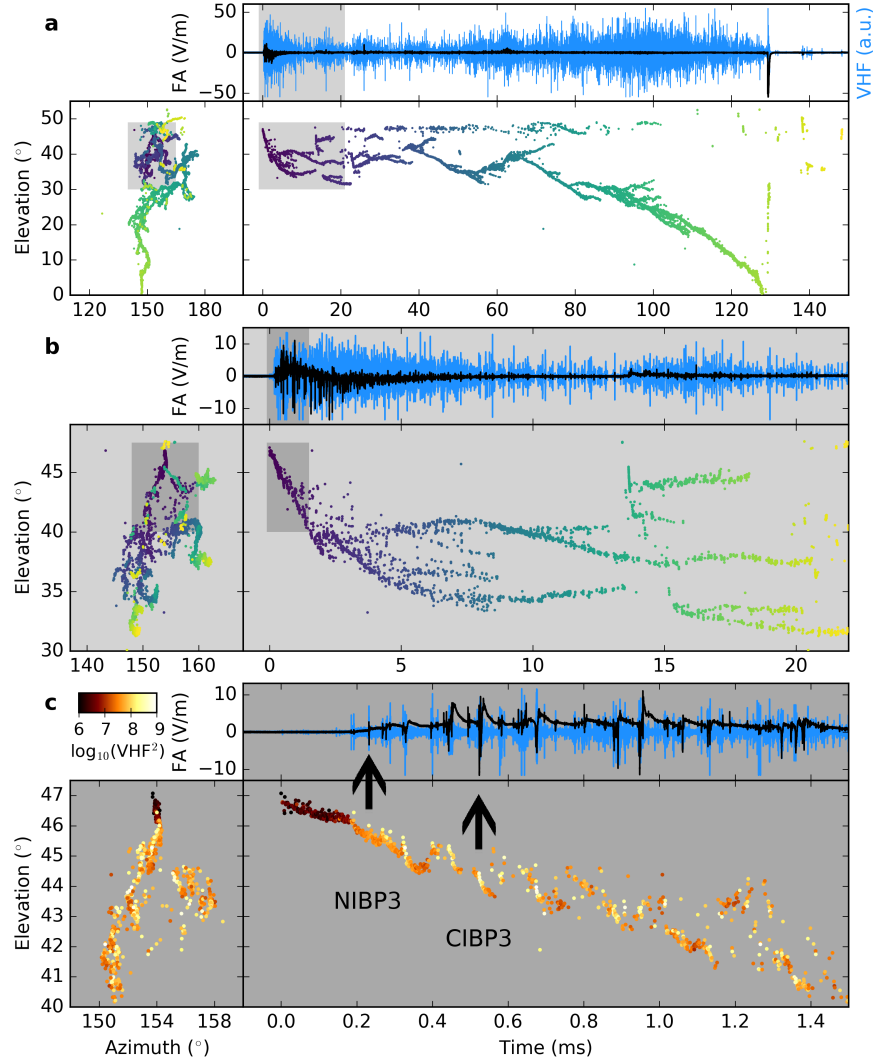


Figure 9.10: 2016.09.02 CG3 flash overview. (a) The whole flash, showing the FA and VHF waveforms (black and blue waveforms, respectively), and INTF sources (markers colored by time) are shown in elevation versus azimuth, and elevation versus time. (b) Same as (a), but for the highlighted light-gray region in (a). The flash initially developed two main branches, each having relatively small branches for the first 1.5 ms, but becoming increasingly branched and developing more horizontally over time, with the leader reaching ground after $\simeq 130$ ms. (c) Same as (b), but for the highlighted dark-gray region in (b) and with INTF sources colored by VHF power. The flash was initiated without an apparent NBE or fast breakdown, and instead was initiated by low-power VHF activity, similar to the FA-quiet INTF sources immediately following the NBE in Figure 9.9c, and lasting $\simeq 180 \mu\text{s}$. From $\simeq 180 \mu\text{s}$ to 1.5 ms, $\simeq 19$ narrow IBPs and 6 classic IBPs occurred, with FA-quiet periods occurring in-between most pulses.

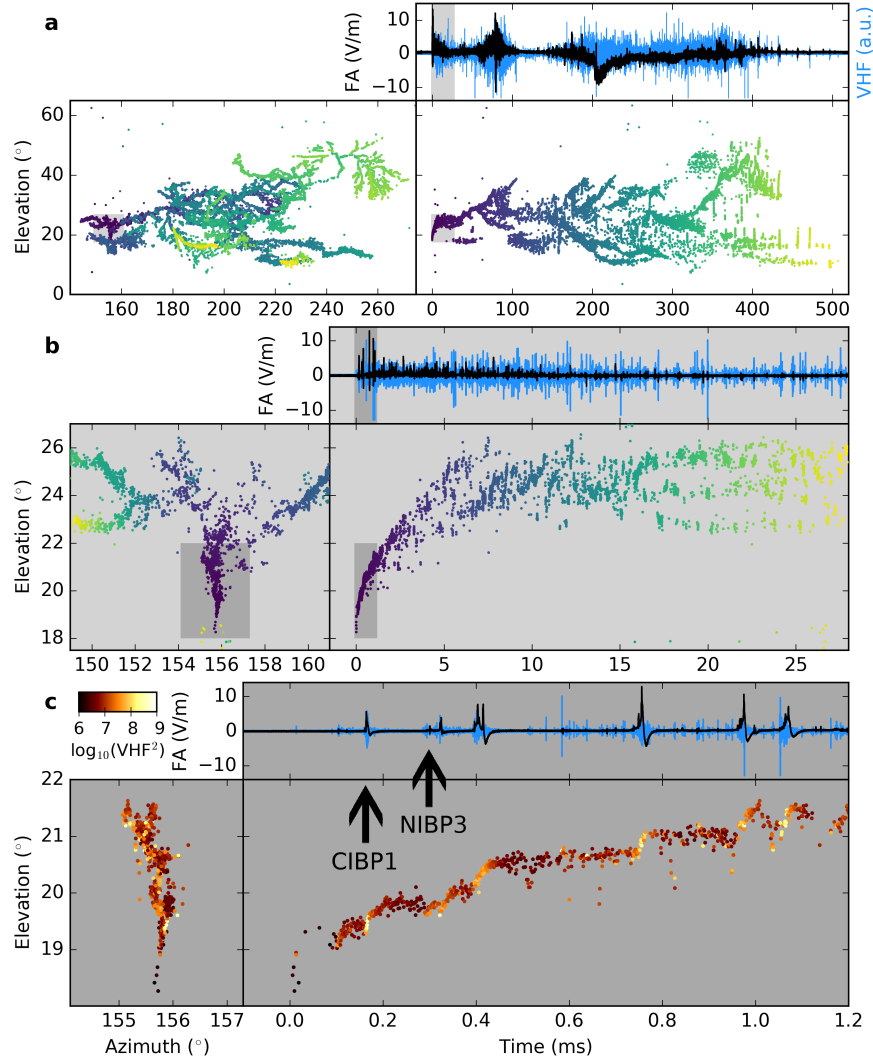


Figure 9.11: 2016.08.09 IC1 flash overview. (a) The whole flash, showing the FA and VHF waveforms (black and blue waveforms, respectively), and INTF sources (markers colored by time) are shown in elevation versus azimuth, and elevation versus time. (b) Same as (a), but for the high-lighted light-gray region in (a). The flash initially developed vertically, but became increasingly branched and developed more horizontally over time. (c) Same as (b), but for the highlighted dark-gray region in (b) and with INTF sources colored by VHF power. The flash was initiated without an apparent NBE or fast breakdown, and instead was initiated by low-power VHF activity, similar to the FA-quiet INTF sources immediately following the NBE in Figure 9.9c and the initiating breakdown in Figure 9.10c, lasting $\simeq 100 \mu\text{s}$. From $\simeq 100 \mu\text{s}$ to 4.0 ms, $\simeq 18$ narrow IBPs and 6 classic IBPs occurred, with FA-quiet periods occurring in-between most pulses.

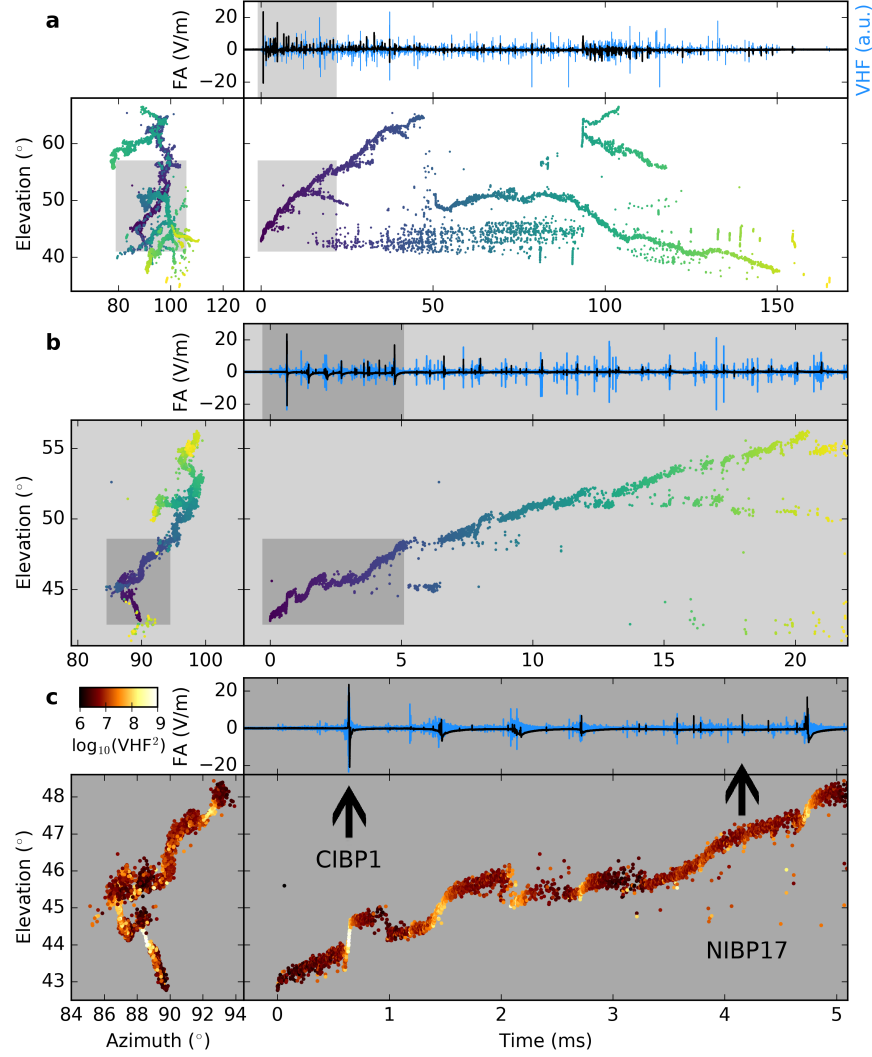


Figure 9.12: 2016.09.02 IC2 flash overview. (a) The whole flash, showing the FA and VHF waveforms (black and blue waveforms, respectively), and INTF sources (markers colored by time) are shown in elevation versus azimuth, and elevation versus time. (b) Same as (a), but for the high-lighted light-gray region in (a). The flash initially developed without visible branching, developing several branches and developing more horizontally over time. (c) Same as (b), but for the high-lighted dark-gray region in (b) and with INTF sources colored by VHF power. The flash was initiated without an apparent NBE or fast breakdown, and instead was initiated by low-power VHF activity, similar to the FA-quiet INTF sources immediately following the NBE in Figure 9.9c and the initiating breakdown in Figures 9.10c and 9.11c, lasting $\simeq 550 \mu\text{s}$. From $\simeq 550 \mu\text{s}$ to 4.0 ms, $\simeq 14$ narrow IBPs and 4 classic IBPs occurred, with FA-quiet periods occurring in-between most pulses.

9.7.2 Events analyzed during the initial stage

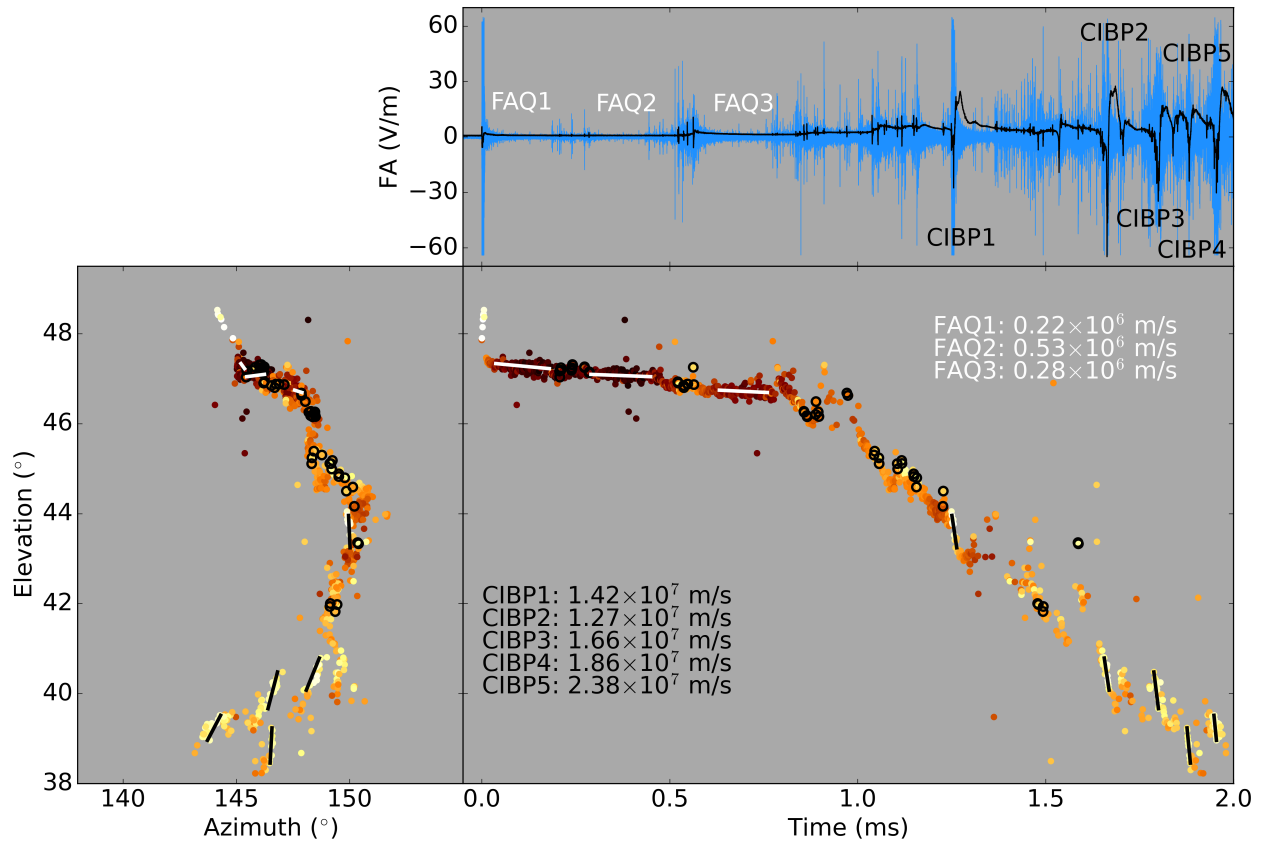


Figure 9.13: 20160824 CG1 analysis. The 2-D speeds of classic IBPs (black lines) and FA-quiet periods (white lines) are shown superimposed on activity during the initial flash development shown in Figure 9.9c. The black circles denote the sources corresponding to each narrow IBP.

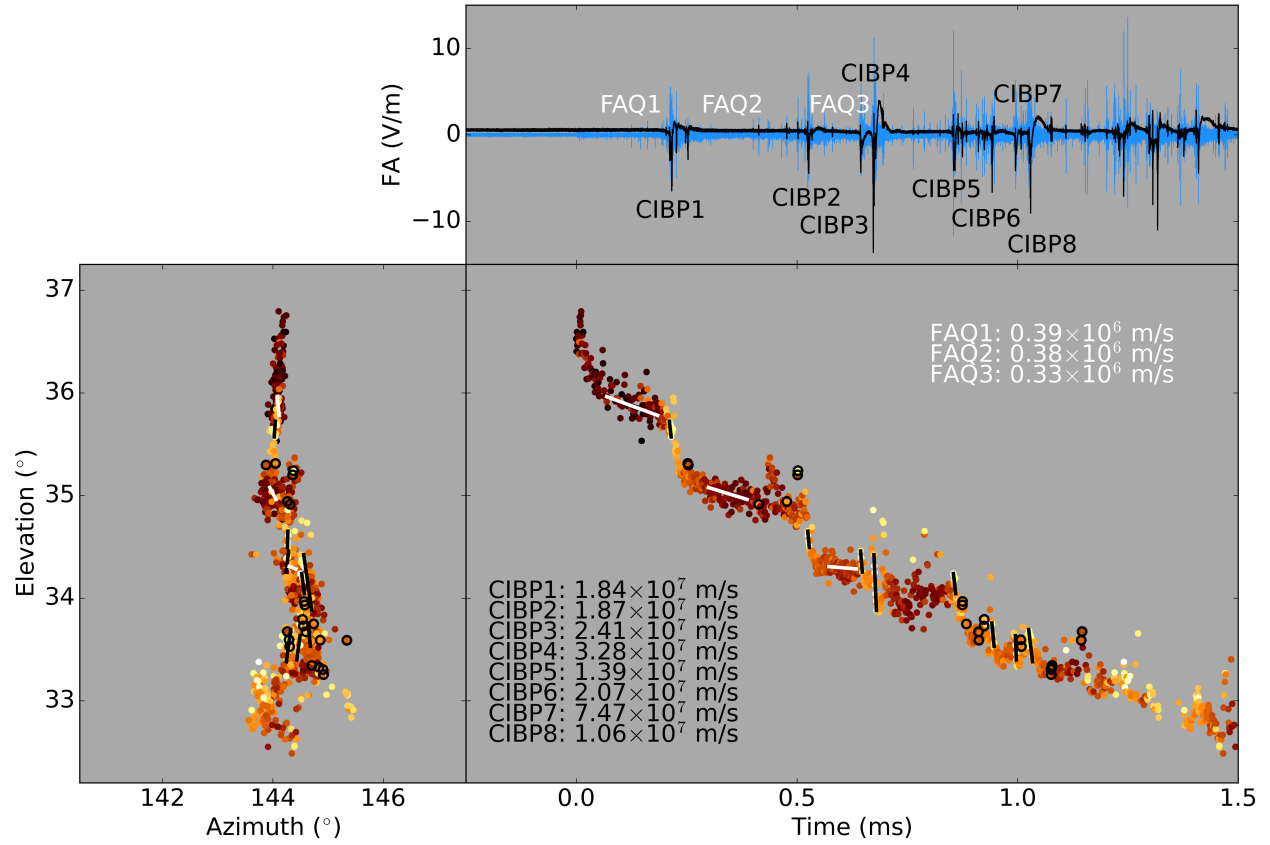


Figure 9.14: 20160824 CG2 analysis. The 2-D speeds of classic IBPs (black lines) and FA-quiet periods (white lines) are shown superimposed on activity during the initial flash development shown in Figure 9.9c. The black circles denote the sources corresponding to each narrow IBP.

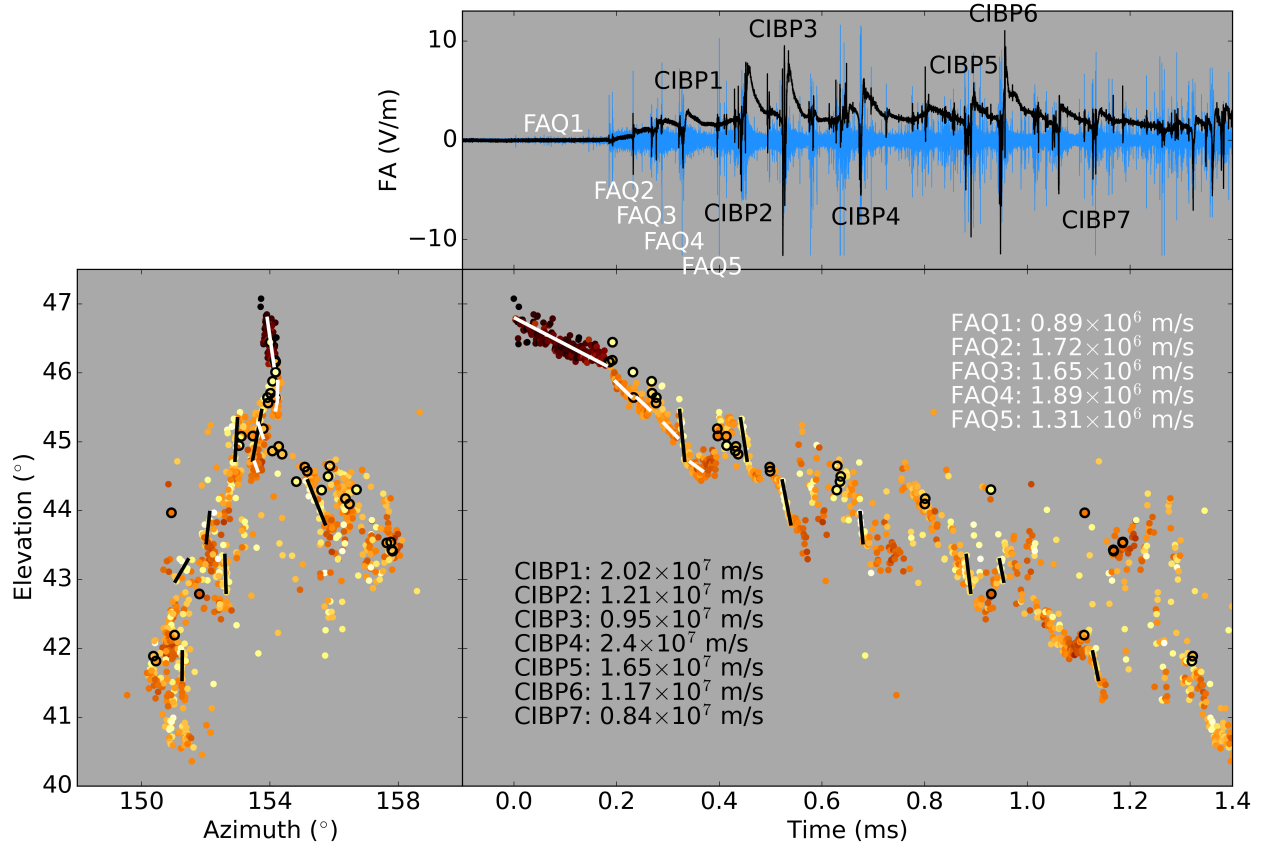


Figure 9.15: 20160902 CG3 flash analysis. The 2-D speeds of classic IBPs (black lines) and FA-quiet periods (white lines) are shown superimposed on activity during the initial flash development shown in Figure 9.10c. The black circles denote the sources corresponding to each narrow IBP.

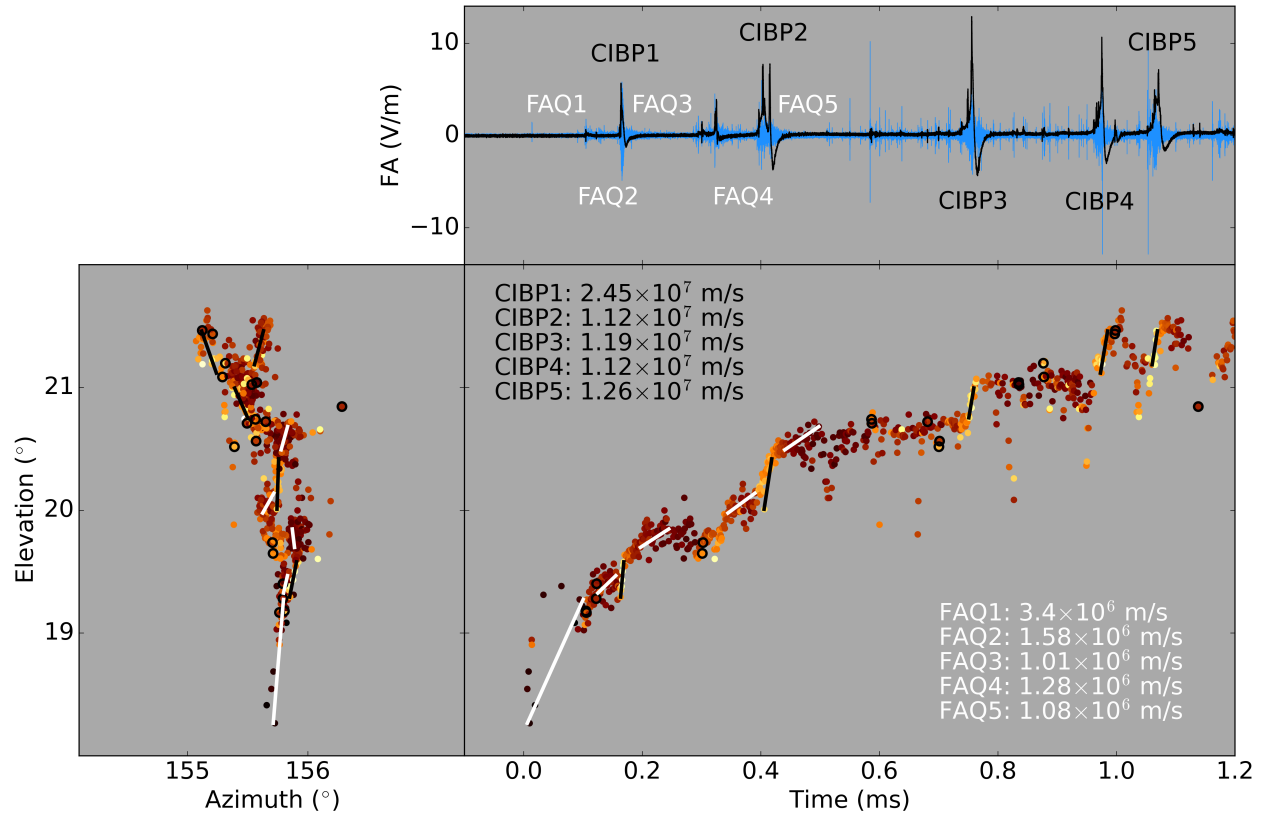


Figure 9.16: 20160809 IC1 analysis. The 2-D speeds of classic IBPs (black lines) and FA-quiet periods (white lines) are shown superimposed on activity during the initial flash development shown in Figure 9.11c. The black circles denote the sources corresponding to each narrow IBP.

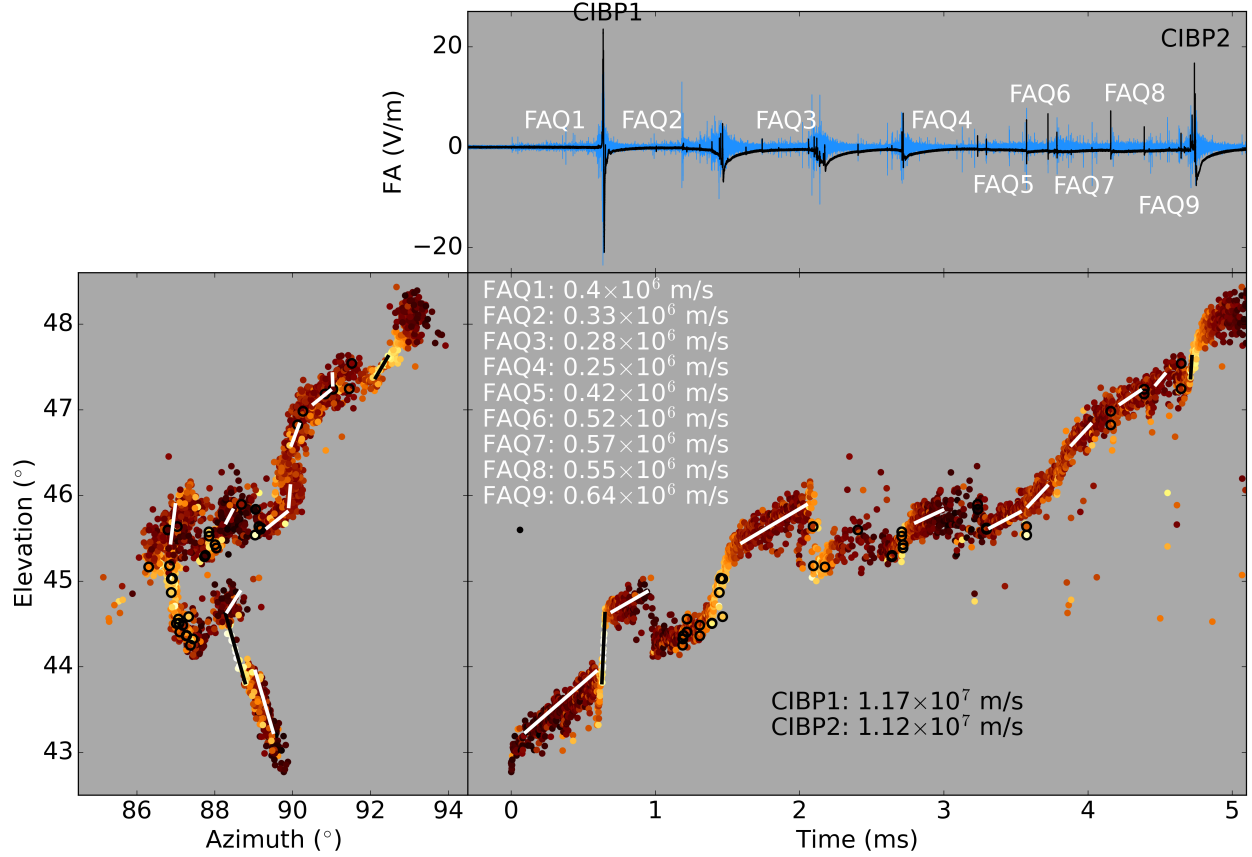


Figure 9.17: 20160902 IC2 analysis. The 2-D speeds of classic IBPs (black lines) and FA-quiet periods (white lines) are shown superimposed on activity during the initial flash development shown in Figure 9.12c. The black circles denote the sources corresponding to each narrow IBP.

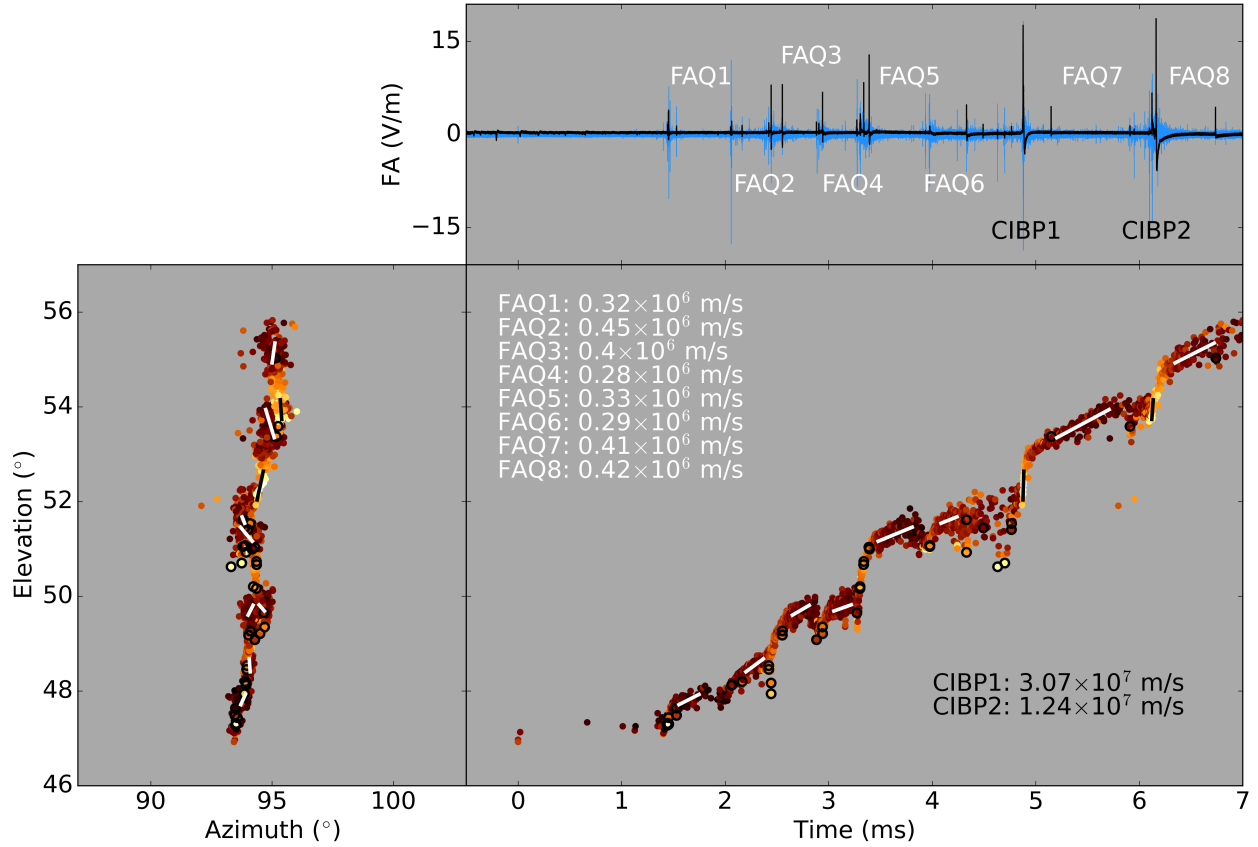


Figure 9.18: 20160914 IC3 analysis. The 2-D speeds of classic IBPs (black lines) and FA-quiet periods (white lines) are shown superimposed on activity during the initial flash development shown in Figure 9.12c. The black circles denote the sources corresponding to each narrow IBP.

9.7.3 Lightning mapping array (LMA) data

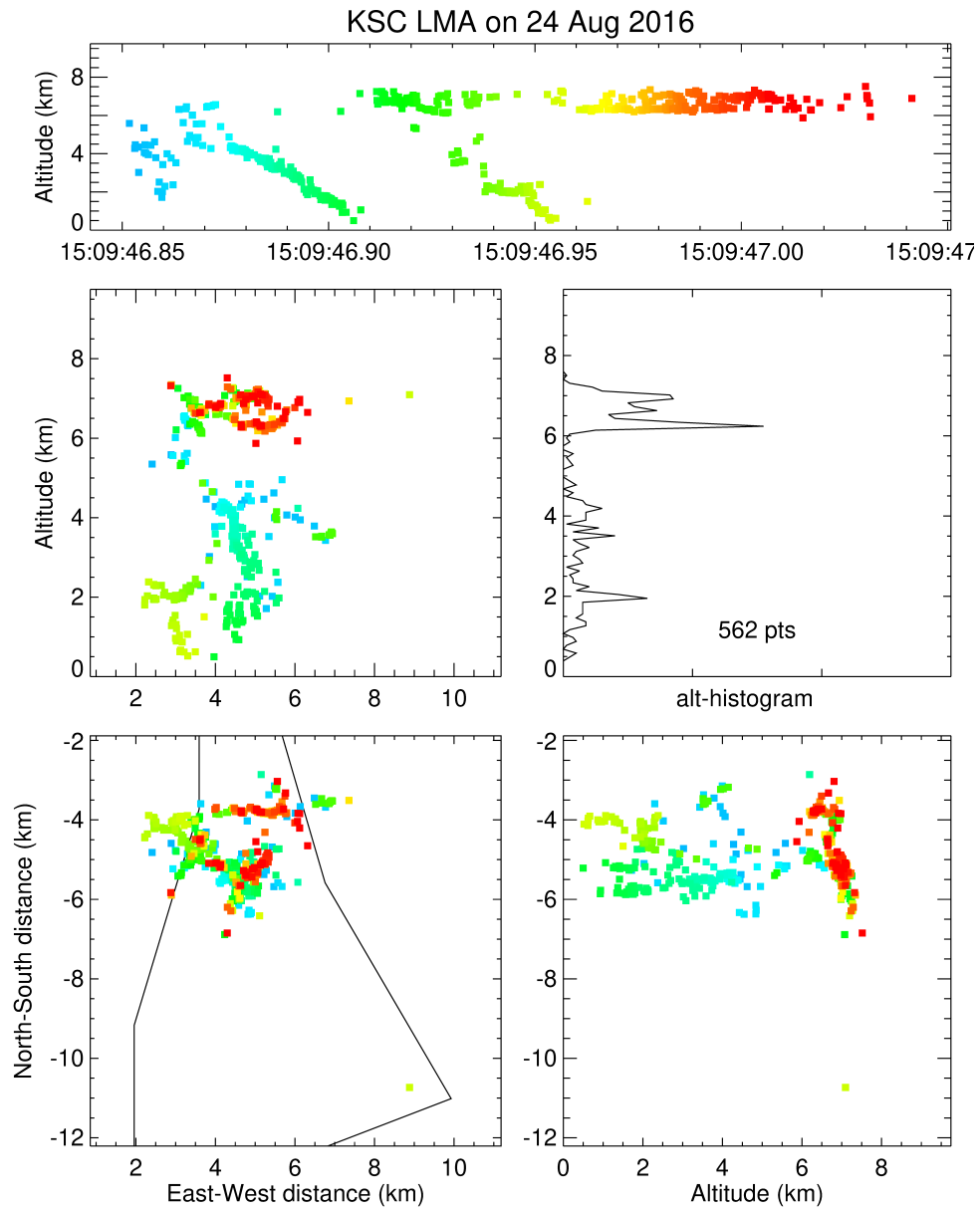


Figure 9.19: 20160824 CG1 lightning mapping array (LMA) data. LMA sources are colored by time, with blue sources indicating earlier times, and red sources indicating later times. The negative cloud-to-ground flash initiated about 6 km plan distance southeast of the INTF, at an altitude of about 6 km.

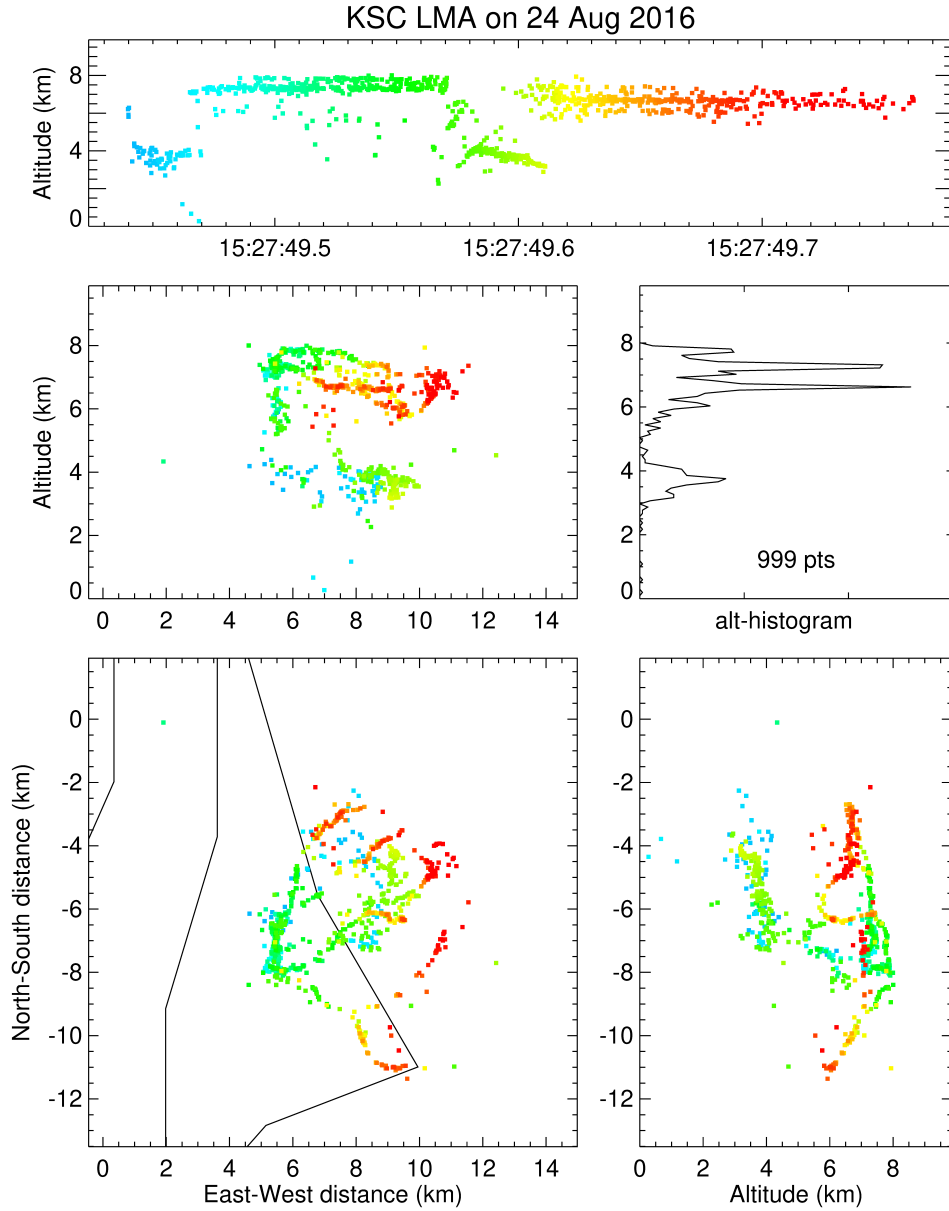


Figure 9.20: 20160824 CG2 lightning mapping array (LMA) data. LMA sources are colored by time, with blue sources indicating earlier times, and red sources indicating later times. The negative cloud-to-ground flash initiated about 9.1 km plan distance southeast of the INTF, at an altitude of about 6.5 km.

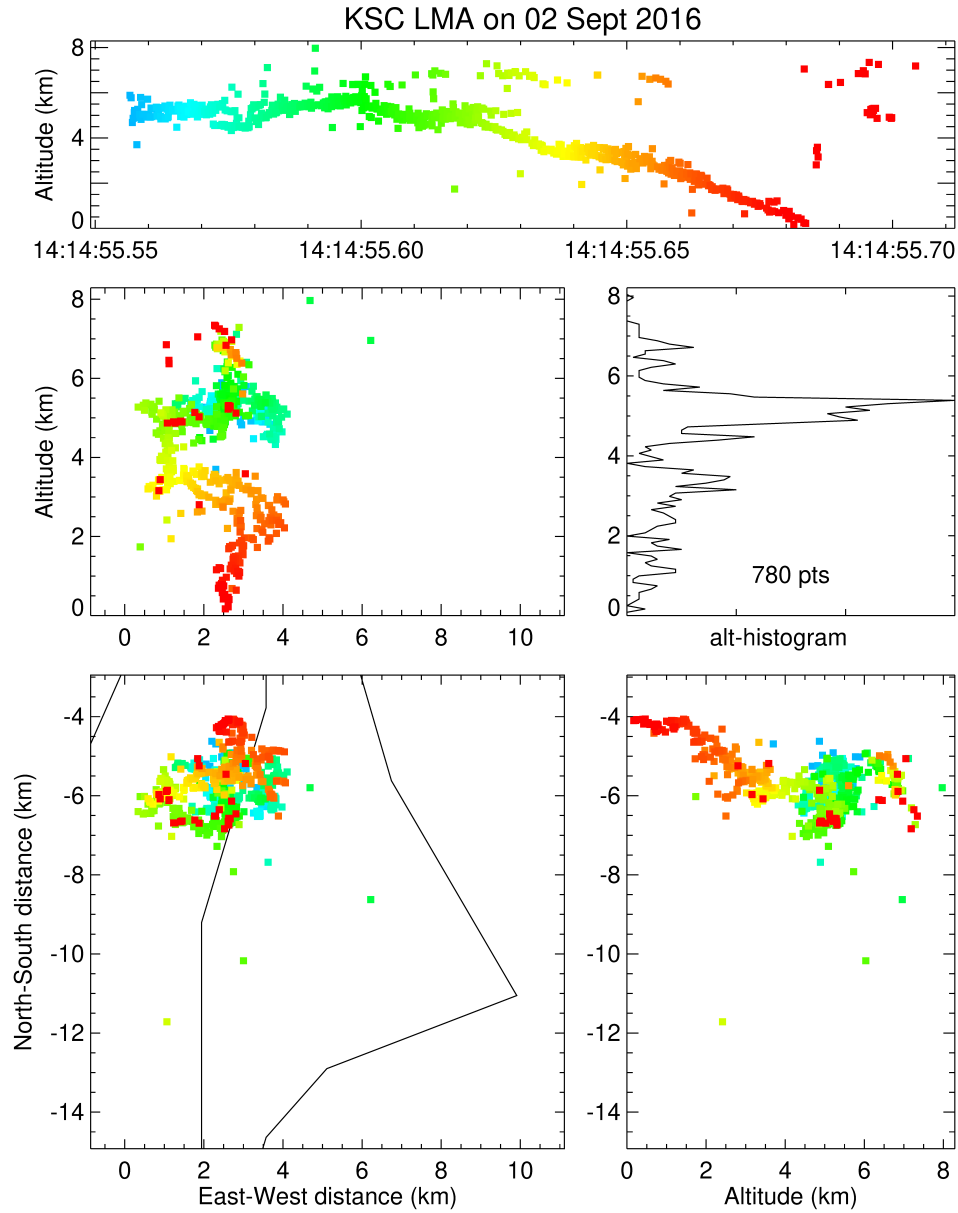


Figure 9.21: 20160902 CG3 lightning mapping array (LMA) data. LMA sources are colored by time, with blue sources indicating earlier times, and red sources indicating later times. The negative cloud-to-ground flash initiated about 6.1 km plan distance nearly due south of the INTF, at an altitude of about 6 km.

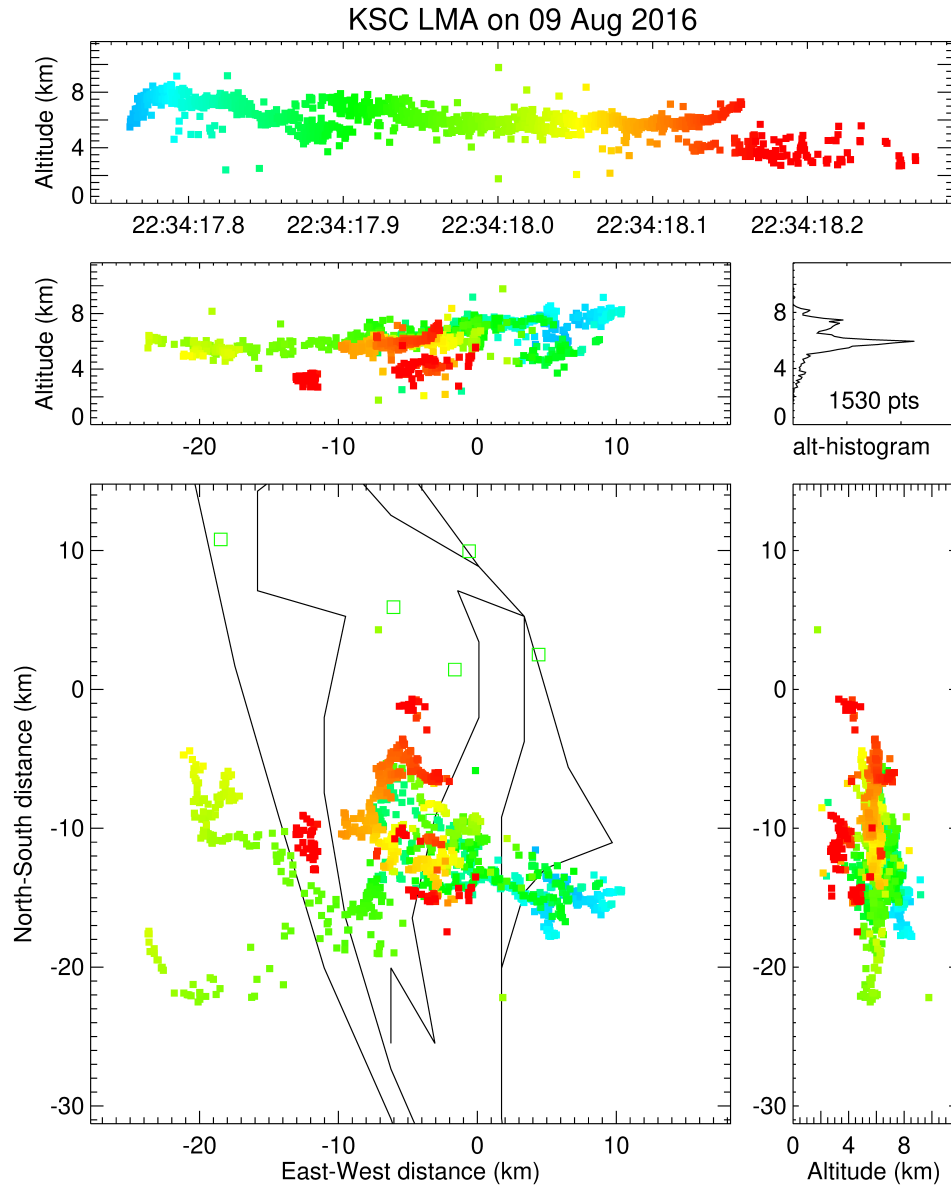


Figure 9.22: 20160809 IC1 lightning mapping array (LMA) data. LMA sources are colored by time, with blue sources indicating earlier times, and red sources indicating later times. The normal-polarity intracloud flash initiated about 15.5 km plan distance southeast of the INTF, at an altitude of about 6 km.

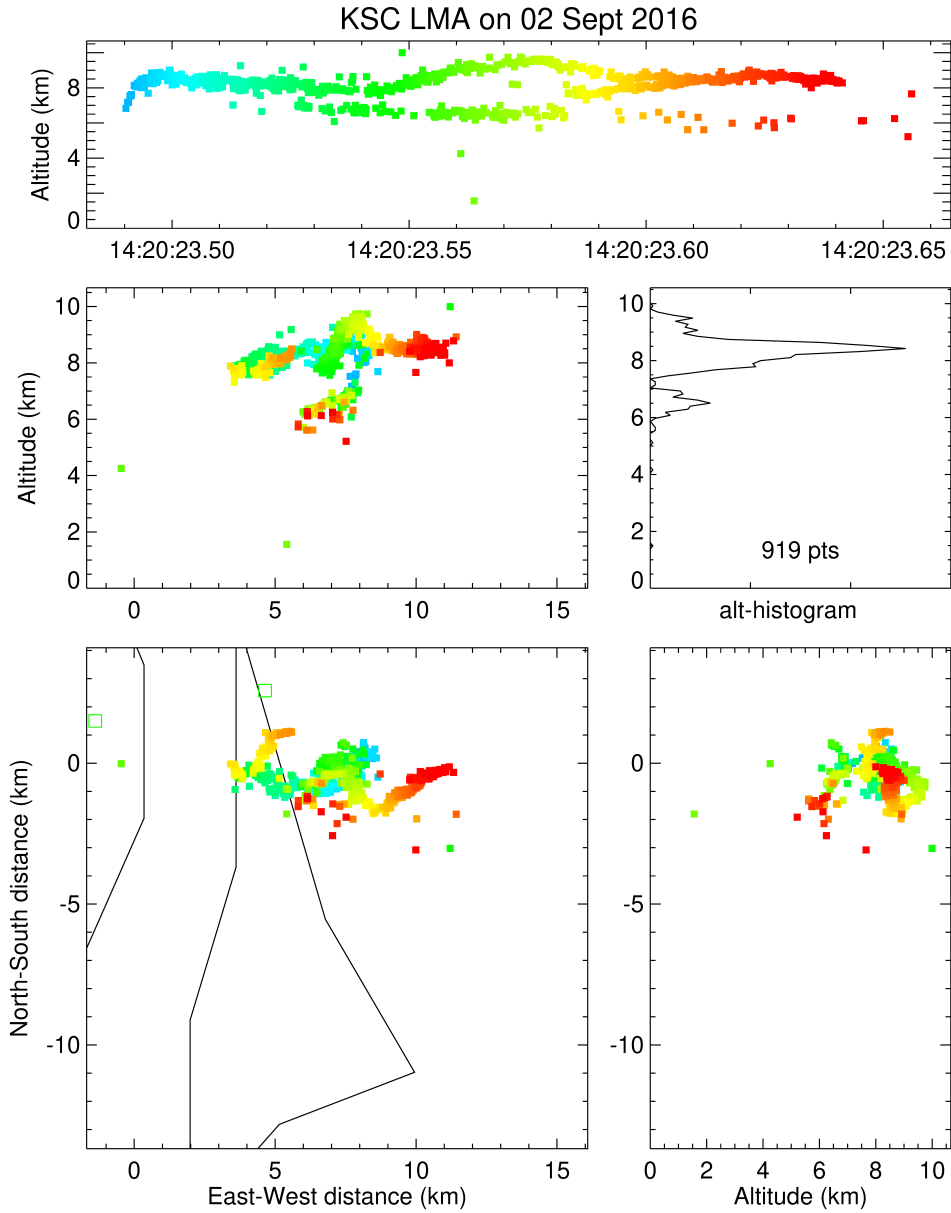


Figure 9.23: 20160902 IC2 lightning mapping array (LMA) data. LMA sources are colored by time, with blue sources indicating earlier times, and red sources indicating later times. The normal-polarity intra-cloud flash initiated about 7.8 km plan distance nearly due east of the INTF, at an altitude of about 7 km.

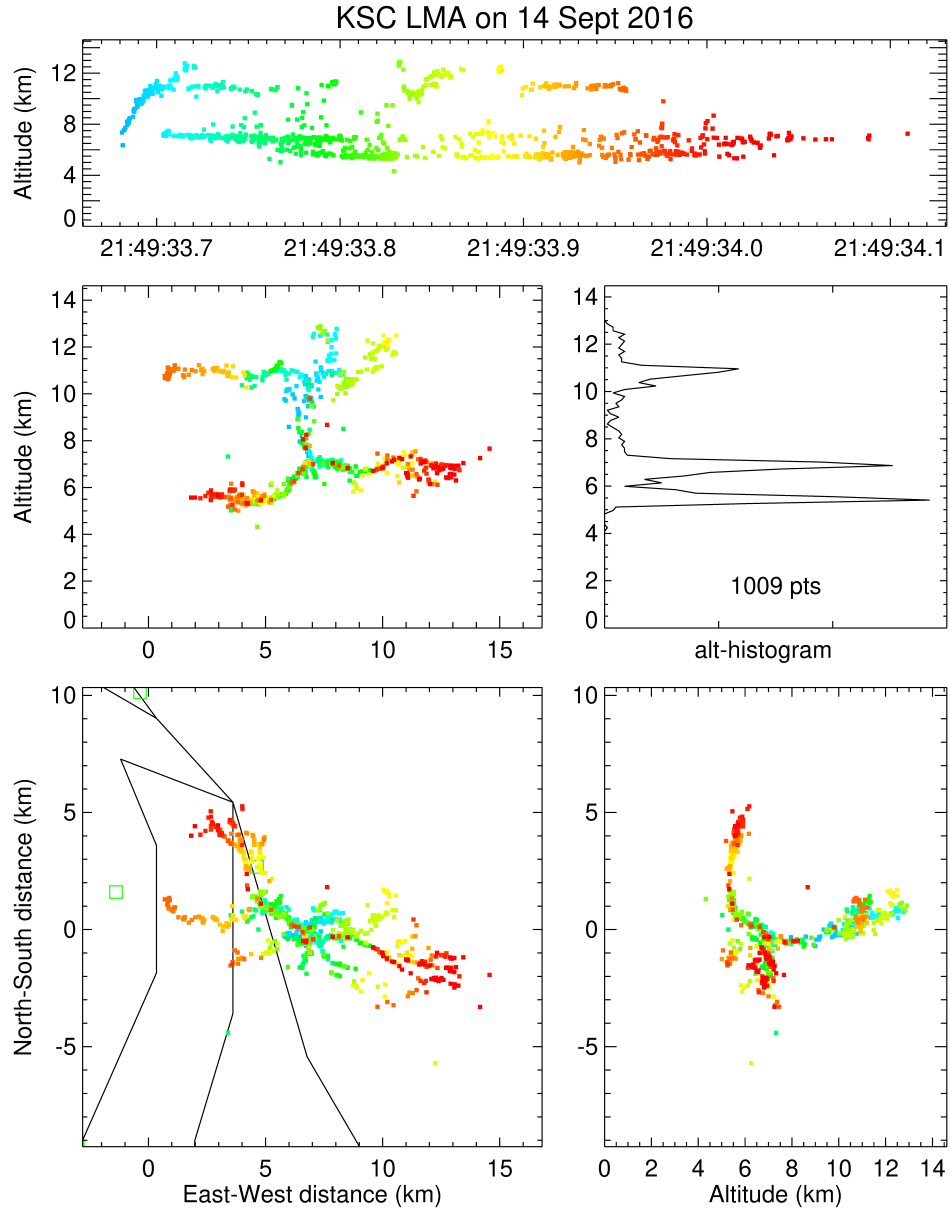


Figure 9.24: 20160914 IC3 lightning mapping array (LMA) data. LMA sources are colored by time, with blue sources indicating earlier times, and red sources indicating later times. The normal-polarity intra-cloud flash initiated about 6.8 km plan distance nearly due east of the INTF, at an altitude of about 7.5 km.

CHAPTER 10

ENERGETIC IN-CLOUD PULSE

10.1 Overview

The production mechanism for terrestrial gamma ray flashes (TGFs) is not entirely understood, and details of the corresponding lightning activity and thunderstorm charge structure have yet to be fully characterized. Here we examine sub-microsecond VHF (14–88 MHz) radio interferometer (INTF) observations of a 247-kA peak-current EIP, or energetic in-cloud pulse, a reliable radio signature of a subset of TGFs (Lyu *et al.*, 2016; Cummer *et al.*, 2017). In combination with LMA and FA data, the observations provide a detailed picture of the altitude, physical extent, propagation speed, and polarity of the EIP-associated breakdown, as well as information about the storm context in which it occurred. The EIP consisted of three high-amplitude sferic pulses lasting $\simeq 60 \mu\text{s}$ in total, which peaked during the second (main) pulse. The EIP occurred during a normal-polarity intracloud lightning flash that was highly unusual, in that the initial upward negative leader was particularly energetic and discharged a highly concentrated region of upper-positive storm charge. The flash was initiated by a high-power (46 kW) narrow bipolar event (NBE) (Rison *et al.*, 2016; Tilles *et al.*, 2019; Liu *et al.*, 2019), and the EIP occurred about 3 ms later after $\simeq 3$ km upward flash development. The EIP was preceded $\simeq 200 \mu\text{s}$ earlier by a fast 6×10^6 m/s upward negative breakdown, and immediately preceded and accompanied by repeated sequences of fast (10^7 – 10^8 m/s) downward then upward kilometer-length streamer events each lasting 10 to 20 μs , which repeatedly discharged a large volume of positive charge. Although the repeated streamer sequences appeared to be a characteristic feature of the EIP and were presumably involved in initiating it, our observations support the idea that the sferic itself was produced by relativistic discharge currents, rather than the streamer processes. Moreover, the relativistic currents during the main sferic pulse

initiated a strong NBE-like event comparable in VHF power (50.6 dBW or 115 kW) to the highest-power NBEs.

10.2 EIP detection

On 24 September 2016 an intense intracloud lightning flash occurred off the east Florida coast near Kennedy Space Center (KSC). The flash was detected by the National Lightning Detection Network (NLDN) as having a peak current of 247.3 kA, and was subsequently confirmed as being an EIP using the Duke low frequency (LF) magnetic field sensor located at the Florida Institute of Technology (FIT). The Duke instrument is sensitive from $\simeq 1$ to 300 kHz, and acts as a dB/dt sensor below 200 kHz (Cummer *et al.*, 2011).

The flash that produced the EIP was initiated by a high-power NBE that had an LMA-detected VHF power of 46.6 dBW (46 kW) and an NLDN-detected peak current of 17 kA. The EIP occurred 3.25 ms into the flash with a much larger peak current of 247.3 kA and an associated peak VHF power of 50.6 dBW (115 kW). A detailed listing of the LMA and NLDN data for the initial $\simeq 4.5$ ms of the flash is presented in Table 10.2 of Section 10.8. Figure 10.1a shows 4.5 ms of the FA electric and LF magnetic field waveforms, spanning from the initiating NBE through the time of the EIP. Panels (c,d) show expanded views of the $E(t)$ and dB/dt waveforms, along with time-integrated estimates of $B(t)$ (blue waveforms). For electromagnetic radiation, the two are related by $B(t) = E(t)/c$, and thus should have matching waveforms. Due to the FA having a broader bandwidth than the magnetic sensor, and also providing a direct measure of the electric field change, $E(t)$ has better temporal resolution and clarity than the $B(t)$ estimate. Nevertheless, for the longer-lasting and slower EIP waveforms of panel (d), the $B(t)$ estimate reproduces the three positive peaks of the FA sferic, as well as the negative undershoot at the end of the EIP. Because the magnetic sensor is a slightly imperfect detector of dB/dt at higher frequencies (Cummer *et al.*, 2011), its time-integrated waveform in panel (d) exhibits unphysical offsets at the comple-

tion of the NBE and EIP. This is exacerbated by the magnetic sensor saturating during the EIP, producing the sawtooth-like integrated waveform.

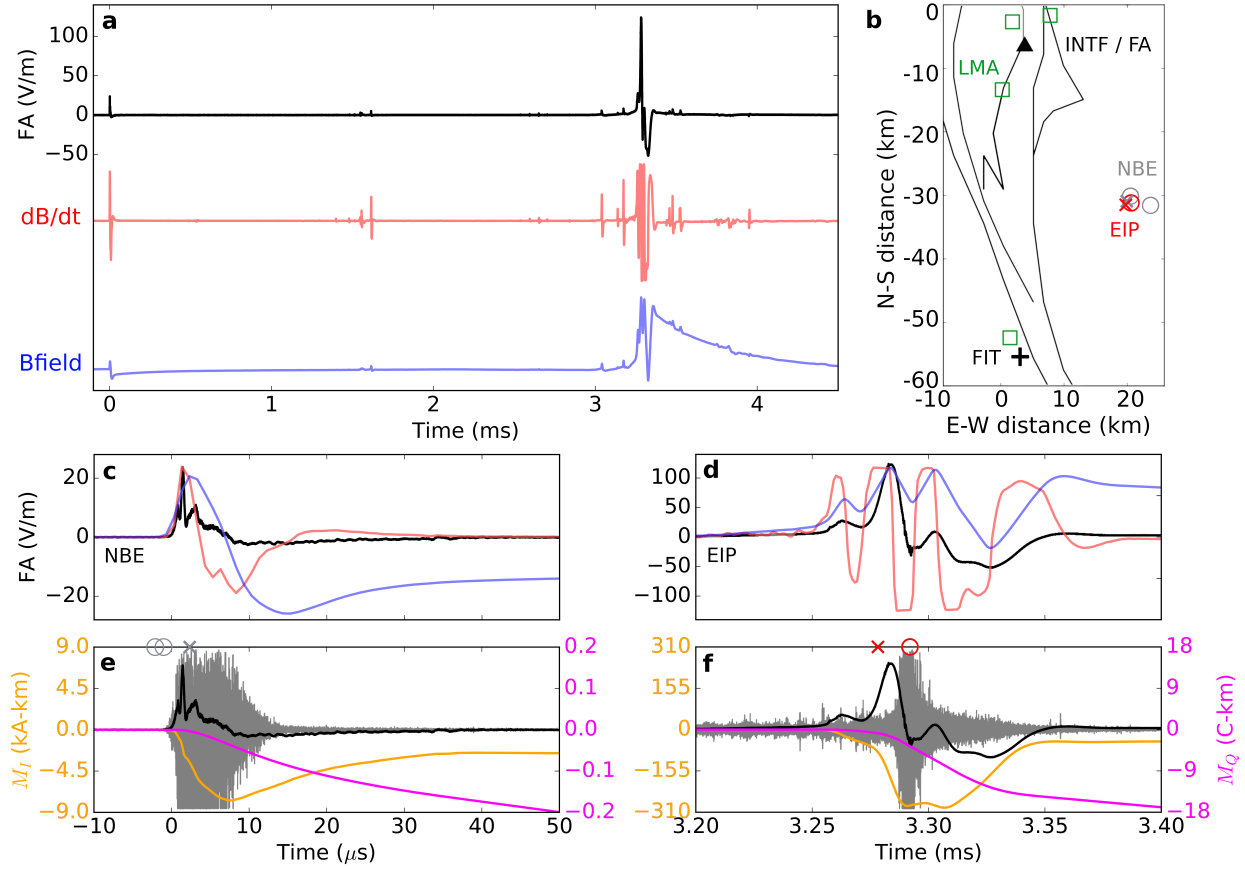


Figure 10.1: Observations of the Florida EIP, showing (a) the fast $E(t)$ and Duke ($\sim dB/dt$) waveforms for the first 4.5 ms of the flash, and (c,d) expanded views of the waveforms for the initiating NBE and EIP event. The panels also show the time-integrated estimate of $B(t)$ (blue waveforms) and their comparison with the directly-measured $E(t)$ waveforms (red). Panels (e) and (f) show the corresponding current- and charge-moment changes, M_I (orange) and M_Q (pink), obtained by integrating the $E(t)$ waveform (black). The changes are superimposed on the VHF waveform from the INTF, along with the times of the LMA and NLDN detections ('o' and 'x' symbols, respectively). The plan view map of panel (b) shows the offshore locations of the NBE and EIP by the LMA and NLDN relative to the INTF at KSC (black triangle), and the Duke sensor at FIT (black '+'), along with the locations of four of the KSC LMA stations (green squares).

According to the criteria established in (Lyu *et al.*, 2015), the spheric of Figure 10.1d is characterized as an EIP due to its long “pulse width” (54 μ s), its less-than-unity “peak ratio” (<0.9), which indicates the secondary peak is higher-amplitude than the initial peak, and its fairly low

“isolation ratio” (18 dB), indicating the EIP was not isolated but had preceding and subsequent activity, as seen in the dB/dt waveform of Figure 10.1a. In contrast, the spheric of the initiating NBE in Figure 10.1c is typical of NBE events, having a short pulse width (14 μ s), a greater-than-unity 1st to 2nd peak ratio (1.3), and a high isolation ratio (73 dB). The current- and charge-moment changes $M_I(t)$ and $M_Q(t)$ as a function of time are obtained by successively integrating the FA waveforms of the NBE and EIP, and are shown in Figures 10.1e,f. The resulting numerical values are summarized in Table 10.1. For the NBE, the peak current moment was $M_I(t=8 \mu\text{s}) = -7.7 \text{ kA-km}$, and was generated by downward fast positive breakdown (FPB) similar to that observed by Rison *et al.* (2016). For the EIP, the integration started at $t=3.2 \text{ ms}$, a few tens of microseconds before the EIP onset, and gives a peak current moment $M_I(t=3.31 \text{ ms}) = -293.0 \text{ kA-km}$. This is consistent with the NLDN peak current estimate of 247.3 kA and the INTF observations showing a $\simeq 1\text{-km}$ vertical extent of the EIP discharge (see Section 10.5). The charge-moment change $M_Q(t)$ is obtained by twice-integrating the FA waveforms, giving a value of $M_Q(t=30 \mu\text{s}) = -0.15 \text{ C-km}$ for the NBE, comparable to the values obtained for NBEs by Rison *et al.* (2016). For the EIP, $M_Q(t=3.38 \text{ ms}) = -16 \text{ C-km}$, two orders of magnitude larger than that of the NBE.

Figure 10.1b shows the plan location of the NBE and EIP relative to the INTF and FIT sites. LMA and NLDN observations show that the two events occurred in close proximity to each other, about 30.5 km south-southeast of the INTF/FA and at a similar distance north-northeast of the FIT magnetic field sensor. As typically happens, the initiating NBE was mislocated by the LMA (see Figure 10.8 of Section 10.8). The mislocation is a consequence of the FPB being VHF noisy during the strong radiation, causing different LMA stations to detect slightly different peaks. This is a characteristic feature of NBEs that is useful in identifying their occurrence and the streamer nature of the breakdown (Rison *et al.*, 2016; Tilles *et al.*, 2019) (see Section 7.2). In addition to being mislocated, the LMA obtained two solutions for the NBE, both having the same VHF powers but substantially different locations and goodness of fit values (see Table 10.2 in Section 10.8). The two solutions were separated in time by $\simeq 1 \mu\text{s}$ and resulted from the NBE’s VHF radiation straddling a boundary between successive 80 μs time windows at some of the LMA stations, which

caused large-amplitude peak values on both sides of the boundary, providing two independent sets of arrival times and solutions. Both solutions were mislocated relative to the weaker, more impulsive and accurately-located LMA sources immediately following the NBE, which were tightly clustered and in good agreement (to better than 200 m) with the NLDN location (see Figure 10.8b in Section 10.8). Consequently, while the NLDN timing (‘x’ in Figure 10.1e) agreed well with the NBE sferic (better than 1 μ s after taking into account the travel time from the NLDN-determined NBE location to the INTF/FA), the NBE timing was poorly determined by the LMA (double circles in Figure 10.1e), with the LMA sources appearing to occur about 4 μ s before the onset of the NBE. In contrast, the LMA solution for the EIP was relatively well-fitted (reduced chi-square of 0.21), and its timing was in good agreement with the peak in the VHF waveform of the EIP (circle in Figure 10.1f). Importantly, and unlike the NBE, both the onset of the 247 kA FA sferic and the NLDN detection of the sferic occurred well before the onset of strong VHF radiation during the EIP, by $\simeq 6\text{--}12$ μ s.

	NLDN I_{pk} (kA)	ΔE_{pk} (V/m)	$M_{I,\text{pk}}$ (kA-km)	M_Q (C-km)	LMA P_{pk} (dBW, kW)	τ_{rise} (μ s)	Δz (km)
NBE	17.0	24	-7.1	-0.15 ($t=[0, 30 \mu\text{s}]$)	46.6, 46	0.25	0.6
EIP	247.3	123	-285.1	-16.0 ($t=[3.2, 3.38 \text{ ms}]$)	50.6, 115	1.2	1.5

Table 10.1: Summary of the EIP and NBE characteristics, namely the NLDN peak current I_{pk} , peak FA sferic ΔE_{pk} , peak current-moment $M_{I,\text{pk}}$, total charge-moment change M_Q , LMA peak power P_{pk} , rise time τ_{rise} of INTF VHF power, and vertical extents Δz of the flash-initiating NBE and the EIP. Note that the peaks in I , ΔE , M_I , and P are not necessarily simultaneous for each event. M_I and M_Q are obtained by once- and twice-integrating the FA signal, respectively. The integration starts at time $t=0$ for the NBE, and at $t=3.2$ ms for the EIP. τ_{rise} is determined by fitting a line to the natural log of the squared INTF VHF signal for each event. The vertical extent of each event is determined from the INTF elevation observations and the plan distance determined by the LMA locations, and depicts the span of INTF sources from the integration start time up to the peak in M_I .

10.3 EIP-generating flash

Figure 10.2 shows an overview of the spatial structure and temporal development of the EIP-generating flash. Panels (a,b) show the LMA source locations for the flash (white dots) super-

imposed on the LMA-determined charge structure of the parent storm. The storm had a normal-polarity tripole charge structure (Krehbiel, 1986), consisting of dominant mid-level negative (blue) and upper positive (red) charges, and a lesser lower positive charge. The storm had a low average flash rate of 1.4 min^{-1} over its 21-minute lifetime between 00:48:15 to 01:09:15 UT. The EIP flash occurred at 00:55:12.7, about seven minutes into the storm, and was in a new, convectively vigorous cell on the eastern side of the storm that started producing lightning about 3 min earlier. It was a normal-polarity intracloud (IC) flash that developed vertically upward in the storm between negative charge at 6–8 km altitude above mean sea level (MSL) and upper positive charge between 10–12 km MSL, as seen in the LMA and INTF observations of panels (a)–(c). As discussed in more detail in Section 10.6, the EIP flash was preceded by a nearly identical IC flash 97 s earlier, which was also initiated by a high-power (51.1 dBW, 129 kW) NBE. In turn, the EIP flash was followed 65 s later by a negative cloud-to-ground (CG) flash, whose initial return stroke had an exceptionally strong peak current of 136 kA. Combined with the EIP flash, this activity shows that the new cell was strongly electrified.

More detailed INTF observations of the flash are shown in panels (c) and (d) of Figure 10.2. The near-vertical trajectory of the sources between about 15° and 21° elevation ($\simeq 8$ and 12 km MSL) in panel (c) was produced by the upward negative leader propagating toward and into the upper positive charge, while the horizontally-extensive portion of the flash between about 12° and 15° elevation is indicative of positive breakdown propagating through mid-level negative charge. In Figure 10.2d, two distinct levels of activity are clearly visible, attributed to breakdown in the upper positive and mid-level charge regions, typical of normal-polarity IC flashes (Shao & Krehbiel, 1996; Rison *et al.*, 1999). The EIP flash was unusual, however, in that the upward negative leader did not continue to propagate through horizontally-distributed upper positive charge, as previous and subsequent IC flashes did. As a result, nearly all of the negative channel development took place during the first 3–4 ms of the flash, ending just after the EIP (see Section 10.4), though the EIP flash continued for another several hundred milliseconds. In particular, the upward channel was repeatedly re-traced by multiple K-events (Shao & Krehbiel, 1996; Akita *et al.*, 2010), which

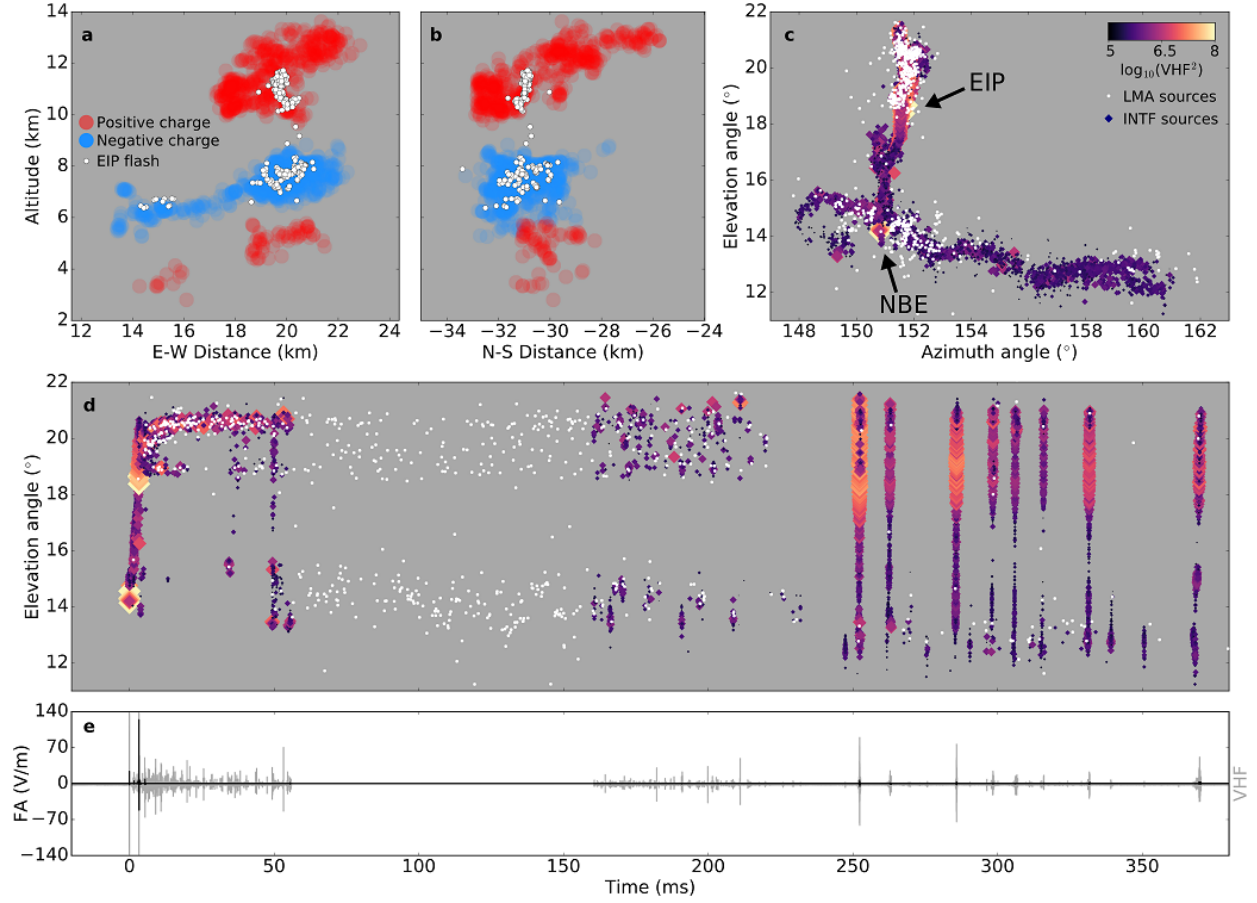


Figure 10.2: Overview of the EIP-generating flash and storm. (a,b) LMA observations of the EIP flash (white dots) overlaid on LMA-determined storm charge structure (red for positive charge, blue for negative charge) in orthogonal East-West and North-South vertical projections. The storm charge corresponds to a $\simeq 5$ -minute period of vertical storm growth that includes the EIP flash. (c,d) INTF observations for the flash, colored and sized by VHF power, and the corresponding LMA observations (white dots), plotted in elevation versus azimuth, and elevation versus time, respectively. The NBE and EIP correspond to the two groupings of high-power INTF sources in the first few milliseconds of the flash, near 14° and 18° elevation, respectively. (e) FA fast electric field change (black) and INTF VHF (gray) waveforms of the EIP flash, corresponding to the same time period as in (c) and (d).

started in the negative charge region (near 12° elevation), travelled back along the previously ionized leader path (Ogawa & Brook, 1964), and terminated in the upper-positive charge region (near 21° elevation) without extending the channel significantly further. The K-events are seen in Figure 10.2d as vertical columns of INTF sources, travelling a large elevation (9° or $\simeq 4.5$ km) over short time periods ($\simeq 300 \mu\text{s}$), or with speeds on the order of 1.5×10^7 m/s. The absence of recorded

INTF and FA data between 60 and 160 ms following an early K-event was due to the VHF radiation being weak and not retriggering the INTF recording until later in the flash. Even then, the LMA and INTF observations show that the negative channel had not developed further into upper-positive charge region. Instead, the ensuing, subsequent K-events repeatedly stopped in a relatively localized upper positive charge at the upper extent of the vertical channel established in the first 3-4 ms of the flash.

The EIP occurred about 3 ms into the flash, and repeatedly discharged a region of localized positive charge at the uppermost end of the flash. The flash-initiating NBE and EIP are depicted in Figure 10.2d by the two groups of high-power INTF sources (large yellow diamonds) near 14° and 18° elevation, respectively. In Figure 10.2c, the NBE and EIP locations are roughly indicated by arrows, and correspond to the two large FA pulses and saturated INTF signals seen in Figure 10.1e,f.

10.4 Pre-EIP breakdown

Figure 10.3 shows an expanded view of the first 3.8 ms of the flash, starting before the NBE and ending about a half millisecond after the EIP. Panel (a) shows the upward development of the negative breakdown versus time, while panels (b)–(h) show the development during successive time intervals in elevation–azimuth projection. The complete elevation vs. azimuthal development is shown in panel (i). The NBE that initiated the flash, panel (b), was produced by downward FPB that descended $\simeq 400$ m in $4 \mu\text{s}$, corresponding to a speed of $\sim 10^8$ m/s, at the upper end of observed FPB speeds (Rison *et al.*, 2016). Expanded views of the flash-initiating NBE are shown in Figure 10.9 of Section 10.8), which also shows that the NBE breakdown exhibited little horizontal spread relative to its vertical extent. The NBE produced a 24 V/m peak electric field change (8 V/m range-normalized to 100 km), and a fast ($\tau_{\text{rise}}=0.24 \mu\text{s}$) exponential rise in VHF power, that quickly saturated the VHF signal. It also initiated breakdown $\simeq 200$ m in vertical extent directly above the NBE starting point.

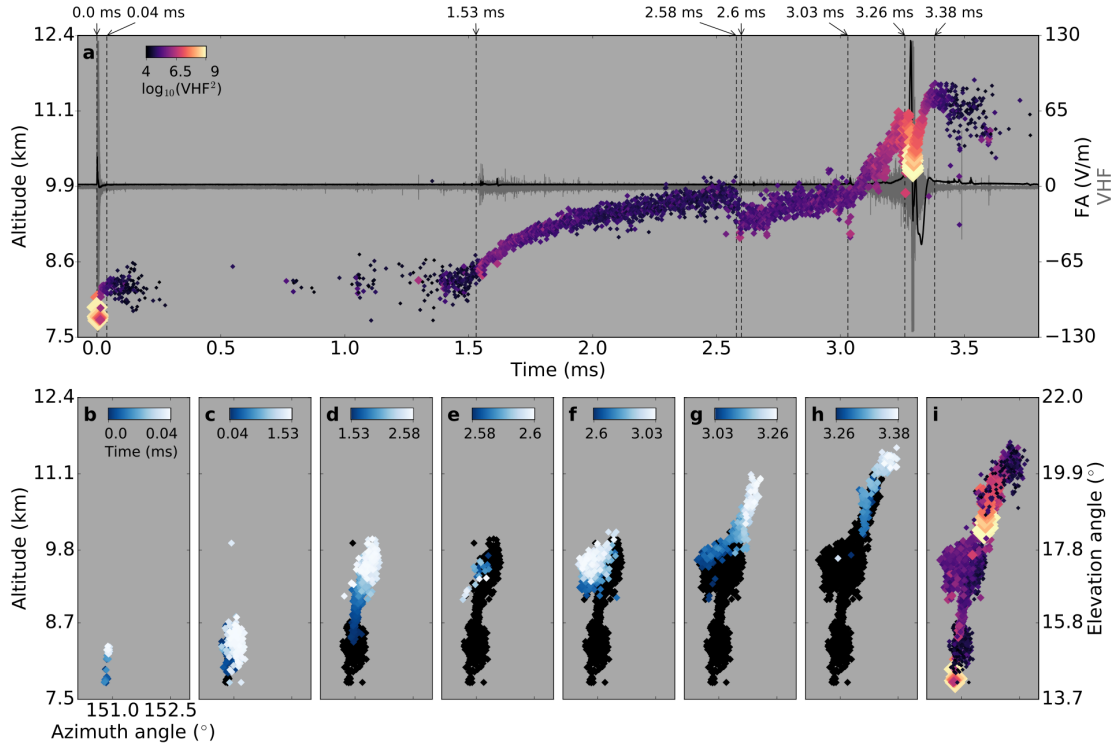


Figure 10.3: Early stages of the EIP-generating flash. (a) INTF sources for the first 3.8 ms of the flash plotted in altitude/elevation versus time, colored and sized by detected VHF power, along with the corresponding FA electric field-change (black) and INTF VHF (gray) waveforms. The vertical dashed lines separate different stages of the flash evolution, shown in altitude/elevation vs. azimuth plots in (b)-(h), where the INTF sources in each stage are colored by time and prior sources are colored in black. The stages consist of: (b) the flash-initiating NBE, lasting about $40 \mu\text{s}$, (c) about 1.5 ms of non-propagating, quiescent and scattered activity after the NBE preceding the negative leader development, (d) onset and development of the initially fast ($\approx 3.2 \times 10^6 \text{ m/s}$) negative leader, (e) a $\approx 10\text{-}\mu\text{s}$ downward “step” that interrupted the upward development of the negative leader, (f) resumption of the slowed-down ($\approx 5 \times 10^5 \text{ m/s}$) leader, (g) exceptionally fast ($6 \times 10^6 \text{ m/s}$) upward progression of INTF sources, and (h) the EIP-associated INTF sources, which depict a rapid succession of fast-propagating ($10^7\text{-}10^8 \text{ m/s}$) breakdown events. (i) INTF sources for the full 3.8 ms interval, colored and sized by detected VHF power.

Despite the strength of the NBE, and instead of launching the upward leader, the discharge appeared to die out after about $\approx 100 \mu\text{s}$, causing the flash to become relatively quiescent. For $\approx 1.4 \text{ ms}$, occasional INTF and LMA sources (Figures 10.3c and 10.8, and Table 10.2) continued to occur immediately above the NBE in the flash start region, which eventually strengthened and

launched an upward negative breakdown about 1.53 ms into the flash (Figure 10.3d). The speed of the upward breakdown was initially fast, $\simeq 3 \times 10^6$ m/s, slowing down to $\simeq 5 \times 10^5$ m/s by the time of the downward step at 2.6 ms (Figure 10.3e). The step was signaled by a transient FA sferic (Figure 10.10) that appears to be produced by new breakdown several hundred meters back down and off to the left side of the slowed-down activity of interval (d). The new breakdown continued to progress up the left side of the (d) activity before reaching the previously attained altitude (interval f), at which point a second, stronger downward FA and INTF transient occurred that initiated exceptionally fast ($\simeq 1.2$ km in $200 \mu\text{s}$, or $\simeq 6 \times 10^6$ m/s) upward negative breakdown into virgin air. In the process, the VHF power of the breakdown increased exponentially with distance by a factor of 6 or so, culminating in the EIP.

10.5 EIP detailed observations

Figure 10.4 shows an expanded view of the temporal and spatial evolution of the EIP activity, corresponding to interval (h) of Figure 10.3. As seen in panels (a) and (c)–(f) of Figure 10.4, the breakdown leading up to and during the EIP consisted of a complex sequence of repeated downward and upward breakdown events of increasing vertical extent, back and forth along the path traversed by the fast 6×10^6 m/s upward breakdown at the end of the pre-EIP interval. The pseudo-oscillatory breakdown behaviour was accompanied by a sequence of three large-amplitude sferic pulses, each lasting $\simeq 20 \mu\text{s}$ between 3.25 and 3.31 ms, with a NLDN-determined peak current of 247 kA. The polarity of the sferics was positive, indicative of downward currents being produced by downward positive or upward negative charge motion. The EIP culminated in a strong burst of VHF radiation produced by a particularly high power downward/upward sequence of the INTF sources during the final part of the EIP. From the LMA observations of the burst (red circle in panel a), the peak power of the burst reached $\simeq 115$ kW.

The INTF sequences preceding the EIP are shown by the black sources at the beginning of panel (a). The propagation speeds during this time were on the order of one to a few times 10^7 m/s,

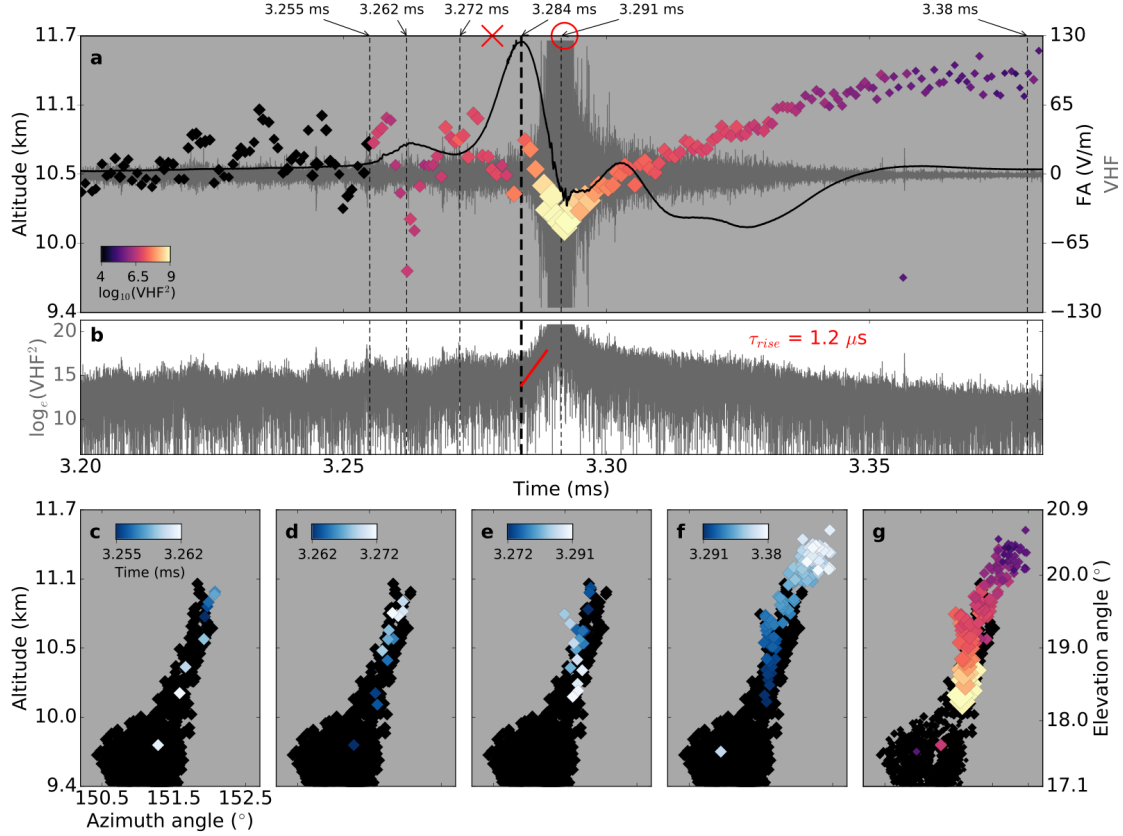


Figure 10.4: EIP detailed evolution. (a) The INTF sources during the EIP (i.e., during the time interval shown in Figure 10.3h) are plotted in altitude/elevation versus time, and are colored and sized by detected VHF power, with sources prior to the EIP colored in black, along with the corresponding FA electric field-change (black) and VHF (gray) waveforms, and the times of the NLDN ('x') and LMA ('o') events. (b) The natural log of the VHF power shows the onset of an exponential rise in VHF power (thick dashed line at 3.284 ms) up to the moment the signal saturated. The thin vertical dashed lines in (a) and (b) identify 4 successive intervals that are examined in altitude/elevation vs. azimuth plots in (c)-(f), where the sources in each interval are colored by time and prior sources are colored in black. A 12- μ s offset is visible between the onset of main EIP pulse (thin dashed line at 3.272 ms) and the onset of the large VHF burst (thick dashed line at 3.824 ms). (c) Apparent downward source motion with speed 2.6×10^8 m/s, (d) apparent upward source motion with speed 1.2×10^8 m/s, (e) apparent downward source motion with an initial speed of 5.7×10^7 m/s, then a faster speed of 1.0×10^8 m/s, and (f) upward fast negative breakdown with an initial speed of 4.2×10^7 m/s, then a slower speed of 1.3×10^7 m/s. (g) The INTF sources during the entire EIP, colored and sized by detected VHF power.

typical of streamer-based fast positive and negative breakdown (Rison *et al.*, 2016; Tilles *et al.*, 2019). As discussed above, the repeated sequences were of increasing vertical extent and occurred back along the same path as the preceding 6×10^6 m/s upward breakdown, indicating the absence

of a leader along the path. Rather, both the 6×10^6 m/s upward breakdown and repeated sequences were likely streamer-based, and were presumably involved in initiating the EIP. Indeed, the black sources were followed by the initial sferic pulse of the EIP, between 3.255 and 3.272 ms and, at the same time, the largest vertically extensive ($\simeq 1.3$ -km) and fastest downward/upward sequence up to that point in the flash (colored sources propagating downward in (c) and upward in (d), centered on 3.262 ms in (a)). The apparent propagation speeds of this complex event are difficult to ascertain, but were on the order of 10^8 m/s and even approaching the speed of light, making it unclear if some of the altitude changes represented a physically propagating breakdown front.

The 1.3 km event was followed by the onset of the main EIP pulse, starting at 3.272 ms in panel (a). The first half of the main pulse was accompanied by downward fast positive breakdown (FPB) having a propagation speed of $\simeq 5.7 \times 10^7$ m/s (the mostly blue sources in panel e), but was otherwise relatively weak in VHF. In particular, it was much less strong than the flash-initiating NBE, and would not have accounted for the highly energetic main sferic of the EIP. Instead, the weaker VHF of the first-half FPB event was overridden by the stronger VHF of a second, much more powerful FPB event during the second half of the sferic, which the sferic apparently initiated. The second-half event is seen as the increasingly yellow symbols in panel (a) and the white sources in panel (e), which started about $\simeq 500$ m back up along the preceding FPB, near the top of the preceding breakdown, and descended $\simeq 700$ m in $5.5 \mu\text{s}$, corresponding to a speed of $\simeq 1.2 \times 10^8$ m/s. In the process, the VHF radiation increased exponentially with time, causing the VHF signal to saturate within a few microseconds. As is typically observed for initial pulses of NBEs (Rison *et al.*, 2016; Tilles *et al.*, 2019), the downward FPB was immediately followed by upward fast negative breakdown (FNB) that propagated back up and beyond the same channel. The FNB lasted $50\text{--}60 \mu\text{s}$, extending the breakdown up to 20.5° elevation ($\simeq 11.5$ km). Its propagation speed was $\simeq 4.2 \times 10^7$ m/s initially, slowing down to $\simeq 1.3 \times 10^7$ m/s by the end.

Figure 10.5 shows the EIP observations in more detail, both in support of the above results and to illustrate how the EIP compares with similarly-scaled NBE observations. Several features of interest are seen in the plots. The first feature, and as also seen in panels (a) and (b) of Figure 10.4, is

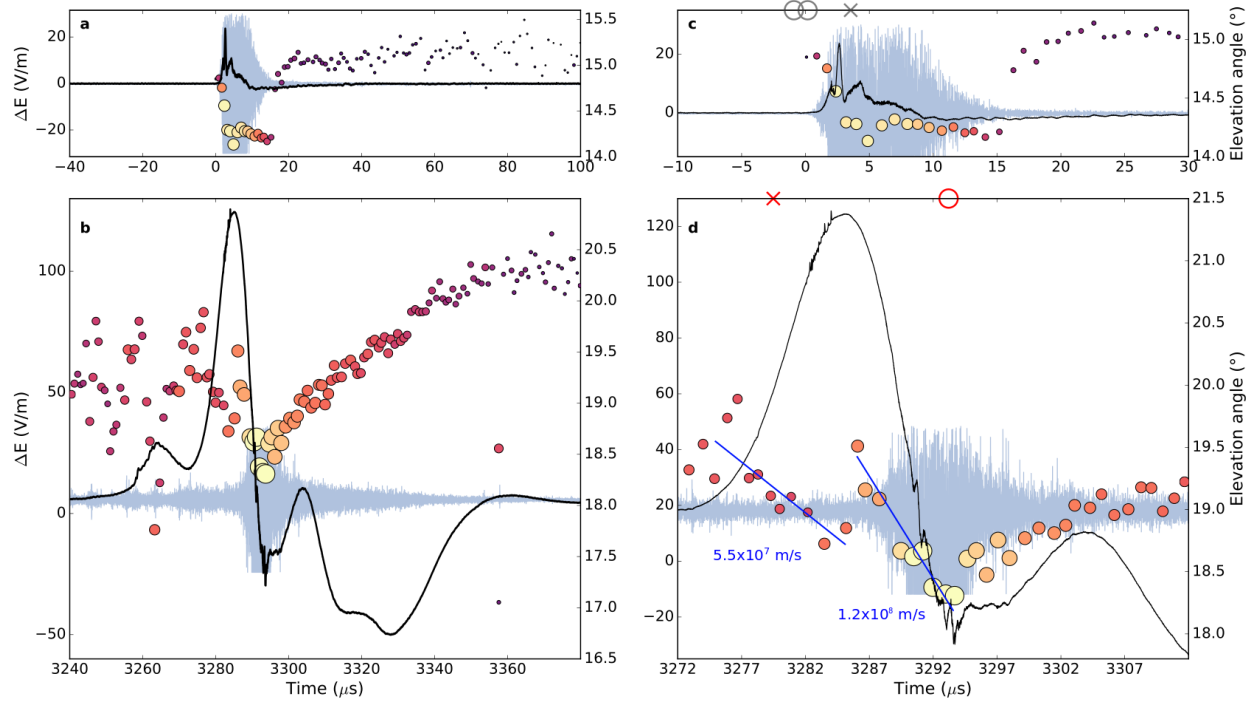


Figure 10.5: Comparisons of the flash-initiating NBE and the EIP. The INTF sources, FA (black) and VHF (light blue) waveforms, and times of the NLDN ('x') and LMA ('o') events for the NBE (a,c) and the EIP (b,d). Displayed on similar vertical scales, (a) and (b) compare the NBE and EIP for a 140 μs interval, and (c) and (d) compare the NBE and EIP in a zoomed-in view for a 40 μs interval. Both the NBE and EIP have a VHF burst associated with fast positive breakdown (FPB) of similar duration, extent, and speed. The FPB is associated with spikey perturbations on the FA waveform in (c), and in (d) similar perturbations are superimposed on the much larger, more smoothly-developing EIP sferic between 3287 and 3297 μs . The perturbation on the smooth EIP pulse near 3282 μs is apparently due to radio frequency interference (RFI) of unknown origin, because similar RFI occurs on only one of the three INTF VHF waveforms.

that the EIP sferic peaked noticeably before the VHF. Rather than the two being closely correlated, as for the NBE, the EIP peak occurred about $\simeq 7 \mu\text{s}$ before the LMA-indicated VHF peak. Significantly, the onset of the strong VHF emissions, and corresponding INTF sources, began at the same time as the sferic peak. This provides clear support for the idea that the relativistic avalanching responsible for the sferic actually initiated the high-power, NBE-like event of the EIP. The second feature is that the sferic associated with the NBE-like event is seen as a perturbation on the falling edge of the otherwise smoothly-varying sferic of the EIP. The two field changes are superimposed upon each other, further indicating they are separate physical processes. Figure 10.11

in Section 10.8) utilizes a simple envelope technique to approximately separate the two components, which shows the perturbations were initially spike-like and became more gradual with time, somewhat similar to the sferic of the flash-initiating NBE in Figure 10.5c. Two other weaker perturbations can be seen in association with the downward fast positive breakdown earlier during the EIP.

Taken together, the above observations provide a clear indication that the smooth component of the EIP sferic was produced separately from that produced by the VHF-radiating fast breakdown processes. The smooth component was presumably produced by electron avalanching, which would not have radiated strongly in VHF (Dwyer & Cummer, 2013), whereas the VHF is generally associated with streamer activity (Rison *et al.*, 2016; Shi *et al.*, 2016, 2019). The fast streamer events were undoubtedly involved in initiating the avalanching breakdown, but the opposite would also appear to be true. In particular, the avalanching that produced the main EIP peak appears to have also initiated the breakdown of the final, strong downward/upward NBE-like streamer event.

10.6 Storm Context

The observations raise interesting questions about the storm conditions that lead to EIP production. Of particular interest is why the EIP-producing flash consistently and repeatedly discharged a relatively localized region of upper positive charge in the storm. The localized nature of the breakdown in the upper positive charge region during the EIP flash is seen in the overlays of Figure 10.2, both before and after the EIP, while previous and subsequent IC flashes propagated more extensively through the upper positive charge region.

Figure 10.6 shows LMA observations that help to answer the above question. Panel (a) shows the lightning activity over a $\simeq 3$ -minute period around the time of the EIP flash, and (b) shows the LMA-inferred charge density over a broader 10 minute time interval. Four flashes are shown in (a), with the EIP flash shown in red. The EIP occurred during the fourth flash in a new cell that developed on the eastern edge of the relatively small and localized storm. Leading up to the

EIP, the lightning activity increased from a maximum altitude of $\simeq 10$ km to a new maximum of $\simeq 13$ km over a $\simeq 5$ -minute time period. Of particular interest is the second preceding flash before the EIP, labelled IC2 and shown in blue in panel (a). IC2 was almost identical to the EIP flash, in that it occurred between mid-level negative storm charge (blue region in panel b) and the upper positive charge (yellow-orange region above the negative charge) in the newly-formed cell. Both flashes were initiated by high power NBEs (51.1 and 46.6 dBW, respectively), and both discharged remnant, horizontally-distributed negative charge toward the end of their development in the older part of the storm to the west. In the process, however, IC2 propagated horizontally through the upper part of the upper positive charge region, whereas the EIP flash did not.

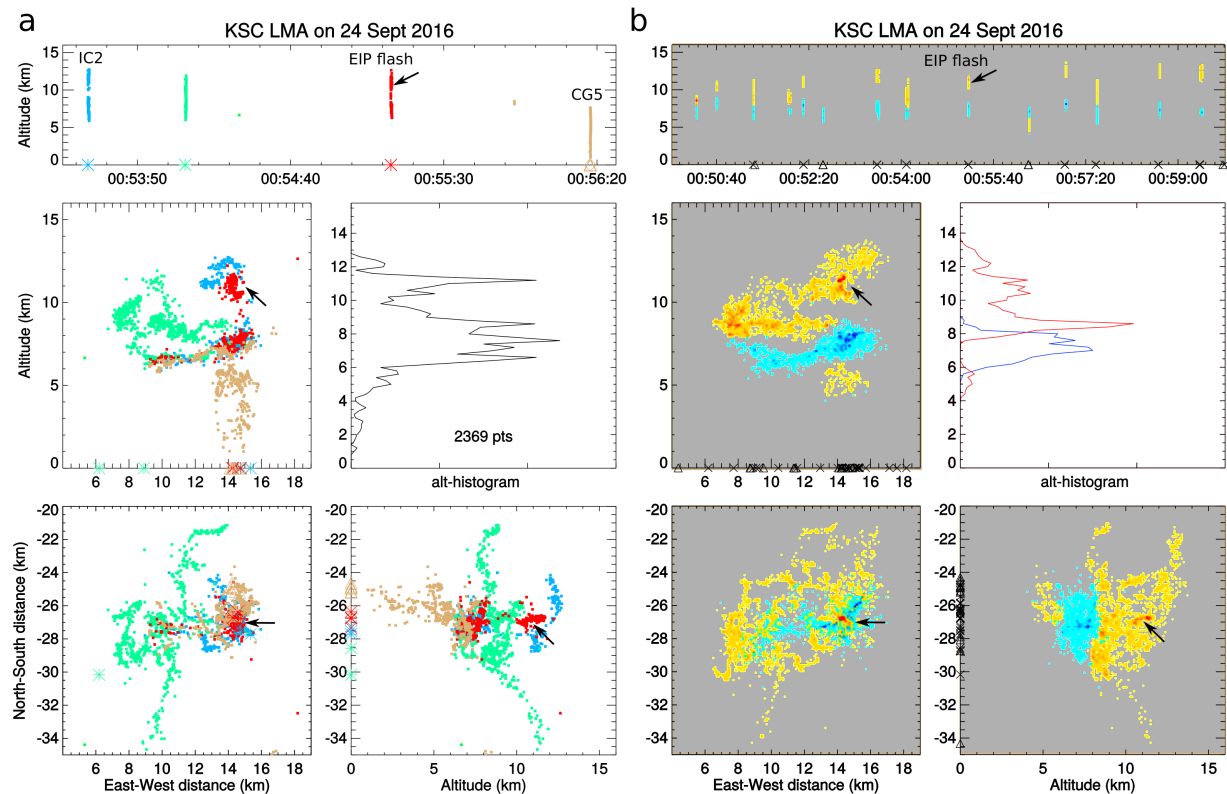


Figure 10.6: EIP storm activity. (a) Flash activity around the EIP flash. Two intracloud flashes (blue and green) preceded the EIP flash (red), and a cloud-to-ground (brown) occurred subsequently. Flashes “IC2” and “CG5” occurred in the same newly-developing eastern cell where the EIP flash occurred, whereas the green flash occurred in the older part of the storm to the west. (b) The LMA-determined flash density. The black arrows point to the approximate location of the EIP.

Comparing the vertical projections of the red and blue LMA sources in panel (a), it appears that IC2 had an effect on the development of the EIP flash. Namely, IC2 discharged a region of upper positive charge that restricted the upper part of the EIP flash to a small localized region that had not been traversed by IC2. The two flashes were separated in time by 97 s, a substantially longer interval than the average flash rate of 1.4 min^{-1} , or every 43 s. The relatively long time difference allowed for additional charging to occur (Hendry & McCormick, 1976; Krehbiel *et al.*, 1996) and for the EIP flash to be as energetic as its predecessor. Ordinarily, this would also have allowed the upper positive region discharged by IC2 to be replenished. But for some reason this appeared not to happen, and the positive charge was highly localized by the time of the EIP flash. The anomalously localized nature of the upper positive charge is also seen as the intense red-orange area over the 10 minute charge density plots of panel (b).

The observations provide a possible explanation for why the EIP flash was confined in the upper positive charge region, while at the same time explaining why the discharges were highly energetic, as being due to the low flash rate and relatively long time interval between the two flashes in question, allowing strong electrical forces to build. That the storm was strongly electrified is further indicated by the next discharge in the storm, occurring 65 s after the EIP flash, labelled CG5 and shown in brown in panel (a). CG5 had an initial return stroke of unusually large peak current (136 kA) for a negative CG flash (Nag & Cummins, 2017).

10.7 Discussion

In an effort to understand how energetic in-cloud pulses (EIPs) are produced, and gain insight into TGF generation, we have presented sub-microsecond VHF radio mapping of an EIP, providing over an order of magnitude finer temporal detail than previously reported TGF-related VHF observations (Lu *et al.*, 2010; Lyu *et al.*, 2016, 2018). Given that EIPs can serve as proxy for a subpopulation of TGFs (Lyu *et al.*, 2016; Cummer *et al.*, 2017), and that the observed EIP sferic developed independently from the VHF emissions generally associated with streamer activity (Ri-

son *et al.*, 2016; Shi *et al.*, 2016, 2019; Liu *et al.*, 2019), our study provides strong evidence that the EIP sferic was not produced by conventional lightning processes (i.e., streamers and leaders), but by the relativistic electrons and associated ionization of a TGF-producing discharge. The VHF and sferics development contrasts the EIP with other lightning processes, including narrow bipolar events (NBEs) and initial breakdown pulses (IBPs), whose sferics and VHF emissions are closely correlated in amplitude and time, appearing to initiate and evolve near-simultaneously (see (Rison *et al.*, 2016; Tilles *et al.*, 2019; Liu *et al.*, 2019) for NBE emissions, and (Krider *et al.*, 1979; Stock, 2014; Wu *et al.*, 2016; Kolmasova *et al.*, 2018; Stanley *et al.*, 2018b) for IBP emissions). Together with recent observations that downward TGFs occur during IBPs (Krehbiel *et al.*, 2019; Abbasi *et al.*, 2019), the contrasting development of the EIP and IBP emissions suggests that the energetic photons produced in each case may be due to different mechanisms. The large amplitude of the EIP sferic, and consequently the large currents ($\simeq 247$ kA) involved, point to relativistic feedback discharges (RFDs) (Dwyer, 2012; Liu & Dwyer, 2013) as the EIP production mechanism. In addition, RFDs can produce a substantial current without necessarily emitting strongly in VHF (Dwyer & Cummer, 2013), and RFD-generated currents can influence streamer development, as has been described both conceptually (Dwyer, 2005; Petersen *et al.*, 2008) and suggested based on detailed modeling work of RFDs (Liu & Dwyer, 2013). The high-power (50.6 dBW) NBE-like event that was triggered during the peak-amplitude EIP sferic pulse was likely an instance of RFD-initiated streamer development. In contrast with the MeV gamma-rays generated during EIPs (Lyu *et al.*, 2016), the ~ 100 keV X-rays observed during negative stepped leaders to ground are likely generated by cold runaway (Dwyer *et al.*, 2003, 2005a), in which relativistic electrons avalanche ahead of advancing stepped leaders, causing the accompanying sferics and VHF radiation to be correlated.

It is not clear how the activity preceding the EIP would initiate a RFD, but the activity likely played a role in generating and accelerating electrons to the required energies and fluences. Our observations are summarized as follows: 1) The EIP flash was initiated by a high-power (46.6 dBW) NBE. 2) The negative leader started about 1.53 ms into the flash, and propagated vertically up-

ward at an unusually fast speed (5×10^5 to 3×10^6 m/s) compared with typical intracloud negative leader speeds of $1\text{--}3 \times 10^5$ m/s (Shao *et al.*, 1995; Shao & Krehbiel, 1996; van der Velde & Montanya, 2013). 3) Faster, 6×10^6 m/s negative breakdown was initiated $\simeq 200$ μ s before the EIP, that propagated vertically upward more than 1 km and was accompanied by increasing VHF power. 4) The EIP was immediately preceded and accompanied by a succession of fast ($10^7\text{--}10^8$ m/s) downward/upward breakdown sequences, each lasting 10 to 20 μ s and growing in extent leading up to the EIP. Each downward/upward sequence retraced the same >1 -km altitude volume as the preceding 6×10^6 m/s negative breakdown. Given that leaders can maintain their conductivity for tens of microseconds up to milliseconds (Bazelyan & Raizer, 1998, p. 226), the volume could not have contained a hot, compact, highly-conductive leader. Thus, the EIP was preceded by and appeared to be triggered by repeated large-scale streamer activity. 5) The EIP occurred about 3 ms into the flash and lasted $\simeq 60$ μ s, having an associated peak current of 247 kA, and consisting of three spheric pulses, presumably caused by RFDs. Fast downward/upward streamer sequences of kilometer extent continued to occur in the same volume during the EIP, but the VHF emissions were weak and apparently not correlated with the sferics. 6) Shortly after the EIP spheric peak, a high-power (50.6 dBW) NBE-like event initiated. As in previous observations of NBEs (Rison *et al.*, 2016; Tilles *et al.*, 2019), the NBE-like event consisted of downward fast positive breakdown (FPB) followed immediately by upward fast negative breakdown (FNB) that propagated vertically upward back along a path previously traversed by FPB, and beyond that into virgin air. By definition, the spheric peak corresponded to the peak in dM_I/dt , the time-derivative of the current-moment. Hence, it appeared that the peak rate of change of the current moment of a relativistic discharge triggered the NBE-like event. 7) The same volume that was discharged by the pre-EIP and EIP activity was further discharged in its entirety by at least nine fast-propagating ($\sim 10^7$ m/s) K-events during the remaining $\simeq 300$ ms of the flash. The K-events did not extend the channel significantly further than during the EIP, terminating instead in the same enhanced upper-positive charge region that was discharged during the EIP.

The unusual lightning flash that generated the EIP resulted from an equally unusual thunderstorm. The storm experienced relatively long charging intervals between lightning flashes, which somehow produced a locally enhanced region of upper positive charge that was repeatedly discharged by the preceding streamer activity, the EIP discharge activity, and subsequent K-events. One question is whether or not a concentrated region of positive charge is a controlling factor in EIP generation. In order for a RFD to take place, the relativistic runaway electron avalanche (RREA) threshold field (2.8×10^5 V/m at sea level) must be exceeded over a large volume so that the relativistic feedback threshold will be crossed (Dwyer, 2003, 2012). The repeated streamer sequences before the EIP indicate that the electric field was at least as high as the critical field for positive streamers (4.4×10^5 V/m at sea level (Qin & Pasko, 2014)) for at least several tens of microseconds over a large (>1 km altitude) volume. It is likely that RREAs took place in the same volume and possibly beyond, so long as the electric field was above the RREA threshold field. The concentrated positive charge would have enhanced the electric field, and this may have increased the feedback factor (Dwyer, 2012; Liu & Dwyer, 2013). Additionally, the 6×10^6 m/s negative breakdown would have enhanced the field ahead of it, possibly pushing the RREAs above the feedback threshold and triggering a RFD, which would become the dominant discharge mode, producing the EIP and masking the sferics of lesser discharges. It is unclear if the repeated streamer sequences immediately preceding the EIP played a critical role in triggering a RFD by providing localized field enhancements within the volume. Alternatively, the repeated sequences may just be an indication that the volume was not discharged uniformly by the 6×10^6 m/s negative breakdown, or might otherwise be a manifestation of the effects of a RFD. It also remains to be investigated if EIPs tend to trigger high-power VHF emissions, as in the high-power NBE-like event that occurred in the latter stage of the EIP. We have shown that perturbations due to streamers can be differentiated from the smooth sferics produced by avalanching electrons, and, together with our observations, this shows a complex interdependence between storm activity, streamer development, and relativistic discharge processes, giving important insight into EIP generation.

10.8 Appendix

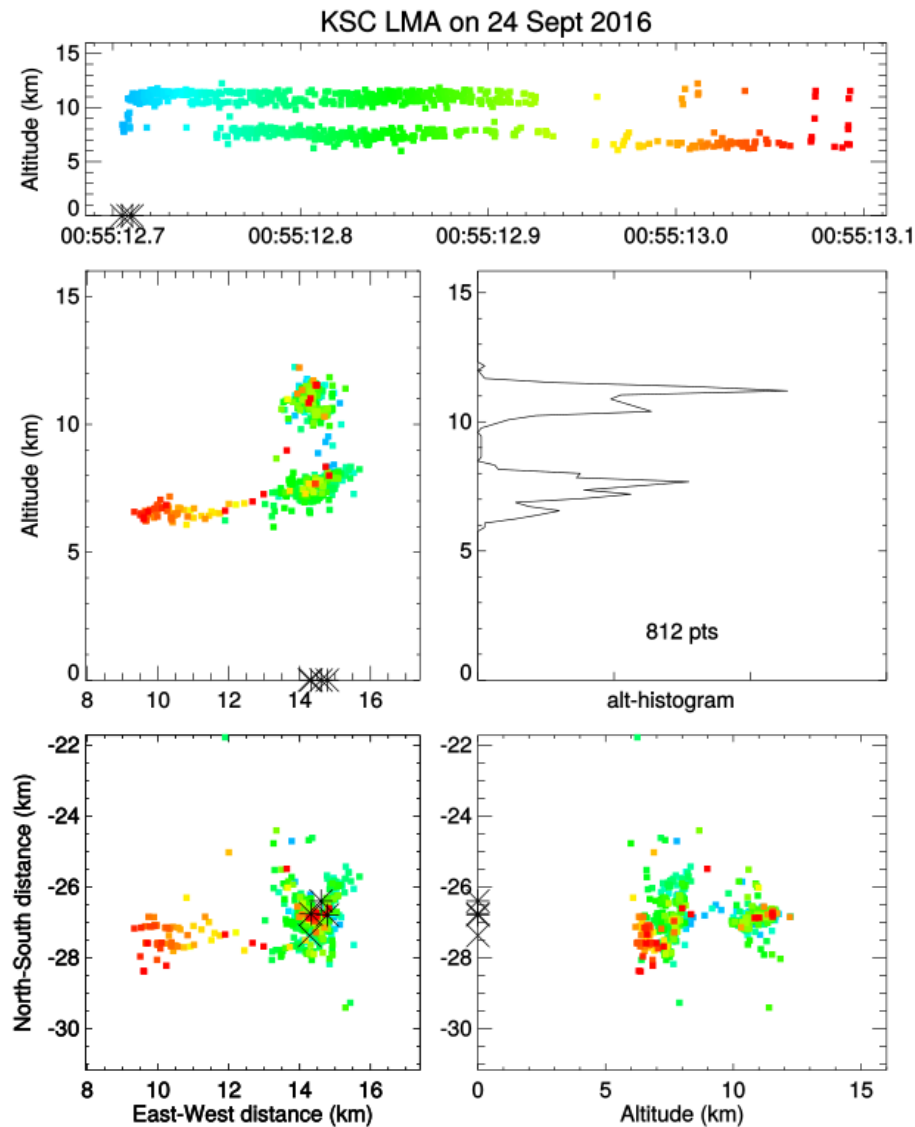


Figure 10.7: LMA and NLDN observations for the EIP flash, showing its bilevel nature between negative charge at 6–8 km altitude MSL and upper positive charge between 10–12 km. The flash began with an upward negative leader into a compact region of positive charge, and produced the EIP as soon as it entered the positive region. Instead of turning horizontal and propagating through horizontally-distributed positive charge, as occurred during other IC flashes in the storm, for about 200 ms the flash continued to discharge relatively localized positive and negative charge regions before shutting off in the upper positive charge and developing horizontally within the negative charge region. positive positive charge region (black ‘*’).

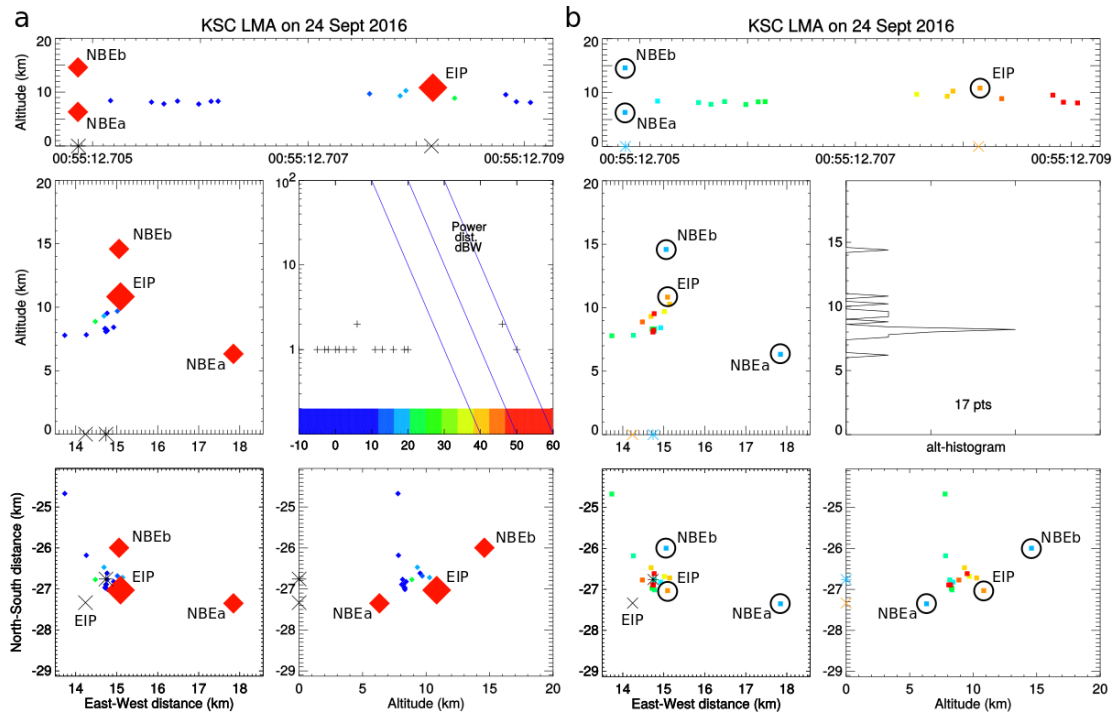


Figure 10.8: LMA and NLDN data for the NBE and EIP. NBE and EIP NLDN sources are indicated by a black '*' and 'x', respectively, and LMA sources are (a) colored and sized by VHF power, and (b) colored by time. Lower-power LMA sources following the NBE can be seen clustered near the NBE NLDN location.

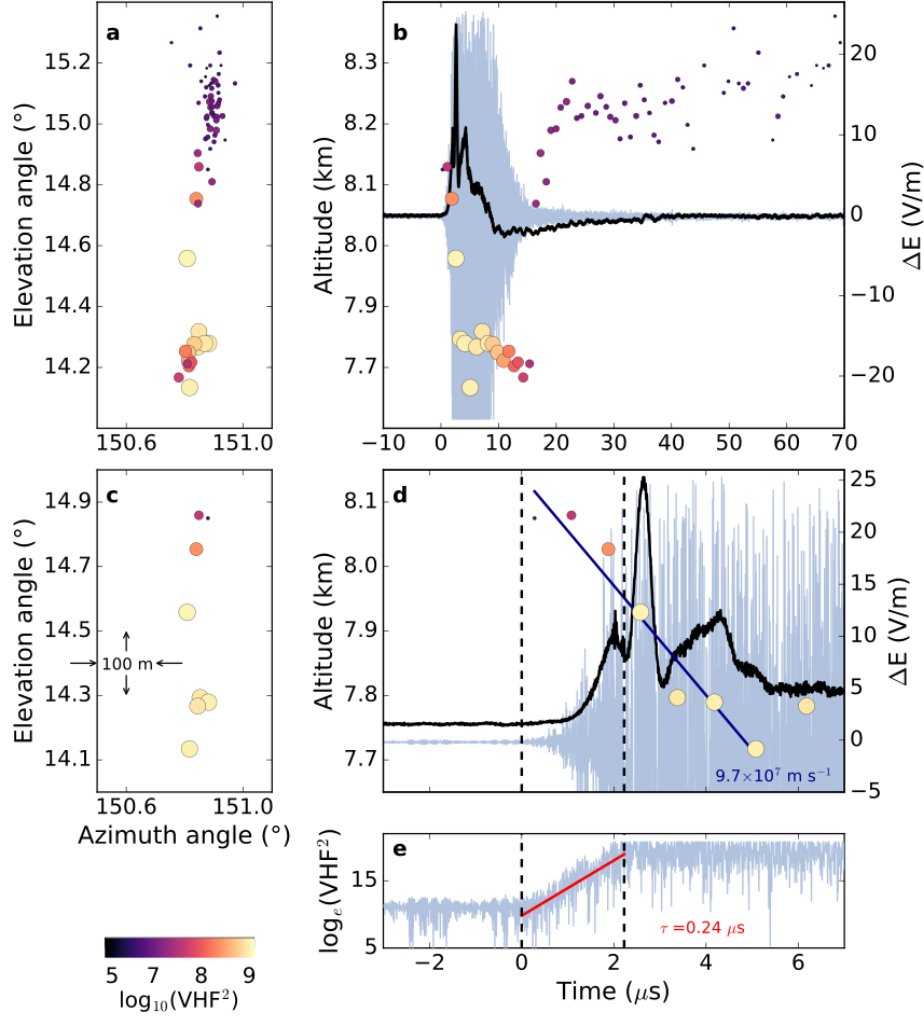


Figure 10.9: Detailed radio observations of flash-initiating NBE. (a), (c) INTF sources (circular markers, colored and sized by VHF power), plotted in elevation vs. azimuth, showing the primarily vertical breakdown activity of the NBE. (b), (d) INTF sources and FA (black) and VHF (light blue) waveforms, showing the downward propagation of the INTF sources. The fast positive breakdown descended about 400 meters in $5 \mu\text{s}$, corresponding to a speed of about 10^8 m/s . (e) Semilog plot of the VHF power vs. time, showing the fast exponential rise of the radiation (rise time $\tau = 0.24 \mu\text{s}$), coincident with the fast rise of the electric field change in (d).

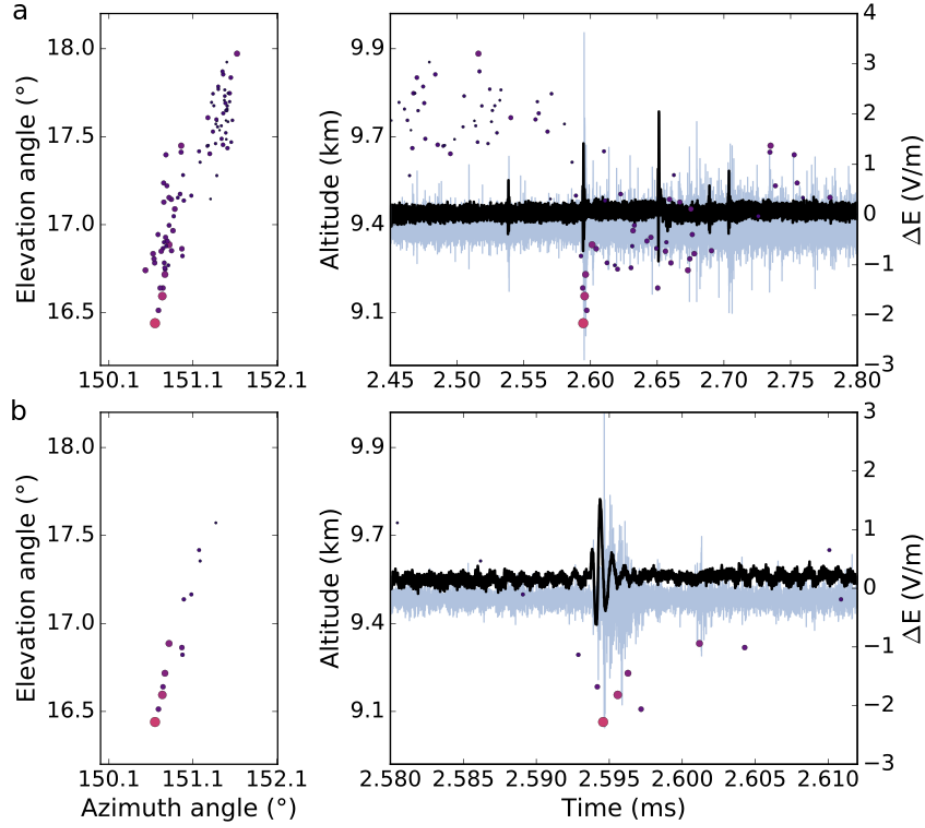


Figure 10.10: Detailed radio observations of step. (a) 350 μ s showing the multi-pulsed FA waveform (black) and VHF waveform (light blue) around the step, along with the downward then upward motion of associated INTF sources. (b) Zoomed-in 30 μ s around the step, showing the $\sim 10^8$ m/s apparent downward then upward INTF source propagation.

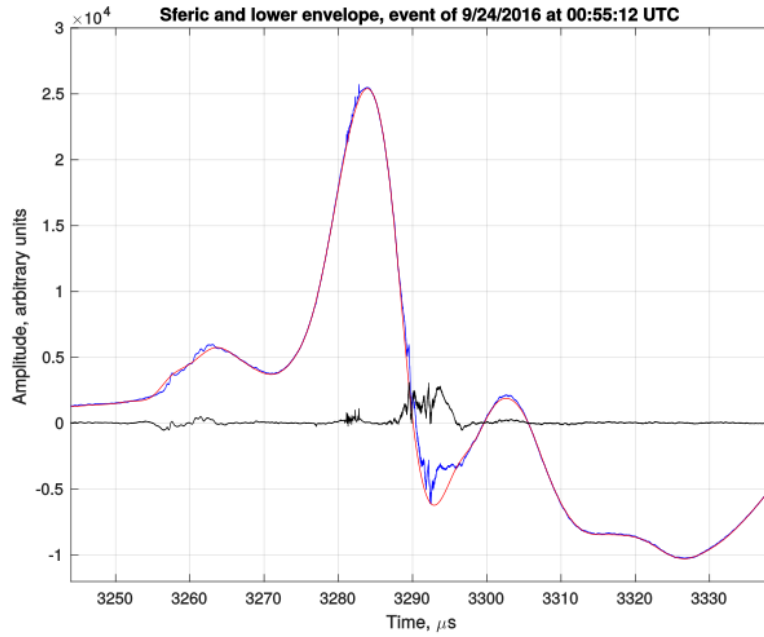


Figure 10.11: Results of a simplified technique for identifying perturbations in the EIP sferic waveform. The blue waveform is the original sferic, which is separated into two components utilizing envelope analysis. The red curve is the lower envelope of the peak sferic values obtained from the Matlab ‘envelope’ function. The black waveform is the difference between original sferic and the lower envelope. Three distinct perturbations are seen, first on the leading edge of the initial sferic peak, which is correlated with fast upward negative and downward positive VHF sources between 3.255 and 3.262 ms in panels (a) and (c) of Figure 4. The second, more impulsive perturbation is produced by a combination of weak positive events associated with downward fast positive breakdown prior to the main sferic peak at 3.284 ms in Figure 4a, and coincidental, brief radio frequency interference (RFI) of unknown origin during the first half of the perturbation. The final, large perturbation is caused by the high power NBE-like fast positive downward and negative upward sequence and strong VHF radiation that was triggered by the main relativistic avalanche. The amplitude of the initial part of the NBE-like perturbation is under-estimated, owing to larger, unknown d.c. offsets (i.e., larger undershoot in the red curve) not being detected by the envelope technique. Still, the technique provides a valuable method for analyzing EIP waveforms.

Selected LMA Events, sources = 18, date = 2016-09-24, start time = 00:55:12.70486367 UT, duration = 4.382536 ms

t (μ s)	P_{pk} (dBW)	χ^2_ν	nsta	lat	lon	alt	t (seconds)	d (km)	azim	elev
0.000	46.6	269.33	6	28.303150	-80.437111	6326.1	3312.704863670	32.689	146.9	10.8
1.075	46.5	0.50	6	28.315384	-80.465561	14589.5	3312.704864745	30.110	149.9	25.7
302.536	-3.0	0.18	6	28.307922	-80.466904	8422.8	3312.705166206	30.737	150.9	15.2
682.125	-4.4	0.12	6	28.308411	-80.468498	8151.6	3312.705545795	30.612	151.1	14.8
797.144	0.9	0.24	7	28.313719	-80.473694	7824.3	3312.705660814	29.849	151.4	14.5
923.147	5.1	0.07	9	28.306213	-80.468414	8333.4	3312.705786817	30.831	151.3	15.0
1234.592	6.2	0.12	7	28.306561	-80.468948	8285.7	3312.706098262	30.772	151.4	14.9
1299.129	11.1	0.14	9	28.306623	-80.469063	8317.7	3312.706162799	30.760	151.4	15.0
2703.231	13.2	4.18	6	28.309179	-80.465973	9694.5	3312.707566901	30.666	150.6	17.4
2986.585	19.7	0.16	7	28.311089	-80.469299	9314.8	3312.707850255	30.320	151.0	16.9
3039.855	16.4	61.15	7	28.308838	-80.464668	10272.9	3312.707903525	30.764	150.5	18.3
3290.209	50.6	0.21	6	28.306049	-80.465195	10832.3	3312.708153879	31.012	150.8	19.1
3491.234	20.8	0.13	9	28.308384	-80.471458	8876.3	3312.708354904	30.479	151.6	16.1
3965.441	-1.2	0.31	8	28.309782	-80.468529	9526.7	3312.708829111	30.528	150.9	17.2
4063.672	1.8	0.18	8	28.307302	-80.468689	8219.8	3312.708927342	30.755	151.2	14.8
4194.237	6.5	0.14	7	28.307291	-80.468842	8079.4	3312.709057907	30.748	151.2	14.6
4278.734	4.8	0.06	6	28.307756	-80.473518	10718.1	3312.709142404	30.497	151.9	19.2
4382.536	0.2	3.21	6	28.304365	-80.471405	16016.4	3312.709246206	30.953	151.9	27.3

Selected NLDN Events, sources = 2, date = 2016-09-24, start time = 00:55:12.704868565 UT, duration = 3.272039 ms

t (μ s)	I_{pk} (kA)	pulse type	lat	lon	t (seconds)
4.895	+17.0	C	28.3085	-80.4688	3312.704868565
3276.934	+247.3	G	28.3033	-80.4739	3312.708140604

Table 10.2: LMA and NLDN output corresponding to Figure 10.8. The LMA data includes the source time in microseconds since the flash-initiating NBE LMA source, the LMA-determined peak VHF power, the χ^2_ν goodness-of-fit value, the number of stations participating in a LMA source solution, the LMA source latitude, longitude, and altitude, the time in seconds since midnight, the LMA source plan distance from the INTF/FA, and the LMA source azimuth and elevation with respect to the INTF/FA. Note that the average LMA plan distance before and after the EIP remains around 30.6 km. For comparison, the NLDN data includes the time in microseconds since the flash-initiating NBE LMA source, the pulse peak current and polarity, the determined pulse type (either 'C' for in-cloud or 'G' for cloud-to-ground), the longitude and latitude of the pulse, and the time of the pulse in seconds since midnight.

CHAPTER 11

SUMMARY AND OUTLOOK

In this dissertation, we investigated lightning initiation, leader formation, and gamma-ray production, and were able to address the questions and hypotheses posed in Chapter 3, summarized below:

Lightning problems, hypotheses, and results	
Problem 1:	Ambient thunderstorm electric fields are ten times lower than the electrical breakdown threshold field of air, so how is lightning initiated?
Hypothesis:	Positive streamers initiate lightning.
Result:	Thunderstorm discharges can begin with breakdown of negative polarity, i.e., fast negative breakdown.
Problem 2:	Lightning begins with streamers, but when/how is the leader or the first hot channel formed?
Hypothesis:	Initial breakdown pulses (IBPs) are involved in initial leader formation.
Result:	A lightning leader is likely formed before the first IBP and IBPs are generated by fast negative breakdown.
Problem 3:	Only a small fraction of lightning events result in terrestrial gamma-ray flashes (TGFs), so how is lightning involved in TGF generation?
Hypothesis:	Enhanced cold runaway and/or relativistic feedback by lightning generates TGFs.
Result:	At least a subset of TGFs are generated by relativistic feedback discharges.

Broadband radio interferometer (INTF) observations of fast electrical processes, coupled with synchronous sferic observations and 3-D VHF mapping capabilities, provide a broad new outlook on the “typical” thunderstorm electrical process. The results herein indicate that fast streamer-based breakdown propagating at $\sim 10^7$ - 10^8 m/s is involved in several seemingly disparate thunderstorm discharge processes, whereas hitherto, fast processes were limited mostly to leader events along channels preconditioned by previous breakdown activity (Jordan *et al.*, 1992; Shao *et al.*, 1995; Shao & Krehbiel, 1996; Rakov, 1998; Akita *et al.*, 2010), and more recently by narrow bipolar events (NBEs) and fast positive breakdown (Rison *et al.*, 2016). Instead, we show that the streamer-based fast breakdown associated with NBEs can come in both breakdown polarities, both equally fast-propagating at $\sim 10^7$ m/s and emitting strongly in VHF, and that both fast positive and negative breakdown are involved in initial breakdown pulses (IBPs) and energetic in-cloud pulses (EIPs). Thus, fast breakdown is apparently ubiquitous in thunderstorm electrical processes, being involved in lightning initiation, leader formation, and energetic photon production.

Furthermore, the sub-microsecond temporal resolution and imaging capabilities of the INTF enabled the development of an algorithm to quantify the morphologies of different radio source types. We ultimately determined that fast breakdown was consistent with a propagating localized source (within the INTF’s angular resolution), but that fast breakdown was not wholly consistent with a single propagating breakdown front, given that noise levels could not account for the scatter in imaged source locations. Clearly, having finer spatial resolution in the future will help resolve the exact nature of the scattered activity, but the results herein provide strong motivation for developing such future instrumentation.

Moreover, by comparing the simultaneous sub-microsecond sferics and VHF measurements, we demonstrated an entirely new way to discern between conventional and relativistic discharges. For instance, the EIP breakdown activity consisted of multiple, repeated downward-then-upward fast positive-then-negative breakdown events. Similar backward-then-forward fast breakdown also occurred at the beginning of classic IBPs, but on a smaller temporal and spatial scale. However, the EIP and IBP similarities diverge when comparing the sferics and the VHF emissions. The

IBP sferics and VHF emissions initiate near-simultaneously (within $0.5 \mu\text{s}$), suggesting that both signals are produced, or at least initiated, by streamer activity. In contrast, the EIP sferics evolved seemingly independent of the VHF emissions, which suggests that the sferic was not solely produced by streamers, but that the repeated streamer activity was somehow involved in generating relativistic electrons and associated ionization that produced the EIP sferic (and a likely terrestrial gamma-ray flash (TGF)). Moreover, strong VHF emissions that are generally associated with the highest-power NBEs were instead initiated in the middle of the EIP activity, with 2×10^7 m/s fast negative breakdown seemingly driven by a relativistic discharge. Our study opens up a new observational means for investigating the complex coupling between conventional and relativistic processes, which has largely been performed in simulation up to this point.

Finally, because the INTF depends on correlations between signals and is not dependent solely on signal amplitude, we can use the INTF to identify and examine new in-cloud processes that might otherwise go fully undetected by traditional electric field sensors or time-of-arrival networks. For instance, the “FA-quiet” breakdown, which we observed during the initial stage of lightning formation, does not generate detectable sferics, nor especially strong VHF signals. Again, this provides strong motivation for advancing the INTF instrumentation, with larger numbers of sensors and more sensitive sensors likely revealing as-of-yet unimaginable new natural phenomena.

BIBLIOGRAPHY

- Abbasi, R., Belz, J., Krehbiel, P., LeVon, R., Remington, J., Rison, W., Rodeheffer, D., & Stanley, M. 2019 (9-13 December). Observation of the Origin of Downward Terrestrial Gamma-ray Flashes in Initial Breakdown Pulses. *In: AGU Fall Meeting*. Abstract AE33A-3126.
- Akita, Manabu, Nakamura, Yoshitaka, Yoshida, Satoru, Morimoto, Takeshi, Ushio, Tomoo, Kawasaki, Zen, , & Wang, Daohong. 2010. What occurs in K process of cloud flashes? *J. Geophys. Res.*, **115**.
- Anastasiia-S. 2018. *Image of blue sky with clouds, circle effect from fisheye lens*. Royalty-free stock photo ID: 678554890. [Online; accessed October 24, 2018].
- Arabshahi, S., Dwyer, J. R., Nag, A., Rakov, V. A., & Rassoul, H. K. 2014. Numerical simulations of compact intracloud discharges as the Relativistic Runaway Electron Avalanche-Extensive Air Shower process. *J. Geophys. Res.*, **119**.
- Aster, Richard C., Borchers, Brian, & Thurber, Clifford H. 2013. *Parameter Estimation and Inverse Problems*. Elsevier Inc.
- Babaeva, N. Y., & Naidis, G. V. 1997. Dynamics of positive and negative streamers in air in weak uniform electric fields. *IEEE Trans. Plasma Sci.*, **25**(2), 375–379.
- Bazelyan, E. M., & Raizer, Yu. P. 1998. *Spark Discharge*. CRC Press LLC.
- Beasley, William, Uman, Martin A., & Rustan Jr., P. L. 1982. Electric Fields Preceding Cloud-to-Ground Lightning Flashes. *J. Geophys. Res.*, **87**.
- Berger, K., & Vogelsanger, E. 1966. Photographische Blitzuntersuchungen der Jahre 1955-1965 auf dem Monte San Salvatore. *Bull. Schweiz. Elektrotech.*, 599–620.
- Beroual, A., & Fofana, I. 2016. *Discharge In Long Air Gaps, Modelling and applications*. Bristol, UK: IOP Publishing Ltd.
- Biagi, C. J., Uman, M. A., Hill, J. D., Jordan, D. M., Rakov, V. A., & Dwyer, J. 2010. Observations of stepping mechanisms in a rocket-and-wire triggered lightning flash. *J. Geophys. Res.*, **115**(D23215).
- Biagi, C. J., Uman, M. A., Hill, J. D., & Jordan, D. M. 2014. Negative leader step mechanisms observed in altitude triggered lightning. *J. Geophys. Res.*, **119**, 8160–8168.
- Bitzer, Phillip M., Christian, Hugh J., Stewart, Mike, Burchfield, Jeff, Podgorny, Scott, Corredor, David, Hall, John, Kuznetsov, Evgeny, & Franklin, Veronica. 2013. Characterization and applications of VLF/LF source locations from lightning using the Huntsville Alabama Marx Meter Array. *J. Geophys. Res. Atmos.*, **118**, 3120–3138.

- Boccippio, Dennis J., Cummins, Kenneth L., Christian, Hugh J., & Goodman, Steven J. 2000. Combined Satellite- and Surface-Based Estimation of the Intracloud-Cloud-to-Ground Lightning Ratio over the Continental United States. *Monthly Weather Review*, **129**, 108–122.
- Briels, T. M. P., Kos, J., Winands, G. J. J., van Veldhuizen, E. M., & Ebert, U. 2008. Positive and negative streamers in ambient air: measuring diameter, velocity and dissipated energy. *J. Phys. D Appl. Phys.*, **41**.
- Briggs, M. S., Fishman, G. J., Connaughton, V., Bhat, P. N., Paciesas, W. S., Preece, R. D., Wilson-Hodge, C., Chaplin, V. L., Kippen, R. M., von Kienlin, A., Meegan, C. A., Bissaldi, E., Dwyer, J. R., Smith, D. M., Holzworth, R. H., Grove, J. E., & Chekhtman, A. 2010. First results on terrestrial gamma ray flashes from the Fermi Gamma-ray Burst Monitor. *Journal of Geophysical Research*, **115**(A14), 7323.
- Bruning, Eric C., & MacGorman, Donald R. 2013. Theory and Observations of Controls on Lightning Flash Size Spectra. *J. Atmospheric Sci.*, **70**(12), 4012–4029.
- Bruning, Eric C., Weiss, Stephanie A., & Calhoun, Kristin M. 2014. Continuous variability in thunderstorm primary electrification and an evaluation of inverted-polarity terminology. *Atmospheric Research*, **135-136**, 274–284.
- Caicedo, J. A., Uman, M. A., & Pilkey, J. T. 2018. Lightning Evolution In Two North Central Florida Summer Multicell Storms and Three Winter/Spring Frontal Storms. *J. Geophys. Res.*
- Campos, Leandro Z. S., & Saba, Marcelo M. F. 2013. Visible channel development during the initial breakdown of a natural negative cloud-to-ground flash. *Geophys. Res. Lett.*, **40**(4756-4761).
- Celestin, S., Xu, W., & Pasko, V. P. 2012. Terrestrial gamma ray flashes with energies up to 100 MeV produced by nonequilibrium acceleration of electrons in lightning. *Journal of Geophysical Research*, **117**(A16), 5315.
- Celestin, Sebastien, Xu, Wei, & Pasko, Victor P. 2015. Variability in fluence and spectrum of high-energy photon bursts produced by lightning leaders. *Journal of Geophysical Research: Space Physics*, **120**(10), 712–723.
- Chang, Xuan, Yuan, Ping, Cen, Jianyong, & Wang, Xuejuan. 2017. Variation of the channel temperature in the transmission of lightning leader. *Journal of Atmospheric and Solar–Terrestrial Physics*, **159**, 41–47.
- Coleman, L. M., & Dwyer, J. R. 2006. Propagation speed of runaway electron avalanches. *Geophys. Res. Lett.*, **33**.
- Cummer, S. A., Lu, G., Briggs, M. S., Connaughton, V., Xiong, S., Fishman, G. J., & Dwyer, J. R. 2011. The lightning-TGF relationship on microsecond timescales. *Geophys. Res. Lett.*, **38**(July), 14810.

- Cummer, S. A., Briggs, M. S., Dwyer, J. R., Xiong, S., Connaughton, V., Fishman, G. J., Lu, G., Lyu, F., & Solanki, R. 2014. The source altitude, electric current, and intrinsic brightness of terrestrial gamma ray flashes. *Geophys. Res. Lett.*, **41**(Dec.), 8586–8593.
- Cummer, Steven A., Lyu, Fanchao, Briggs, Michael S., Fitzpatrick, Gerard, Roberts, Oliver J., & Dwyer, Joseph R. 2015. Lightning leader altitude progression in terrestrial gamma-ray flashes. *Geophys. Res. Lett.*, **42**(18), 7792–7798. 2015GL065228.
- Cummer, Steven A., Lyu, Fanchao, Briggs, Michael S., Cramer, Eric, Stanbro, Matthew, Roberts, Oliver, & Smith, David Miles. 2017 (11-15 Dec). The Connection Between Terrestrial Gamma-Ray Flashes and Energetic In-Cloud Lightning Pulses. *In: AGU Fall Meeting*.
- da Silva, Caitano L., & Pasko, Victor P. 2013. Dynamics of streamer-to-leader transition at reduced air densities and its implications for propagation of lightning leaders and gigantic jets. *J. Geophys. Res.*, **118**, 13561–13590.
- da Silva, Caitano L., & Pasko, Victor P. 2015. Physical mechanism of initial breakdown pulses and narrow bipolar events in lightning discharges. *J. Geophys. Res.*, **120**, 4989–5009.
- Dawson, G. A., & Winn, W. P. 1965. A model for streamer propagation. *Zeitschrift für Physik*, **183**(2).
- Dwyer, J. R. 2003. A fundamental limit on electric fields in air. *Geophys. Res. Lett.*, **30**(20).
- Dwyer, J. R. 2004. Implications of x-ray emission from lightning. *Geophys. Res. Lett.*, **31**(12).
- Dwyer, J. R. 2007. Relativistic breakdown in planetary atmospheres. *Physics of Plasmas*, **14**(042901).
- Dwyer, J. R. 2012. The relativistic feedback discharge model of terrestrial gamma ray flashes. *Journal of Geophysical Research*, **117**(FEB 14).
- Dwyer, J. R., Uman, M. A., Rassoul, H. K., Al-Dayeh, M., Caraway, E. L., Jerauld, J., Rakov, V. A., Jordan, D. M., Rambo, K. J., Corbin, V., & Wright, B. 2003. Energetic Radiation Produced During Rocket-Triggered Lightning. *Science*, **299**(694).
- Dwyer, J. R., Rassoul, H. K., Al-Dayeh, M., Caraway, L., Chrest, A., Wright, B., Kozak, E., Jerauld, J., Uman, M. A., Rakov, V. A., Jordan, D. M., & Rambo, K. J. 2005a. X-ray bursts associated with leader steps in cloud-to-ground lightning. *Geophys. Res. Lett.*, **32**.
- Dwyer, J. R., Rassoul, H. K., Saleh, Z., Uman, M. A., Jerauld, J., & Plumer, J. A. 2005b. X-ray bursts produced by laboratory sparks in air. *Geophys. Res. Lett.*, **32**(L20809).
- Dwyer, J. R., Schaal, M., Rassoul, H. K., Uman, M. A., Jordan, D. M., & Hill, D. 2011. High-speed X-ray images of triggered lightning dart leaders. *J. Geophys. Res.*, **116**(D20208).
- Dwyer, Joe R. 2008. Source mechanisms of terrestrial gamma-ray flashes. *J. Geophys. Res.*, **113**.
- Dwyer, Joseph R. 2005. The initiation of lightning by runaway air breakdown. *Geophys. Res. Lett.*, **32**(L20808).

- Dwyer, Joseph R., & Cummer, Steven A. 2013. Radio emissions from terrestrial gamma-ray flashes. *J. Geophys. Res.*, **118**, 3769–3790.
- Dwyer, Joseph R., Smith, David M., & Cummer, Steven A. 2012. High-Energy Atmospheric Physics: Terrestrial Gamma-Ray Flashes and Related Phenomena. *Space. Sci. Rev.*, **173**, 133–196.
- Eack, Kenneth B. 2004. Electrical characteristics of narrow bipolar events. *Geophys. Res. Lett.*, **31**.
- Ebert, U., Montijn, C., Briels, T. M. P., Hundsdorfer, W., Meulenbroek, B., Rocco, A., & van Veldhuizen, E. M. 2006. The multiscale nature of streamers. *Plasma Sources Science and Technology*, **15**(2), S118–S129.
- Edens, H. E., Eack, K. B., Eastvedt, E. M., Trueblood, J. J., Winn, W. P., Krehbie, P. R., Aulich, G. D., Hunyady, S. J., Murray, W. C., Rison, W., Behnke, S. A., & Thomas, R. J. 2012. VHF lightning mapping observations of a triggered lightning flash. *Geophys. Res. Lett.*, **39**(L19807).
- Emersic, Christopher. 2006. *Investigations into Thunderstorm Electrification Processes*. PhD dissertation, University of Manchester (UK).
- Falconer, Isobel. 1997. J J Thomson and the discovery of the electron. *Phys. Educ.*, **32**(226).
- Fishman, G. J., Bhat, P. N., Mallozzi, R., Horack, J. M., Koshut, T., Kouveliotou, C., Pendleton, G. N., Meegan, C. A., Wilson, R. B., Paciesas, W. S., Goodman, S. J., & Christian, H. J. 1994. Discovery of intense gamma-ray flashes of atmospheric origin. *Science*, **264**(5163), 1313.
- Franklin, Benjamin. 1751. A Letter of Benjamin Franklin, Esq; to Mr. Peter Collinson, F. R. S. concerning an Electrical Kite. *Philosophical Transactions (1683-1775)*, **47**, 565–567.
- Fuchs, B. R., Rutledge, S. A., Bruning, E. C., Pierce, J. R., Kodros, J. K., Lang, T. J., MacGorman, D. R., Krehbiel, P. R., & Rison, W. 2015. Environmental controls on storm intensity and charge structure in multiple regions of the continental United States. *J. Geophys. Res. Atmos.*, **120**(6575-6596).
- Gorin, B. N., Levitov, V. I., & Shkilev, A. V. 1976. Some principles of leader discharge of air gaps with a strong non-uniform field. *IEE Conf. Publ.*, **143**, 274–278.
- Griffiths, R. F., & Phelps, C. T. 1976. A Model for Lightning Initiation Arising From Positive Corona Streamer Development. *J. Geophys. Res.*, **81**(21).
- Gurevich, A. V., Milikh, G. M., & Roussel-Dupre, R. 1992. Runaway electron mechanism of air breakdown and preconditioning during a thunderstorm. *Physics Letters A*, **165**(5-6), 463–468.
- Hamlin, T. D. 2004. *The New Mexico Tech Lightning Mapping Array*. PhD dissertation, New Mexico Institute of Mining and Technology.
- Hendry, A., & McCormick, G. C. 1976. Radar Observations of the Alignment of Precipitation Particles by Electrostatic Fields in Thunderstorms. *J. Geophys. Res.*, **81**(30).

- Hill, J. D., Uman, M. A., & Jordan, D. M. 2011. High-speed video observations of a lightning stepped leader. *J. Geophys. Res.*, **116**.
- Hoinka, Klaus P. 1999. Temperature, Humidity, and Wind at the Global Tropopause. *Monthly Weather Review*, **127**(10).
- Holden, D. N., Munson, C. P., & Davenport, J. C. 1995. Satellite observations of transionospheric pulse pairs. *Geophys. Res. Lett.*, **22**(8).
- Jacobson, Abram R., & Heavner, Mathew J. 2005. Comparison of Narrow Bipolar Events with Ordinary Lightning as Proxies for Severe Convection. *Mon. Weather Rev.*, **113**.
- Jordan, Douglas M., Idone, Vincent P., Rakov, Vladimir A., Uman, Martin A., Beasley, William H., & Jurenka, Henry. 1992. Observed dart leader speed in natural and triggered lightning. *J. Geophys. Res.*, **97**.
- Jordan, Douglas M., Idone, Vincent P., Orville, Richard E., Rakov, Vladimir A., & Uman, Martin A. 1995. Luminosity characteristics of lightning M components. *J. Geophys. Res. Atmos.*, **100**(D12).
- Karunarathna, Nadeeka, Marshall, Thomas C., Stolzenburg, Maribeth, & Karunarathne, Sumedhe. 2015. Narrow bipolar pulse locations compared to thunderstorm radar echo structure. *J. Geophys. Res. Atmos.*, **120**, 11690–11706.
- Karunarathne, Nilmini, Marshall, Thomas C., Karunarathne, Sumedhe, & Stolzenburg, Maribeth. 2020. Studying Sequences of Initial Breakdown Pulses in Cloud-to-Ground Lightning Flashes. *J. Geophys. Res. Atmos.*, **125**(3).
- Karunarathne, S., Marshall, T. C., Stolzenburg, M., & Karunarathna, N. 2016. Electrostatic field changes and durations of narrow bipolar events. *J. Geophys. Res.*, **121**.
- Karunarathne, Sumedhe, Marshall, Thomas, Stolzenburg, Maribeth, Karunarathna, Nadeeka, Vickers, Lauren, Warner, Tom, & Orville, Richard. 2013. Locating initial breakdown pulses using electric field change network. *J. Geophys. Res.*, **118**, 7129–7141.
- Karunarathne, Sumedhe, Marshall, Thomas, Stolzenburg, Maribeth, & Karunarathna, Nadeeka. 2014. Modeling initial breakdown pulses of CG lightning flashes. *J. Geophys. Res.*, **119**, 9003–9019.
- Karunarathne, Sumedhe, Marshall, Thomas C., Stolzenburg, Maribeth, & Karunarathna, Nadeeka. 2015. Observations of positive narrow bipolar pulses. *J. Geophys. Res.*, **120**, 7128–7143.
- Kochkin, P. O., Nguyen, C. V., van Deursen, A. P. J., & Ebert, U. 2012a. Experimental study of hard x-rays emitted from metre-scale positive discharges in air. *J. Phys. D: Appl. Phys.*, **45**(425202).
- Kochkin, P. O., Nguyen, C. V., van Deursen, A. P. J., & Ebert, U. 2012b. Experimental study on hard x-rays emitted from metre-scale negative discharges in air. *J. Phys. D: Appl. Phys.*, **48**(025205).

- Kolmasova, Ivana, Santolík, Ondřej, Defer, Eric, Rison, William, Coquillat, Sylvain, Pédeboy, Stéphane, Lán, Radek, Uhlř, Luděk, Lambert, Dominique, Pinty, Jean-Pierre, Prieur, Serge, & Pont, Véronique. 2018. Lightning initiation: Strong pulses of VHF radiation accompany preliminary breakdown. *Scientific Reports*, **8**.
- Korolev, A., McFarquhar, G., Field, P. R., Franklin, C., Lawson, P., Wang, Z., Williams, E., Abel, S. J., Axisa, D., Borrmann, S., Crosier, J., Fugal, J., Krämer, M., Lohmann, U., Schlenczek, O., Schnaiter, M., & Wendisch, M. 2017. Mixed-Phase Clouds: Progress and Challenges. *Meteorological Monographs*, **58**, 5.1–5.50.
- Krehbiel, P., Rison, W., Thomas, R. J., Maggio, C., Marshall, T., Stolzenberg, M., Hamlin, T., & Wiens, K. 2005. Lightning and dual-polarization radar structure of small convective storms. *In: Proc., 32nd Conf. Radar Meteor., Amer. Meteor. Soc.*
- Krehbiel, P. R., Chen, T., McCrary, S., Rison, W., Gray, G., & Brook, M. 1996. The Use of Dual Channel Circular-Polarization Radar Observations for Remotely Sensing Storm Electrification. *Meteorol. Atmos. Phys.*, **59**, 65–82.
- Krehbiel, P. R., Belz, J., Abbasi, R., Remington, J., Stanley, M., & Rison, W. 2019 (9-13 December). Discharge Processes During Downward TGFs at the Telescope Array in Utah. *In: AGU Fall Meeting*. Abstract AE33A-3127.
- Krehbiel, Paul R. 1986. The Electrical Structure of Thunderstorms. *Chap. 8, pages 90–113 of: The Earth's Electrical Environment*. Studies in Geophysics: A Series. National Academies Press.
- Krehbiel, Paul R., Rioussset, Jeremy A., Pasko, Victor P., Thomas, Ronald J., Rison, William, Stanley, Mark A., & Edens, Harald E. 2008. Upward electrical discharges from thunderstorms. *Nat. Geosci.*, **1**.
- Krider, E. P., Weidman, C. D., & Le Vine, D. M. 1979. The Temporal Structure of the HF and VHF Radiation Produced by Intracloud Lightning Discharge. *J. Geophys. Res.*, **84**.
- Krider, E. Philip, Weidman, Charles D., & Noggle, R. Carl. 1977. The Electric fields produced by lightning stepped leaders. *J. Geophys. Res.*, **82**(6).
- Lang, Timothy J., Miller, L. Jay, Weisman, Morris, Rutledge, Steven A., III, Llyle J. Barker, Bringi, V. N., Chandrasekar, V., Detwiler, Andrew, Doesken, Nolan, Helsdon, John, Knight, Charles, Krehbiel, Paul, Lyons, Walter A., MacGorman, Don, Rasmussen, Erik, Rison, William, Rust, W. David, & Thomas, Ronald J. 2004. The Severe Thunderstorm Electrification and Precipitation Study. *Bulletin of the American Meteorological Society*, **85**(8), 1107–1126.
- Le Vine, David M. 1980. Sources of the Strongest Radiation From Lightning. *J. Geophys. Res.*, **85**(C7), 4091–4095.
- Lehtinen, N. G., Walt, M., Inan, U. S., Bell, T. F., & Pasko, V. P. 1996. Gamma-ray emission produced by a relativistic beam of runaway electrons accelerated by quasi-electrostatic thundercloud fields. *Geophys. Res. Lett.*, **23**, 2645–2648.

- Liu, N., & Dwyer, J. R. 2013. Modeling terrestrial gamma ray flashes produced by relativistic feedback discharges. *Journal of Geophysical Research: Space Physics*, **118**, 2359–2376.
- Liu, Ningyu. 2010. Model of sprite luminous trail caused by increasing streamer current. *Geophys. Res. Lett.*, **37**.
- Liu, Ningyu, & Pasko, Victor P. 2004. Effects of photoionization on propagation and branching of positive and negative streamers in sprites. *J. Geophys. Res.*, **109**.
- Liu, Ningyu, Kosar, Burcu, Sadighi, Samaneh, Dwyer, Joseph R., & Rassoul, Hamid K. 2012. Formation of Streamer Discharges from an Isolated Ionization Column at Subbreakdown Conditions. *Phys. Rev. Lett.*, **109**.
- Liu, Ningyu, Dwyer, Joseph R., Stenbaek-Nielsen, Hans C., & McHarg, Matthew G. 2015. Sprite streamer initiation from natural mesospheric structures. *Nat. Comm.*, **6**.
- Liu, Ningyu, Boggs, Levi D., & Cummer, Steven A. 2016. Observation-constrained modeling of the ionospheric impact of negative sprites. *Geophys. Res. Lett.*, **43**.
- Liu, Ningyu, Dwyer, Joseph R., & Cummer, Steven A. 2017. Elves accompanying terrestrial gamma ray flashes. *J. Geophys. Res.*, **122**, 10,563–10,576.
- Liu, Ningyu, Dwyer, Joseph R., Tilles, Julia N., Stanley, M. A., Krehbiel, P. R., Rison, W., Brown, Robert G., & Wilson, Jennifer G. 2019. Understanding the radio spectrum of narrow bipolar events. *J. Geophys. Res.*, **124**.
- Loeb, L. B., & and, J. M. Meek. 1940. The Mechanism of Spark Discharge in Air at Atmospheric Pressure. I. *Journal of Applied Physics*, **11**(6), 438–447.
- Loeb, Leonard B. 1966. The mechanisms of stepped and dart leaders in cloud-to-ground lightning strokes. *J. Geophys. Res.*, **71**(20), 4711–4721.
- Lu, G., Cummer, S. A., Li, J., Han, F., Smith, D. M., & Grefenstette, B. W. 2011. Characteristics of broadband lightning emissions associated with terrestrial gamma ray flashes. *Journal of Geophysical Research*, **116**(A15).
- Lu, Gaopeng, Blakeslee, Richard J., Li, Jingbo, Smith, David M., Shao, Xuan-Min, McCaul, Eugene W., Buechler, Dennis E., Christian, Hugh J., Hall, John M., , & Cummer, Steven A. 2010. Lightning mapping observation of a terrestrial gamma-ray flash. *Geophys. Res. Lett.*, **37**.
- Lyu, F., Cummer, S. A., & McTague, L. 2015. Insights into high peak current in-cloud lightning events during thunderstorms. *Geophys. Res. Lett.*, **42**(Aug.), 6836–6843.
- Lyu, Fanchao, Cummer, Steven A., Briggs, Michael, Marisaldi, Martino, Blakeslee, Richard J., Bruning, Eric, Wilson, Jennifer G., Rison, William, Krehbiel, Paul, Lu, Gaopeng, Cramer, Eric, Fitzpatrick, Gerard, Mailyan, Bagrat, McBreen, Sheila, Roberts, Oliver J., & Stanbro, Matthew. 2016. Ground detection of terrestrial gamma ray flashes from distant radio signals. *Geophys. Res. Lett.*, **43**(16), 8728–8734. 2016GL070154.

- Lyu, Fanchao, Cummer, Steven A., Krehbiel, Paul R., Rison, William, Briggs, Michael S., Cramer, Eric, Roberts, Oliver, & Stanbro, Matthew. 2018. Very High Frequency Radio Emissions Associated With the Production of Terrestrial Gamma-Ray Flashes. *Geophys. Res. Lett.*, **45**.
- Lyu, Fanchao, Cummer, Steven A., Qin, Zilong, & Chen, Mingli. 2019. Lightning Initiation Processes Imaged With Very High Frequency Broadband Interferometry. *J. Geophys. Res. Atmos.*, **124**, 2994–3004.
- MacGorman, Donald R., & Burgess, Donald W. 1994. Positive Cloud-to-Ground Lightning in Tornadoic Storms and Hailstorms. *Monthly Weather Review*, **122**(8), 1671–1697.
- Marisaldi, M., Fuschino, F., Labanti, C., Galli, M., Longo, F., Del Monte, E., Barbiellini, G., Tavani, M., Giuliani, A., Moretti, E., Vercellone, S., Costa, E., Cutini, S., Donnarumma, I., Evangelista, Y., Feroci, M., Lapshov, I., Lazzarotto, F., Lipari, P., Mereghetti, S., Pacciani, L., Rapisarda, M., Soffitta, P., Trifoglio, M., Argan, A., Boffelli, F., Bulgarelli, A., Caraveo, P., Cattaneo, P. W., Chen, A., Cocco, V., D’Ammando, F., De Paris, G., Di Cocco, G., Di Persio, G., Ferrari, A., Fiorini, M., Froyland, T., Gianotti, F., Morselli, A., Pellizzoni, A., Perotti, F., Picozza, P., Piano, G., Pilia, M., Prest, M., Pucella, G., Rappoldi, A., Rubini, A., Sabatini, S., Striani, E., Trois, A., Vallazza, E., Vittorini, V., Zambra, A., Zanello, D., Antonelli, L. A., Colafrancesco, S., Gasparrini, D., Giommi, P., Pittori, C., Preger, B., Santolamazza, P., Verrecchia, F., & Salotti, L. 2010. Detection of terrestrial gamma ray flashes up to 40 MeV by the AGILE satellite. *J. Geophys. Res.*, **115**(A14), 0.
- Marshall, T., Stolzenburg, M., Karunarathna, N., & Karunarathne, S. 2014. Electromagnetic activity before initial breakdown pulses of lightning. *J. Geophys. Res. Atmos.*, **119**(12558-12574).
- Marshall, T. C., Rust, W. D., & Stolzenburg, M. 1995a. Electrical structure and updraft speeds in thunderstorms over the southern Great Plains. *J. Geophys. Res.*, **100**(1001-1015).
- Marshall, T. C., Stolzenburg, M., Maggio, C. R., Coleman, L. M., Krehbiel, P. R., Hamlin, T., Thomas, R. J., & Rison, W. 2005. Observed electric fields associated with lightning initiation. *Geophys. Res. Lett.*, **32**.
- Marshall, Thomas, Stolzenburg, Maribeth, Karunarathne, Sumedhe, Cummer, Steve, Lu, Gaopeng, Betz, Hans-Dieter, Briggs, Michael, Connaughton, Valerie, & Xiong, Shaolin. 2013. Initial breakdown pulses in intracloud lightning flashes and their relation to terrestrial gamma ray flashes. *J. Geophys. Res.*, **118**.
- Marshall, Thomas, Bandara, Sampath, Karunarathne, Nilmini, Karunarathne, Sumedhe, Kolmasova, Ivana, Siedlecki, Raymond, & Stolzenburg, Maribeth. 2019. A study of lightning flash initiation prior to the first initial breakdown pulse. *Atmospheric Research*, **217**, 10–23.
- Marshall, Thomas C., & Rust, W. David. 1991. Electric Field Soundings Through Thunderstorms. *J. Geophys. Res.*, **96**(D12), 22297–22306.
- Marshall, Thomas C., McCarthy, Michael P., & Rust, W. David. 1995b. Electric Field Magnitudes and Lightning Initiation in Thunderstorms. *J. Geophys. Res.*, **100**(D4), 7097–7103.

- McHarg, Matthew G., Haaland, Ryan K., Moudry, Dana, & Stenbaek-Nielsen, Hans C. 2002. Altitude-time development of sprites. *J. Geophys. Res.*, **107**(A11).
- Moss, G. D., Pasko, V. P., Liu, N., & Veronis, G. 2006. Monte Carlo model for analysis of thermal runaway electrons in streamer tips in transient luminous events and streamer zones of lightning leaders. *J. Geophys. Res.*, **111**.
- Nag, Amitabh, & Cummins, Kenneth L. 2017. Negative first stroke leader characteristics in cloud-to-ground lightning over land and ocean. *Geophys. Res. Lett.*, **44**, 1973–1980.
- Nag, Amitabh, & Rakov, Vladimir A. 2010. Compact intracloud lightning discharges: 2. Estimation of electrical parameters. *J. Geophys. Res.*, **115**(D20103).
- Nag, Amitabh, DeCarlo, Brian A., & Rakov, Vladimir A. 2009. Analysis of microsecond- and submicrosecond-scale electric field pulses produced by cloud and ground lightning discharges. *Atmospheric Research*, **91**, 316–325.
- Nag, Amitabh, Rakov, Vladimir A., Tsalikis, Dimitris, & Cramer, John A. 2010. On phenomenology of compact intracloud lightning discharges. *J. Geophys. Res.*, **115**.
- Neubert, Torsten, Østgaard, Nikolai, Reglero, Victor, Chanrion, Olivier, Heumesser, Matthias, Dimitriadou, Krystallia, Christiansen, Freddy, Budtz-Jørgensen, Carl, Kuvvetli, Irfan, Rasmussen, Ib Lundgaard, Mezentsev, Andrey, Marisaldi, Martino, Ullaland, Kjetil, Genov, Georgi, Yang, Shiming, Kochkin, Pavlo, Navarro-Gonzalez, Javier, Connell, Paul H., & Eyles, Chris J. 2020. A terrestrial gamma-ray flash and ionospheric ultraviolet emissions powered by lightning. *Science*, **367**, 183–186.
- Ogawa, Toshio, & Brook, M. 1964. The mechanism of the intracloud lightning discharge. *J. Geophys. Res.*, **69**, 5141–5150.
- Orville, Richard E. 1968. A High-Speed Time-Resolved Spectroscopic Study of the Lightning Return Stroke: Part II. A Quantitative Analysis. *J. Atmospheric Sci.*, **25**, 839–851.
- Pasko, Victor P., Inan, Umran S., & Bell, Timothy F. 1998. Spatial structure of sprites. *Geophys. Res. Lett.*, **25**(12).
- Petersen, D., Bailey, M., Hallett, J., & Beasley, W. H. 2006. Laboratory investigation of positive streamer discharges from simulated ice hydrometeors. *Q. J. R. Meteorolog. Soc.*, **132**(615), 263–273.
- Petersen, Danyal, & Beasley, William. 2014 (June). High-Speed Video Observations of the Preliminary Breakdown Phase of a Negative Cloud-to-Ground Lightning Flash. *In: XV International Conference on Atmospheric Electricity*.
- Petersen, Danyal, Bailey, Matthew, Beasley, William H., & Hallett, John. 2008. A brief review of the problem of lightning initiation and a hypothesis of initial lightning leader formation. *J. Geophys. Res.*, **113**.

- Petersen, Danyal, Bailey, Matthew, Hallett, John, & Beasley, William. 2015. Laboratory investigation of corona initiation by ice crystals and its importance to lightning. *Q. J. R. Meteorolog. Soc.*, **141**, 1283–1293.
- Petersen, Danyal A., & Beasley, William H. 2013. High-speed video observations of a natural negative stepped leader and subsequent dart-stepped leader. *J. Geophys. Res.*, **118**, 12,110–12,119.
- Picard, J.-F. 1676. Experience faite à l’observatoire sur la barometre simple touchant un nouveau phenomene qu’on y a decouvert [Experiment made at the observatory on a simple barometer concerning a new phenomenon that was discovered there]. *Le Journal des Sçavans*, **4**, 112–113.
- Piel, Alexander. 2010. *Plasma Physics: An Introduction to Laboratory, Space, and Fusion Plasmas*. Berlin: Springer-Verlag.
- Pu, Y., Cummer, S. A., Lyu, F., Briggs, M., Mailyan, B., Stanbro, M., & Roberts, O. 2019. Low frequency radio pulses produced by terrestrial gamma-ray flashes. *Geophys. Res. Lett.*, **46**, 6990–6997.
- Pu, Yunjiao, Jiang, Rubin, Qie, Xiushu, Liu, Mingyuan, Zhang, Hongbo, Fan, Yanfeng, & Wu, Xueke. 2017. Upward negative leaders in positive triggered lightning: Stepping and branching in the initial stage. *Geophys. Res. Lett.*, **44**(7029-7035).
- Qin, Jianqi, & Pasko, Victor P. 2014. On the propagation of streamers in electrical discharges. *J. Phys. D: Appl. Phys.*, **47**(435202).
- Raizer, Yuri P. 1991. *Gas Discharge Physics*. Berlin: Springer-Verlag.
- Rakov, Vladimir A. 1998. Some inferences on the propagation mechanisms of dart leaders and return strokes. *J. Geophys. Res.*, **103**.
- Reess, Th, Ortega, P., Gibert, A., Domens, P., & Pignolet, P. 1995. An experimental study of negative discharge in a 1.3 m point-plane air gap: the function of the space stem in the propagation mechanism. *J. Phys. D: Appl. Phys.*, **28**, 2306–2313.
- Rhodes, C., & Krehbiel, P. R. 1989. Interferometric observations of a single stroke cloud-to-ground flash. *Geophys. Res. Lett.*, **16**.
- Riousset, Jeremy A., Pasko, Victor P., Krehbiel, Paul R., Thomas, Ronald J., & Rison, William. 2007. Three-dimensional fractal modeling of intracloud lightning discharge in a New Mexico thunderstorm and comparison with lightning mapping observations. *J. Geophys. Res.*, **112**(D15203).
- Rison, W., Thomas, R. J., Krehbiel, P. R., Hamlin, T., & Harlin, J. 1999. A GPS-based Three-Dimensional Lightning Mapping System: Initial Observations in Central New Mexico. *Geophys. Res. Lett.*, **26**(23), 3573–3576.
- Rison, W., Krehbiel, P. R., Stock, M. G., Edens, H. E., Shao, X., Thomas, R. J., Stanley, M. A., & Zhang, Y. 2016. Observations of narrow bipolar events reveal how lightning is initiated in thunderstorms. *Nat. Comm.*, **7**.

- Saba, Marcelo M. F., Cummins, Kenneth L., Warner, Tom A., Krider, E. Philip, Campos, Leandro Z. S., Ballarotti, Mauricio G., Jr., Osmar Pinto, & Fleenor, Stacy A. 2008. Positive leader characteristics from high-speed video observations. *Geophys. Res. Lett.*, **35**(L07802).
- Sadighi, Samaneh, Liu, Ningyu, Dwyer, Joseph R., & Rassoul, Hamid K. 2015. Streamer formation and branching from model hydrometeors in subbreakdown conditions inside thunderclouds. *J. Geophys. Res.*, **120**, 3660–3678.
- Shao, X. M., & Krehbiel, P. R. 1996. The spatial and temporal development of intracloud lightning. *J. Geophys. Res.*, **101**.
- Shao, X. M., Krehbiel, P. R., Thomas, R. J., & Rison, W. 1995. Radio interferometric observations of cloud-to-ground lightning phenomena in Florida. *J. Geophys. Res.*, **100**(D2), 2749–2783.
- Shao, Xuan-Min, Hamlin, Timothy, & Smith, David M. 2010. A closer examination of terrestrial gamma-ray flash-related lightning processes. *J. Geophys. Res.*, **115**.
- Shi, F., Liu, N. Y., Dwyer, Joseph R., & Ihaddadene, K. 2019. VHF and UHF electromagnetic radiation produced by streamers in lightning. *Geophys. Res. Lett.*, **46**, 443–451.
- Shi, Feng, Liu, Ningyu, & Rassoul, Hamid K. 2016. Properties of relatively long streamers initiated from an isolated hydrometeor. *J. Geophys. Res.*, **121**, 7284–7295.
- Smith, D. A., Shao, X. M., Holden, D. N., Rhodes, C. T., Brook, M., Krehbiel, P. R., Stanley, M., Rison, W., & Thomas, R. J. 1999. A distinct class of isolated intracloud lightning discharges and their associated radio emissions. *J. Geophys. Res.*, **104**(D4).
- Smith, D. A., Heavner, M. J., Jacobson, A. R., Shao, X. M., Massey, R. S., Sheldon, R. J., & Wiens, K. C. 2004. A method for determining intracloud lightning and ionospheric heights from VLF/LF electric field records. *Radio Science*, **39**(RS1010).
- Smith, D. M., Lopez, L. I., Lin, R. P., & Barrington-Leigh, C. P. 2005. Terrestrial gamma-ray flashes observed up to 20 MeV. *Science*, **307**(5712), 1085–1088.
- Smith, Stephan B., LaDue, James G., & MacGorman, Donald R. 2000. The Relationship between Cloud-to-Ground Lightning Polarity and Surface Equivalent Potential Temperature during Three Tornado Outbreaks. *Monthly Weather Review*, **128**(9), 3320–3328.
- Stanley, M. A., Shao, X.-M., Smith, D. M., Lopez, L. I., Pongratz, M. B., Harlin, J. D., Stock, M., & Regan, A. 2006. A link between terrestrial gamma-ray flashes and intracloud lightning discharges. *Geophys. Res. Lett.*, **33**.
- Stanley, M.A., Rison, W., Tilles, J., Krehbiel, P.R., Brown, R.G., Wilson, J., & Liu, N. 2018a (March). Broadband VHF Interferometry within the Kennedy Space Center Lightning Mapping Array. In: *25th International Lightning Detection Conference and 7th International Lightning Meteorology Conference*.
- Stanley, Mark, Krehbiel, Paul, Brook, Marx, Moore, Charles, Rison, William, & Abrahams, Bill. 1999. High speed video of initial sprite development. *Geophys. Res. Lett.*, **26**(20), 3201–3204.

- Stanley, Mark A., Rison, William, Tilles, Julia N., Krehbiel, Paul R., Brown, Robert G., Wilson, Jennifer G., & Liu, Ningyu. 2018b (June). Broadband VHF Interferometry Observations at the Kennedy Space Center. *In: XVI International Conference on Atmospheric Electricity*.
- Stock, M. 2014. *Broadband interferometry of lightning*. PhD dissertation, New Mexico Institute of Mining and Technology.
- Stock, M. G., Akita, M., Krehbiel, P. R., Rison, W., Edens, H. E., Kawazaki, Z., & Stanley, M. A. 2014. Continuous broadband digital interferometry of lightning using a generalized cross-correlation algorithm. *J. Geophys. Res.*, **119**, 3134–3165.
- Stock, Michael, & Krehbiel, Paul. 2014 (October). Multiple baseline lightning interferometry - Improving the detection of low amplitude VHF sources. *In: International Conference on Lightning Protection (ICLP)*.
- Stolzenburg, M., Marshall, T. C., Karunarathne, S., Karunarathna, N., Vickers, L. E., Warner, T. A., Orville, R. E., & Betz, H.-D. 2013. Luminosity of initial breakdown in lightning. *J. Geophys. Res.*, **118**, 2918–2937.
- Stolzenburg, M., Marshall, T. C., Karunarathne, S., Karunarathna, N., & Orville, R. E. 2014. Leader observations during the initial breakdown stage of a lightning flash. *J. Geophys. Res. Atmos.*, **119**, 12198–12221.
- Stolzenburg, Maribeth, & Marshall, Thomas C. 2008. Serial profiles of electrostatic potential in five New Mexico thunderstorms. *J. Geophys. Res.*, **113**.
- Stolzenburg, Maribeth, Rust, W. David, & Marshall, Thomas C. 1998. Electrical structure in thunderstorm convective regions 2. Isolated storms. *J. Geophys. Res.*, **103**.
- Stolzenburg, Maribeth, Marshall, Thomas C., Rust, W. David, Bruning, Eric, MacGorman, Donald R., & Hamlin, Timothy. 2007. Electric field values observed near lightning flash initiations. *Geophys. Res. Lett.*, **34**.
- Stolzenburg, Maribeth, Marshall, Thomas C., Karunarathne, Sumedhe, & Orville, Richard E. 2016. Luminosity with intracloud-type lightning initial breakdown pulses and terrestrial gamma-ray flash candidate. *J. Geophys. Res.*, **121**, 10919–10936.
- Suszcynsky, D. M., & Heavner, M. J. 2003. Narrow Bipolar Events as indicators of thunderstorm convective strength. *Geophys. Res. Lett.*, **30**(17).
- Takahashi, T. 1978. Riming electrification as a charge generation mechanism in thunderstorms. *J. Atmos. Sci.*, **35**, 1536–1548.
- Taylor, G. B., Carilli, C. L., & Perley, R. A. (eds). 1999. *Synthesis Imaging in Radio Astronomy II*. Astronomical Society of the Pacific Conference Series, vol. 180.
- Thomas, R.J., Krehbiel, P.R., Rison, W., Hamlin, T., Harlin, J., & Shown, D. 2001. Observations of VHF source powers radiated by lightning. *Geophys. Res. Lett.*, **28**(1).

- Thomas, Ronald J., Krehbiel, Paul R., Rison, William, Hunyady, Steven J., Winn, William P., Hamlin, Timothy, & Harlin, Jeremiah. 2004. Accuracy of the Lightning Mapping Array. *J. Geophys. Res.*, **109**.
- Tilles, J. 2015. *Charge Structures in New Mexico, Colorado, and South Dakota*. MSc dissertation, New Mexico Institute of Mining and Technology.
- Tilles, Julia, Liu, Ningyu, Stanley, Mark A., Krehbiel, P. R., Rison, W., Stock, M. G., Dwyer, Joseph R., Brown, Robert, & Wilson, Jennifer. 2019. Fast negative breakdown in thunderstorms. *Nat. Comm.*, **10**(1648).
- Tilles, Julia N, Liu, Ningyu, Krehbiel, Paul R, Rison, William, Stanley, Mark A, Brown, Robert G, Wilson, Jennifer G., Boggs, Levi, & Stock, Michael. 2016 (December). Interferometer study of Narrow Bipolar Events (NBEs) in Florida. *In: AGU Fall Meeting*.
- Tilles, Julia N., Liu, Ningyu, Krehbiel, Paul R., Stanley, Mark A, Rison, William, Dwyer, Joseph R., Brown, Robert G., & Wilson, Jennifer. 2020a. Initial breakdown in intra-cloud and cloud-to-ground lightning. *Geophys. Res. Lett.* to be submitted.
- Tilles, Julia N., Krehbiel, Paul R., Stanley, Mark A, Rison, William, Liu, Ningyu, Lyu, Fanchao, Cummer, Steven A., Dwyer, Joseph R., Senay, Seda, Edens, Harald, Brown, Robert G., & Wilson, Jennifer. 2020b. Radio interferometer observations of an energetic in-cloud pulse reveal large currents generated by relativistic discharges. *J. Geophys. Res.* under review.
- Townsend, J. S. 1900. The Conductivity produced in Gases by the Motion of Negatively-charged Ions. *Nature*, **62**(340).
- Uman, Martin A. 2001. *The Lightning Discharge*. Mineola, New York: Dover Publications.
- Ushio, Tomoo, Heckman, Stan J., Boccippio, Dennis J., Christian, Hugh J., & Kawasaki, Zen-Ichiro. 2001. A survey of thunderstorm flash rates compared to cloud top height using TRMM satellite data. *J. Geophys. Res.*, **106**(D20).
- van der Velde, Oscar A., & Montanya, Joan. 2013. Asymmetries in bidirectional leader development of lightning flashes. *J. Geophys. Res.*, **118**.
- Villanueva, Y., Rakov, V. A., Uman, M. A., & Brook, M. 1994. Microsecond-scale electric field pulses in cloud lightning discharges. *J. Geophys. Res.*, **99**, 14353–14360.
- Weidman, Charles D., & Krider, E. Philip. 1979. The Radiation Field Wave Forms Produced by Intracloud Lightning Discharge Processes. *J. Geophys. Res.*, **84**(C6).
- Wiens, Kyle C., Hamlin, Timothy, Harlin, Jeremiah, & Suszcynsky, David M. 2008. Relationships among Narrow Bipolar Events, “total” lightning, and radar-inferred convective strength in Great Plains thunderstorms. *J. Geophys. Res.*, **113**.
- Willett, J. C., Bailey, J. C., & Krider, E. P. 1989. A Class of Unusual Lightning Electric Field Waveforms With Very Strong High-Frequency Radiation. *J. Geophys. Res.*, **94**(D13), 16,255–16,267.

- Williams, E. R. 1989. The Tripole Structure of Thunderstorms. *Geophys. Res. Lett.*, **94**, 13151–13167.
- Williams, Earle R. 2006. Problems in lightning physics—the role of polarity asymmetry. *Plasma Sources Science and Technology*, **15**, S91–S108.
- Wilson, C. T. R. 1925. The acceleration of β -particles in strong electric fields such as those of thunder-clouds. *Mathematical Proceedings of the Cambridge Philosophical Society*, **22**(4), 534–538.
- Winn, William P., Schwede, G. W., & Moore, C. B. 1974. Measurements of Electric Fields in Thunderclouds. *J. Geophys. Res.*, **79**(12).
- Wu, Bin, Zhang, Guangshu, Wen, Jun, Zhang, Tong, Li, Yajun, & Wang, Yanhui. 2016. Correlation analysis between initial preliminary breakdown process, the characteristic of radiation pulse, and the charge structure on the Qinghai-Tibetan Plateau. *J. Geophys. Res.*, **121**.
- Wu, Ting, Dong, Wansheng, Zhang, Yijun, & Wang, Tao. 2011. Comparison of positive and negative compact intracloud discharges. *J. Geophys. Res.*, **116**.
- Wu, Ting, Dong, Wansheng, Zhang, Yijun, Funaki, Tsuyoshi, Yoshida, Satoru, Morimoto, Takeshi, Ushio, Tomoo, & Kawasaki, ZenIchiro. 2012. Discharge height of lightning narrow bipolar events. *J. Geophys. Res.*, **117**(D05119).
- Wu, Ting, Takayanagi, Yuji, Funaki, Tsuyoshi, Yoshida, Satoru, Ushio, Tomoo, Kawasaki, ZenIchiro, Morimoto, Takeshi, & Shimizu, Masahito. 2013. Preliminary breakdown pulses of cloud-to-ground lightning in winter thunderstorms in Japan. *Journal of Atmospheric and Solar-Terrestrial Physics*, **102**, 91–98.